Chair of Ferrous Metallurgy

Doctoral Thesis

Development of characterization methods for the evaluation of the kinetic behavior and the fluidization of iron ore fines during hydrogen-induced fluidized bed reduction
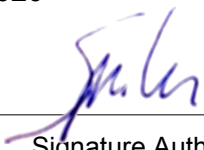
Dipl.-Ing. Daniel Spreitzer, BSc

July 2020

AFFIDAVIT

I declare on oath that I wrote this thesis independently, did not use other than the specified sources and aids, and did not otherwise use any unauthorized aids.

I declare that I have read, understood, and complied with the guidelines of the senate of the Montanuniversität Leoben for "Good Scientific Practice".

Furthermore, I declare that the electronic and printed version of the submitted thesis are identical, both, formally and with regard to content.

Date 07.07.2020

_____
Signature Author
Daniel, Spreitzer

Preface

The preparation of a doctoral thesis is an endeavor which is not possible without the assistance of competent people. First, I would like to express my gratitude to my supervisor, Prof. Johannes Schenk, for his great support and input during the research work. I would also like to thank Prof. Hermann Hofbauer for the time spent in discussions and peer-reviewing of the thesis.

I wish to thank my graduate and undergraduate students who contributed to the scientific work within the research project for their kind assistance and cooperation. In addition, I am thankful to all my colleagues for the good collaboration and the interesting conversations.

Lastly and most importantly, I wish to thank my family and girlfriend for their support throughout my studies.

Abstract

The hydrogen-induced fluidized bed reduction of iron ore fines might be a promising process technology for future-minded ironmaking. Recently, conventional ironmaking processes have typically been based on fossil energy carriers. As a result, the production of iron and crude steel ends in the emission of enormous amounts of carbon dioxide, which is in fact not sustainable. To decrease the emissions of carbon dioxide to an acceptable level, the use of hydrogen as an energy carrier and reducing agent might be the only solution for the long-term, sustainable production of iron and crude steel. In general, conventional ironmaking processes, such as the blast furnace, cannot be operated with pure hydrogen because of the process concept used. The use of fluidized bed reactors for the reduction of iron ores makes an exclusive input of hydrogen probable. Aside from that it is also possible to treat iron ore fines directly without prior agglomeration steps. This ends in the avoidance of these energy-intensive process steps.

In the present study, the kinetic behaviors of different iron ore fines during hydrogen-induced fluidized bed reduction are investigated by using a developed approach based on the model designed by Johnson, Mehl and Avrami. The results show that the total reduction process, from hematite to metallic iron, can be described well by using the defined approach. It is shown that the rate-limiting mechanisms chemical reaction and nucleation are the most important steps during hydrogen-induced fluidized bed reduction. Because of the widespread availability of magnetite-based iron ore fines on the market, different opportunities for the treatment of such iron ores without troubles regarding de-fluidization and reducibility are investigated and possible process concepts for successful treatment are presented. It is shown that a prior oxidation of the magnetite still has an influence on the fluidization behavior and the reducibility but a successful operation is only possible with an addition of MgO to the material. The best combination of the properties can be attained with partial prior oxidation. A direct use of hematite and magnetite-based ultra-fines for hydrogen-induced fluidized bed reduction is also examined regarding its suitability for direct ironmaking. In contrast to results reported in literature, a stable fluidization of this fine-grained material is also possible at high metallization degrees without any sticking troubles for hematite-based ores. Different reduction experiments with different laboratory fluidized bed reactors were carried out in

combination with morphological investigations of the raw materials as well as the reduced samples after reduction.

Kurzfassung

Die wasserstoffbasierte Reduktion von Feineisenerzen mittels Wirbelschichttechnologie stellt eine Alternative für die zukünftige Herstellung von Eisen dar. Typische Verfahren zur Eisen- und Rohstahlherstellung arbeiten heutzutage üblicherweise mithilfe von fossilen Energieträgern. Die Emittierung von großen Mengen an Kohlenstoffdioxid ist daher unumgänglich. Die Verwendung von Wasserstoff als Energieträger und Reduktionsmittel stellt die einzige sinnvolle Maßnahme dar, um die Emissionen von Kohlenstoffdioxid auf ein angemessenes Level zu reduzieren und um Stahl auch in Zukunft nachhaltig produzieren zu können. Konventionelle Verfahren zur Eisen- bzw. Stahlherstellung, wie zum Beispiel der Hochofenprozess, besitzen nicht die Möglichkeit, auf reinem Wasserstoff umgestellt werden zu können. Dies ist auf das Verfahrenskonzept zurückzuführen. Eine Verwendung der Wirbelschichttechnologie hingegen erlaubt einen ausschließlichen Einsatz von Wasserstoff als Energieträger und Reduktionsmittel. Des Weiteren können Feineisenerze ohne vorgeschaltete Agglomeration direkt dem Prozess zugeführt werden, wodurch diese energieintensiven Prozesse vermieden bzw. eingespart werden können.

In dieser Arbeit wird das kinetische Verhalten von unterschiedlichen Feineisenerzen während der wasserstoffbasierten Wirbelschichtreduktion mittels der Anwendung eines entwickelten Ansatzes, welcher auf dem Model von Johnson, Mehl und Avrami basiert, untersucht. Die Untersuchungen zeigen, dass der gesamte Reduktionsprozess von Hämatit bis zum metallischen Eisen sehr gut mit dem angewendeten Model beschrieben werden können. Als reaktionslimitierende Schritte treten während der wasserstoffbasierten Wirbelschichtreduktion hauptsächlich die chemische Reaktion selbst sowie der Vorgang der Keimbildung auf. Aufgrund der weltweiten Verfügbarkeit von magnetitischen Eisenerzen werden unterschiedliche Möglichkeiten der Verwendung solcher Erze in der Wirbelschicht aufgezeigt. Dabei wird vor allem auf das Fluidisierungsverhalten und die Reduzierbarkeit eingegangen und unterschiedliche Möglichkeiten zur Beeinflussung aufgezeigt sowie ein optimiertes Prozesskonzept entwickelt. Es zeigt sich, dass eine vorangehende Oxidation des Magnetits zu einer Beeinflussung der Fluidisierung und der Reduzierbarkeit führt wobei eine vollständige Fluidisierung nur durch Zugabe von MgO zum Eisenerz erreicht werden kann. Die beste Kombination der Eigenschaften Fluidisierungsverhalten und Reduzierbarkeit kann mit teilweise oxidiertem Material erreicht werden. Des Weiteren wird die Möglichkeit einer

direkten Verwendung von hämatitischen und magnetitischen Feinsteisenerzen in der Wirbelschicht untersucht. Im Gegensatz zu in der Literatur veröffentlichten Ergebnissen konnte für hämatitische Erze eine stabile Fluidisierung ohne eintretendes Sticking erreicht werden, selbst bei hohen Reduktionsgraden. Die Untersuchungen wurden in unterschiedlichen Wirbelschichtreaktoren im Labormaßstab durchgeführt. Zusätzlich wurden morphologische Untersuchungen der Einsatzstoffe sowie der reduzierten Proben durchgeführt.

Table of contents

Nomenclature

a	Nucleation rate constant (1/s)
A	Pre-exponential factor (1/s)
A,B	Constants of defined components
a_i	Activity of component i (-)
Ar	Archimedes number (-)
$A_{Reactor}$	Free reactor area (m²)
c_D	Drag coefficient (-)
c_i	Concentration of gaseous reactant i
D	Reactor diameter (m, mm)
DFI	De-fluidization index (-)
d_p	Particle diameter (m, mm)
$d_p{}^*$	Dimensionless particle diameter (-)
$\overline{dp}$	Mean particle diameter (m)
d_{sv}	Diameter of a sphere with the same surface to volume ratio (m)
E_a	Apparent activation energy (kJ/mol)
F	Ratio between reaction time and overall reaction time (-)
f(x)	Mathematical function (-)
F_A	Buoyancy force (N)
F_G	Gravitational Force (N)
F_w	Drag force (N)
$F_{\Delta p}$	Force by pressure loss (N)
g	Gravitational constant (m/s²)
g(x)	Integrated expression of mathematical function (-)

GOD	Gas oxidation degree (-)
H,L	Bed height (m)
H_f, L_f	Bed height in fluidized state (m)
H_{mf}, L_{mf}	Bed height at minimum fluidization conditions (m)
K	Equilibrium constant (-)
k(T)	Arrhenius rate constant (1/s)
K_1, K_2	Constants, used in Equations 26 to 28 (-)
$K_{ih}*$	Elutriation rate constant (kg/m²·s)
m	Sample mass (g)
M_B	Sample mass bed material (g)
Met	Metallization (-)
M_i	Molecular weight of component l (g/mol)
$m_{i,t}$	Mass of size fraction i carried over at time t (g)
m_p	Mass of a single particle (g)
n	Kinetic exponent (-)
p_i	Partial pressure of component i (bar)
R	Gas constant (J/K·mol)
RD	Degree of reduction (-)
Re	Reynolds number (-)
$Re_{p,mf}$	Particle Reynolds number at minimum fluidization conditions (-)
SGR	Specific gas rate (Nm³/t)
SGR_{95}	Specific gas rate to reach 95 % degree of reduction (Nm³/t)
T	Temperature (°C, K)
t	Time (min, s)
u	Superficial gas velocity (m/s)
u*	Dimensionless gas velocity (-)
u_{mf}, w_{mf}	Minimum fluidization velocity (m/s)
u_t, w_t	Terminal velocity (m/s)
V	Volume (m³)
$\dot{V}$	Volumetric flow rate (l/min)
w	Weight factor (-)
w_i	Mass Fraction of component i (-)
x	Conversion (-)
x_{Bi}	Equilibrium concentration of size d_{pi} particles (-)
x_{calc}	Calculated values of conversion (-)
x_{exp}	Conversion observed during the experiments (-)
x_i	Molar ratio of component i (-)

ΔG	Free enthalpy (J)
ΔH	Enthalpy (J)
Δp	Pressure drop (mbar)
Δp_{Bed}	Pressure drop across bed material (mbar)
$\Delta p_{Distributor}$	Pressure drop across gas distributor (mbar)
ΔS	Entropy (J/K)
ε	Voidage (-)
ε_{mf}	Voidage at minimum fluidization conditions (-)
η	Dynamic viscosity fluid (Pa·s, N·s/m²)
ρ_F	Density fluid (kg/m³)
ρ_S	Density solids (kg/m³)
ϕ_s	Sphericity of the solid particles (-)
$\phi_{i,j}$	Interaction coefficients between the components i and j (-)

Abbreviations

B.E.T.	Brunauer-Emmet-Teller
BF	Blast furnace
BOF	Basic oxygen furnace
CDRI	Cold direct reduced iron
DR	Direct reduction
DRI	Direct reduced iron
EAF	Electric arc furnace
FBR	Fluidized bed reactor
HBI	Hot briquetted iron
HDRI	Hot direct reduced iron
JMA	Johnson-Mehl-Avrami
LOI	Loss on ignition
MG	Melter gasifier
NM	Natural Magnetite
OLM	Optical light microscope
OM	Oxidized magnetite
PCI	Pulverized coal injection
POM	Partial oxidized magnetite
R^2	Coefficient of determination
SATP	Standard ambient temperature and pressure (T = 25 °C, p = 1 atm)
SEM	Scanning electron microscope
SR	Smelting reduction
SRA	Substitute reducing agents
SRC	Standard reduction conditions

Chemical Elements and Molecules

Al	Aluminum
Al_2O_3	Alumina
Ca	Calcium
CaO	Calcium oxide
CO	Carbon monoxide
CO_2	Carbon dioxide
Fe, Fe_{met}	Metallic iron
Fe_2O_3	Hematite
Fe_3O_4	Magnetite
FeO	Wüstite
Fe_{tot}	Total iron content
H_2	Hydrogen
H_2O	Water vapor
Mg	Magnesium
MgO	Magnesium oxide
O	Oxygen
Si	Silicon
SiO_2	Silica
W	Tungsten

List of figures

List of tables

1 Introduction and purpose of the work

1.1 Introduction

Steel is one of the most important materials which can be used for several different types of applications. This is possible because of the wide range of properties which can be achieved using different alloying compositions and production procedures. From the simplest application in concretes, steel can also be used for high quality applications such as aircraft landing gears. Iron, as the main carrier of steel, can be produced easily out of its ores compared to other construction materials, such as aluminum or titanium. Although the energy demand for the production of crude steel is lower compared to other materials, the enormous amount of steel produced makes the iron and steel producing industry a big energy-consuming industrial sector. Overall steel production more than doubled in the last 20 years, from 850 in 2000 to approximately 1800 million tons of production in 2018, as shown in Figure 1, which also includes the average growth rates per annum.[1] This mainly contributes to the big expansion of the production capacities in China. In 2000, the production share of China was only 15.0 %, which increased to 51.1 % in 2019, shown in Figure 2.[2,3] Right now, the production of crude steel is primarily based on the conventional process route blast furnace (BF) and basic oxygen converter (BOF). Ironmaking using the BF-BOF route requires a high amount of fossil energy carriers, especially coking coal. On the one hand, it is necessary to provide the required energy for the process; on the other hand, carbon from the coke acts as a reducing agent. This ends in a high amount of corresponding carbon dioxide emissions formed in such an integrated steel plant. A typical value of carbon dioxide emissions per ton of produced crude steel is approximately 1.9 tons.[4] It depends on the operation mode and the boundary conditions of the steel plant, such as carbon dioxide load of raw material transport, etc. Because of the high production volume of crude steel and the fact that the production is mainly done via the BF-BOF route, the iron and steel producing industry is responsible for approximately 6-9 % of anthropogenic carbon dioxide emissions. Considering the fact that the iron and steelmaking industry is only one industrial sector, 6-9 % of carbon dioxide emissions represents a huge amount.
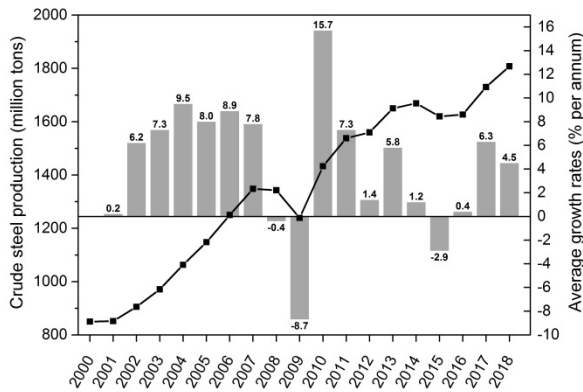
Figure 1: Steel production and average growth rates from 2000 to 2018.[1]
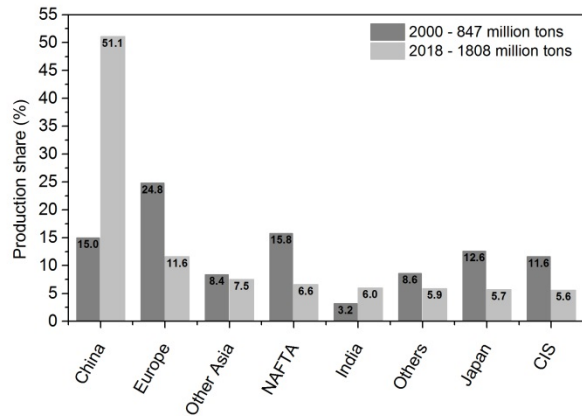
Figure 2: Comparison of production share by countries in 2000 and 2018.[2,3]

Carbon dioxide belongs to the harmful greenhouse gases responsible for the greenhouse effect and therefore, for global warming. In recent years, public and political pressure have increased and the iron and steelmaking industry has been faced with the challenge of decreasing their carbon dioxide emissions. The European Union has defined a roadmap where the emission of greenhouse gases should be reduced to a level of -95 % compared to the 1990s. Figure 3 shows the trends of the carbon dioxide equivalent over the last 20 years including linear paths to reach the defined targets. Emissions from the land use sector are not included. As shown, the defined goals can only be achieved by using additional measures, representing the substitution of fossil energy sources by other energy sources, such as hydrogen. This is also the only solution for energy intensive industrial sectors. Hydrogen should thus be produced from renewable energy sources without carbon dioxide load.
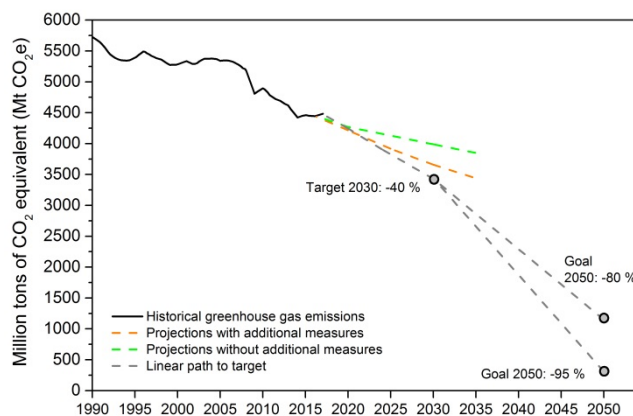
Figure 3: Trend of CO_2 equivalent for the European Union including projections to reach the targets by 2050.[5]

In the case of the iron and steel producing industry, changing the production processes based on fossil fuels to hydrogen based processes is not an easy step. To use hydrogen as

an energy source and reducing agent, new process concepts are required. It is not possible to substitute coke completely with hydrogen in a blast furnace because coke is required in the cohesive zone to ensure sufficient gas permeability as well as in the metallurgical zone to guarantee gas, metal and slag drainage. As a result, the blast furnace process is not an option to meet the requirements concerning future environmental issues. To get rid of this problem, other production technologies are required. One solution is the direct reduction (DR) for the production of direct reduced iron (DRI), which can be further used in the electric arc furnace (EAF) alone or together with scrap to be melted to crude steel. In principle, DR processes are able to use only hydrogen as a reducing agent because they operate at temperatures below the melting point of all phases involved in the process. So, the iron ore is reduced directly by the reducing gas in solid state. Aside from the typical shaft furnace technology, direct reduction can be also done using the fluidized bed technology. Iron ore fines can be used directly in the process which prevents the necessity of a prior agglomeration step. Right now, direct reduction processes using natural gas as an energy source and reducing agent are state of the art. The natural gas is reformed with water vapor and/or carbon dioxide to hydrogen and carbon monoxide mixtures. As a result, accompanying carbon dioxide emissions can be reduced compared to the conventional BF-BOF route. Another possibility to decrease the carbon dioxide emissions is the scrap-based crude steel production using an EAF. One problem for increasing the scrap-based crude steel production right now is the availability of scrap in sufficient amounts and quality as well as the limited product quality, which pertains to the scrap quality. To get rid of this problem, more attention has to be paid to the classification and separation of the scrap in the future. Figure 4 shows average values for the carbon dioxide emissions in kg per ton of liquid steel. Detailed explanations concerning assumptions for the calculations are given in [4]. The carbon dioxide emissions for the DR-EAF route are much lower compared to the BF-BOF route because of the use of natural gas as an energy source. For the scrap-EAF route a further decrease could be achieved because no reduction work needs to be done. Figure 5 shows the production share between BOF and EAF for different countries in 2018. In China, more than 90 % of total production is done using the BF-BOF, route which is due to the rapid growth in the last 20 years as well as the decreased scrap availability.
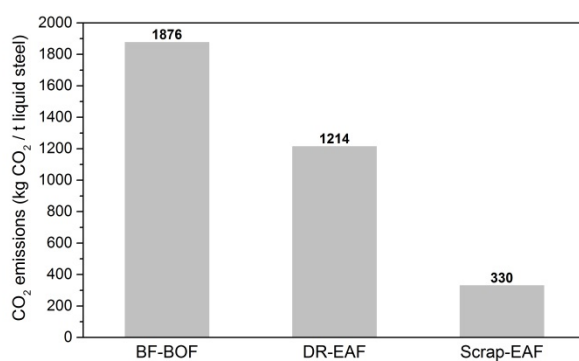
Figure 4: Comparison of CO_2 emissions for different production routes.[4]
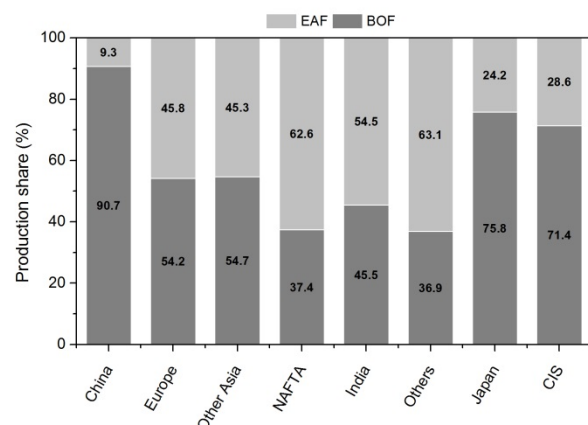
Figure 5: Production share BOF/EAF by country in 2018.[1]

To reach climate targets, the production share of BF-BOF has to be further reduced within the next few years. To ensure an almost carbon-free steel production, DR processes based on hydrogen should also be further developed. Over the next few years, a sufficient amount of hydrogen to satisfy the big demand will not be available, which is why the use of DR processes based on natural gas should be further intensified. Afterwards, natural gas can be substituted step by step with green hydrogen produced from renewable energy sources.

1.2 Purpose of the work

This thesis deals with the topic of fluidized bed reduction of iron ore fines using hydrogen as a reducing agent. Fluidized bed reduction is a future-minded technology to meet upcoming requirements regarding environmental issues. On the one hand, pure hydrogen can be used as an energy source and reducing agent; on the other hand, iron ore fines can be used directly without prior agglomeration. This avoids an energy-intensive agglomeration process such as pelletizing. The research carried out in this work can be classified into three work packages:

The first one deals with the general investigation of the fluidization behavior of different iron ore fines and the kinetics of the hydrogen-induced reduction using the fluidized bed technology. The fluidization behavior of the iron ore fines is one of the major issues during the reduction procedure. Especially at high degrees of reduction, the particles tend to stick together, representing the so-called sticking phenomenon. As a result, it is required to operate the process in a way that is suitable to reach high degrees of reduction without the sticking phenomenon occurring. Different iron ores are tested and evaluated regarding their kinetical behavior. Different models are used and the results are checked regarding their plausibility. In literature, kinetic analysis of the iron oxide reduction is often carried out by focusing on only one sequence of the reduction progress using one model for the description of the limiting mechanism. Consequently, is not possible to describe the reduction accurately because of the possibility that more than one rate-limiting step takes place at the same time. In order to avoid this problem, a model is developed which is able to describe the total reduction process from hematite to metallic iron, taking into account that more than one rate limiting mechanism can act in a parallel way. The model is based on the one developed by Johnson, Mehl and Avrami. As a basis for the investigations, experimental results obtained from the experiments with a laboratory fluidized bed reactor, installed at the Chair of Ferrous Metallurgy of the Montanuniversitaet Leoben, are used.

The second area involves the topic of the direct use of magnetite-based iron ores for fluidized bed reduction with hydrogen. Magnetite-based ores show a high sticking tendency and a poor reducibility because of their dense structure. Therefore, the effect of a prior oxidation to Fe_2O_3 and the addition of additives on the reducibility and the fluidization behavior are discussed. Currently, no general concept for the successful treatment of magnetite-based iron ores during fluidized bed reduction is available in literature. One possible methodology is developed and presented within this work.

The last area considers the direct use of iron ore concentrate (ultra-fines) for hydrogen-induced fluidized bed reduction. The direct use of this material is interesting because the

availability of ultra-fine ores is increasing due to deteriorating iron ore reserve qualities. From 2010 to 2015 the global ultra-fines supply rose from approximately 100 to 300 million tons per year.[6] Iron ore ultra-fines are typically characterized by their very small grain size distribution; all particles usually have a size below 125 μm. Such small particle size distributions can lead to troubles concerning stable fluidization because of cohesive forces acting between the small particles. These forces can become bigger than those which the fluid can exert to the particles. Another problem might be the high amount of elutriation which will occur already at very low superficial gas velocities inside the reactor. For that reason, the fluidization behavior, reducibility and elutriation of such materials are investigated for hematite and magnetite-based concentrates. Thus, the general suitability of iron ore ultra-fines for hydrogen-based direct reduction using the fluidized bed technology is assessed within this work.

2 Theoretical considerations

In the following sections, theoretical considerations are shown which are important for the work carried out within this thesis. This represents a brief overview of different steel production routes and thermodynamics of the iron ore reduction, an overview of the kinetical mechanisms during the reduction and the principles of the fluidization phenomenon.

2.1 Steel production routes – an overview

To produce crude steel, different production routes are available and state of the art. The main differences between the production routes are the type of input materials and the energy sources used, which ends in different process concepts. Based on iron ore as an iron carrier, three different production routes can be distinguished: the integrated blast furnace-basic oxygen converter route, smelting reduction processes (SR) and direct reduction processes. If scrap is used as an iron carrier, the crude steel production occurs mainly with an electric arc furnace (EAF). Figure 6 shows the different steel production routes schematically. The different routes based on iron ore are described briefly below.
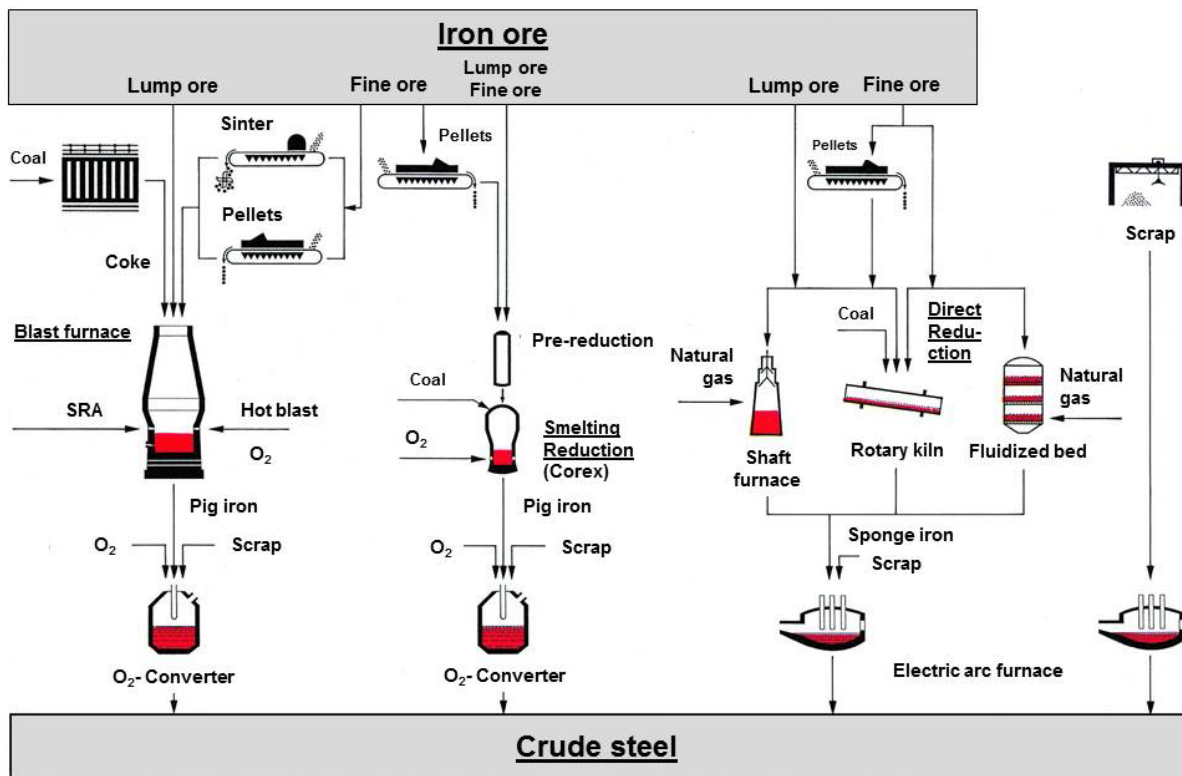
Figure 6: Different state of the art steel production routes.[7]

Integrated blast furnace – basic oxygen converter route

Generally, the integrated BF-BOF route uses a BF to produce liquid pig iron with high carbon content (4-4.7 %-wt.). Further processing of the liquid pig iron takes place in a basic oxygen converter to decrease the carbon and the phosphorous content. The blast furnace itself represents a typical shaft furnace where the solid input materials are fed from the top of the reactor. The hot blast is injected in the lower section of the furnace, passing it from the bottom to the top. To guarantee sufficient gas permeability as well as a good metal and slag drainage in the metallurgical zone, lumpy input materials are required. Sinter, pellets and lump ores are used as iron carriers. Thus, a prior agglomeration step is required to produce sinter or pellets out of iron ore fines. This is done using sintering or pelletizing plants. Coke acts as an energy source in the process. Coke has to be produced out of coking coal using a coking plant and it is also charged from the top of the reactor, together with the iron carriers. To reduce the required specific coke rate, substitute reducing agents (SRA) can also be used in the process. Together with the hot blast, they are injected in the lower section of the furnace. Pulverized coal injection (PCI) is one development of the past few decades, which is why fine coal is injected into the furnace. As a result, the specific coke rate can be decreased.[8,9] The integrated route has two main disadvantages representing the necessity of lumpy input materials as well as the high amount of carbon dioxide emissions leaving the steel plant because coal is used as the main energy carrier.

Smelting reduction processes

Smelting reduction processes consist of two process units; a pre-reduction unit where the iron ore is reduced to a certain degree of reduction and a melting unit (melter gasifier-MG) where the final reduction and the melting of the reduced iron takes place. Generally, coal is used as an energy carrier which is fed directly to the MG. The off-gas of the MG is then used in the pre-reduction stage for the reduction work. The product of the MG is similar to that of the BF. As a result, a further BOF processing of the product is also required. During the last few decades, numerous different smelting reduction processes have been developed.[10,11] Different process concepts are used depending on the type of input materials. The two most important smelting reduction processes are the Corex® and Finex® processes. Both are industrially proven technologies. The main difference between these two routes is the layout of the pre-reduction stage. The Finex®-process uses a 3-stage fluidized bed reactor cascade for the pre-reduction of the iron ore,[12,13] making it possible to charge iron ore fines directly to the process. The Corex® process uses a shaft furnace as a pre-reduction stage,[14] so lumpy iron carriers are required. Compared to the integrated route, smelting reduction processes have the advantage of a direct use of coal. Accordingly, there is no necessity for a coking plant. In the case of Finex®, a prior iron ore agglomeration is not required, either. No advantages can be achieved regarding carbon dioxide emissions. Both process routes are in the same range compared to the BF-BOF route because again carbon acts as an energy source and reducing agent.

Direct reduction processes

Direct reduction processes operate below the melting temperature of all phases involved in the process. Accordingly, the input materials and the product of the processes are in a solid state. The product is called direct reduced iron or sponge iron with a high metallization rate, typically >85%.[15] The reduction of the iron oxides takes place by a gaseous reactant, typically provided by the partial oxidation of coal or reforming of natural gas. Similar to the smelting reduction processes, a lot of different process concepts have been developed during the last few decades. The two most important direct reduction processes are based on the shaft furnace technology, known as Midrex® and HYL-Energiron.[16,17] In these processes natural gas is used as an energy source and reducing agent. Other process concepts use the rotary kiln technology for the reduction procedure. In those cases, coal is used as an energy source. Another concept is the use of the fluidized bed technology for the reduction, where iron ore fines can be used directly. These processes are explained later on more in detail because of their importance for the work carried out within this thesis. Direct reduction processes based on natural gas have the advantage of lower carbon monoxide emissions compared to the typical BF-BOF route because of the presence of higher amounts of hydrogen in the natural gas.

2.1.1 Direct reduction processes – general considerations

Since the first DRI was produced in the 1970s, the production amount has increased continuously and reached a level of 100 million tons in 2018 for the first time, as shown in

Figure 7. In 2018, 79 % of the total production was done by the Midrex[®] and HYL/Energiron facilities, 20.2 % by rotary kiln based processes and only 0.8 % by other technologies such as fluidized bed-based technologies.[18] The two biggest producing countries of DRI in 2018 were India and Iran, with a production of 28.11 and 25.75 million tons, respectively.[18]
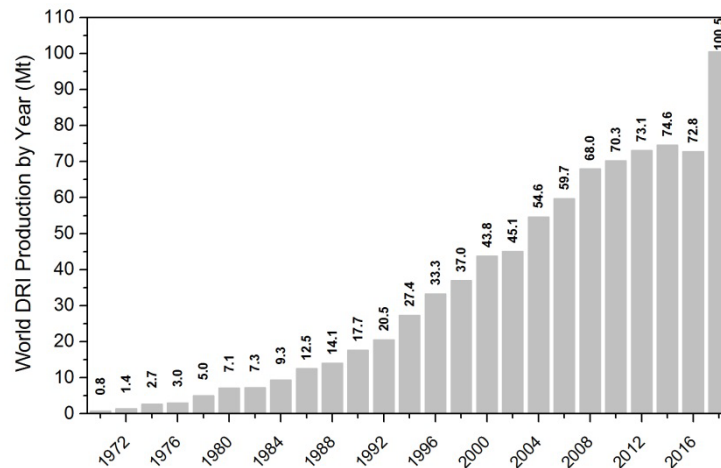
Figure 7: Development of world DRI production from 1970 to 2018.[18]

Three different product types of direct reduction processes can be distinguished - cold direct reduced iron (CDRI), hot direct reduced iron (HDRI) and hot briquetted iron (HBI). Generally, HDRI is directly charged from the reduction unit in a hot state to the subsequent melting or steelmaking facility. This represents the most energy-efficient way of using DRI. On the one hand the sensible heat of the HDRI can be used and therefore the energy consumption of the melting unit is reduced; on the other hand the DRI has less possibility for re-oxidation. HBI is hot briquetted DRI. The briquetting process decreases the specific surface of the DRI produced. This is beneficial for handling, shipping and storage in order to prevent re-oxidation of the DRI. In 2018, the production shares of HBI, HDRI and CDRI were 9.0, 11.1 and 79.9 %, respectively.[18] 21.5 million tons were shipped in 2018, so most of the DRI was consumed captively.[18]

DRI can be used in different steelmaking facilities, representing the BF, BOF and EAF. In the BF, CDRI or HBI can be charged as an iron carrier in order to decrease the specific coke rate and to increase the productivity.[19] As a result, on-site carbon dioxide emissions can be reduced. In the BOF, DRI can be used as a scrap substitute, acting as a cooling agent during the blowing period. The most common way of using DRI is melting it in an EAF. For the production of high quality steel grades based on scrap, scrap with high quality demands is required. Due to the low availability of high quality scrap, DRI can be used as a scrap substitute in the EAF for the production of those high quality steels.[20,21] With an increasing production share of EAF steelmaking, the demand for DRI will also rise in the next few years.

2.1.1.1 Selected direct reduction processes

As already mentioned above, during the last few decades, a lot of different direct reduction processes have been developed. Figure 8 shows an overview of DR processes which are

able to use iron ore fines directly without a separate prior thermal treatment of the agglomerates. Aside from the conventional shaft furnaces such as Midrex® and HYL/Energiron, only some other DR processes are operating on an industrial scale right now, such as the Finmet® process and some rotary hearth-based processes (marked with 3). Other processes had been in industrial operation, like the Circored® process (marked with 2), but the operation was stopped due to different reasons. Some other processes are still in pilot scale and not industrially proven (marked with 1).
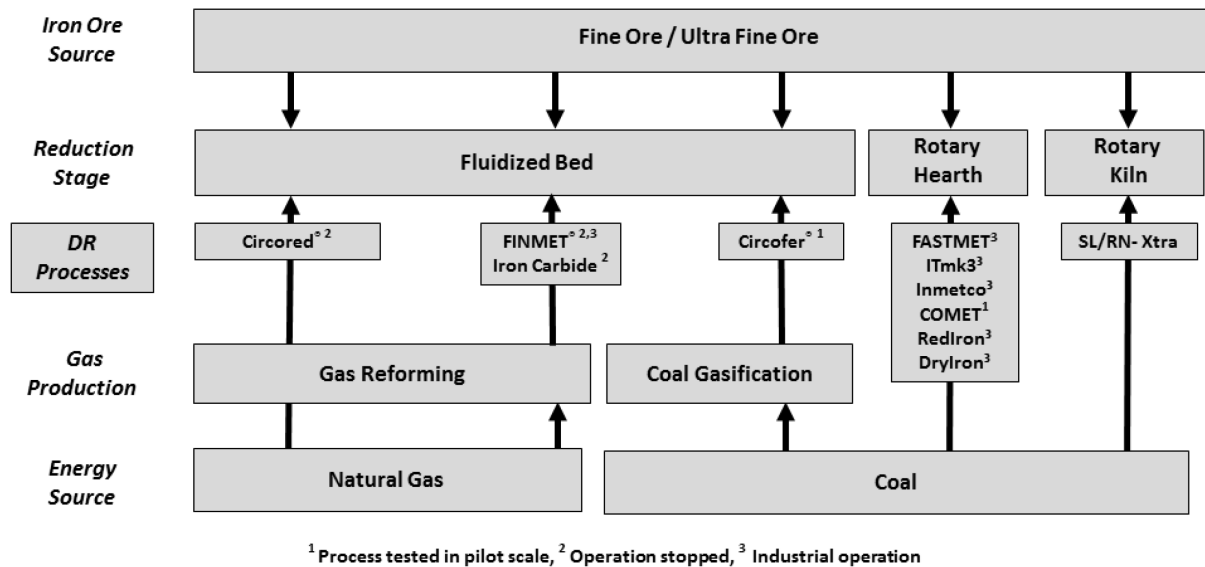
Figure 8: Overview of direct reduction processes based on iron ore fines.

In the following section, two fluidized bed-based direct reduction processes are described in more detail, namely the Circored® and the Finmet® processes, which were selected because of the process concept which fits to the topic discussed in this thesis.

The Circored® process

The Circored® process is based on a two-stage fluidized bed reactor system. The first one is a circulating fluidized bed for a fast pre-reduction of the iron ore; the second stage represents a bubbling fluidized bed for the final reduction up to high metallization degrees. Figure 9 shows the schematic flowsheet of the process.

The iron ore is dried and pre-heated up to 850°C in a circulating fluidized bed before charging it into the first reduction stage, a circulating fluidized bed reactor. At high gas velocities (up to 5 m/s) and short residence times (only up to 40 min), the pre-reduction up to 70 % degree of metallization takes place. Afterwards, the material is charged into the second reduction stage, a bubbling fluidized bed where the final reduction work takes place. It operates at lower superficial gas velocities (up to 0.5 m/s) and longer residence times (up to 240 min). The second stage is characterized by a typical cross-current flow of reducing gas and solids. The unique feature of the Circored® process compared to other DR processes is

the composition of the reducing gas, which contains hydrogen only. The hydrogen is produced via steam reforming in combination with a shift reactor and a carbon dioxide removal unit. Because of the low operation temperature in the bubbling fluidized bed (<650 °C), the DRI produced must be preheated again before the hot briquetting can take place. Another option is the direct use of the fines in an EAF.[22–24]

Only one industrial Circored® facility (500,000 t HBI/a) has been built and was in operation between 1999 and 2006 in Trinidad. The Circored® process might be one option for future steelmaking. On the one hand, iron ore fines can be used directly; on the other hand the process is able to run with pure hydrogen, resulting in almost carbon dioxide-free ironmaking.

Figure 9: Schematic flowsheet of the Circored® process.[22,25]

The Finmet® process

The Finmet® process uses a four-stage fluidized bed reactor series for a stepwise reduction of iron ore fines. The schematic flowsheet of the process is shown in Figure 10.

The iron ore fines are charged via a pressure lock feeding system into the first stage of the fluidized bed reactor series (R4). The pressure inside the reactor is in the area of 12 bar. In R4, the pre-heating and the first reduction of the iron ore take place. After that the material moves from one reactor to the next. Due to different conditions in each stage (different gas compositions and temperatures), the iron ore is reduced stepwise from hematite to magnetite, from magnetite to wüstite and finally to metallic iron. The temperature increases from 550 °C in R4 to approximately 780 °C in R1. The off-gas of the last reactor, R1, is used as inlet gas in R2, and so on. An overall counter current flow of reducing gas and solids can be achieved, leading to good gas utilization and high efficiency of the process. The DRI produced is charged into a briquetting facility to produce HBI. The off-gas of reactor R4 is

cooled down and de-dusted in a scrubber and returned to the process where it is mixed together with reformed natural gas.[26,27] Because of the use of natural gas as an energy source, the carbon dioxide production is much lower compared to coal-based DR processes.

Two industrial facilities were built in 1999 with production capacities of 2-2.5 million tons; one in Australia, the second one in Venezuela. The Finmet® plant in Australia was shut down in 2004; the plant in Venezuela is still in operation.

Figure 10: Schematic flowsheet of the Finmet® process.[28]

2.2 Thermodynamics of iron oxide reduction – comparison between hydrogen and carbon monoxide

On earth, iron mainly appears in the form of its oxides. Hydroxides, carbonates and sulfides are also common. The two most important oxides are hematite (Fe_2O_3) and magnetite (Fe_3O_4). To get metallic iron, the iron oxide has to be reduced from the trivalent (or divalent) state to metallic iron. A reducing agent is required which has a higher affinity to oxygen than the iron itself, under given process conditions. At present, the iron ore reduction is mainly based on carbon as an energy source and reducing agent, but hydrogen can also be used for the reduction work. The thermodynamic principles for the iron oxide reduction are described below.

2.2.1 Iron oxides and their manifestations

As already mentioned, hematite and magnetite are the two most important iron oxides which can be found all over the world. Hematite (Fe_2O_3) contains up to 70 %-wt. Fe, whereas generally, all Fe occurs in the trivalent state (Fe^{3+}). Magnetite (Fe_3O_4) is a compound of FeO and Fe_2O_3 in spinel structure with a maximum content of Fe of 72.3 %-wt.

Wüstite, FeO, is the oxide with the highest possible iron content (up to 77.7 %-wt.), which is important as an intermediate product during the reduction. Below 570 °C, FeO is not stable, and it decomposes to Fe_3O_4 and Fe. Because of changing amounts of Fe^{2+} and Fe^{3+} as well as iron vacancies in the crystal lattice (depending on the composition), the chemical formula of wüstite is generally written as $Fe_{1-y}O$, where y represents the iron deficit or the vacancy concentration. Figure 11 demonstrates the binary Fe-O system. As shown, wüstite is not stable below 570 °C. With increasing temperature and oxygen partial pressure, the stability area of wüstite expands because of the increasing vacancy concentration in the crystal lattice. A similar behavior can be observed for the magnetite while it appears nearly stoichiometric at temperatures below 900 °C. Magnetite is also stable at room temperature at a certain oxygen partial pressure.

In nature, iron oxides are commonly accompanied by other oxides, so-called gangue. Typical oxides are SiO_2, Al_2O_3, CaO and MgO. The content and type of accompanying oxides are very important as they are also introduced to the steelmaking processes, together with the iron oxide. They are responsible for the need and type of additives that have to be added to the system in order to obtain slags with the required properties.
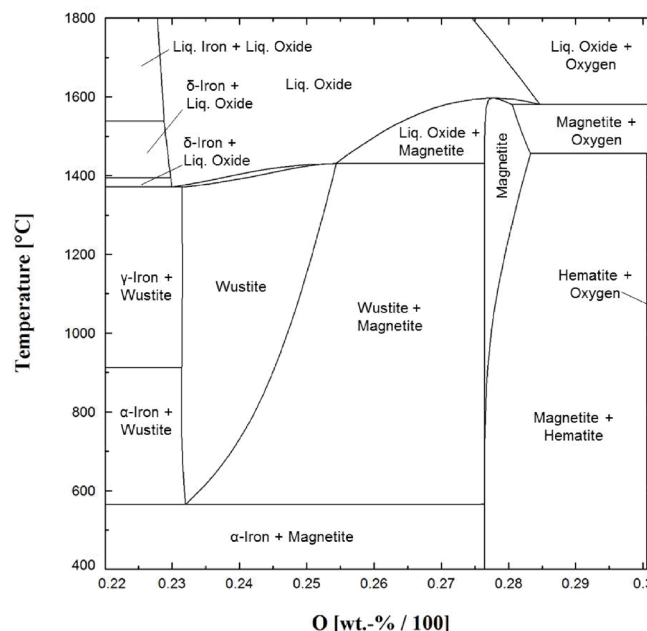
Figure 11: Binary Fe-O system calculated with Fact Sage7.2[TM] (Database: FactPS, FToxid).[29]

2.2.2 Reduction of iron oxides

In general, the reduction of Fe_2O_3 does not occur directly to metallic iron. If the reduction temperature is below 570 °C, the reduction to Fe occurs stepwise from Fe_2O_3 to Fe_3O_4, and continues to Fe. The intermediate oxide, $Fe_{(1-y)}O$, is not stable at temperatures lower than 570 °C. At reduction temperatures higher than 570 °C, $Fe_{(1-y)}O$ must also be considered in the reduction process. In this case, the reduction occurs from Fe_2O_3 via Fe_3O_4 to $Fe_{(1-y)}O$ and continues afterward to Fe. The reduction sequence for hydrogen and for the indirect reduction with carbon monoxide can be defined as follows (Equations 1-4):

$$3\,Fe_2O_3 + H_2\,(CO) \rightarrow 2Fe_3O_4 + H_2O\,(CO_2) \tag{1}$$

$$H_2: \Delta H_{700°C} = -2.17\ kJ/mol \quad CO: \Delta H_{700°C} = -37.21\ kJ/mol$$

T< 570°C

$$Fe_3O_4 + 4H_2\,(CO) \rightarrow 3Fe + 4H_2O\,(CO_2) \tag{2}$$

$$H_2: \Delta H_{500°C} = +111.28\ kJ/mol \quad CO: \Delta H_{500°C} = -37.16\ kJ/mol$$

T> 570°C

$$(1-y)Fe_3O_4 + (1-4y)H_2(CO) \rightarrow 3Fe_{(1-y)}O + (1-4y)H_2O\,(CO_2) \tag{3}$$
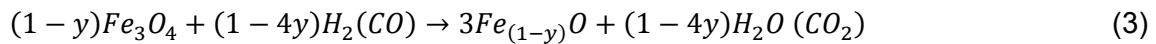
$$H_2: \Delta H_{700°C} = +52.16\ kJ/mol \quad CO: \Delta H_{700°C} = +17.17\ kJ/mol$$

$$Fe_{(1-y)}O + H_2(CO) \rightarrow (1-y)Fe + H_2O\,(CO_2) \tag{4}$$
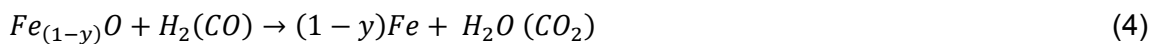
$$H_2: \Delta H_{700°C} = +15.42\ kJ/mol \quad CO: \Delta H_{700°C} = -19.62\ kJ/mol$$

In the equations, y represents the iron deficiency in the wüstite lattice.[30] Aside from the reduction reactions, values for ΔH are shown for the defined temperatures, calculated with the thermodynamic software FactSage™7.2 (Database: FactPS, FToxide). Generally the overall reduction with hydrogen is endothermic, so energy has to be added to the system to achieve a constant reduction temperature. In contrast to hydrogen, the overall indirect reduction with carbon monoxide is exothermic. This means energy is produced during the reduction procedure. In the next section, equilibrium diagrams are shown describing the thermodynamic circumstances of the iron oxide reduction.

2.2.2.1 Equilibrium diagrams describing the thermodynamic circumstances

A useful tool for describing the possibility of the reduction of metal oxides by reducing agents is the oxygen potential of corresponding reduction reactions. A general oxidation reaction is shown in Equation (5).

$$A + O_2 \leftrightarrow AO_2 \tag{5}$$

The metal A reacts with oxygen to form the related oxide. The corresponding equilibrium constant K can be defined as follows:

$$K = \frac{a_{AO_2}}{a_A * p_{O_2}} = \frac{1}{p_{O_2}} \tag{6}$$

The activities of the oxide and the pure substance can be defined as 1. This ends in the fact that the equilibrium constant only depends on the oxygen partial pressure. K can be used for the determination of the free enthalpy ΔG, which represents the oxygen potential:

$$\Delta G = -RT \ln(K) = RT \ln p_{O_2} = \Delta H - T\Delta S \tag{7}$$

R represents the gas constant, T the temperature, and H and S the enthalpy and entropy, respectively. The oxygen potential against temperature for iron and its oxides and for some other selected oxides is shown in Figure 12 (left). It has to be noted that in the diagram, only FeO is used instead of $Fe_{1-y}O$. This type of diagram is known as a Richardson-Ellingham diagram. As shown, the oxygen potential of the oxidation reactions of Si, Al and Mg are much lower compared to those of the iron and different iron oxides, which means that the affinity of Si, Al and Mg to react with oxygen is higher compared to iron.
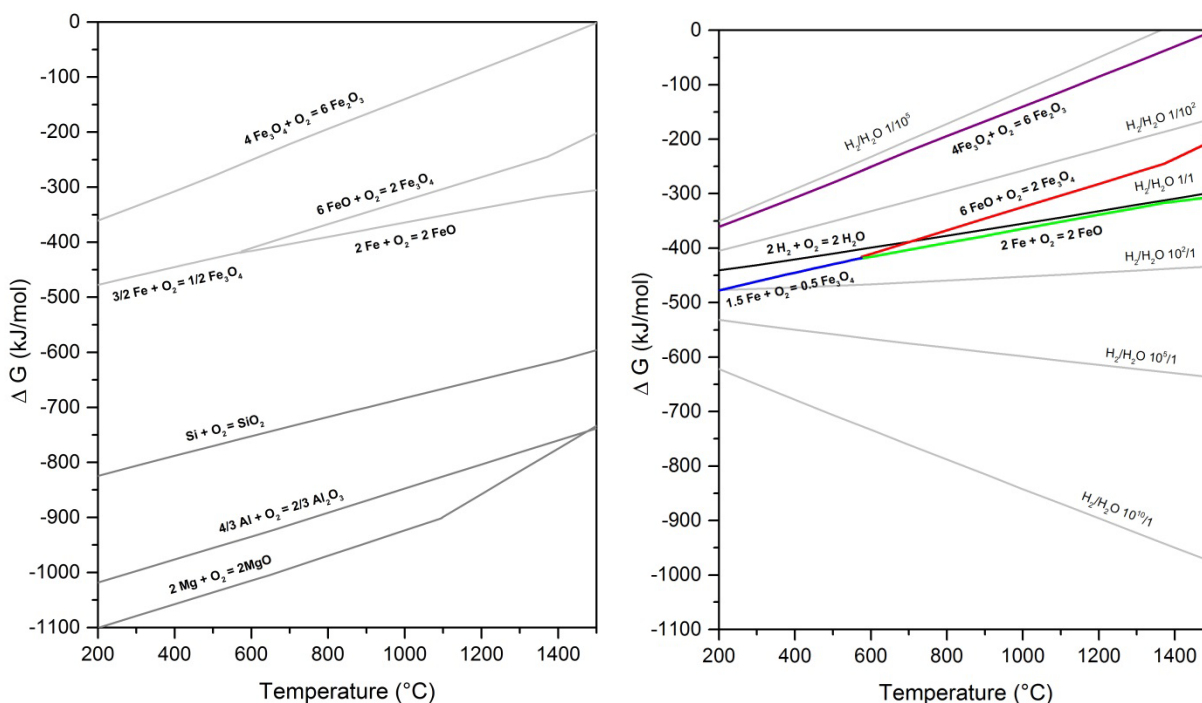
Figure 12: Richardson-Ellingham diagram for selected reactions: left- different iron oxides in comparison to other oxides; right- effect of different H_2 partial pressures on the reduction potential of H_2/H_2O gas mixtures.

During iron oxide reduction, a reducing agent should be provided which has a higher affinity to oxygen than the oxide to be reduced, representing that the oxygen potential of the metal/oxide should be higher than that of the reducing agent:

$$\Delta G_{Ox-Metall} > \Delta G_{Ox-Reducing\ agent} \tag{8}$$

If hydrogen is used as a reducing agent for iron oxide reduction, it is oxidized by the oxygen from the iron oxide to form water vapor:

$$2H_2 + O_2 \leftrightarrow 2H_2O \qquad K = \frac{p_{H_2O}^2}{p_{H_2}^2 * p_{O_2}} \tag{9}$$

The equilibrium constant K from this reaction also depends on the ratio of water and hydrogen in the gas mixture. For that reason, the oxygen potential of the reaction also varies at different partial pressure ratios of hydrogen and water:

$$\Delta G = -RT \ln\left(\frac{p_{H_2O}^2}{p_{H_2}^2 * p_{O_2}}\right) = RT \ln p_{O_2} + 2RT \ln\left(\frac{p_{H_2}}{p_{H_2O}}\right) \tag{10}$$

Figure 12 right shows the dependency of the ΔG of the hydrogen oxidation reaction on different ratios of hydrogen and water vapor in the gas mixture. With increasing hydrogen content in the gas mixture, the ΔG value of the reaction becomes more negative, signifying a stronger reduction potential of the gas mixture. The interception points of certain gas mixtures at different temperatures with the lines of different iron oxides can be determined from this information; e.g. at a ratio H_2/H_2O of 1/1, the line hits those of FeO oxidation to Fe_3O_4 at a temperature of approximately 680°C, representing the equilibrium state of the two oxides under those conditions. With this method, it is possible to determine stability areas of different iron oxides dependent on the gas composition and the temperature. The resulting diagram (Baur-Glässner diagram) for hydrogen is shown in Figure 13 (dashed lines). A similar procedure as that explained can be done for the oxidation reaction of CO to CO_2. The resulting stability areas are also shown in Figure 13 (solid lines).
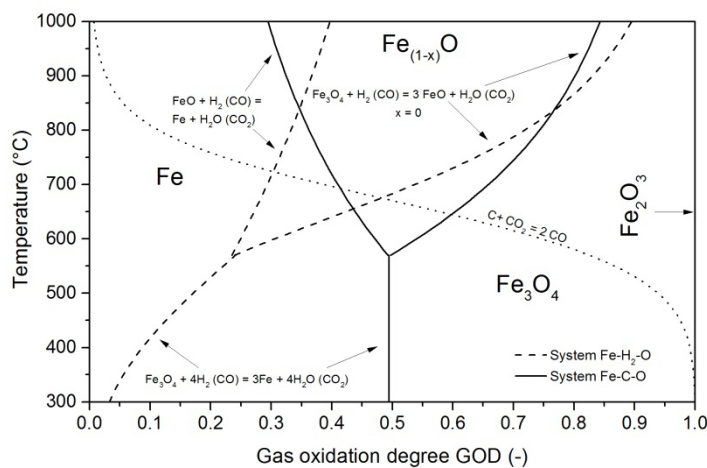
Figure 13: Baur-Glässner diagram for the Fe-O-H_2 and Fe-O-C system including the Boudouard-equilibrium for 1 bar and a carbon activity of 1.[29]

On the abscissa, the gas composition is expressed as gas oxidation degree (GOD), which is defined as follows:

For gas mixtures containing hydrogen and water:
$$GOD = \frac{x_{H_2O}}{x_{H_2}+x_{H_2O}} \qquad (11)$$

For gas mixtures containing CO and CO_2:
$$GOD = \frac{x_{CO_2}}{x_{CO}+x_{CO_2}} \qquad (12)$$

where x_i represents the molar ratio of component i in the gas mixture. A lower value of GOD represents a higher reduction force of the gas mixture. To form metallic iron, the temperature and gas composition has to be in the stability area of iron. As can be seen for the system Fe-O-H_2, the stability areas of metallic iron and wüstite expand with increasing temperatures. As a result, a reducing gas mixture with a similar GOD has a higher reduction potential if the reduction temperature is higher. Therefore, from a thermodynamic point of view, the reduction temperature, if hydrogen is used as a reducing agent, should be as high as possible. The Fe-O-C system shows a different behavior. The stability area of iron expands at lower temperatures. In this case, a lower reduction temperature would be beneficial from a thermodynamic point of view because of higher possible gas utilizations but this could end in kinetical problems. At 810°C, both, hydrogen and carbon monoxide have the same reduction potential. Additionally the equilibrium line of the Boudouard reaction is shown in the diagram for 1 bar and a carbon activity of 1, which is defined as follows:

$$C + CO_2 \leftrightarrow 2CO \qquad\qquad \Delta H_{700°C} = +170.9 \; kJ/mol \qquad (13)$$
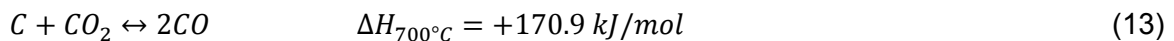
The Boudouard equilibrium splits the Baur-Glässner diagram into two areas. If a CO/CO_2-containing gas mixture has a temperature and composition below the equilibrium line, carbon precipitation will occur. This can impede the reduction; however, a temperature and gas composition above the line does not hinder the reduction procedure. The Boudouard equilibrium depends on the pressure and the carbon activity.

From the information in the Baur-Glässner diagram and the binary Fe-O system, shown in Figure 11, a phase diagram for the analysis of the mass balance can be determined, taking the thermodynamic boundary conditions into account. It is called Rist diagram, named after Prof. Andre Rist.[31] The diagram is shown in Figure 14 for the systems Fe-O-H_2 and Fe-O-C, linked to the corresponding Baur-Glässner diagrams. The abscissa shows the GOD, similar to the Baur-Glässner diagram; the ordinate shows the molar ratio O/Fe, representing the different iron oxides and metallic iron (O/Fe=0). A ratio of 1.5 represents Fe_2O_3; 1.33 represents Fe_3O_4. The ratio of wüstite is 1.05, not 1, in order to consider the iron deficit in the wüstite lattice. With the gas equilibrium information between Fe/FeO and FeO/Fe_3O_4 from the Baur-Glässner diagram, a so-called thermodynamic forbidden area can be defined at selected temperatures. This area shows the thermodynamic limitations of the reduction processes. The point showing the equilibrium between Fe and FeO, W, is the so-called wüstite point. As can be seen, W moves to values of lower GOD with decreasing temperatures for the system Fe-O-H_2. In case of Fe-O-C, it moves to values of higher GOD with decreasing temperatures. With this information, the operation of different reduction processes can be checked using a so-called operation line. This line represents the exchange of oxygen between the solids and the gas phase. In case of a DR shaft furnace, the iron ore is charged from the top into the reactor, moving downwards. The reducing gas mixture is injected in the lower part of the furnace, moving upwards. Thus, a typical counter current flow of solids and gases takes place. While passing through the furnace, the iron ore

is reduced from Fe_2O_3 to Fe. At the same time the reducing gas is oxidized while passing from the lower part of the furnace to the top. This behavior is shown by the operation line OL SF. To avoid thermodynamic limitations, the operation line should always pass W on the left side. The slope of the operation line represents the reducing agent demand; the stronger the slope, the higher the demand. The operation line should pass the wüstite point (W) as closely as possible.

In case of single-stage fluidized bed reduction, the composition of the off-gas should be on the left side of W in order to form metallic iron, represented by the operation line OL FBR_{1st}. The reason for this is that in fluidized bed reduction, the particles move inside the reactor and are mixed completely. It does not represent a counter-current flow. So the reducing gas always needs a reducing potential which is in the area of metallic iron. This ends in a steep increase of the operation line and therefore in a high demand for reducing agent. This is the reason why industrial fluidized bed reduction is carried out with more than one stage, which ends in better gas utilization and higher efficiency of the process, also in terms of energy consumption.
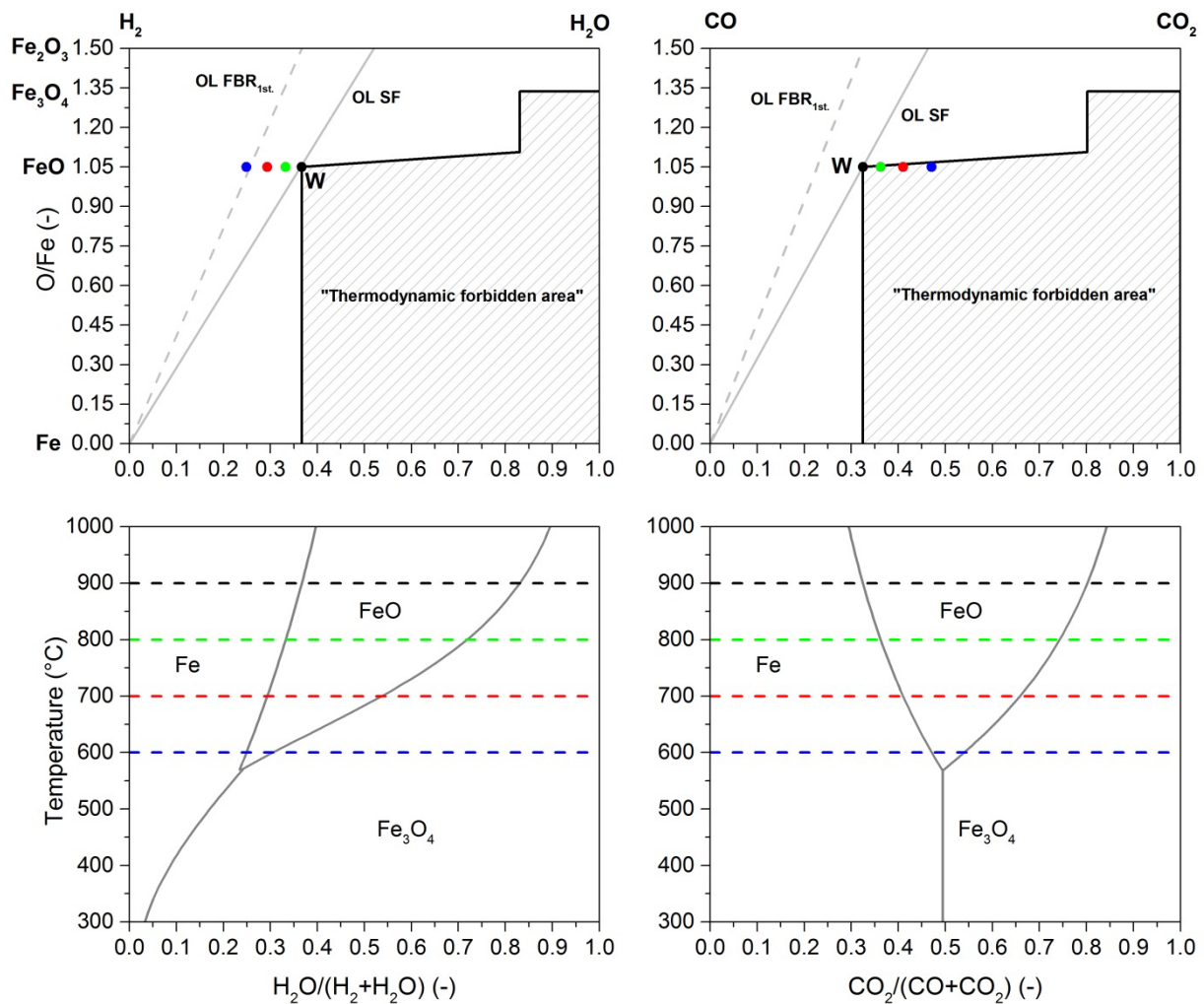
Figure 14: Rist diagram linked to the Baur-Glässner diagram with different operation lines: left-system $Fe-O-H_2$; right: system Fe-O-C.

2.3 Kinetics of iron oxide reduction with focus on hydrogen acting as a reducing agent

Aside from the thermodynamic point of view, the kinetics during iron oxide reduction play an important role because they can limit the production rate of the reduction process and therefore, the efficiency of the process is controlled by the kinetics. If the thermodynamic boundary conditions say that the process works, kinetic limitations can lead to constraints. This can end in a low reduction rate, so only low gas utilization can be achieved, signifying a poor efficiency of the reduction process. Knowledge regarding the possible rate-limiting mechanism is required, which will be discussed in the following sections. Most of the points shown have been already summarized and published in [29].

2.3.1 Rate-limiting mechanism during iron oxide reduction

In terms of iron oxide reduction, it is necessary to distinguish between porous and non-porous particles. The reduction of porous iron ore particles includes the following process steps:[32–35] Mass transfer of the gas components (hydrogen and carbon monoxide) from the gas stream through the fluid film of the oxide to the particle surface; diffusion through macro- and micro-pores to the oxide interface; adsorption at the oxide interface; oxygen removal via phase-boundary reaction (formation of water vapor and carbon dioxide and iron ions); desorption of gaseous reaction products; solid state diffusion of solid reaction products, nucleation and growth of nuclei; diffusion of gaseous reaction products back to the fluid film and mass transfer of gaseous products through the fluid film back to the gas stream.

If the iron ore particles have a dense structure, the reduction runs differently. In that case, the reducing gas is not able to penetrate the particle because of low permeability. The chemical reaction takes place after adsorption at the oxide interface. This leads to the formation of different iron activities in the particle and ends in diffusing iron ions and electrons to the internal phase boundary where the further reduction occurs. The gaseous reduction products, formed on the external oxide surface, diffuse back to the gas stream. Such behavior is characterized by typical layer growing of the reduction products.[33]

For both cases, the slowest mechanism is responsible for the speed of the reduction, which is called rate-limiting mechanism. At low temperatures, the chemical reaction might be the rate-limiting step because of the strong temperature dependence; however, the reaction rate increases exponentially. Then, other mechanisms become rate-limiting, such as the mass transfer.[36] If the chemical reaction occurs faster than the transport of reactants and products, mass transport is rate-limiting. In the case of limitation by chemical reaction, the transport of reactants and products occurs faster than the chemical reaction.

Different rate-limiting steps results in different gas concentration profiles of the gaseous reactant between the gas stream and the reaction interface, summarized for different rate-limiting steps in Figure 15. The mass transport of the gas component to the reaction interface is rate-limiting if the reaction itself occurs faster. The mass transport is driven by the concentration difference of the gaseous component between the gas stream and the reaction interface. This can be explained by Fick's law of diffusion. Figure 15 (a) shows schematically

the concentration profile of the gaseous reactant A in case of a limitation by mass transfer. C_{Ag} represents the concentration of reactant A in the gas mixture and C_{As} those on the outer surface of the particle. C_{As} is equal to the concentration on the surface of the unreacted core, C_{Ac}, which represents the equilibrium concentration of the reaction. A limitation by mass transfer is independent of the product layer formed. As a result, a distinction between porous and non-porous particles is not required. The mechanism of mass transfer is only slightly temperature-dependent compared to other limiting mechanisms, such as chemical reactions. Limitation via mass transfer probably occurs at high reduction temperatures.
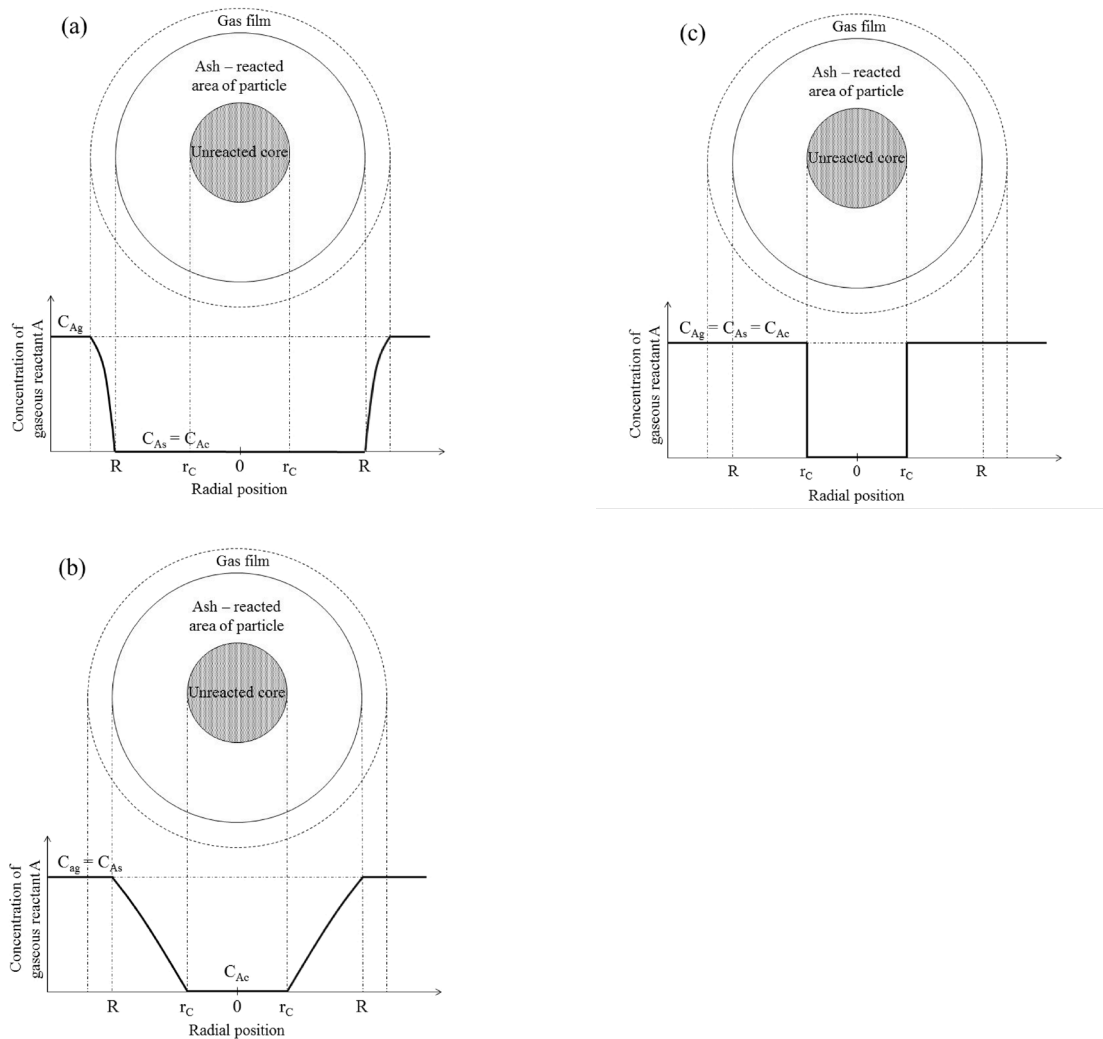
Figure 15: Gas concentration profile of gaseous reactant A at a particle with limitation by mass transfer through gas film (a), pore diffusion (b) and chemical reaction (c).[34]

The resulting gaseous concentration profile caused by a limitation by pore diffusion is shown in Figure 15 (b). Different types of pores have to be distinguished; pores in the raw material and pores formed during the reduction procedure; however, the different sizes and shapes of the pores also have an influence on the diffusion mechanism. If the mass transport through the pores limits the reduction, the progress can be described using the shrinking core model. As a result, the concentration in the gas stream, C_{Ag}, is equal to the

concentration at the product surface, C_{As}. At the reaction interface, the concentration is equal to the equilibrium concentration of the reaction, C_{Ac}. The reduction of iron ore pellets is one typical example. The particles on the outer surface become reduced to metallic iron while the particles inside the pellet remain unreacted because of the diffusion resistance of the gaseous reactants through the metallic iron product formed. The gaseous concentration decreases in the porous product layer with increasing distance until the non-reacted particles in the center. Accordingly, the reduction proceeds from the outer surface to the center.

The effect of a limitation by the phase-boundary reaction on the gaseous profile of reactant A is shown in Figure 15 (c). The phase-boundary reaction represents the removal of oxygen by the chemisorbed reducing agent by a simultaneous formation of reaction products. The reaction rate is influenced by various parameters such as temperature, reducing gas concentration at the interface, or type of iron oxide. In case of a limitation by the phase-boundary reaction, the concentration of the reactant in the gas stream is similar to the concentration at the reaction interface. For a non-porous particle, the reaction occurs stepwise according to the shrinking core model, which is known as a topochemical reaction. In a porous particle, the reducing gas is able to penetrate the particle and the reduction starts on all surfaces at the same time. This limitation does not depend on the particle size.

The formation of non-porous product layers around the particles can lead to a limitation by solid-state diffusion through the product layer formed. As a result the reducing gas is not able to penetrate the particle and the reduction rate strongly decreases because solid-state diffusion becomes rate-limiting. In case of the reduction of iron oxides with non-porous character, especially magnetite-based iron ores, solid-state diffusion is of great importance. Solid-state diffusion mainly occurs through lattice defects and at interstitial sites. At reduction temperatures higher than 570 °C, wüstite is formed as an intermediate product. Wüstite is characterized by a lot of vacancies which support the diffusion of iron ions in the lattice. If dense iron layers are formed, further reduction occurs because of oxygen diffusion to the outer surface. The diffusion coefficient of solid-state diffusion is much lower compared to the diffusion coefficient of gaseous diffusion. Consequently, the reduction rate becomes lower. The reduction of hematite-based ores is less critical because of the formation of porous intermediate products during reduction.

The process of nucleation and growth of nuclei is also of importance and has an influence on the structure of the reaction products formed. At the reaction interface, the removal of oxygen changes the ratio of iron to oxygen. An oversaturation of the oxide with iron ions is the result. Therefore, the precipitation of oxides with a lower oxidation number or metallic iron occurs. If a certain size is reached, the nucleolus starts to grow.

2.3.2 Parameters influencing the kinetics during iron oxide reduction

Numerous parameters have a great impact on the kinetics of iron oxide reduction, such as process parameters (temperature, pressure and gas composition). Additionally, the properties of the material which should be reduced have an influence on the reduction progress such as grain size, morphology and porosity. The effect of the different influencing parameters is discussed below. Table 1 shows an overview of selected publications regarding the investigation of the reduction behavior, including the main results of the investigations.

Table 1: Summary of selected results regarding reduction behavior reported in literature.[29]

Reference	Type of test	Reducing agent	Temperature [°C]	Oxide used	Main outcomes
Bahgat et al.[37]	Isotherm reduction	H_2	900–1100	Fe_3O_4 single crystals	• Increasing reduction rate with increasing temperature • Reaction rate slows down at 900 and 950 °C at 83 and 89 % reduction, respectively. • Rate limitation by solid state diffusion
Chen et al.[38]	Isotherm reduction with fluidized bed	CO	700–850	Fe_2O_3, 100–150 µm	• Increasing reduction rate with increasing temperature • Rate-limiting step varies with temperature and progress of reduction. • Apparent activation energy for the reduction to FeO and to Fe is determined as 83.6 and 80.4 kJ/mol, respectively.
El-Geassy et al.[39]	Isotherm reduction	H_2	500–1100	Fe_2O_3 samples with different porosity	• The reduction rate of samples with high porosity (54%) increases with increasing temperature until complete reduction. • Less porous and dense samples (35 and 8% porosity) show a minimum in reduction rate at 650°C because of the formation of a dense iron layer.
El-Rahaiby et al.[40]	Isotherm reduction	H_2	238–417	FeO (produced via oxidation of Fe)	• Rate-limiting due to phase boundary reaction • Sigmoidal shape of reduction extent over time • An estimation of the reaction rate is done.
Bondale et al.[41]	Isotherm reduction	H_2/CO/ mixtures	850	Fe_2O_3-pellets 10–12mm	• Reduction with pure H_2 is faster compared to CO and gas mixtures. • Reduction with H_2 is limited by phase boundary reaction and gas diffusion. • Reduction with CO also shows a limitation by phase boundary reaction and gas diffusion; the areas where the mechanisms are limiting, are different.
El-Geassy et al.[42]	Isotherm reduction	H_2/CO/ mixtures	900–1100	FeO micro-pellets	• Highest reduction rate with H_2; increasing amount of CO in the reducing gas lowers the reduction rate • Longer incubation time for the reduction with CO lowers the reduction rate at the initial stage
Teplov[43]	Isotherm reduction	H_2	300–750	Fe_3O_4 concentrate	• Development of a model to predict the reduction behavior of concentrates and pellets. • The calculated results are in good agreement with the experimental results.
Corbari et al.[44]	Isotherm reduction	$CO-CO_2$	590–1000	Fe_2O_3-fines	• Reduction from Fe_2O_3 to FeO occurs stepwise via Fe_3O_4. • Reduction from Fe_2O_3 to Fe_3O_4 is limited by external mass transfer; independent of temperature. • Reduction from Fe_3O_4 to FeO: Rate-limiting step depends on the raw material used (external mass transfer and phase-boundary reaction).
Higuchi et al.[45]	Isotherm reduction	$CO-CO_2$	350–800	Fe_2O_3 agglomerates with different porosity	• Investigation of strength before and after reduction. • Cold strength shows a minimum at a pore size of 0.25–0.5 mm. • Strength after reduction depends on strength before reduction and on reduction parameters.
Edström[46]	Isotherm reduction	H_2/CO	450–1100	Fe_2O_3 and Fe_3O_4	• The reduction of Fe_2O_3 occurs faster than that of Fe_3O_4 due to the formation of pores. • Fe_3O_4 with prior oxidation to Fe_2O_3 shows comparable reduction rates to natural Fe_2O_3. • Reduction with H_2 proceeds faster compared to CO. • The difference in reduction rate between Fe_2O_3 and Fe_3O_4 becomes smaller with decreasing temperatures.
Turkdogan et al.[47–49]	Isotherm reduction	H_2/CO-CO_2	400–1000	Fe_2O_3	• Investigation of the effect of temperature and grain size, definition of rate-limiting steps. • Investigation of pore characteristics of iron formed during reduction. • Investigations of reduction-oxidation of porous and dense iron oxides and iron.
Liu et al.[50]	Isotherm reduction	H_2/CO	800–1000	Fe_2O_3 briquettes	• Reduction rate increases with temperature and H_2-content in the reducing gas mixture.

2.3.2.1 The temperature effect on the reduction rate

Concerning kinetics, higher temperatures are generally always preferred because of the dependency of possible rate-limiting steps on the temperature such as diffusion or phase boundary reaction. For these examples, the rate increases with rising temperatures. Thermodynamics of the reduction reactions show that the reduction can also proceed at low temperatures but because of kinetical limitations, the achievable gas utilization and therefore the process efficiency will be insufficient. As a result, a certain temperature is required to reach a gas utilization that fits the economic requirements of an industrial process. According to the Baur-Glässner diagram, an increasing driving force can be observed with rising temperatures if hydrogen is used as a reducing agent. For hydrogen-based reduction, a higher temperature is thus beneficial for both thermodynamics and kinetics.

If a reducing gas mixture consists of carbon monoxide, a decreasing reduction potential is the result of increasing the reduction temperature. As a conclusion, a higher temperature is only preferable for decreasing the impact of kinetics. The temperature can also influence the morphology of the iron formed during the reduction. A formation of dense iron layers should be avoided because this can end in a limitation by solid state diffusion and therefore very low reduction rates. The temperature effect on the rate of reduction has been investigated by many authors. Bahgat et al.[37] investigated the reducibility of magnetite single crystals using hydrogen in a thermogravimetric analyzer within a temperature range of 900 and 1100 °C. The results show a strong decreasing reduction rate at 900 and 950 °C after 80 and 90 % degree of reduction, respectively. This happens as a result of the formation of dense iron layers that inhibit direct gas contact with the reaction interface. With rising temperatures, the reduction occurs faster and a complete reduction can be attained in a suitable time.
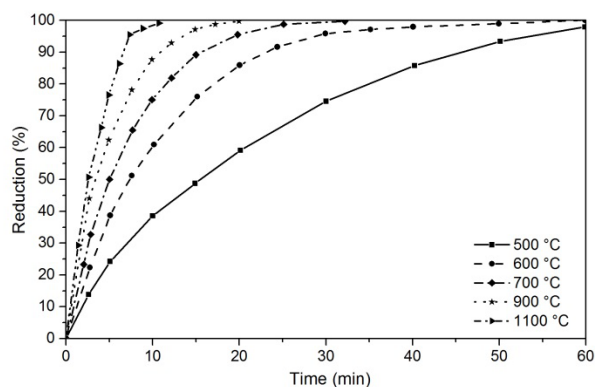
Figure 16: Reduction of hematite compacts with hydrogen at different temperatures.[39]
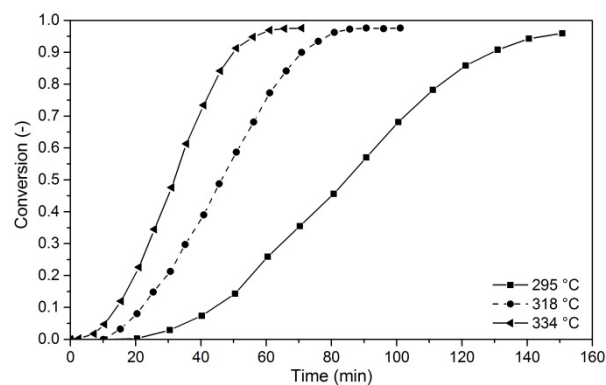
Figure 17: Effect of temperature on reduction rate for reducing wüstite with hydrogen.[40]

The reducibility of hematite compacts at different temperatures was researched by El-Geassy et al.[39], as shown in Figure 16. The results show a fast conversion until 80 % degree of reduction for temperatures between 700 and 1100 °C. At lower temperatures (500 °C), the reduction rate decreases significantly. A complete reduction is achieved at all tested temperatures. The reduction of quenched wüstite, produced via oxidation of iron foils with a CO/CO_2 gas mixture, at low reduction temperatures using hydrogen as a reducing agent was investigated by El-Rahaiby et al.[40], as exhibited in Figure 17. The progresses of

conversions are sigmoid-shaped, which can be separated into three stages: first, an incubation period which belongs to the formation of the iron nuclei and decreases with increasing reduction temperatures; second, an acceleration period where the iron nuclei grow successively and third, a decreasing reduction rate due to the growing iron nuclei impinging on one another.[40]

2.3.2.2 The influence of pressure during reduction

In addition to temperature, pressure is another process parameter which influences the progress of reduction. From a thermodynamic point of view, the pressure does not affect the reduction rate but it can still have an influence on the kinetics, e.g. the pressure dependence of the diffusion coefficients. Thüns et al.[51] studied the effect of hydrogen pressure on the reduction rate of hematite at temperatures of 200°C. It is reported that the reduction rate increases with increasing hydrogen pressure by a factor of 2.5 and 2 for increasing the pressure from 3 to 6 and 6 to 8 MPa, respectively.

A study regarding the effect of the total pressure on the reduction of hematite with a fluidized bed reactor facility using hydrogen and a constant superficial gas velocity was carried out by Habermann et al.[32] At constant hydrogen partial pressure within the reducing gas mixture (constant molar flow), the reduction rate cannot be increased by an increase of the total pressure during the initial and medium stages of reduction. Only the decreasing reduction rate at the end of reduction can be shifted to higher conversions in case of higher total pressure. With increasing pressure and constant partial pressure of hydrogen in the gas mixture, which ends in a higher molar flow of hydrogen, an increasing reduction rate can be observed. Comparable investigations were done by Sato et al.[52] They found that the reduction rate increases with increasing pressure at a constant molar flow rate. The increase slows down as the gas concentration at the outlet reaches the equilibrium gas composition. In this case, the increasing pressure results in lower gas velocities inside the reactor and therefore to longer residence time of the gas. As a conclusion, these results are not comparable to the investigations of Habermann et al.[32] Kawasaki et al.[53] also found that varying the absolute pressure has no effect on the reduction rate.

2.3.2.3 Effect of different reducing agents on the reduction rate

The reducing gas composition has a major impact on the reduction rate. A low value of GOD of the gas mixture represents a high reduction potential, as can be observed within the Baur-Glässner diagram. Aside from the GOD, the type of reducing agent (hydrogen or carbon monoxide) influences the reduction rate. It is well known that differences in reduction rate can occur if hydrogen or carbon monoxide is used as a reducing agent. These differences are a result of different kinetical influences. Figure 18 demonstrates the influence of the reducing gas composition on the reduction rate of hematite pellets at 850 °C, determined by Bondale et al.[41] The tests are done with carbon monoxide, hydrogen and a gas mixture consisting of 55.7 % H_2, 34 % CO, 6.3 % CO_2 and 4 % CH_4. At a reduction temperature of 850 °C, hydrogen and carbon monoxide have nearly the same reduction potential, but the results show a big difference in reduction rate, which is much higher for hydrogen. After 15 min of reduction with hydrogen, the reduction is nearly complete while at the same time, only 50 % of conversion is achieved by using carbon monoxide.
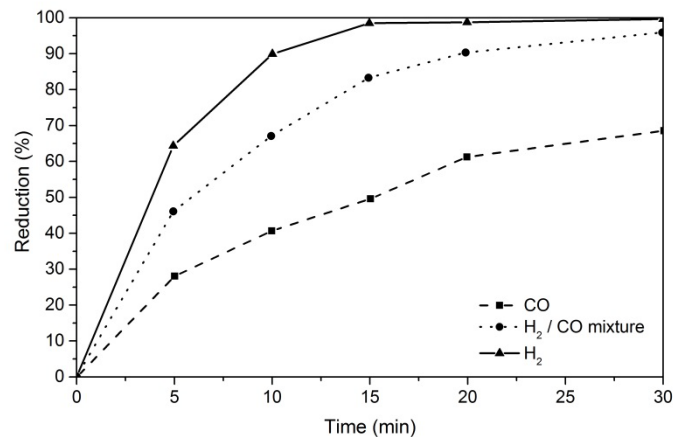
Figure 18: Effect of different gas compositions on the reduction rate of hematite-based pellets at 850 °C reduction temperature.[41]

El-Geassy et al.[42] investigated the reducibility of wüstite micropellets with H_2, CO, and mixtures of both gases at temperatures between 900 and 1100 °C. It is shown that an addition of carbon monoxide to the reducing gas mixture leads to an extreme decrease of the reduction rate while small additions of hydrogen to carbon monoxide increases the reduction rate because of an easier formation of iron nuclei at the reaction interface. Using only carbon monoxide as a reducing agent results in an incubation period responsible for the low reduction rate at the initial stage. Turkdogan et al.[54] investigated the reducibility of iron ore pellets with different additions of additives. The results indicate that the reduction in a carbon monoxide atmosphere takes more time compared to hydrogen because of better effective gas diffusivities of the H_2-H_2O mixture.

Reasons for higher reduction rates by using hydrogen compared to carbon monoxide

Hydrogen and carbon monoxide show the same reduction potential at a reduction temperature of 810 °C. At lower temperatures, that of carbon monoxide is higher while at higher temperatures, hydrogen shows a bigger reduction potential. A lot of different kinetic studies confirm the better reduction properties of hydrogen compared to carbon monoxide. Zuo et al.[55] tested the reducibility of iron ore pellets with different gas mixtures consisting of hydrogen and carbon monoxide. Figure 19(a) shows the results occurring with different gas mixtures and 800 °C reduction temperature. With an increasing ratio of carbon monoxide to hydrogen, the reduction rate decreases. This is a result of the better diffusion behavior of hydrogen compared to carbon monoxide and also from water vapor compared to carbon dioxide.[55] It seems that the diffusion rate is more important than the thermodynamic reduction potential. Figure 19 (b) shows a method for the evaluation of the effective diffusion coefficient occurring in different gas mixtures based on the unreacted shrinking core model, including intrinsic reduction, pore diffusion, and mass transfer through the gas film.[55] t_1 represents the overall reduction time if the reduction rate is only controlled by exterior diffusion. *F* gives the ratio between reaction time and overall reaction time. The expression on the abscissa (3F-2F²) is a result of taking the intrinsic reduction, pore diffusion and gas-

film mass transfer into account, considering the unreacted core model. The effective diffusion coefficients and the reduction rate can be determined by a linear regression, using the slopes and the intercepts of the regression lines, respectively. In principle, the effective diffusion coefficient is influenced by the temperature, pressure and physical properties of the gas mixture such as viscosity and molecule size. The results show an increasing effective diffusion coefficient with increasing temperatures because of a faster movement of the gas molecules, which is preferable for the diffusion behavior. The molecule size of hydrogen is lower compared to carbon monoxide, which is also preferable for the diffusion. This ends in lower activation energies of diffusion for hydrogen compared to carbon monoxide.
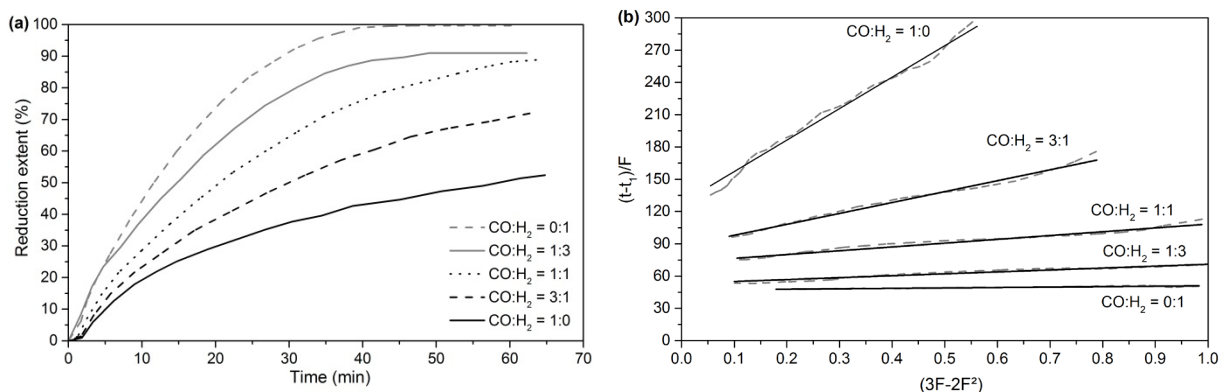
Figure 19: Determination of the effective diffusion coefficient for different gas mixtures: (a) Progresses of reduction over time for different gas mixtures, (b) Procedure for determining the effective diffusion coefficient.[55]

Zuo et al.[55] also showed that the effective diffusion coefficient decreases drastically if carbon monoxide is present. Aside from the changing physical properties of the gas mixture, another reason is defined. Carbon monoxide molecules can block the diffusion paths of hydrogen. As a result, the chemical reaction becomes inhibited. Only small amounts of carbon monoxide in the gas mixture are required for this phenomenon. In addition to the diffusion effects, the overall reduction by hydrogen is endothermic, whereas that with carbon monoxide is exothermic. Therefore, a higher temperature is preferable for the reduction with hydrogen.

Mazanek et al.[56] also examined the effect of hydrogen on the dynamics of the reduction process. They found that hydrogen always acts as a better reducing agent compared to carbon monoxide, especially between 700 and 900 °C. At higher temperatures, a decreasing difference in the reduction rate is observed.

Effect of water vapor on the progress of reduction

The reduction rate can be drastically influenced by the presence of water vapor in the reducing gas mixture. First, the reduction potential of the gas mixture is decreased by water vapor (higher GOD values); second, water vapor can block free reaction sites by adsorption at the reaction interface. The influence of water vapor on the growth rate of iron on magnetite during reduction with $H_2/H_2O/Ar$ mixtures at different temperatures was observed in-situ by Steffen et al.[57] as shown in Figure 20. The results indicate a strongly decreasing growth rate

of iron at the wüstite surface at all tested temperatures, if the partial pressure of water vapor is increased. This behavior is explained by the adsorption of water molecules at the free reaction sites on the iron-magnetite/wüstite interface which hinders the further progress of reduction.[57]
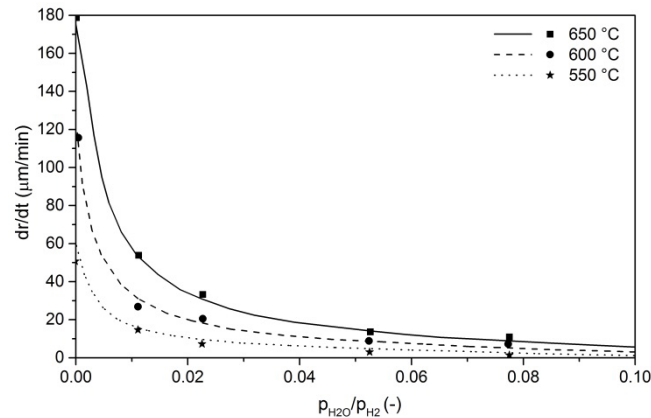
Figure 20: Effect of water vapor in the gas mixture on the growth rate of iron on a magnetite or wüstite surface.[57]

Kim et al.[58] examined the influence of water vapor on the reducibility of magnetite in a temperature range between 500 and 1000 °C, while at low reduction temperatures (500-700 °C) a strongly decreasing reduction rate is observed in the presence of water vapor. Lorente et al.[59] investigated the influence of water vapor on the kinetics of reduction. An addition of 0-5 % water vapor to the reducing gas mixture does not affect the reduction of hematite to magnetite, whereas the reduction from magnetite to metallic iron slows down radically. Water vapor formed during reduction by hydrogen does not affect the reducibility.

2.3.2.4 Influence of particle size on the reduction rate

Another influencing parameter on the reduction rate is the grain size of the iron ore particles. Different particle sizes can affect the rate-limiting step. Teplov[43] investigated the reducibility of magnetite fines with different grain sizes using hydrogen at a temperature range within 300-570 °C. Figure 21 shows the results obtained at 400 °C reduction temperature for grain sizes varying from 1 to 160 µm. An increasing reduction rate for a decreasing particle size is observed because of changing rate-limiting mechanisms.
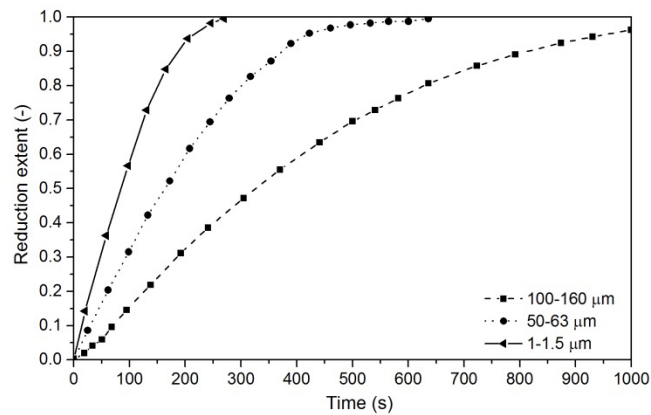
Figure 21: Effect of particle size on the reduction rate of magnetite concentrate with hydrogen at 400°C.[43]

Corbari et al.[44] explored the reducibility of iron oxide fines to wüstite using a carbon monoxide-based gas mixture at 1000 °C reduction temperature. The particle sizes investigated are in the range of 110 µm and 3 mm. For particle sizes between 110 and 508 µm, a similar reduction rate is observed. As a result, gas diffusion through the pores occurs fast enough and does not limit the reduction rate.[44] Pore diffusion becomes important for particles bigger than 508 µm because of bigger diffusion distances, ending in a decreasing reduction rate. The particle size effect on reducibility becomes less important at lower reduction temperatures because other rate-limiting steps become relevant.

Chen et al.[60] studied the reducibility of hematite particles with an average particle size of 21 µm in a temperature range of 1150 to 1350 °C using a flash reactor. The results indicate that a degree of reduction higher than 90 % is achieved in a few seconds because of the good kinetic behavior of the ultra-fine material used in combination with hydrogen acting as a reducing gas.

2.3.2.5 Effect of iron oxide porosity on the reduction rate

In principle, a higher porosity of the raw material, to be reduced ends in a higher reducibility due to better gas permeability of the reducing gas to the reaction interface. Pore diffusion of the reducing gas can be the rate-limiting step during iron ore reduction, so it is of great importance. Skorianz[61] investigated the reducibility of different iron ore brands with different porosities in a laboratory fluidized bed reactor. The results demonstarte that limonite-based ores with the highest initial porosity have the best reducibility, followed by hematite and magnetite with lower initial porosity.

Weiss[62] studied the reducibility of hematite to magnetite in a lab-scale fluidized bed reactor at different temperatures, also measuring the change of the specific surface area and mean pore diameter during the progress of reduction. It is observed that the specific surface area and mean pore diameter change during the reduction procedure. As a result, the overall porosity also changes while the effect depends strongly on the process parameters used, especially on the reduction temperature. Higuchi[45] showed that the presence of macro-pores

is more important for higher reduction rates compared to that of micro-pores (<15 μm) for the reduction of pellets and sinter.

2.3.2.6 Effect of iron oxide mineralogy on the reduction rate

Different iron oxides show a difference in reducibility while generally, hematite-based ores are better reducible than magnetite-based ones. There is no industrial DR process in operation which uses untreated magnetite ore. These kinds of ores are typically characterized by a non-porous morphology, which ends in the formation of dense iron layers around the particles during reduction. Shaft furnace-based DR processes often use magnetite-based pellets which are oxidized to Fe_2O_3 during the pelletizing process. The oxidation of magnetite ends in nearly the same reducibility compared to natural hematite. An investigation of the reducibility of different iron oxides by hydrogen and carbon monoxide at a reduction temperature was done by Edström[46], as demonstrated in Figure 22. Within the study, hematite shows a better reducibility in both cases, using hydrogen and carbon monoxide as a reducing agent. A very slow reduction progress is observed for the reduction of magnetite with carbon monoxide. The main reason for the differences is the formation of different morphologies and different porosities that strongly depend on the raw material used. Limonite-based ores, consisting of hydrated oxides, are also known to have a good reducibility fowing to their high initial porosity.

Mali and Spuida[63] defined a reducibility order for different types of iron ore. In it, limonite shows the best reducibility followed by hematite and magnetite-based ores. The criteria for ordering also include the specific surface area of the initial iron ore grains.
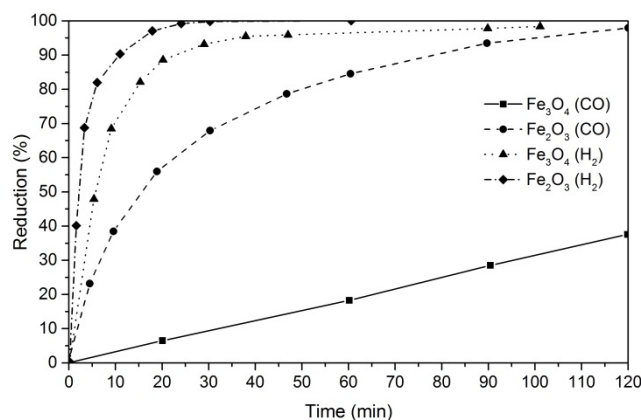
Figure 22: Effect of iron oxide mineralogy on the reduction rate using different reducing agents.[46]

2.3.2.7 Effect of iron oxide gangue on the reduction rate

Iron ores typically contain some accompanying oxides while the type and amount of oxides depend on the iron ore deposit and the beneficiation processes. SiO_2, CaO, MgO and Al_2O_3 represent typical accompanying oxides. The different oxides remaining in the iron ore can

also have an influence on the reducibility. Wang and Sohn[64] studied the role of CaO and SiO_2 on the swelling behavior and on iron whisker formation during the reduction. The results show that SiO_2 does not affect the reduction rate, while at low SiO_2 content, the reduction becomes faster with increasing CaO content. Turkdogan and Vinters[54] investigated the effect of CaO and SiO_2 on the reduction behavior of iron ore pellets. Accordingly, the effect of different oxides on the reduction rate depends on the sintering temperature and the porosity of the ores while no general trends are observed. These results are in disagreement with those of other authors[65,66], who mention that CaO is beneficial for the reduction rate. The sintering process itself is of great importance because a large variety of different phases can be formed out of the iron oxides and the accompanying oxides, for example calcioferrite or fayalite. All of them show a difference in reducibility. As a rule, silica-containing phases give a worse reducibility compared to other phases.[67,68] An increasing MgO content is also not beneficial for the reduction behavior of sinter.[69] As a conclusion, according to the study by Yadav et al.[70], the decrease in hematite and calcioferrite and an increase in spinel phases with low reducibility are responsible for that behavior.

Kapelyushin et al.[71,72] investigated the influence of Al_2O_3 on the reducibility of magnetite at different temperatures using a CO/CO_2 gas mixture. Un-doped magnetite reduces topochemically because of the formation of dense iron layers during reduction, which avoids the direct contact of the reducing gas and the reaction interface. The presence of up to 3 % alumina leads to the formation of a network-like wüstite structure. As a result, metallic iron is formed along this structure, preventing the formation of dense iron layers and increasing the reduction rate while the effect is influenced by the reduction temperature and the alumina doping amount. Higher Al_2O_3 amounts have a negative effect on the reduction rate because of enriching the Fe_3O_4-$FeAl_2O_4$ solution which has a lower reducibility [71,72], as shown in Figure 23. Paananen et al.[73] made similar observations. They explained that the presence of Al cations increases the crack formation due to higher expansion in the presence of the hercynite spinel structure. The Al-doped samples also reduce faster compared to the un-doped magnetite.
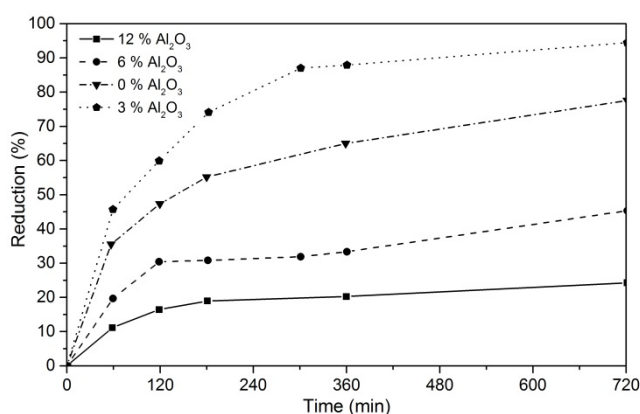
Figure 23: Effect of Al_2O_3 doping amount on the reduction rate of magnetite at 750°C.[72]

2.3.2.8 Influence of type of iron formation on the reduction procedure

The gaseous reduction of iron oxides can lead to different metallic iron formations across the particles. The type of iron formed depends on the process conditions, such as

temperature and reducing gas composition as well as on the raw material itself. Generally, three different types of iron formation can be differentiated: dense, porous and fibrous. Gudenau et al.[74], Moujahid et al.[75] and Matthew et al.[76] estimated areas for different iron formations depending on the composition of the reducing gas mixture and the reduction temperature. For gas mixtures with low reduction potential, the formation of iron whiskers is supported. A high reduction potential leads to the formation of dense and porous iron but there are still some discrepancies between the results of each author. One of the reasons for the differences in the results might be that the properties of the material used are not taken into account.

One of the major problems during fluidized bed reduction is the occurrence of iron whiskers because it supports the sticking phenomenon. This can lead to a de-fluidization of the material.[10,77,78] The principles of sticking are explained in more detail in Section 2.5.3. The formation of dense iron layers is not beneficial, either, because it can act as a barrier for the reducing gas, causing a strong decrease in the reduction rate and impairing the efficiency of the process.

Habermann[79] blames the different interactions between phase-boundary reaction and solid-state diffusion for the different iron formations. Wüstite, as an intermediate product during reduction, is formed at temperatures above 570 °C. At first occurrence, wüstite has a composition near the FeO/Fe_3O_4 equilibrium. Further reduction leads to changing ratios of Fe to O, which increases until reaching the equilibrium between Fe and FeO. Afterwards, the formation of an iron-oversaturated wüstite layer occurs. Iron nuclei can be formed, if the chemical reaction rate is higher compared to the rate of solid-state diffusion. As a result of the high chemical reaction rate, many nuclei are formed, which ends in the creation of an iron layer. In case of a higher solid state diffusion rate, an oversaturated wüstite is formed in the whole particle, not only at the surface, due to the balancing of the concentration differences. If an iron nucleus appears at the surface, iron ions diffuse to the nucleus and an iron whisker forms. Subsequently, a low nucleation rate and high diffusivity are required for the formation of iron whiskers.

A similar explanation is given by Guo et al.[80] They did an in-situ investigation of iron whisker formation during the gaseous reduction of hematite-based iron ore fines. Layered iron forms when the chemical reaction rate is faster compared to the diffusion rate; if it acts in the opposite way, iron whiskers are formed. Lu et al.[81] reported that iron whiskers cannot grow if the iron oxide is already reduced, the reason being that the iron ions diffuse from areas with high oxygen content to areas with low oxygen during wüstite reduction. This is not possible anymore if the iron oxide already has a certain degree of reduction.

Abdel Halim et al.[82] studied the formation of metallic iron whiskers during wüstite reduction with carbon monoxide. The reduction at 800 °C leads to a low reduction rate and only 40 % of conversion. The reason is the formation of dense iron layers because of low concentration gradient of iron ions between the particle´s surface and the core. With increasing temperatures, the porosity of the iron formed also increases. At 1100 °C reduction temperature, a formation of iron whiskers is observed. Gong et al.[83] demonstrated that the formation of metallic iron whiskers can be inhibited by doping the iron oxides with other oxides because of decreasing iron solid-state diffusion rates. Depending on the type of oxide, different doping amounts are required.

Fruehan et al.[84] investigated the final stage of the reduction of iron ores using hydrogen as a reducing agent. The results demonstrate that the reduction rate decreases at certain reduction extents, depending on the iron ore used. The reason is the formation of dense iron layers. A 1 µm thick iron layer is sufficient for a radical decrease in the reduction rate, so oxygen diffusion through the iron layer becomes the rate-limiting mechanism. The observations also show that a certain partial pressure of hydrogen in the reducing gas can damage the iron layer, ending in better gas diffusion through the layer and a higher reduction rate.

2.4 Methods for kinetical investigation of gas-solid reactions

In the following sections, different approaches for describing gas-solid reactions are shown, starting with the apparent activation energy. Many authors deal with the determination of the apparent activation energy because it is quite a useful tool to give information regarding the reduction procedure. Another frequently investigated topic is the determination of the rate-limiting steps occurring using different approaches of model analysis. Therefore, the general methods used in literature are shown and discussed.

2.4.1 Role of the apparent activation energy

A lot of investigations in literature deal with the determination of the apparent activation energy of the reduction reactions of iron oxides because of its importance. It defines reactor dimensions and thus, energy consumption.[85] The apparent activation energy shows the temperature dependence of the reaction rate and should therefore not be interpreted as the real energy barrier. Table 2 shows a summary of apparent activation energy values for the reduction of iron oxides with hydrogen, reported in literature.

Table 2: Summary of values of apparent activation energy of iron oxide reduction with hydrogen reported in literature.[29]

Reference	Reduction step	Ea (kJ/mol)	Experimental method
Sastri et al.[86]	$Fe_2O_3 \rightarrow Fe$	57.1	Isothermal (H_2)
	$Fe_2O_3 \rightarrow Fe$	72.7	Isothermal (H_2)
	$Fe_2O_3 \rightarrow Fe$	89.9	Isothermal (H_2)
Munteanu et al.[87]	$Fe_2O_3 \rightarrow Fe_3O_4$	246	Non-isothermal (H_2)
	$Fe_3O_4 \rightarrow Fe$	93.2	Non-isothermal (H_2)
	$Fe_2O_3 \rightarrow Fe_3O_4$	162.1	Non-isothermal (H_2)
	$Fe_3O_4 \rightarrow Fe$	103.6	Non-isothermal (H_2)
Munteanu et al.[88]	$Fe_2O_3 \rightarrow Fe_3O_4$	139.2	Non-isothermal (H_2)
	$Fe_3O_4 \rightarrow FeO$	77.3	Non-isothermal (H_2)
	$FeO \rightarrow Fe$	85.7	Non-isothermal (H_2)

Abd Elhamid et al.[89]	$Fe_2O_3 \rightarrow Fe_3O_4$	30.1	Isothermal (H_2)
Lin et al.[90]	$Fe_2O_3 \rightarrow Fe_3O_4$	89.1	Non-isothermal (H_2)
	$Fe_3O_4 \rightarrow Fe$	70.4	Non-isothermal (H_2)
Barde et al.[91]	$Fe_3O_4 \rightarrow FeO$	47.0	Isothermal (H_2)
	$FeO \rightarrow Fe$	30.0	Isothermal (H_2)
Lee et al.[92]	$Fe_2O_3 \rightarrow Fe$	47.2	Isothermal (H_2)
	$Fe_2O_3 \rightarrow Fe$	51.5	Isothermal (H_2)
Kuila et al.[93]	$Fe_3O_4 \rightarrow FeO$	42.0	Isothermal (H_2)
	$FeO \rightarrow Fe$	55.0	Isothermal (H_2)
Kuila et al.[94]	$Fe_3O_4 \rightarrow FeO$	33.0	Isothermal (H_2)
	$FeO \rightarrow Fe$	11.0	Isothermal (H_2)
Jozwiak et al.[95]	$FeO \rightarrow Fe$	104.0	Non-isothermal (H_2)
Hou et al.[96]	$FeO \rightarrow Fe$	75.9	Isothermal (H_2-Ar)

Within the table, different values of the apparent activation energy for the same reduction sequence from one author refer to different input materials. As shown, the values vary enormously, from 11 to 246 kJ/mol. This is a result of the dependence of the apparent activation energy on many different factors, such as input material, the composition of the reducing gas, impurities in the reducing gas, reduction temperature area, type and shape of the particles, impurities in the material and the type of experiment. All these factors have an influence on the progress of reduction and therefore on the resulting apparent activation energy.

2.4.1.1 Determination of apparent activation energy

The principle procedure for determining the apparent activation energy is explained below. In principle, the rate constant of isothermal gas-solid reactions is defined as follows:[97,98]

$$\frac{dx}{dt} = k(T) * f(x) \tag{14}$$

$$g(x) = \int_0^x \frac{dx}{f(x)} = k(T) * t \tag{15}$$

where *k(T)* gives the Arrhenius rate constant, which considers the dependence of the reduction rate on the temperature, and *f(x)* represents a mathematical function which depends on the kinetic model used and remains constant at a given temperature and gaseous concentration.[38] For isothermal reaction kinetics, Equation (14) can be integrated to get the integral expression *g(x)*. Using experimental data of conversion over time in Equation (15), the rate-limiting mechanism can be determined via a model-fitting method. The relationship among *k(T)*, temperature *T*, and the apparent activation energy E_a is given by the Arrhenius equation, Equation (16):

$$k(T) = A * e^{-\frac{E_a}{R*T}} \tag{16}$$

where *A* denotes the pre-exponential factor, and *R* shows the gas constant. To determine the apparent activation energy, a combination of Equation (14) and Equation (16) is required.

$$\frac{dx}{dt} = A * e^{-\frac{E_a}{R*T}} * f(x) \tag{17}$$

$$ln\left(\frac{\frac{dx}{dt}}{f(x)}\right) = -\frac{E_a}{R*T} + ln(A) \tag{18}$$

Using the experimental data for *dx/dt*, the apparent activation energy can be determined using the linear regression method. Based on the ordinate intercept, the pre-exponential factor can be evaluated.

Isoconversional methods allow researchers to distinguish between single-step kinetics und multi-stage kinetics.[97,99] Single-step kinetics can be described well by Equation (18). In other cases, if the apparent activation energy varies with the conversion, the question of validity must be asked. This is because dependence of the Arrhenius equation on temperature, the f(x) dependence of conversion, or both, do not correctly describe the rate variations with temperature and/or conversion.[97]

Pineau et al.[100] studied the reduction kinetics of magnetite by hydrogen at moderate temperatures, focusing on the determination of the apparent activation energy. The reduction was investigated in a thermogravimetric analyzer at temperatures between 227 and 426 °C. The results of the reduction curves are shown in Figure 24, which are characterized by the typical sigmoid shape. To reach a conversion of 50 %, the duration is about 2000, 500, 140, 11 and 3 min at 227, 239, 258, 352 and 426 °C reduction temperature, respectively.[100] The resulting Arrhenius plot is shown in Figure 25, while the reaction rates from experimental results in the range between 20 and 60 % reduction extent are used, because of the nearly constant slopes at all tested temperatures.
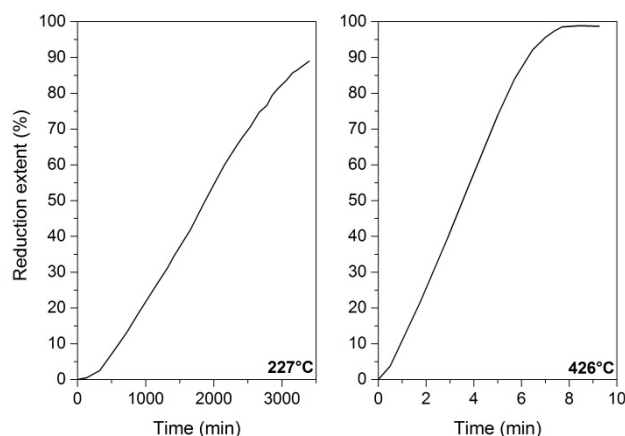
Figure 24: Examples of progress of reduction of magnetite by hydrogen at moderate temperatures: left-227 °C; right- 426 °C.[100]

As indicated, the apparent activation energy differs for different temperature areas. For low temperatures (<250 °C), a value of approximately 200 kJ/mol is defined. An increasing reduction temperature ends in lower values of apparent activation energies, representing 71 and 44 kJ/mol for temperature areas of 250-390 °C and > 390 °C, respectively. The high

value of apparent activation energy for temperatures <250 °C is a result of the sample used, which was produced by reducing hematite to magnetite at 600 °C. The same investigations with magnetite produced at 1200 °C do not demonstrate the drastic decrease in reduction rate at the lowest tested temperatures; however the reduction rates between 250 and 500°C are comparable. This is probably due to annealing point defects during the magnetite synthesis.[100]
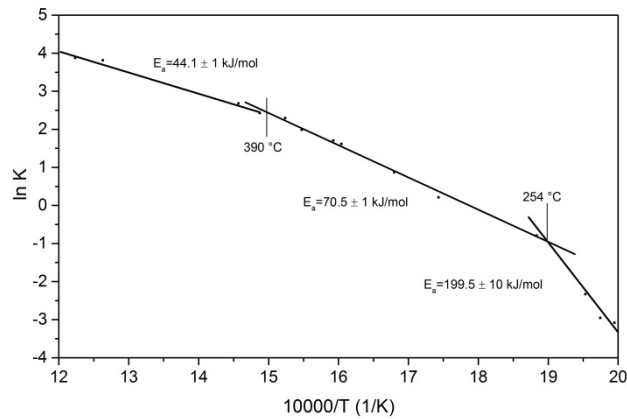
Figure 25: Arrhenius plot for the reduction of magnetite with hydrogen at low temperatures.[100]

Piotrowski et al.[101] studied the influence of different reducing gas compositions on the reduction behavior of hematite to wüstite completed by the determination of the apparent activation energy. For the reduction, a temperature area of 700 to 910 °C is used while the reducing gas consists of nitrogen, hydrogen and carbon monoxide. The resulting Arrhenius plot is given in Figure 26. For the observation of the reduction, the phase boundary-controlled model is applied, which does not fit exactly to the experimental data obtained. As a result, the defined values of apparent activation energy do not represent the real behavior exactly. As shown, the apparent activation energy increases from 28.1 to 93.7 and 122.5 kJ/mol for gas mixtures with H_2, H_2/CO, and CO, respectively.[101] A higher content of carbon monoxide leads to longer reduction times and higher values of apparent activation energy; nevertheless, hydrogen has a better reducing capability compared to carbon monoxide. Similar trends regarding the effect of gas composition were found by Wang et al.[102] for the reduction of hematite pellets. The apparent activation energy increases with increasing carbon monoxide content in the gas mixture from 27.4 to 39.9 kJ/mol.
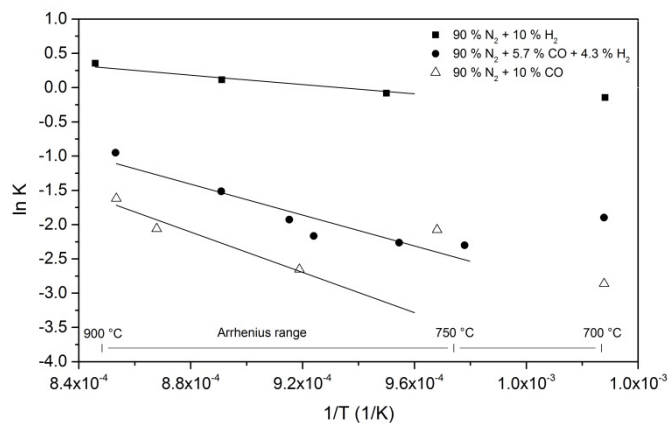
Figure 26: Arrhenius plot for the phase-boundary controlled reaction model.[101]

2.4.2 Determination of rate-limiting steps – conventional methods

Mathematical models are often used for the determination of rate-limiting mechanisms. A model is a theoretical, mathematical description of experimentally observed data.[103] Two types of kinetical analysis are the model-fitting and model-free methods. Model-free methods have the advantage in that the activation energy can be calculated without modelistic assumptions. Generally, a reaction model is usually needed for a complete kinetical analysis of experimental results.[103] A lot of different models are available in literature; some of them are based on mechanistic assumptions, while others are developed empirically.

Table 3 shows commonly used mathematical models. Based on mechanistic assumptions, models can be divided into phase-boundary controlled models, diffusion models, reaction order models and nucleation models.

Table 3: Mathematical models to describe gas-solid reactions [99,103–107]

Model		f(x)	g(x)
Phase-boundary controlled			
PBC 1	Infinite slab	1	x
PBC 2	Contracting cylinder	$2(1-x)^{1/2}$	$1-(1-x)^{1/2}$
PBC 3	Contracting sphere	$3(1-x)^{1/3}$	$1-(1-x)^{1/3}$
Diffusion models			
D1	One-dimensional	$1/(2x)$	x^2
D2	Two-dimensional	$(-\ln(1-x))^{-1}$	$x+(1-x)\ln(1-x)$
D3	Three-dimensional- Jander	$3/2(1-x)^{2/3}(1-(1-x)^{1/3})^{-1}$	$(1-1-x)^{1/3})^2$
D4	Three-dimensional- Ginstling	$3/2((1-x)^{-1/3}-1)^{-1}$	$(1-2/3x)-(1-x)^{2/3}$
Reaction order models			
ROM 1	first order	$1-x$	$-\ln(1-x)$
ROM 2	1.5 order	$(1-x)^{3/2}$	$2((1-x)^{-1/2}-1)$

ROM 3	second order	$(1-x)^2$	$(1-x)^{-1}-1$
ROM 4	third order	$(1-x)^3$	$1/2((1-x)^{-2}-1)$
Nucleation models			
NM 1	n=1.5	$2/3(1-x)(-\ln(1-x))^{1/3}$	$(-\ln(1-x))^{2/3}$
NM 2	n=2	$2(1-x)(-\ln(1-x))^{1/2}$	$(-\ln(1-x))^{1/2}$
NM 3	n=3	$3(1-x)(-\ln(1-x))^{2/3}$	$(-\ln(1-x))^{1/3}$
NM 4	n=4	$4(1-x)(-\ln(1-x))^{3/4}$	$(-\ln(1-x))^{1/4}$
Power law models			
PL 1		$4x^{3/4}$	$x^{1/4}$
PL 2		$3x^{2/3}$	$x^{1/3}$
PL 3		$2x^{1/2}$	$x^{1/2}$
PL 4		$2/3x^{-1/2}$	$x^{3/2}$

Phase-boundary controlled models take into account that the process of nucleation occurs very fast. In that case, the reaction progress is limited by the phase-boundary reaction while the phase-boundary is moving to the particle center. Different models for different particle shapes are available.[103] During gas-solid reactions, gaseous diffusion always has to be kept in mind because it is required to transport reactants to and reaction products away from the reaction interface. If diffusion is the rate-limiting step, the speed of reduction slows down with increasing product layer thickness, while the porosity of the product layer has a great impact on the diffusion behavior.[103] For reaction-order based models, the reaction rate is proportional to the concentration of remaining reactants raised to a particular power, the reaction order n. The first order model is a special case nucleation model with n=1. Three half, second and third order models can also be used, as shown in Table 3.

Nucleation models describe the nucleation and growth of the nuclei during the reaction. In particular, the Avrami-Erofeyev models are often used to describe the kinetics of gas-solid reactions in the case of nucleation as the rate-limiting step. The power law models are a special case of the nucleation models.[103]

Aside from mechanistic assumptions, the progress of gas-solid reactions can be categorized according to the shape of a plot of the first derivative of conversion with time against conversion. For that purpose, four groups can be defined: sigmoid-shaped, linear, acceleratory, and decceleratory models, as schematically shown in Figure 27. Sigmoid-shape functions typically represent nucleation models with a low reaction rate at the beginning and the end. Decceleratory-shaped functions describe diffusion models, phase-boundary controlled models, and, for example, first-order controlled models. Acceleratory models include power law models as a special case of nucleation models. A constant reaction rate is typically represented by a zero-order controlled reaction. Based on this information, many authors have performed model analysis for iron oxide reduction to determine rate-limiting steps.[93,100,108,109]
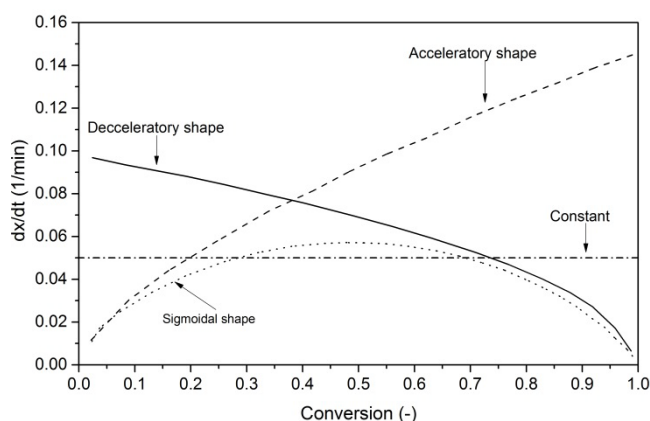
Figure 27: Different schematic shapes of reaction rate against conversion.[103]

2.4.2.1 Determination of rate-limiting steps using model analysis

In this section, the determination of rate-limiting mechanisms using different approaches is shown using examples from literature. Piotrowski et al.[108] studied the kinetics of the reduction from hematite to wüstite using nitrogen, hydrogen and carbon monoxide gas mixtures including a modeling procedure to describe the reduction. Figure 28 demonstrates the contrast between experimental results and the mathematical modeling at a reduction temperature of 775 °C. The modeling procedure includes two different physical-chemical phenomena: the Avrami-Erofeyev topochemical model with an exponent n = 1.6 and the 1D diffusion model (D1).[108] The use of only one single model does not lead to an accurate prediction of the reduction behavior, so two models are combined. At around 50 % of conversion, the Avrami-Erofeyev model starts to deviate from the experimental data, indicating a change of the rate-limiting step. In the current case, the progress becomes diffusion controlled and follows the 1D diffusion model (D1 - Table 3). The further progress is highly overestimated by the Avrami-Erofeyev model because it does not take physical phenomena like mass transfer through a product layer into account.[108] This simple example shows that a prediction of the reduction process using only one single model is not possible with high accuracy. Because of changing conditions during iron oxide reduction, there is also a possibility for changing rate-limiting steps depending on of the conversion degree.
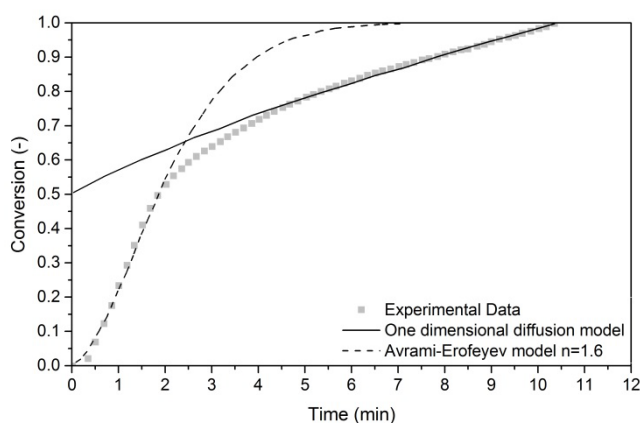
Figure 28: Model analysis for the reduction from hematite to wüstite at a reduction temperature of 775 °C.[108]

Pineau et al.[100] did a model analysis for the experimental results obtained from magnetite reduction at moderate temperatures using some of the models shown in Table 3. Plotting the integral expression g(x) against reduction time should end in a straight line if the model used describes the progress of reduction. Models with coefficient of determination > 0.995 are selected to be those which limit the reduction. The phase-boundary controlled models fit best at lower reduction temperatures while with increasing temperature, the rate-limiting step changes to two-dimensional growths of nuclei.

Such a model analysis only uses the coefficient for determination for the assessment and that is way the question of validity has to be asked. If more than one model shows a similar high coefficient of determination it is not possible to define one rate-limiting step precisely, especially if the whole reduction sequence is used for the analysis. Furthermore, the reduction occurs stepwise from iron with a high valence to iron with a lower valence, and it is also possible that the different reduction sequences occur in parallel. This makes the prediction more difficult.

Nyankson et al.[109] studied the reduction behavior of iron ore pellets with different gas mixtures. The initial stage of reduction shows a limitation by a phase boundary. At the end, gas diffusion becomes important. In accordance with Table 3, the models PBC3 and D4 are used. The investigations also show that the effective diffusion coefficient decreases with increasing content of carbon monoxide in the gas mixture. Kuila et al.[93] conducted kinetic investigations for the reduction of magnetite by hydrogen. A limitation by pore diffusion is observed while the model D1 is used for the kinetic investigation. This limitation occurs during the reduction from magnetite to wüstite and wüstite to metallic iron.

Table 4 summarizes defined rate-limiting steps of iron oxide reduction reported in literature by different authors. In general, during reduction with hydrogen, the phase-boundary reaction is often defined as the occurring rate-limiting step. Diffusion only seems to be important in case of the formation of a non-porous product layer. In fact, the occurring limiting mechanism also strongly depends on the input material used.

Table 4: Summary of rate-limiting steps of iron oxide reduction reported in literature.[29]

Reference	Reduction step	Temperature range (°C)	Reduction controlled mechanism	Experimental method
Sastri et al.[86]	$Fe_2O_3 \rightarrow Fe$	460-500	Phase-boundary	Isothermal (H_2)
Piotrowski et al.[101]	$Fe_2O_3 \rightarrow FeO$	700–910	Phase-boundary	Isothermal (H_2)
Lin et al.[90]	$Fe_2O_3 \rightarrow Fe$	300–900	First-order and nucleation	Non-isothermal (H_2)
Pineau et al.[100]	$Fe_3O_4 \rightarrow Fe$	220–430	Phase-boundary and nucleation	Isothermal (H_2)
Tiernan et al.[110]	$Fe_2O_3 \rightarrow Fe_3O_4$	25–650	Phase-boundary	Constant rate thermal analysis (H_2)
Du et al.[111]	$Fe_2O_3 \rightarrow Fe_3O$	400–500	Phase-boundary and product layer diffusion	Isothermal (H_2)
Shimokawabe et al.[112]	$Fe_2O_3 \rightarrow Fe_3O_4$	250–800	Random nucleation	Non-isothermal (H_2)
Wang et al.[113]	$Fe_2O_3 \rightarrow Fe_3O_4$	800–900	Phase-boundary	Isothermal (CO)
	$Fe_3O_4 \rightarrow FeO$	800–900	Phase-boundary	Isothermal (CO)
	$FeO \rightarrow Fe$	800–900	Nucleation and growth	Isothermal (CO)
Hua et al.[114]	$Fe_2O_3 \rightarrow Fe$	700–900	Phase-boundary and diffusion	Isothermal (CO)
Moon et al.[115]	$Fe_2O_3 \rightarrow FeO$	800–950	Phase-boundary and diffusion	Isothermal (H_2, CO)

2.5 The fluidization phenomenon

During fluidization, solid particles are transformed into a fluid-like state by an upward passing fluid, a gas or a liquid.[116] To bring solid particles into a fluidized state, the fluid should exert a certain force to the particles, representing the force created by pressure loss. The force depends on the properties of the fluid such as density and on the process conditions like superficial gas velocity. Figure 29 shows the pressure drop occurring at increasing superficial gas velocity. A higher gas velocity represents a higher pressure loss force if all other parameters remain constant. If it is too low, the particles will remain in a fixed bed while the fluid is passing through the void spaces between the particles. Under conditions of higher fluid forces, a point can be reached where the weight of the particles is counterbalanced and the system changes from a fixed bed to a fluidized bed. This point is known as minimum fluidization point, identified by the minimum fluidization velocity, w_{mf} or u_{mf}. A further increase in the gas velocity does not affect the pressure drop across the material because it is still in fluidized state. Only the expansion of the bed increases, resulting in a higher void fraction. When particles are fluidized at sufficiently high superficial gas velocities, they are carried out of the bed together with the gas and a pneumatic transport of the particles takes place. This defined velocity is known as terminal velocity, w_t or u_t.
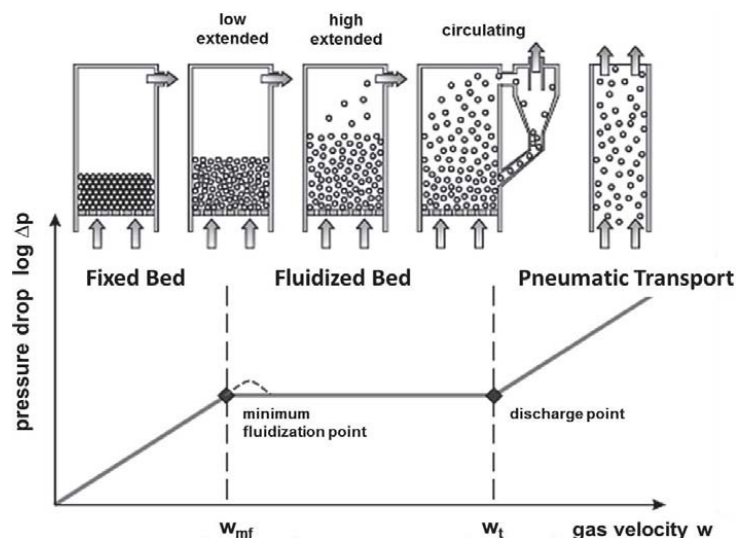
Figure 29: Dependence of pressure drop against superficial gas velocity and the corresponding forms of the solids during fluidization.[117]

Figure 30 shows the different fluidization regimes occuring during gas-solid fluidization with increasing superficial gas velocity. At the minimum fluidization point, the bed height is even higher compared to the fixed bed ($L_{mf} > L_m$) because of the increasing bed porosity. A well defined minimum fluidization point can only be determined for particles with a monodisperse particle size distribution. At higher superficial gas velocities a formation of gas bubbles occurs. The bubbles are nearly free of solids. Bubbles grow while passing the bed material; they can also coalescent together. If the size of the bubbles reaches dimensions similar to

the reactor cross-sectional area, the material starts to slug. This phenomenon usually happens in long, narrow fluidized beds. A further increase in the superficial gas velocity leads to a turbulent fluidization state. In that case, an elatruation of the smallest particles already takes place. As a result, the interface between material and gas cannot be clearly defined anymore. The concentration of the solids decreases over the height of the bed. Instead of gas bubbles, a turbulent solid cluster formation occurs. Between these clusters, gas voids are present. For steady state fluidization, a cyclone is required which separates the particles from the gas stream and returns the particles into the fluidized bed. A further increase in the gas velocity will lead to a pneumatic transport of the particles with a lean-phase fluidized bed.
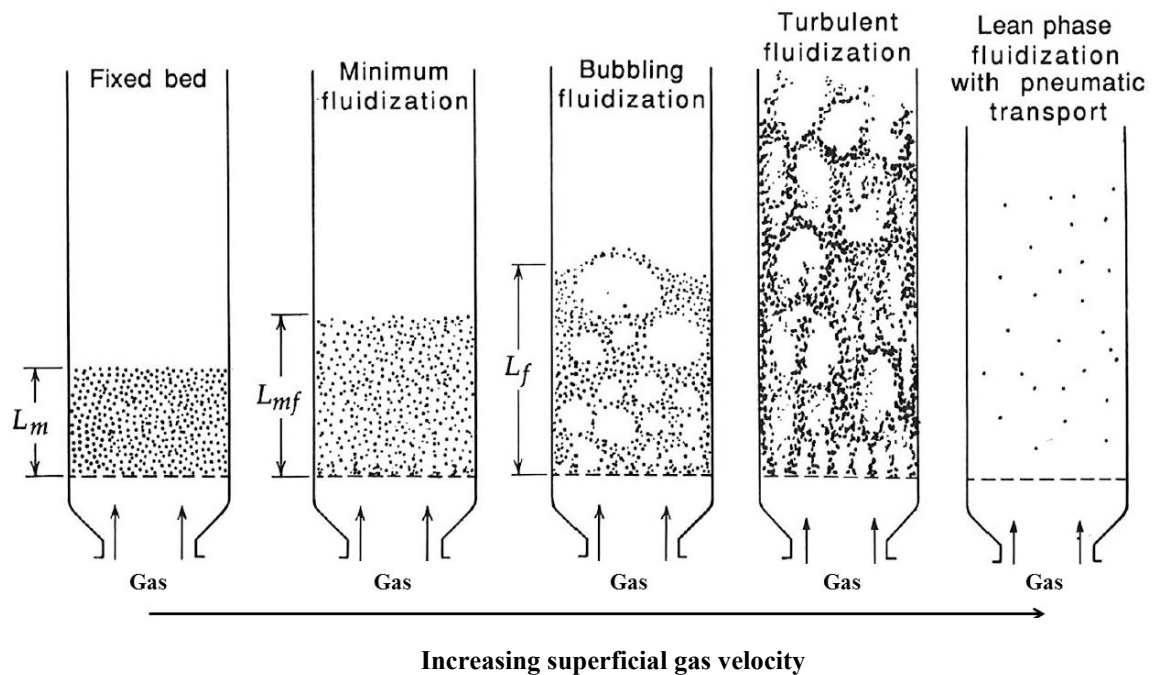
Figure 30: Changing fluidization regimes with increasing superficial gas velocity.[116,118]

2.5.1 Determination of operation conditions of gas-solid fluidized bed system-flow regime diagrams

For fluidization experiments, it is always important to predict the behavior of the specific gas-solid system used in advance or rather what contacting regime will occur. In that case, the use of fluidization regime diagrams is a simple method. Fluidization regime diagrams show different operation areas depending on the process conditions used. It can be distinguished between fixed bed operations, fluidized bed operations and also other types of operations, e.g. circulating fluidized beds. As a result, it is possible to adjust the process conditions of the given gas-solid system to end in the preferred fluidization regime. A lot of authors have created diagrams to predict the different fluidization regimes; e.g. Reh[119], who displayed the inverse drag coefficient against the particle Reynolds number or Grace[120], who used the dimensionless gas velocity against dimensionless particle diameter, which are defined as follows:

$$u^* = u \left[\frac{\rho_F^2}{\eta(\rho_S - \rho_F)g} \right]^{1/3} \tag{19}$$

$$d_p^* = Ar^{1/3} = d_p \left[\frac{\rho_F(\rho_S - \rho_F)g}{\eta^2} \right]^{1/3} \tag{20}$$

The fluidization regime diagram developed by Grace is shown in Figure 31. The coordinates used by Grace seem to be the most useful form of presentation. The usage of dimensionless particle diameter and gas velocity is helpful because each of them only includes the particle diameter or the gas velocity and properties which are constant for a given gas-solid system. Hence, different process conditions can be shown quite easily. It is also possible to show the different Geldart particle groups directly in the diagram. The definition and properties of each group are explained below.
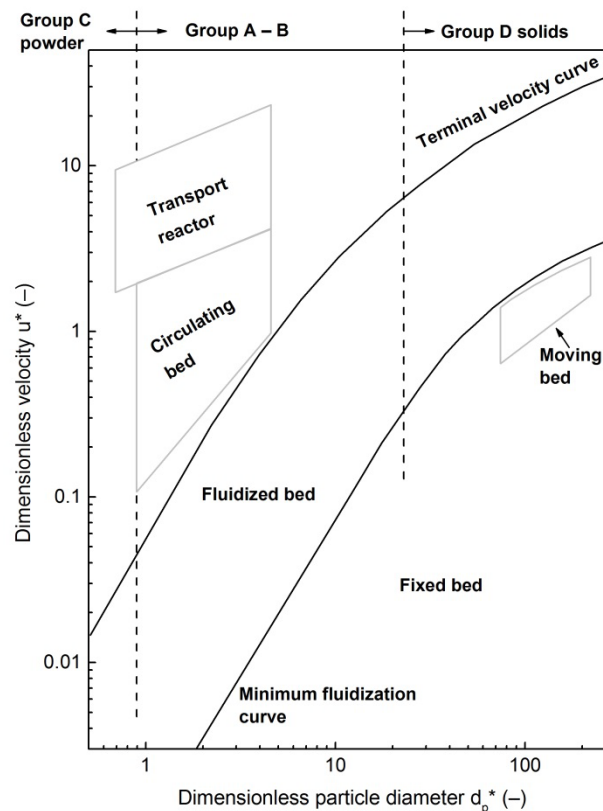
Figure 31: Fluidization regime diagram according to Grace.[120,121]

The different regimes are separated by the curve of minimum fluidization velocity and the curve of the terminal velocity. On the right side of the minimum fluidization curve, representing big particle diameters and low superficial gas velocities, the material will remain in a fixed bed. In the area between the minimum fluidization velocity and the terminal velocity, the fluidization of the material occurs. Materials which belong to Group A or B typically form a bubbling fluidized bed, whereby the gas velocity for Group A particles should be close to the terminal velocity for the formation of a bubbling bed. On the left side of the

terminal velocity curve, elutriating of particles takes place, which ends in a circulating fluidized bed or even in a material transport.

The classification of powders according to their fluidization behavior into different groups was done by Geldart[122] according to the mean particle diameter and the difference in densities of solids and fluid. The corresponding diagram is shown in Figure 32.
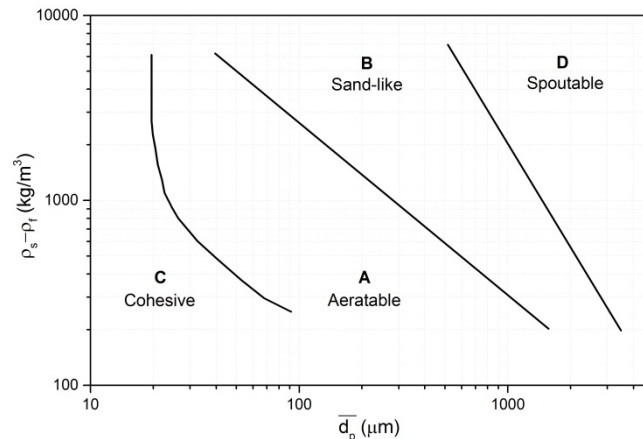
Figure 32: Geldart classification diagram for powders in air at atmosphere temperature and pressure.[122]

Geldart defines the properties of each group as follows:[121]

Group A particles (aeratable)

Most commercial fluidized bed reactor systems operate with particles which belongs to Group A. They are characterized by a bubble-free range of fluidization at gas velocities slightly above u_{mf}, because such powders are slightly cohesive. Above u_{mf}, the beds expand considerably with increasing gas velocity until the formation of the bubbles starts. The behavior of bubbles is characterized by frequent splitting and recoalescencing, which ends in a restricted bubble size. The frequent splitting of the gas bubbles leads to a high gas exchange between bubbles and solids.

Group B particles (sand-like)

For Group B, inter-particle forces can be ignored. The bubble formation starts immediately after reaching the minimum fluidization velocity. The bed expansion is lower compared to Group A particles. The bubbles rise faster than the interstitial gas velocity and the size increases with bed height and gas velocity. On the surface of the bed, the bubbles burst. Back-mixing of dense phase gas is low, because of gas exchange between the bubbles and the gas phase (no splitting of bubbles).

Group D particles (spoutable)

Group D consists of particles with a large grain size and/or high density. Bubbles rise slower than the interstitial fluidization gas, ending in a gas exchange inside the bubble. Gas

enters the bubble at the base and leaves it at the top, which is different compared to other particle groups. The mixing of the solid is poor and therefore, back-mixing of the dense phase gas is low. The expansion of the bed is also low, even at high gas velocities.

Group C particles (cohesive)

Powders which belong to Group C are characterized by a poor fluidization behavior because of cohesive forces acting between the particles. These forces can be bigger than those which the fluid can exert to the particles. The heat transfer between a surface and the bed material is also worse compared to other particle groups. Normal fluidization is difficult because the material can lift as a plug. After fluidization, the particles stay aerated for a long time because the gas can escape only very slowly. The fluidization of such fine-grained material can be improved, e.g., by the use of vibrators.[123–125]

Based on this simple classification of materials into different groups, a first valuation regarding the behavior of different materials during fluidization can be carried out. Shaul et al.[126,127] investigated the behavior of the pressure drop at increasing superficial gas velocities for different Geldart group particles. They found that the shape of the pressure drop of the packed bed changes from linear to parabolic shape for Group A and Group D particles, respectively. Thus, materials can be linked to certain groups by using only the pressure drop curve.

2.5.1.1 Determination of the minimum fluidization point

The fluidization state is reached if the drag force by the upwards moving gas is equal to the weight of the particles (decreased by the buoyancy force of the particles in the fluid), signifying that the force by pressure loss ($F_{\Delta p}$) is equal to the gravitational force minus the buoyancy force (F_G-F_A).[116]
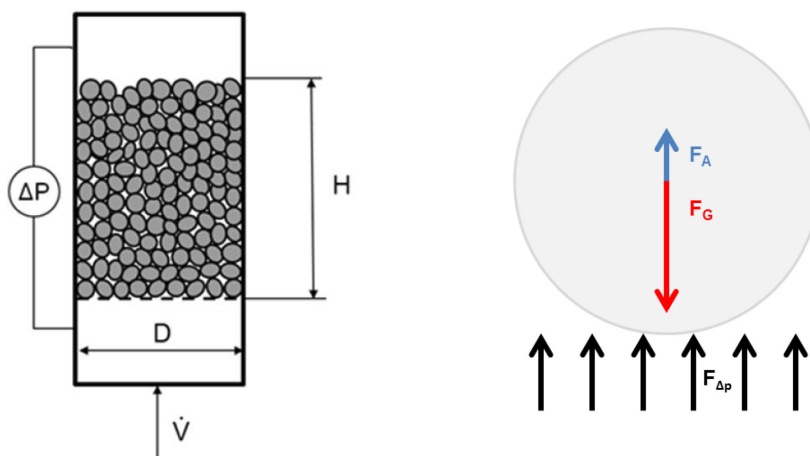
Figure 33: Conditions at minimum fluidization point.[117]

The difference between the gravitational force and the buoyancy force (F_G-F_A) and the force by pressure loss ($F_{\Delta p}$) are defined as follows with regard to the system shown in Figure 33:

$$(F_G - F_A) = (m \cdot g) - F_A = \frac{D^2\pi}{4} H (1 - \varepsilon)(\rho_S - \rho_F) \cdot g \tag{20}$$

$$F_{\Delta p} = \Delta p \cdot \frac{D^2\pi}{4} \tag{21}$$

where m is the sample mass, g the gravitational constant, D the reactor diameter, H the bed height, ε the voidage, ρ_s the density of the solids, ρ_g the density of the gas and Δp the pressure loss across the bed material. At the minimum fluidization point, both forces are equal. ε_{mf} is used for the bed voidage at the minimum fluidization point:

$$(F_G - F_A) = F_{\Delta p} \rightarrow \frac{\Delta p}{H} = (\rho_S - \rho_F)(1 - \varepsilon_{mf})g \tag{22}$$

For the calculation of the pressure drop under minimum fluidization conditions, the correlation developed by Ergun can be used, which works satisfactorily for a wide range of the Reynolds number:[116,121,128]

$$\frac{\Delta p}{H} = 150\frac{(1-\varepsilon_{mf})^2}{\varepsilon_{mf}^3}\frac{\eta \cdot u_{mf}}{d_{sv}^2} + 1.75\frac{1-\varepsilon_{mf}}{\varepsilon_{mf}^3}\frac{\rho_F u_{mf}^2}{d_{sv}} \tag{23}$$

d_{sv} shows therein the diameter of a sphere with the same surface to volume ratio as the particles used.[121] A combination of Equation (22) and Equation (23) and a rearrangement leads to Equation (24):

$$\frac{\rho_F d_{sv}^3(\rho_S - \rho_F)g}{\eta^2} = \frac{150(1-\varepsilon_{mf})}{\varepsilon_{mf}^3}\frac{\rho_F d_{sv}}{\eta}u_{mf} + \frac{1.75}{\varepsilon_{mf}^3}\frac{\rho_F^2 d_{sv}^2}{\eta^2}u_{mf}^2 \tag{24}$$

d_{sv} can be substituted by the particle diameter based on the sieve analysis d_p using the following correlation, where ϕ_s gives the particle´s sphericity, leading to Equation (26):

$$d_{sv} = d_p \cdot \phi_s \tag{25}$$

$$\frac{\rho_F d_p^3(\rho_S - \rho_F)g}{\eta^2} = \frac{150(1-\varepsilon_{mf})}{\varepsilon_{mf}^3\phi_s^2}\frac{\rho_F d_p}{\eta}u_{mf} + \frac{1.75}{\varepsilon_{mf}^3\phi_s}\frac{\rho_F^2 d_p^2}{\eta^2}u_{mf}^2 \tag{26}$$

The term on the left side represents the dimensionless Archimedes number. On the right side, the Reynolds number at minimum fluidization conditions ($Re_{p,mf}$), shown in Equation (27), is included twice, multiplied by terms which can be summarized as K_1 and K_2. This ends in Equation (28):

$$Re_{p,mf} = \frac{\rho_F d_p u_{mf}}{\eta} \tag{27}$$

$$Ar = K_2 Re_{p,mf} + K_1 Re_{p,mf}^2 \tag{28}$$

Wen and Yu[129] were among the first researchers to note that K_1 and K_2 stayed nearly constant for different particles over a big range of Re. Thus, u_{mf} can be also defined if ε_{mf} and/or ϕ_s are not known for the given system.[116] Anantharaman et al.[130] presented a review

of a wide range of correlations for predicting the minimum fluidization velocity for different particle groups during gas-solid fluidization reported in literature. They found that the difference in prediction is in an order-of-magnitude for the particle groups A, B and D. The biggest deviations occur for Group A particles due to the presence of inter-particle forces, which still have not been well understood to this day. It must be noted that the correlations are highly empirical and specified for defined systems. The best way to determine u_{mf} is the experimental measurement of pressure drop at increasing superficial gas velocities.

Table 5 summarizes the parameters influencing the minimum fluidization velocity and shows the impact on it.

Table 5: Effect of different parameters on the minimum fluidization velocity.

Parameter	Minimum fluidization velocity u_{mf}		Remark
Particle diameter dp	↑	↑	Bigger weight of single particles
Particle density ρ_s	↑	↑	Bigger weight of single particles
Sphericity ϕ_s	↑	↑	Lower force by pressure loss
Density fluid ρ_F	↑	↓	Higher force by pressure loss
Viscosity fluid η	↑	↓	Higher force by pressure loss
Temperature T	↑	↓↑	Depending on changes concerning gas density and viscosity; Generally u_{mf} decreases because of higher impact of increasing gas viscosity
Pressure p	↑	↓	Gas density increases

2.5.1.2 Particle elutriation and carryover

The elutriation of solid particles during fluidization plays an important role because it defines the necessity of a recirculation of particles. For the determination of the amount of particle elutriation, knowledge regarding the terminal velocity, u_t, is required. At the elutriation point of a single particle, the gravitational force of the particle is balanced by the drag force (F_W) and the buoyancy force (F_A), as shown in Figure 34 and Equation (29).
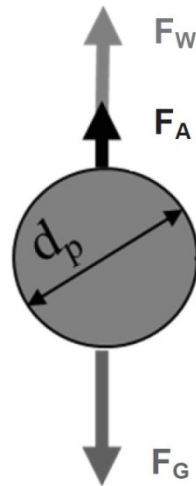
Figure 34: Force balance on a single particle at the elutriation point.[117]

$$F_G = F_W + F_A \tag{29}$$

The gravitational force F_G and the occurring buoyancy force F_A in a fluid of a single particle with diameter d_p are defined as follows:

$$F_G = m_P \cdot g = \frac{d_P^3 \pi}{6} \rho_s g \tag{30}$$

$$F_A = \frac{d_P^3 \pi}{6} \rho_F g \tag{31}$$

The drag force can be expressed in the following way, where C_D is the drag coefficient and u_t the corresponding terminal velocity that defines the falling velocity of particles in a fluid:

$$F_W = \frac{d_P^2 \pi}{4} \rho_F C_D \frac{u_t^2}{2} \tag{32}$$

Inserting Equations (30), (31) and (32) in Equation (29) and a rearrangement to u_t yields the following equation for the terminal velocity:

$$u_t = \left(\frac{4 \, d_p (\rho_s - \rho_F) g}{3 \, \rho_F \, C_D} \right)^{0.5} \tag{33}$$

Generally, the drag coefficient depends on the particle Reynolds number, where three areas can be distinguished: a laminar flow area at low values of $Re_{p,t}$ ($Re_{p,t} < 0.2$), a transition region ($0.2 < Re_{p,t} < 1000$) and a turbulent region ($Re_{p,t} > 1000$). Haider and Levenspiel[131] proposed the following equation for the drag coefficient for non-spherical particles, which covers the whole range from laminar flow to turbulent region:

$$C_D = \frac{24}{Re_p} [1 + (8.1716 e^{-4.0655 \Phi_s}) Re_p^{0.0964 + 0.5565 \Phi_s}] + \frac{73.9(e^{-5.0748 \Phi_s}) Re_p}{Re_p + 5.378 e^{6.2122 \Phi_s}} \tag{34}$$

A lower value of sphericity will increase the value of c_D and therefore decrease the terminal velocity of the particles. Table 6 shows the different parameters influencing the terminal velocity.

Table 6: Effect of different parameters on the terminal velocity.

Parameter	Terminal velocity u_t		Remark
Particle diameter dp	↑	↑	Higher weight of single particles
Particle density ρ_s	↑	↑	Higher weight of single particles
Sphericity ϕ_s	↑	↑	Decrease C_D
Density fluid ρ_F	↑	↓	Higher drag and buoyancy force
Viscosity fluid η	↑	↓	Increase C_D
Temperature T	↑	↓↑	Depending on changes concerning gas density and viscosity; Generally u_{mf} decreases because of higher impact of increasing gas viscosity
Pressure p	↑	↓	Gas density increases

The terminal velocity alone is not responsible for the elutriation occurring during fluidization. Geldart[121] reported that there is no general statement possible regarding the mechanisms responsible for the ejection of solids into the freeboard. Bursting bubbles on the bed surface are important, while the ejection depends on superficial gas velocity and bubble size. Other influencing parameters are, e.g., stratification of fines at the bed surface in case of beds with a certain grain size distribution or the formation of clusters in the freeboard, which also allows fine particles to remain in the reactor at high superficial gas velocities. In fact, the real behavior is not well understood up to now.

In literature, the elutriation rate constant (K_{ih}*) is often used for the prediction of the elutriation, which is based on empirical assumptions. K_{ih}* can be used in the following arrangement:[121]

$$\frac{d}{dt}(x_{Bi}M_B) = K_{ih}^* \cdot A \cdot x_{Bi} \tag{35}$$

where the left side of the equation shows the rate of removal of solids of size d_i, x_{Bi} shows the equilibrium concentration of size d_{pi} in the bed, M_B the mass of solids in the bed and A the cross-sectional area of the bed.

For a batch operation, x_{Bi} decreases with time and the total M_B should not change more than 15 %. Equation (35) has to be integrated in that case. The mass of size fraction d_{pi}, $m_{i,t}$, carried over in time t increases asymptotically as follows:[121]

$$m_{i,t} = x_{Bi0} \cdot M_B \left[1 - exp\left(-K_{ih}^* \frac{A \cdot t}{M_B}\right)\right] \tag{36}$$

Many parameters influence the elutriation rate constant, e.g. the particle size distribution. Some authors have found that the elutriation rate constant decreases with increasing amounts of fines (<40 μm) in the bed material because of cohesive forces between the particles and clustering effects.[132,133] The effect of fines on the elutriation rate constant is reduced with increasing gas velocity.[134] Chew et al.[135] prepared a review on available elutriation correlations for gas-sold fluidization, also summarizing the effects of different parameters on the elutriation rate constant. They defined a big discrepancy between the empirical predictions and the experimental data, which are a hundredfold in some cases. So there is a need for more physically based models to get a more accurate prediction of the entrainment and elutriation phenomena.

2.5.1.3 *The gas distributor's role during fluidizing experiments*

The gas distributor is one of the major construction parts in a fluidization system. It is responsible for a uniform gas distribution over the whole bed cross-section area. The distributor is also responsible for preventing solids backflow into the wind boxes. Additionally, the distributor should be able to resist the force which occurs by the pressure drop associated with the gas flow through the distributor as well as the gravitational force of the particles during a shutdown.[121]

Different types of gas distributor systems can be applied, such as distributor plates using a porous material or perforated plates (metal sheets with drilled holes).[121] Some special designs are also common, e.g. a nozzle stand pipe design, sparge tubes with standpipe nozzles or a cap design.[136] In general, porous plates show an ideal behavior because they have a sufficiently high flow resistance, which ends in a uniform gas distribution. For industrial applications they have several drawbacks, for instance low construction strength, high production costs and low resistivity against thermal stresses.[116] As a result, perforated plates are often used for industrial applications.

The design of the gas distributor is important, as it is responsible for the uniform gas distribution. The main design criterion for distributors is the pressure drop occurring by a passing gas stream. The ratio of pressure drop across the distributor, Δp_D, and pressure drop across the bed material, Δp_B, should exceed a certain value. Qureshi and Creasy[137] suggested the following correlation which has to be fulfilled, based on a study of successful and unsuccessful fluidization experiments:

$$\frac{\Delta p_D}{\Delta p_B} \geq 0.01 + 0.2 \cdot \left[1 - exp\left(-0.5\, \frac{D}{H_B} \right) \right] \tag{37}$$

where D is the bed diameter and H_B the bed height. In case hydrogen is used as fluidization gas, a special grid design is required to get sufficiently high values of Δp_D because of the low gas density at high temperatures. This ends in a high number and a low diameter of orifices, resulting in high construction costs.

2.5.2 Iron ore reduction by fluidized bed technology- related research work

In literature, many authors deal with the topic of fluidized bed reduction of iron ore fines by means of fluidized bed technology. Table 7 shows a summary of selected publications including the operation conditions and the main outcomes of the investigations. Detailed explanations of the results are not provided in this section.

Table 7: Summary of research work related to fluidized bed iron ore reduction.

Reference	Reducing agent	Temperature [°C]	Reduction-stage	Main results regarding reduction behavior
Feilmayr et al.[33]	H_2, CO, CH_4 mixtures	350-600	$Fe_2O_3 \rightarrow$ Fe_3O_4	• A formation of dense magnetite layers during reduction is observed. • The reducibility depends on the mineralogy and petrography of the grains. • Limonite shows the best reducibility followed by martite and different types of hematite.
Dilmac et al.[138]	H_2	600-800	$Fe_2O_3 \rightarrow$ Fe	• A determination of different rate-limiting steps in different regions of reduction is done. • The first stage is controlled by the nucleation of wüstite; the second stage is controlled by the gas-solid reaction (wüstite to iron).
Guo et al.[139]	H_2	800-1000	$Fe_2O_3 \rightarrow Fe$	• A higher H_2 concentration increases the metallization rate and the gas utilization. • The H_2 concentration and the reduction temperature affect the particle surface morphology, thus affecting the reaction rate, the occurrence of sticking and the metallization ratio. • A higher reduction temperature is not always preferable for a faster reduction procedure.
He et al.[140]	H_2	650-800	$Fe_2O_3 \rightarrow Fe$	• Conical fluidized beds are compared to cylindrical fluidized bed in terms of fluidization behavior, avoidance of sticking and reduction efficiency.
Pang et al. [141]	H_2	700-800	$Fe_2O_3 \rightarrow Fe$	• Particles <1mm already show a high reduction rate at 750 °C, while a higher temperature is required for bigger particles to achieve similar reduction rates. • The H_2O content in the gas mixture should not exceed 10 % for an efficient reduction rate.
Schuster et al.[142] Thurnhofer at al.[143]	H_2, CO	350-800	$Fe_2O_3 \rightarrow Fe$	• Investigations of the effect of different parameters during pre-reduction on the final reduction degree are carried out. • The morphology and texture of the iron ore and the product after pre-reduction influence the final reduction degree. • A higher porosity after pre-reduction leads to higher final degrees of reduction.
Weiss et al.[144]	H_2, CO, CH_4 mixtures	400-700	$Fe_2O_3 \rightarrow FeO$	• The reduction from hematite to magnetite and magnetite to wüstite occur topochemically if it is done stepwise. • The single stage reduction from hematite to wüstite is different. Magnetite appears as an intermediate product, which is formed topochemically while progressive conversion of magnetite to wüstite is found.
Chen et al. [38,145]	CO	700-950	$Fe_2O_3 \rightarrow Fe$	• Kinetic analyses are carried out using different methods. • The controlling mechanism varies with temperature and conversion. The initial stages of reduction are controlled by the gas-solid reaction. Then, the reduction is controlled by nucleation and diffusion. • Saddle-shaped curves of apparent activation energy as a function of conversion were obtained.

2.5.3 Sticking phenomena during iron ore reduction

During fluidized bed reduction of iron ores, the most important thing is to keep the fluidization running, also at high degrees of reduction. The metallic iron formed can lead to the so-called sticking phenomenon. Sticking describes the agglomeration of partly reduced iron ore particles, which can end in a de-fluidization of the bed material if the size of the agglomerates formed reaches a critical level. As a general rule, three different types of sticking can be distinguished:[36,146]

- Type 1- <u>Bonding effect of iron whiskers</u>

If the conditions for diffusion are good and the reaction rate is low, a formation of iron whiskers can occur. The whiskers can act as hooks between the particles and lead to an agglomeration of the particles. The contact areas can sinter together during further reduction. As a result, solid iron bridges are formed. The formation of iron whiskers can be influenced by the process conditions like temperature and gas composition and gas flow rate.

- Type 2- <u>Bonding effect of highly active iron</u>

The activity of freshly segregated iron is higher compared to previously segregated iron. Because of the high activity, particles strive to reduce the surface. This leads to big adhesion forces occurring, which can in turn end in an agglomeration of the particles. As a precondition, a high amount of newly formed iron is required. High temperatures and reduction rates support this type of sticking.

- Type 3- <u>Components with low melting point</u>

At high operation temperatures (> 850 °C), liquid phases can occur. Wüstite and gangue can form low temperature melting eutectica. These components tend to soften and bond the particles. As a result, an agglomeration takes place. This type of sticking typically occurs at lower degrees of reduction because the presence of wüstite is required. If iron ores with high iron and low gangue content are used, this type of sticking is not relevant.

The phenomenon of sticking is influenced by a lot of different parameters, such as operation temperature, reducing gas composition and flow rate, type of iron ore, grain size distribution, specific particle surface and the addition of additives. In the following section, the most important influencing factors are explained briefly.

Effect of temperature

Sticking typically occurs above a critical temperature, the so-called critical sticking temperature. This temperature depends on the process conditions. In general, the sticking tendency increases with increasing reduction temperatures. Zhang et al.[147] investigated the sticking behavior of Fe_2O_3 particles under carbon monoxide atmosphere. They found that at higher temperatures, the sticking occurs at lower metallization rates, and the sticking time also decreases if all other parameters remain constant. The sticking time is defined as the time period when the sticking starts and ends if a complete de-fluidization takes place. They reported that the influence of temperature on the surface characteristics of generated iron might be the reason for different sticking times. As a result, a common measure to reduce the sticking tendency is lowering the reduction temperature. This can lead to troubles regarding the reduction rate and the efficiency of the process. As already explained, the temperature clearly affects the type of iron formations.

Metallization ratio

The sticking phenomenon usually occurs after the first metallic iron formation has taken place. This refers to the sticking mechanisms Type 1 and 2 where the formation of iron whiskers and the high activity of freshly generated iron are responsible for sticking, respectively. At higher metallization rates, a greater amount of iron whiskers and freshly

formed iron is available, ending in a higher sticking tendency. Zhong et al.[148] determined the de-fluidization temperature of partly reduced samples with different metallization ratios using nitrogen in a non-isothermal state. The results show that the de-fluidization temperature decreases with an increasing degree of metallization.

Gas composition and flow rate

The composition of the reducing gas mixture is one of the most important parameters influencing the occurrence of sticking. Hydrogen shows a different behavior compared to carbon monoxide. Du et al.[149] investigated the effect of different gas compositions on the morphology of the newly formed metallic iron. They observed that the sticking tendency decreases by changing the gas composition from carbon monoxide-rich to hydrogen-rich. This can be explained by the different morphologies formed during the reduction, from fibrous for a carbon monoxide-rich gas to dense in a hydrogen rich gas. Aside from different iron formations related to different gas compositions and process parameters, different gases have different behaviors regarding fluidization because of their divers properties. Zhong et al.[150] investigated the de-fluidization temperature of iron powder occurring in different gas components. They found that if hydrogen is used as a fluidization gas, de-fluidization already occurs at temperatures around 400 °C, slightly depending on the superficial gas velocity. For carbon monoxide, the de-fluidization temperature was around 700 °C and therefore much higher compared to hydrogen. The use of high viscosity gases results in a decrease in the de-fluidization tendency.

A higher gas flow rate leads to a higher superficial gas velocity. As a result, a more intensive collision among the particles takes place, which ends in a shorter contact time and a lower sticking tendency.[146] A higher gas velocity can help to avoid the sticking phenomenon, but will also lead to a lower reducing gas utilization because of lower contact times between the gas and the solids.

Iron ore characteristics

The properties of the iron ore used for fluidized bed reduction also affect the fluidization and sticking behavior. Relevant properties are the type of the mineral, the gangue content of the ore, the grain size distribution and the shape of the particles.

It is hard to predict the sticking behavior of different ores in advance, because of the considerable number of influencing factors. Magnetite-based ores show a higher tendency for dense iron formations compared to hematite, which typically has a higher number of vacancies. This supports the fibrous iron formation and increases the sticking tendency.[36] Gangue in the ore tends to inhibit the sticking phenomena due to lower concentration of iron atoms on the surface of the particles. Ore grades with higher iron content have lower gangue contents. This can support the sticking.[36,146] On the other hand, the gangue can be responsible for the Type 3 sticking mechanism at high temperatures. A smaller particle size leads to a higher specific surface area. Hence a bigger contact area between the particles appears which increases the sticking tendency.[146] A lower grain size would also end in a lower operating superficial gas velocity and a smaller momentum is exerted from the gas to the particles, which also increases the sticking tendency.[146] The external shape of the particles also plays an important role since it ends in different frictional forces between the

particles. Hayashi and Iguchi[151] tested several ore types concerning their sticking tendency. They classified the ores into three groups with regard to the external shape: spheroid, rectangular prism and angular. The spheroid-shaped particles can be fluidized well without any issues, while angular-shaped particles showed a high sticking tendency. For rectangular prism shaped particles, both, fluidization and sticking were observed, depending on the iron ore used.

Effect of additives

Additives can exist as gangue in the iron ore or they can be added separately to the process. The effect of additives on the reduction process and the sticking phenomena is manifold. First, it has to be distinguished how the additives are added to the material. The two simplest methods are the powder mixing method and the solution method.[152,153] The powder mixing method represents the mixing of the iron ore together with the additive powder. In the case of the solution method, an additive containing solution is applied to the iron ore sample followed by a drying procedure. Additives added in that way create a protecting surface around the particles, which prevents the direct iron-iron contact between the particles during the reduction. The solution method will lead to a more uniform distribution of the additives around the particles compared to the powder mixing method but it is still more elaborate process.[36]

Typical additives that can be added to influence the sticking phenomenon are MgO, CaO, Al_2O_3 and SiO_2. The addition of those oxides to the process does not only have an effect on the occurrence of sticking. It has to be kept in mind that the additives cannot be removed after the fluidized bed reduction. They will remain in the product, so they will influence the slag formation and the amount of slag occurring in the subsequent steelmaking facility. The addition of MgO and CaO would be beneficial because they are required in the melting aggregate to get slags with a required basicity. However, the amount of additives which can be added is also limited. The addition of Al_2O_3 and SiO_2 would be detrimental because it would lead to a higher demand for basic additives in the melting stage, resulting in bigger slag amounts and lower process efficiency, but it still depends on the type of gangue of the iron ore. Typically, iron ores have an acidic gangue content. Because of this, only the effect of the addition of MgO and CaO is discussed.

MgO is completely soluble in wüstite. Mg^{2+} cations are dissolved in the wüstite lattice, resulting in a decrease of the number of vacancies. This leads to a degradation of the diffusion and the formation of iron whiskers is therefore more difficult.[36] Zhong et al.[154] investigated the effect MgO has on the prevention of de-fluidization during fluidized bed reduction of Fe_2O_3 by carbon monoxide. They found a generated coating layer containing magnesio-wüstite, formed by reactions between MgO and Fe_2O_3/FeO during the reduction procedure. This coating layer avoids the direct contact between the freshly generated iron and improves the fluidization behavior. They also found that the inhibition effect is reduced with increasing temperatures. Depending on the coating method used, different authors have defined different required amounts of MgO addition for a successful operation, ranging from 0.4 to 1.0 %-wt. MgO.[155,156]

The role of CaO on the sticking behavior is not really clear. Zhong et al.[154] found that CaO can have a positive effect on the avoidance of de-fluidization because a coating layer

consisting of calcio-wüstite is formed but it is not as effective as those formed by MgO. Zhao et al.[157] found that CaO doping can postpone the formation of iron whiskers while MgO strongly inhibits the formation and growth of whiskers under carbon monoxide atmosphere. Gudenau et al.[36] summarized, based on different sources, that CaO can also promote the formation of iron whiskers, affacting the fluidization behavior in a negative way. So the role of CaO on the fluidization and sticking phenomenon still has not been well defined.

Table 8 summarizes additional important research work related to the sticking phenomenon during fluidized bed reduction of iron ores.

Table 8: Summary of additional research work related to the sticking phenomenon during fluidized bed reduction of iron ore.

Reference	Reducing agent	Temperature [°C]	Main results regarding sticking behavior
Fang[158]	Different gas compositions	Different temperatures	• A general summary of the principles of the sticking mechanism is prepared. • An investigation of nearly all different influencing parameters on the sticking mechanism is carried out.
Gong et al.[159]	H_2, CO	700 (for previous reduction)	• A determination of the de-fluidization temperature of iron particles with different morphologies is done. The de-fluidization temperature decreases when the morphology changes from an iron layer with pores to iron whiskers.
Hayashi et al.[160]	H_2	900	• The effect of coating by different oxides on the sticking is investigated. Different required coating amounts are defined. • The sulfur activity in the bed influences the iron morphology and the surface energy of the iron formed.
Xu et al.[161]	H_2, CO	650-750	• Optimized process parameters for the sticking free reduction of the iron ore fines used are defined. • The required content of MgO additives is defined to be 2 %-wt. of the total quantity of the fine ore.
Zhong et al.[162]	CO	Different temperatures	• Controlled de-fluidization experiments of previously reduced samples are carried out. • The particle cohesiveness and agglomeration tendency strongly depend on the amount of iron precipitation. With increasing amounts, the particles stick easier and an agglomeration occurs.
Zhong et al.[163]	CO	700-900	• Sticking is also observed when the iron formation is dense or porous. • Sticking occurs when the fresh iron is in contact, even at low metallization. • Above the minimum sintering temperature, reduced particles become cohesive and agglomerates are formed.

3 Experimental facilities

In the following section, the experimental facilities used within this work including different laboratory-scale fluidized bed reactors and methods for material characterizations are shown and explained.

3.1 Laboratory-scale facilities for fluidized bed reduction experiments

At the Chair of Ferrous Metallurgy at Montanuniversitaet Leoben, different lab-scale fluidized bed reactor facilities are installed. For the investigation of the reducibility and fluidization behavior of different iron ore fines, two reactors are available which are used for the investigations for this thesis. One of them has an inner diameter of 68 mm representing an input sample mass of iron ore used for the experiments between 400 to 650 g. The second one has an inner diameter of 160 mm. The input sample mass is between 3500 and 5000 g. These two facilities are explained in more detail below.

3.1.1 Fluidized bed reactor (FBR) 68 mm

The fluidized bed reactor with an inner diameter of 68 mm is used for the investigation of the kinetic behavior of different iron ore fines during hydrogen-induced fluidized bed reduction and for the investigations of the fluidization and reduction behavior of magnetite-based iron ores, as shown in Section 4 and Section 5, respectively.

The principles of this fluidized bed reactor are already explained in [164] and [165]. Figure 35 shows the schematic layout of the reactor, Figure 36 the assembled reactor and the gas mixing unit. The facility mainly consists of the reactor itself, a three-stage electrical resistance heating furnace and a gas supply unit. The required reducing gas components are stored in gas bottles and the demanded reducing gas mixture is provided by mass flow controllers

(Bronkhorst EL-Flow F201-CV/AV) in the gas mixing section. The system is able to provide gas mixtures consisting of H_2, CO, CO_2, CH_4 and N_2. If water vapor is required in the reducing gas mixture, the gas passes through a humidifier (Bronkhorst Evaporator W-303A-333-K), where the H_2O is added to the gas mixture. For these investigations, only H_2, H_2O and N_2 are used in the gas mixture. The preheating of the reducing gas mixture takes place while the gas passes through the gas supply pipe located inside the three-stage electrical heating shells, where the reactor itself is also positioned during the experiments. The reducing gas enters the reactor from the bottom, passes the grid and fluidizes the material. During fluidization, fine particles will leave the reactor together with the gas stream. To remove accompanying dust from the gas, an internal cyclone and a dust filter unit are installed before the off-gas leaves to the atmosphere. To controll the pressure inside the system, a pressure-control valve (Masoneilan 28-23131) is installed in the off-gas duct after the dust filter unit. During the experiments it is necessary to check the fluidization behavior of the material. Differential pressure measurements (Kobold Smart pressure transmitter) are carried out below the grid and above the material. To control the temperature of the entering reducing gas mixture and the sample portion, two thermocouples (Type N) are installed. One is located below the grid to measure the temperature of the inlet gas mixture. The temperature measured by the thermocouple below the grid is responsible for the heating performance of the lowest section of the three-stage heating shells. The second thermocouple measures the temperature directly inside the bed material. This temperature measurement is directly controlled by the heating performance of the middle and upper sections of the three-stage heating system. The weight loss sustained during the reduction of iron oxides is measured via a scale (Mettler Toledo XP64000L), which shows the weight of the whole reactor including the material. An in-situ measurement of the sample weight is required to get information regarding the reduction rate. During fluidized bed reduction, some attrition and elutriation of the fines will also occur, which ends in an elutriation of very fine particles. In the present setup, the weight of the dust filter is also measured together with that of the whole reactor. All elutriated particles are collected in the dust filter unit, so the measured weight change can be linked directly to the reduction procedure. To minimize material losses, the upper part of the reactor is designed in a conical shape in order to reduce the superficial gas velocity. For all experiments, a distributor with 33 orifices is used. Detailed information regarding the reactor dimensions is given in [166].
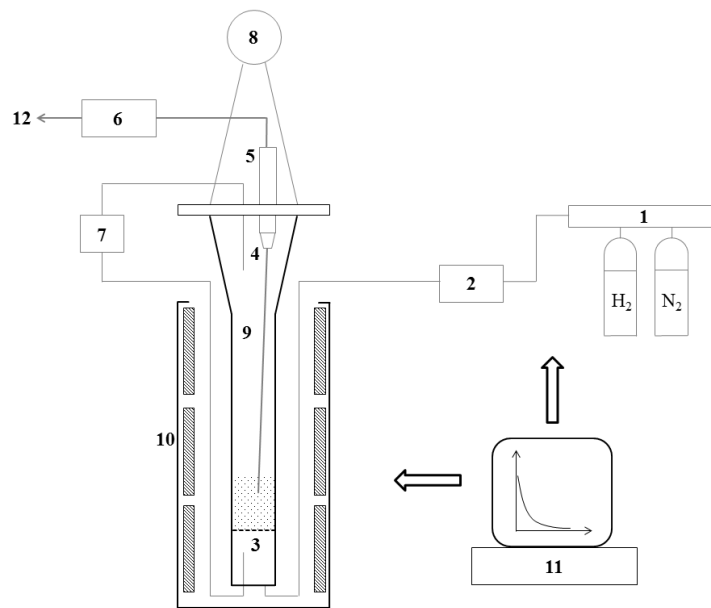
Figure 35: Lab-scale fluidized bed reactor 68 mm: 1- gas supply unit; 2- evaporator; 3- gas distributor; 4- internal cyclone; 5- dust filter; 6- pressure control valve; 7- differential pressure measurement; 8- scale; 9- reactor; 10- heating furnace; 11- process control; 12- off-gas to atmosphere.[164]
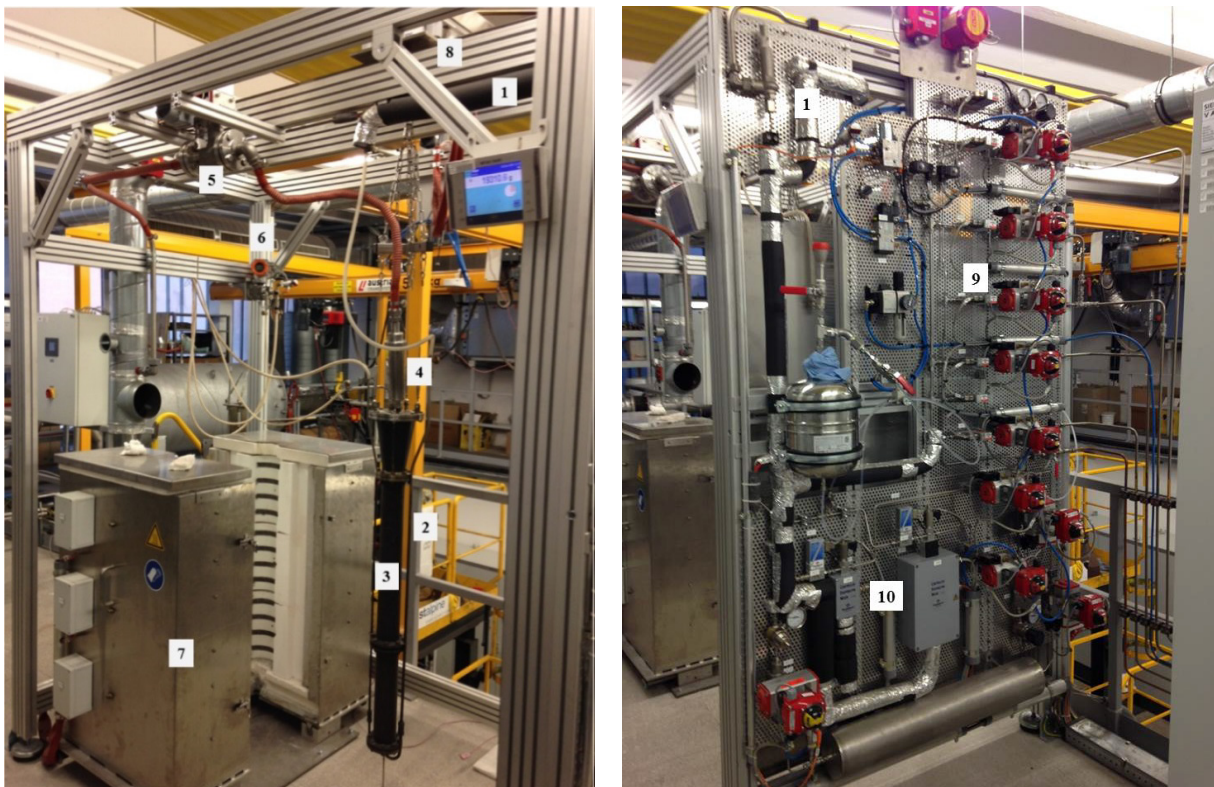
Figure 36: Lab-scale fluidized bed reactor 68 mm: left- reactor; right- gas supply system: 1- gas supply pipe; 2- gas preheating section; 3- reactor; 4- dust filter; 5- pressure control valve; 6- differential pressure measurement; 7- heating furnace; 8- scale; 9- mass flow controllers; 10- evaporator.[165]

Table 9 summarizes the possible process conditions for the fluidized bed reactor with an inner diameter of 68 mm.

Table 9: Possible operation range of the FBR 68 mm.

Temperature	up to 1100	°C
Pressure	up to 1.4	bar abs.
Gas flow rates		
H_2	0-25	l/min (SATP)
CO	0-38	l/min (SATP)
CO_2	0-30	l/min (SATP)
CH_4	0-3	l/min (SATP)
N_2	0-100	l/min (SATP)
H_2O	0-5.2	l/min (SATP)
Bed diameter	68	mm
Free reactor area	0.0036	m²
Sample mass	400-650	g

Figure 37 shows the user interface of the FBR 68 mm. During the experiment, all important process parameters such as gas flow rates, temperatures, absolute pressure and differential pressure can be controlled. There are two possibilities for running an experiment, the first of which is an automatic procedure. Therefore, a program has to be prepared before the experiment which contains all required process information. The system goes through the program automatically step by step. The second possibility is to change all parameters manually. To be more flexible, all experiments are done in a semi-automatic way.
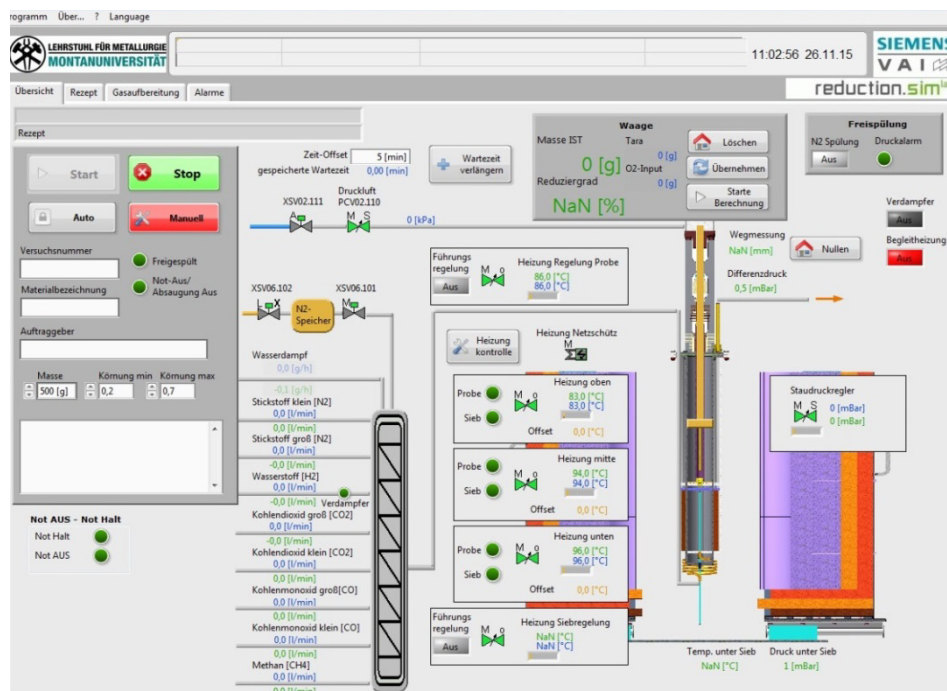
Figure 37: User interface FBR 68 mm.

3.1.1.1 Execution of reduction experiments with the FBR 68 mm

To get reproducible results of the experiments, all tests should be carried out in a similar manner. Before starting the tests, the assembling of the reactor takes place. The cover plate and dust filter units are assembled together with the reactor system. After that, the reactor is connected to the scale and all other parts such as the gas supply pipe, thermocouples, differential pressure measurement and off-gas pipe are fixed to the system. Attention must be paid to each connection to avoid any leakage because dangerous gases are used during the experiments. Therefore, before each experiment, a leakage test is carried out for safety reasons. Later, the reactor is moved between the heating shells which get closed afterwards. The system is then ready for the experiment itself. The material is charged into the reactor in cold state and purged with N_2. To avoid material passing through the grid, a certain flow of N_2 is also applied during the charging procedure. The charging takes place through a small aperture at the top of the reactor. The heating period to the desired reduction temperature takes place under constant N_2 flow. The flow rate of N_2 is defined in a way to ensure a superficial gas velocity inside the reactor higher than the minimum fluidization velocity of the material. After that, a temperature equilibrium period of approximately 10 min is applied to ensure a uniform temperature distribution through the material. N_2 is then replaced by the defined reducing gas mixture and the reduction procedure starts. The change in sample weight and differential pressure through the grid and sample portion as well as all other important process parameters are measured and stored in situ during the whole experiment. The stored data is used afterwards for the test evaluation. The reduction is assumed to be complete after reaching a constant weight signal. After the reduction period, the reducing gas mixture is substituted by N_2 again and the sample portion is cooled down to ambient temperature. To discharge the material, the cover plate of the reactor is removed and the reduced material is discharged by tilting the reactor; the weight of the reduced sample is measured again to complete the mass balance. After that, the particles are stored in gas tight bags for further investigations.

As mentioned above, the differential pressure measurement during the experiment is carried out through the grid and sample portion. For the evaluation of the experiments and to check the fluidization behavior of the material only, knowledge regarding the pressure drop across the distributor at reducing conditions is required. Differential pressure measurements across the distributor only under reduction conditions are carried out for each test condition. The measured value can be subtracted afterwards during test evaluation to get the actual pressure drop of the sample portion only. The process conditions used are explained in the appropriate sections.

3.1.2 Fluidized bed reactor (FBR) 160 mm

The fluidized bed reactor with an inner diameter of 160 mm is used for the experiments with iron ore ultra-fines, shown in Section 6.

The FBR 160 mm was already in operation at the laboratories of voestalpine between 1999 and 2005. Experiments concerning the fluidized bed-based iron ore reduction processes FIOR[®] and FINMET[®] were carried out. In 2009, the facility was reinstalled at the

Chair of Ferrous Metallurgy to perform reduction experiments based on process conditions representing the FINEX® process.[61]

The principal layout of the FBR 160 mm has already been explained by [167–169]. Figure 38 shows the schematic layout of the facility. The installation mainly consists of a gas supply unit including an evaporator and a gas preheating unit, the reactor itself (inner diameter 160 mm), a three-stage heating system, an off-gas cleaning system, a post combustion unit and a process control system. Each gas component is stored in separate bottles. The flow rate of each component is controlled by mass flow controllers (Bronkhorst F113 (201,202,203)-AC(AV)) and mixed together in a gas mixing unit. The system is able to apply gas mixtures containing H_2, CO, CO_2, CH_4 and N_2. After mixing, the gas passes through a humidification and preheating unit. The evaporator (Adrop humidification unit ATMOS-RS-MK-T-0908-1) is installed to add water vapor to the reducing gas mixture, if required. After that, the reducing gas mixture enters the reactor from the bottom and passes a heating helix located in the lowest section of the three-stage heating system. In the helix, preheating of the reducing gas mixture to the desired reduction temperature takes place, after which the gas passes the distributor and comes into in contact with the material.
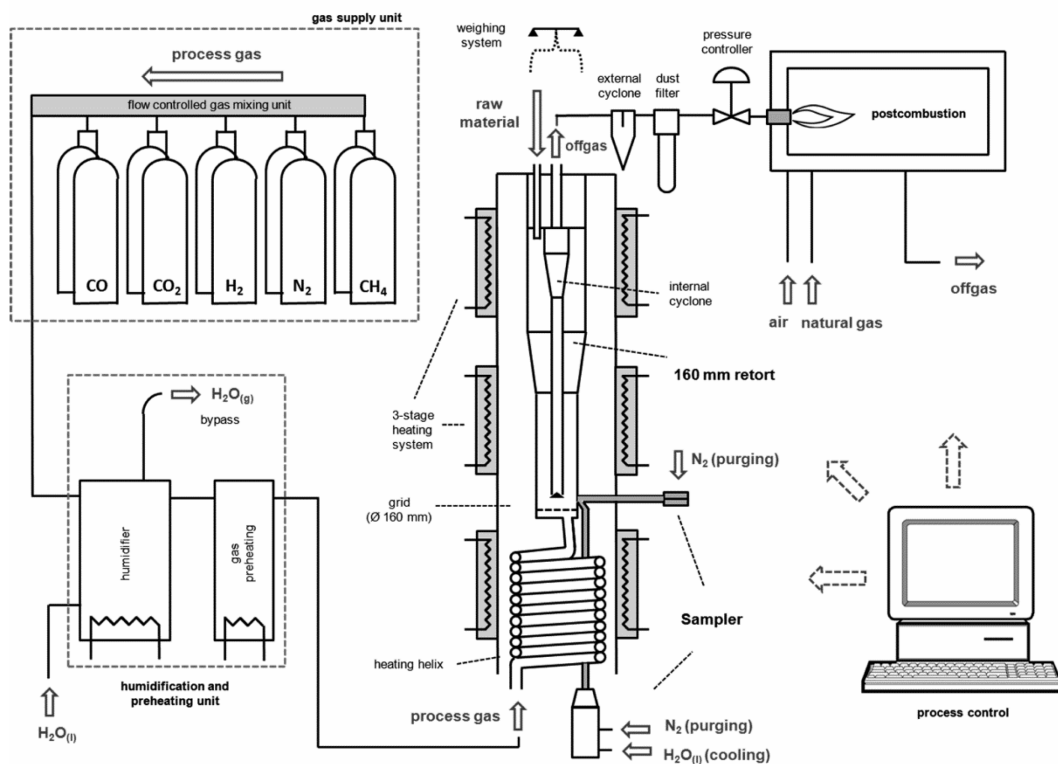
Figure 38: Schematic layout of the lab-scale FBR 160 mm.[61,168,169]

The diameter of the core reactor is, as mentioned above, 160 mm followed by a cross-section expansion to 265 mm and a freeboard. This design of the reactor is defined in such a way to decrease the superficial gas velocity and therefore decrease the material elutriation. Inside the reactor, an internal cyclone is installed to remove dust from the off-gas and return the particles to the fluidized bed. The off-gas duct is also equipped with an external cyclone and two dust filter units in order to also remove very fine particles from the gas stream. After

that, the cleaned off-gas passes the post-combustion system where unreacted gas components (H_2 and CO) are burnt before the off-gas leaves to the atmosphere. The reactor is connected to a weighing system (HBM RSCC C3/200 kg) to determine the change in sample weight during the experiments. Thermocouples (Type K) are installed below the distributor (to control the temperature of the reducing gas mixture), both inside the sample portion and inside the freeboard. The heating performance of the lowest section of the three-stage heating system is controlled by the gas temperature. The sample temperature is linked to the heating performance of the middle and upper sections of the heating system. The facility is also equipped with a sampling system that allows samples to be taken out during the experiment for further evaluation of the reduction progress. The pressure inside the whole system is controlled by a pressure control valve (Contrans P AMD 230), located in the off-gas duct behind the dust filter units. Differential pressure measurements are carried out below the gas distributor and above the sample portion. Figure 39 shows the FBR 160 mm installation, the off-gas duct and the post combustion system, the gas mixing unit and the three-stage heating system.
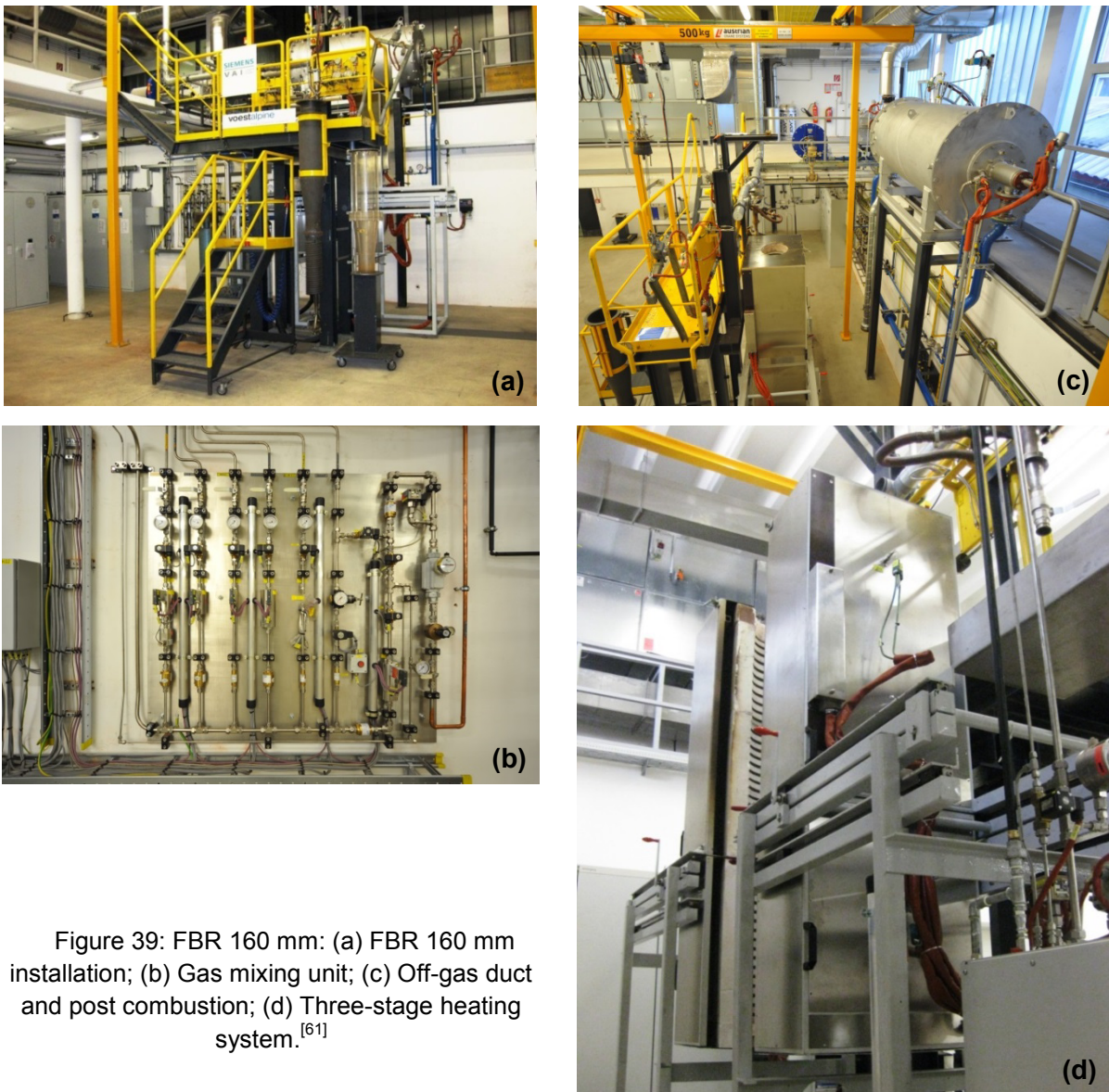
Figure 39: FBR 160 mm: (a) FBR 160 mm installation; (b) Gas mixing unit; (c) Off-gas duct and post combustion; (d) Three-stage heating system.[61]

Particles that leave the reactor together with the gas stream are collected in the external cyclone or in the dust filters. The weight of the external cyclone and the dust filters is not included in the measured weight signal, so the amount of elutriated material has to be considered during the test evaluation.

Table 10 summarizes the possible operation conditions for the FBR 160 mm installation. Because of the limited heating performance, the maximum possible operation temperature is approximately 800 °C. The maximum temperature also depends on the gas flow rate used. If the flow rate reaches a critical value, the system is not able to preheat the reducing gas to the required reduction temperature anymore. As a result, with lower gas flow rates, higher reduction temperatures can be achieved.

Table 10: Possible operation range of the FBR 160 mm installation.

Temperature	up to 800	°C
Pressure	up to 1.6	bar abs.
Gas flow rates		
H_2	0-300	l/min (SATP)
CO	0-200	l/min (SATP)
CO_2	0-200	l/min (SATP)
CH_4	0-50	l/min (SATP)
N_2	0-500	l/min (SATP)
H_2O	0-100	l/min (SATP)
Bed diameter	160	mm
Free reactor area	0.02	m²
Sample mass	3.5-5	kg

Figure 40 shows the user interface of the FBR 160 mm. During the experiments, all important process parameters such as gas flow rates, temperatures, parameters of the humidification and preheating unit, pressures and the post combustion system can be controlled. Similar to the FBR 68 mm, experiments can be done automatically using a defined program but a manual change of the process parameters is also possible.
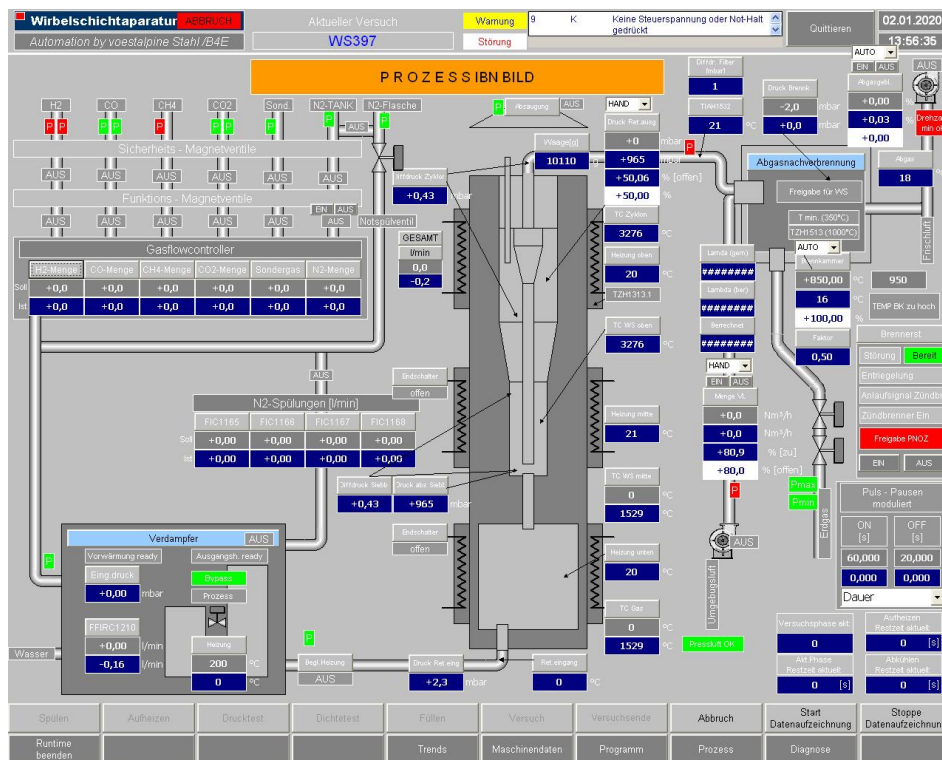
Figure 40: User interface FBR 160 mm.

3.1.2.1 Execution of reduction experiments with FBR 160 mm

The first step is again the assembling of the reactor components including the cover plate and the scale. After that, the reactor is moved from the maintenance position to the working position (between the heating furnaces). Then, all pressure measurements and thermocouples along with the gas supply pipe and the off-gas system can be connected to the reactor. Again, all connections should be checked carefully because of the use of dangerous gases during the experiments.

Before the experiment can be started, the software requires passing through a security chain. The first step is a purging procedure with nitrogen to remove the remaining oxygen from the system. After that, the reactor is preheated to the demanded reduction temperature, which must be defined before the experiment. After reaching the temperature, a pressure test is required. Different flow rates of nitrogen are injected into the reactor and the measured values of total pressure and pressure drop across the distributor are quoted and compared with values from previous experiments. The pressure test has two main targets; from the values of total pressure inside the reactor at a given flow rate, first information regarding gas tightness of the system can be achieved. From the measured pressure drop across the gas distributor it can be seen if orifices from the distributor are blocked by material from previous experiments. If the measured pressure drop does not fit to the values of former experiments, the procedure has to be stopped and the distributor must be removed from the reactor for cleaning. The next step after the pressure test is the leakage test, where a small amount of carbon monoxide is injected into the system and all connections are checked by a leak detector for gas tightness. If a leakage is observed, the system must be cooled down again for an inspection. Otherwise, the reactor is purged again by N_2 to remove remaining carbon

monoxide from the system. Before charging the material, the pressure drop across the gas distributor is measured under the same conditions as those used during the reduction experiment.

After that, the system is ready for charging the material. Charging takes place from the top of the reactor through a charging aperture. The material is placed into a charging hopper which must be connected with the reactor. The charging hopper is equipped with a ball valve. After opening the valve, the material flows into the reactor. Then, the material is preheated to the reduction temperature under constant nitrogen flow. After reaching the reduction temperature, a temperature equilibrium period of 10 min is selected to get a uniform temperature distribution. Next, the nitrogen is substituted by the defined reducing gas mixture and the reduction itself starts. The change in sample weight and differential pressure through the distributor and sample portion as well as all other important process parameters are measured and stored in-situ during the whole experiment, similar to the FBR 68 mm.

After the experiment, the reducing gas mixture is replaced by nitrogen to cool down the system to ambient temperature. The reactor is then moved back to the maintenance position and the discharging of the material takes place. The cover plate is removed and the reactor is tilted for 140°. The material is collected and stored in air-tight bags to avoid re-oxidation and the sample weight is measured again. To complete the mass balance, the elutriated material from the off-gas duct must also be removed for weight measuring. This includes the material collected in the external cyclone, the dust filter units and the connection pipe between the reactor and the off-gas duct. The process conditions employed are explained in the appropriate section.

3.2 Investigations of raw materials and reduced samples

Based on the reduction experiments, the results obtained can only be linked to the occurring change of the sample weight. Two possibilities are probable in this case; the first one is the measured weight change during the reduction, while the second one is the mass balance of the material (difference in weight between input material and reduced sample). To get more information about the reduction procedure, investigations of the raw materials used and of the reduced samples are required. The easiest way is the preparation and investigation of polished micro-sections using an optical light microscope (OLM). This way, information regarding the reduction behavior of single particles can be received and different iron morphologies can be distinguished, which is essential for the description of the reduction process. The second possibility is the use of a scanning electron microscope (SEM). With the SEM it is possible to observe the surface structure of particles. This is a very useful tool to investigate e.g. the sticking behavior of different iron ores.

3.2.1 Optical light microscope

For the optical light microscopy, the Polivar Reichert-Jung MEF2 microscope is used, shown in Figure 41. It is equipped with six objectives (magnifications 2.5, 5, 10, 20, 50 and

100) and a diamond marker. For the morphological greyscale-based evaluations, a 4MPix camera and Clemex Vison PE software version 7.0 is used.
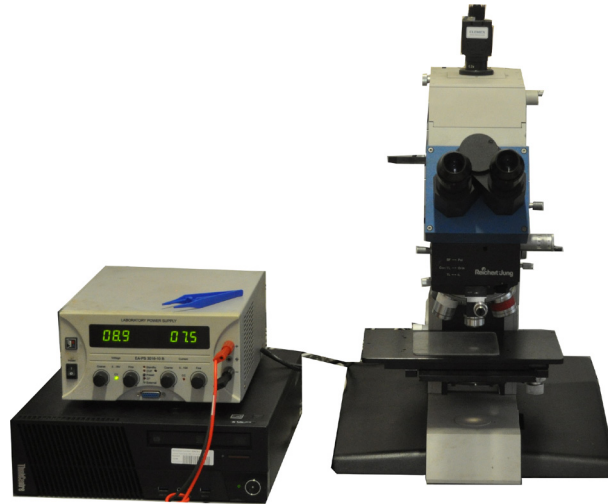
Figure 41: Optical light microscope Polivar Reichert-Jung MEF2

3.2.2 Scanning electron microscope

For the investigations of the morphology of the particle surface, the scanning electron microscope FEI Quanta 200Mk2 is used, which is shown in Figure 42. The SEM is able to produce high-resolution images of conductive and non-conductive samples. The Quanta 200 Mk2 has a high performance thermal emission SEM column (W). The SEM is equipped with the following detectors: LED, BED, LFD and EDS.
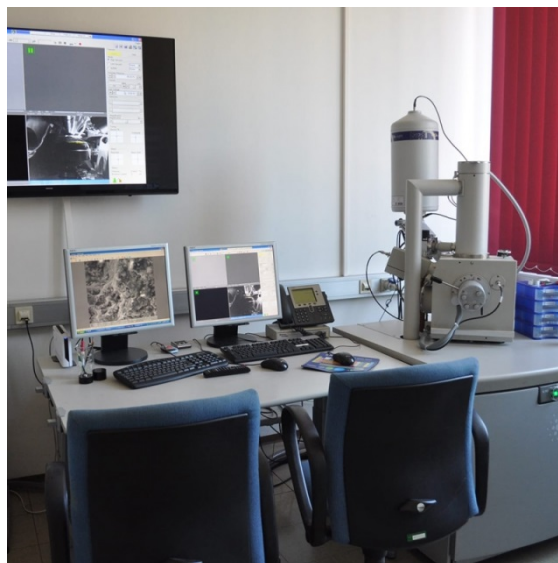
Figure 42: Scanning electron microscope FEI Quanta 200Mk2

3.3 Oxidation procedure for magnetite-based samples

For the oxidation of magnetite-based iron ore samples to Fe_2O_3, as required for different experiments, a conventional heat treatment furnace is used. The possible maximum temperature that can be reached is 1150 °C at a chamber volume of approximately 130 dm³. During the oxidation experiments, the atmosphere inside the furnace is replaced approximately every 30 min by opening the furnace door. This is required to provide a sufficient amount of oxygen for the oxidation reaction.

4 Kinetic investigation of hydrogen-induced fluidized bed reduction of iron ore fines

The kinetics of reduction processes are of major importance as they define the gas utilization and therefore the efficiency of the process. To gain knowledge concerning the kinetic limitations occurring during hydrogen-induced fluidized bed reduction of iron ore fines, different approaches are shown starting with the determination of the apparent activation energy against the degree of reduction. Next, different approaches carried out in literature are used to define the rate-limiting mechanisms during the reduction procedure. Because of the low accuracy of such analyses, a new approach based on the model developed by Johnson, Mehl and Avrami (JMA) is defined and used for further analysis. The idea behind it is that more than one limiting step can act together in a parallel way. All approaches are shown using one defined iron ore; later on, results are also compared for different iron ore types. Aside from using the defined standard conditions for the reduction, a variation of process parameters and raw material properties is also carried out representing changing specific gas rates, variation of the grain size and an addition of water vapor to the reducing gas mixture. At the end of this section, the behavior of the pre-reduction steps from Fe_2O_3 to Fe_3O_4 and Fe_2O_3 to FeO are shown. Some results of the investigations have already been published in Metallurgical and Materials Transactions B and Particuology.[164,165]

4.1 Process conditions of the experiments- standard reduction conditions (SRC)

For the investigation of the kinetics, experimental results at different temperatures are required. For the experiments, the fluidized bed reactor with an inner diameter of 68 mm is used, explained already in Section 3.1.1. As a suitable temperature range for fluidized bed-based iron ore reduction, temperatures are defined to be between 600 and 800 °C. As a pre-

condition for the kinetical analysis, it is always important that the material remains in completely fluidized state during the whole reduction procedure. If this is not the case, the test results cannot be used for the analysis. The fluidization is controlled by an in-situ measurement of the pressure drop across the bed material during the experiments.

Running fluidization experiments at different temperatures can lead to some issues regarding the achievement of uniform process conditions. On the one hand a constant gas flow rate at different temperatures leads to different superficial gas velocities which can affect the fluidization regime; on the other hand, a constant superficial gas velocity ends in different availability of the reducing gas mixture, which can affect the kinetics of the reduction procedure. One possibility might be to control the superficial gas velocity by an inert gas component in the mixture. This would end in different partial pressures of the reducing component in the gas mixture, which can also affect the kinetics of reduction. For the kinetic investigations, it was decided to keep the total flow rate constant, ending in slightly different superficial gas velocities at different temperatures, but there is no change in the availability of the reducing agent and partial pressure of the reducing agent in the gas mixture.

For the evaluation of the reduction kinetics, the reduction experiments are done at different temperatures. As a suitable temperature range for fluidized bed reduction, 600-800 °C is selected, as already mentioned. At each 50 °C temperature step, one reduction test is done. The flow rate of the reducing gas mixture is defined to be 25.9 l/min (SATP), which is similar for all tested temperatures. This represents a superficial gas velocity of 0.35 and 0.43 m/s for 600 and 800 °C, respectively. The reducing and fluidization gas contains 65 %-vol. hydrogen and 35 %-vol. nitrogen. The addition of nitrogen should support the fluidization of the material. An absolute pressure of 1.1 bar inside the system is selected for all experiments. The process conditions explained are defined as standard reduction conditions (SRC) for the kinetical investigations. Any changes in the conditions for the evaluation of different influencing factors are explained in the appropriate sections. Concerning the iron ore sample used, the grain size is defined to be between 250 and 500 μm, which was extracted from a wide grain size distribution by sieving. The sample weight is defined to be 400 g for all experiments. The related chemical analysis of the ore used in this section (Ore A) and the specific surface area determined by B.E.T. measurement as well as a summary of the process conditions are given in Table 11.

Table 11: Chemical analysis of Ore A and summary of process conditions (SRC).[164]

Chem. analysis Ore A		Test parameters (SRC)	
Fe_{tot}[a]	63.6 %-wt.	Input iron ore	400 g
FeO	0.58 %-wt..	Particle size	250–500 μm
SiO_2	3.48 %-wt.	Gas mixture	H_2/N_2 65/35 %-vol.
Al_2O_3	2.07 %-wt.	Flow rate	25.9 l/min (SATP)
LOI[b]	2.2 %-wt.	Temperature	600–800°C
B.E.T.[c]	11.83 m²/g	Pressure	1.1 bar abs.

[a]Total iron content; [b]Loss on ignition; [c]Specific surface (Brunauer- Emmett-Teller)

Before the experiments, the process conditions of the given gas-solid system are checked using the Grace diagram to be sure to operate the experiments in the fluidized bed area. The principles of the Grace diagram and the calculation procedure were already explained in

Section 2.5.1. Table 12 summarizes the parameters used for the calculation of the Grace diagram.

Table 12: Calculation parameters Grace diagram.[164]

Density fluid 700 °C	ρ_F	0.076	kg/m³
Density solids	ρ_S	3,500	kg/m³
Viscosity fluid 700°C	η	3.71 10^{-5}	Pa s
Minimum fluidization porosity	ε_{mf}	0.39	-
Sphericity solids	ϕ_s	0.86	-

The density and viscosity of the fluid are calculated according to the proposed procedure shown within the VDI Heat Atlas.[170] The calculation of the density of the fluid, ρ_F, consisting of different gas components, can be done using Equation (38):

$$\rho_F(T) = \left(\sum_{i=1}^{n} \frac{w_i}{\rho_i(T)}\right)^{-1} \qquad (38)$$

where w_i represents the mass fraction of component i in the mixture and $\rho_i(T)$ shows the density of component i at the given temperature which can be calculated by using the ideal gas law. The calculation of the kinematic viscosity is more difficult because of interactions occurring between gas molecules which have to be considered in the calculation procedure. Equation (39) is used for the calculations:

$$\eta(T) = \sum_{i=1}^{n} \frac{x_i \eta_i(T)}{\sum_j x_j \phi_{ij}(T)} \qquad (39)$$

$x_{i,j}$ gives the mole fractions of the components, $\eta_i(T)$ the kinematic viscosity of component i at the given temperature and $\phi_{i,j}$ the interaction coefficient between the components, which can be calculated using Equation (40), where $M_{i,j}$ gives the molecular weight of the different components:

$$\phi_{ij}(T) = \frac{1}{2\sqrt{2}}\left(1 + \frac{M_i}{M_j}\right)^{-\frac{1}{2}} * \left[1 + \left(\frac{\eta_i(T)}{\eta_j(T)}\right)^{-\frac{1}{2}}\left(\frac{M_j}{M_i}\right)^{\frac{1}{4}}\right]^2 \qquad (40)$$

The temperature-dependent kinematic viscosity of a single component, $\eta_i(T)$, can be calculated using Equation (41):

$$\eta i(T) = \eta i(20\,°C) * \left(\frac{T}{273}\right)^{\left(\frac{A}{T}+B\right)} \qquad (41)$$

A and B represent constants for each gas component.

For the minimum fluidization porosity, ε_{mf}, a value of 0.39 is used. The sphericity of the solids is fixed to 0.86, which is defined as the ratio of the surface of a sphere to the surface of the particle with the same volume. As a result, the sphericity of an ideal sphere is 1. To consider the non-spherical shape of the iron ore particles, a value of 0.86 is used for the calculations. Previous iron ore u_{mf} measurements were done to define the sphericity of particles by comparing the experimentally measured values of u_{mf} with the calculated ones. The investigations showed that a value in the range between 0.82 and 0.9 is suitable for iron ore particles, which is the reason for selecting a value of 0.86.

The resulting Grace diagram is shown in Figure 43, including the experimental operation points for 600, 700 and 800°C reduction temperatures. As can be seen, the defined standard reduction conditions with a constant gas flow rate at different temperatures are in the area of the fluidized bed, while the operation points are closer to the curve of terminal velocity than to the curve of minimum fluidization. As a result, a bubbling fluidized bed can be expected during the experiments.
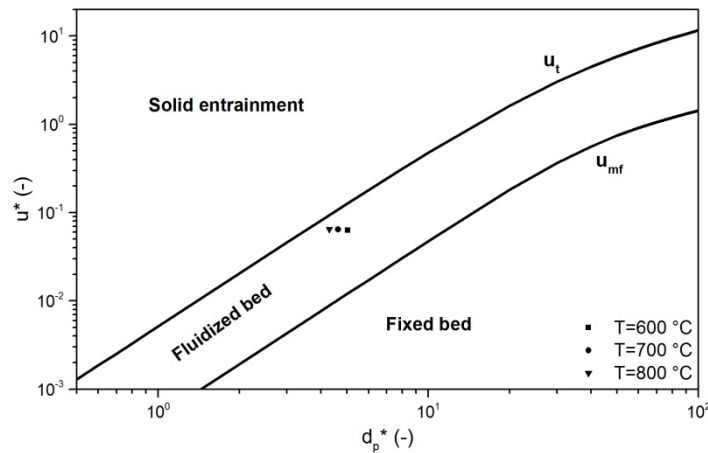
Figure 43: Grace diagram showing the experimental conditions of the reduction tests.[164]

4.2 Procedure of kinetic investigation- experimental results

As a basis for further kinetical investigations, experiments at different temperatures are done, as explained above. During every experiment, the most important parameters are measured and stored, representing the weight change of the sample portion, the pressure drop across the gas distributor and bed material, the total pressure inside the system, the different measured temperatures and the gas flow rates. The measured data can be used for further test evaluation. Figure 44 summarizes the evaluated test results for two different reduction temperatures, 700 and 600 °C. Figure 44 (a) and (d) shows the achieved weight change of the sample portion during the reduction procedure and the measured sample temperature for 700 and 600 °C reduction temperature, respectively. The reduction is assumed to be completed if the weight signal remains constant. As already mentioned in Section 3.1.1, the attrition and elutriation of fines don't have to be considered in the evaluation because it is collected in the dust filter unit. The weight of the dust filter is included in the weighing system and therefore does not affect the overall weight signal. A complete reduction could be achieved after 4250 s of reduction at 700 °C reduction temperature and 6100 s at 600 °C reduction temperature. As can also be observed, the sample temperature is not constant at the beginning of the reduction procedure. A temperature drop of approximately 20 °C occurs during the reduction from Fe_3O_4 to FeO because of the strong endothermal behavior of the reduction reaction. As a result, it takes some minutes to reach the defined reduction temperature again, which can have an impact on the procedure of further kinetical analysis. This temperature drop is observed for all experiments in nearly the

same range. The reason for that behavior can be linked to the thermal inertia of the system. Figure 44 (b) and (e) shows the measured pressure drops occurring while the reducing gas passes the distributor and the bed material (solid black lines). In the case of lower reduction temperatures, the level of total pressure drop is lower compared to higher reduction temperatures because of the constant gas flow rate. The solid gray lines show the pressure drop across the material only, without the gas distributor. In the case of complete fluidization, these lines should be equal to the dashed black lines, which represent the theoretical pressure drop of the material, calculated by using Equation (42):

$$\Delta p_{Bed} = \frac{m \cdot g}{A_{Reactor}} \qquad (42)$$

where m is the mass of the sample portion, g is the gravitational constant and A the free reactor area.
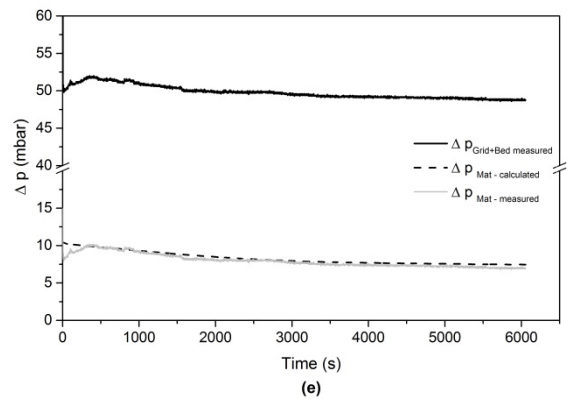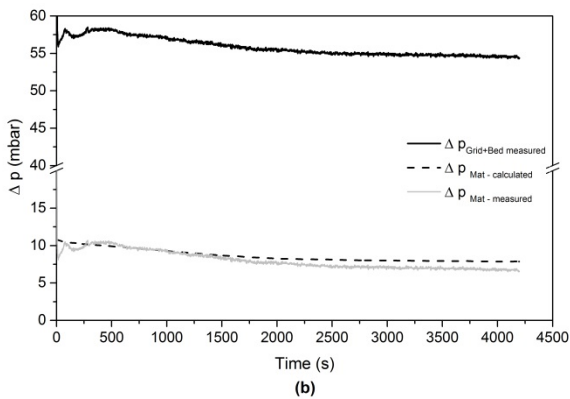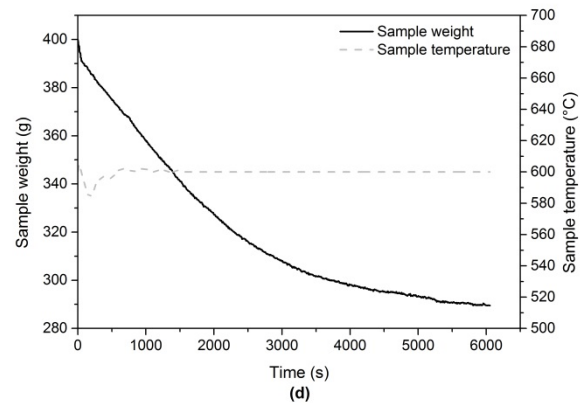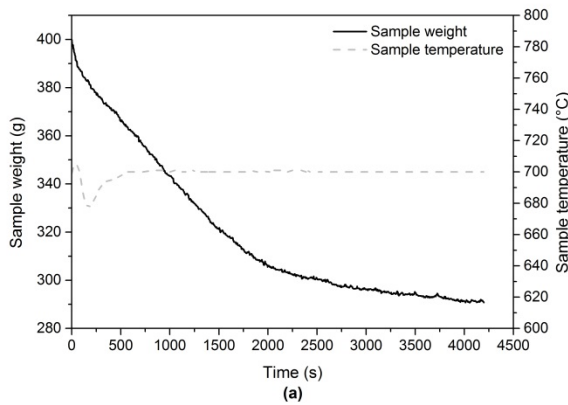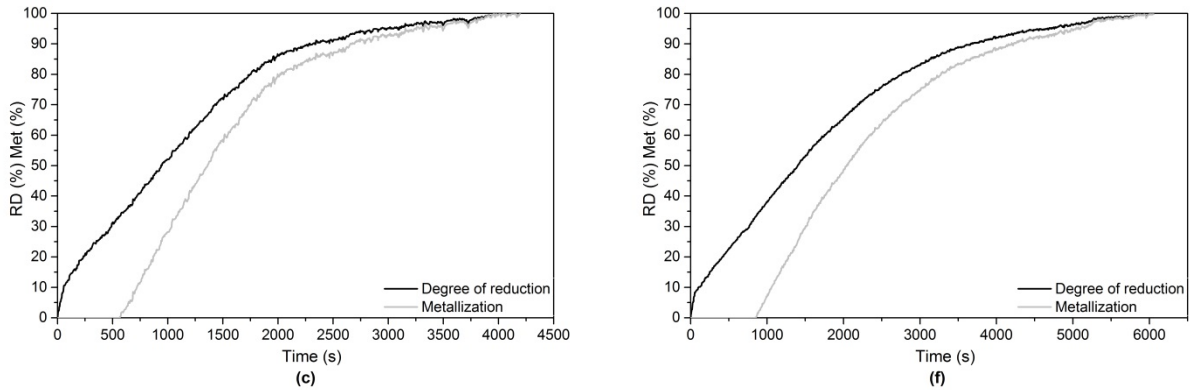
Figure 44: Experimental results for different reduction temperatures: 700°C, left[164]- (a) weight loss and temperature against time, (b) pressure drop grid and material against time, (c) degree of reduction and metallization against time; 600°C, right- (d) weight loss and temperature against time, (e) pressure drop grid and material against time, (f) degree of reduction and metallization against time.

During reduction, the sample mass becomes lower, so the theoretical pressure drop also decreases. As it can be seen, small deviations between the measured and calculated curves occur. Two reasons might be responsible for that. First, the elutriated material is not taken into account during the calculation of the theoretical pressure drop. The amount of elutriation is 21.4 g for the experiment at a reduction temperature of 700°C. This amount of material represents a pressure drop of 0.6 mbar. Second, there are still some inexactitudes while measuring the pressure across the distributor at reduction conditions both before and during the reduction experiment. Figure 44 (c) and (f) shows the calculated degree of reduction and metallization against reduction time. The degree of reduction is calculated using the data for the measured weight change during the experiment and the chemical analysis of the iron ore by the following equation:

$$RD\ (\%) = \left(1 - \frac{O}{1.5 \cdot Fe_{tot}}\right) \cdot 100 \tag{43}$$

where Fe_{tot} represents the total iron amount in the iron ore sample and O the amount of oxygen bonded on iron given in mol. The metallization of the sample can be calculated by:

$$Met\ (\%) = \frac{Fe_{met}}{Fe_{tot}} \cdot 100 \tag{44}$$

where Fe_{met} shows the amount of metallic iron in the sample portion, again given in mol. On the assumption that first metallic iron is only formed after the reduction to FeO is complete, the metallization can be also calculated using Equation (45):

$$Met(\%) = \frac{RD\ (\%) - 33.33}{66.66} \cdot 100 \tag{45}$$

This equation is applied for the calculation of the curve of metallization against reduction time. Based on the curves of degree of reduction, a separation into three stages is possible; a fast initial reduction stage to approximately 11 % degree of reduction, representing the conversion from hematite to magnetite. After that, the reduction rate remains nearly constant until high degrees of conversion, which depends on the reduction temperature. At the end of the reduction progress, the reduction rate slows down until a complete conversion is achieved. Figure 45 shows the comparison of the progress of reduction at all different tested

temperatures. As explained, all other parameters remained constant, except the superficial gas velocity.
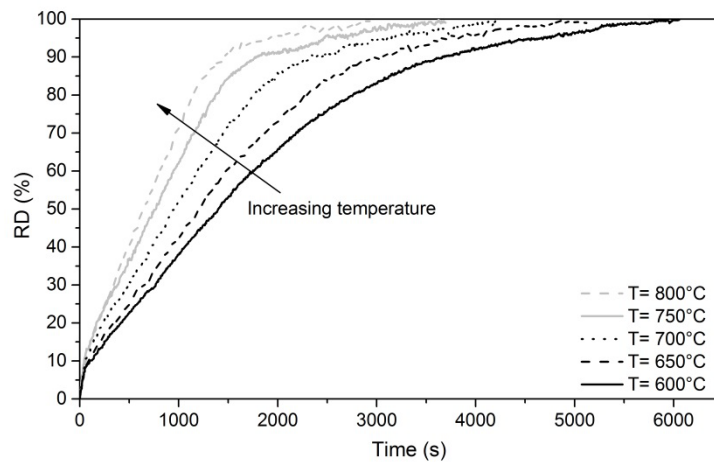
Figure 45: Comparison of the progress of reduction at different reduction temperatures.[164]

As shown, an increasing reduction temperature leads to higher reduction rates, mainly occurring in the middle and final stages of reduction. From a kinetical point of view, a higher reduction temperature is generally advantageous because of the temperature dependence of different rate-limiting steps, e.g. chemical reaction, nucleation and growth of nuclei or diffusion. In case of using hydrogen as a reducing agent, a higher temperature is also beneficial regarding thermodynamic limitations due to expanding stability areas of metallic iron and wüstite with increasing temperatures, as shown in Figure 13.

To confirm the complete reduction after the experiments, polished micro-sections of the reduced samples are prepared. Figure 46 shows the samples after reduction at 800 and 700 °C reduction temperature. As can be seen, the samples only consist of metallic iron (white areas) after reduction. Nearly no remaining oxide phases can be observed.
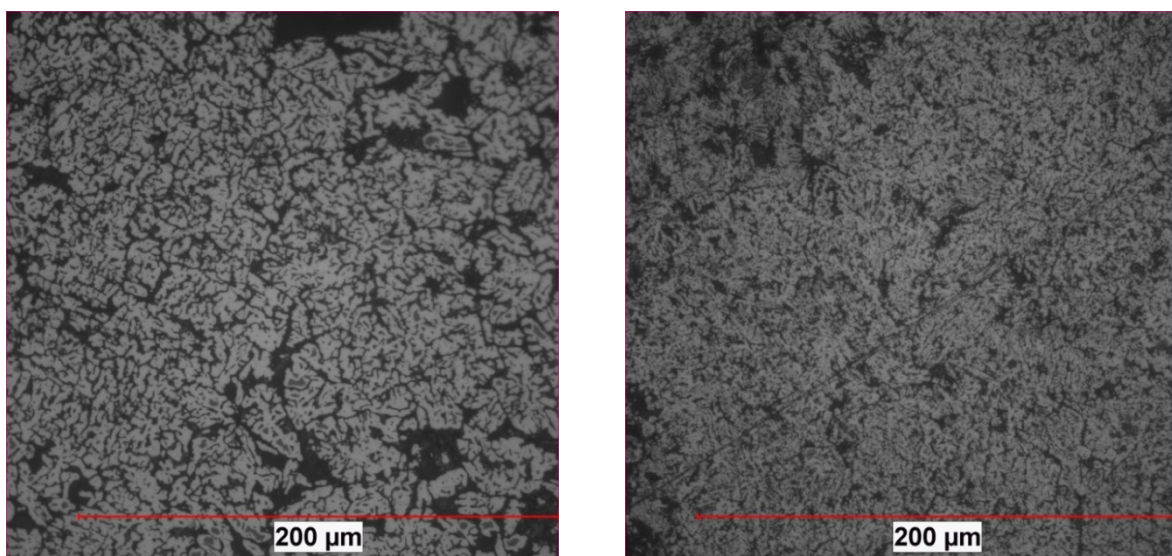
Figure 46: Polished micro-sections of reduced samples at different reduction temperatures: left- 800 °C; right- 700 °C.

Figure 47 demonstrates the comparison of the experimental results with the fastest possible reduction resulting from thermodynamic boundary conditions at 600 and 800 °C reduction temperatures. The thermodynamic limitations are calculated by using FactSage[TM]7.2 (Databases: Fact PS and FT Oxide). As input parameters for the calculation, the experimental parameters are chosen, representing a hydrogen flow rate of 16.9 l/min (SATP) and 400 g of iron ore with the given chemical analysis. The reduction temperature is assumed to be constant during the whole reduction procedure. The reduction temperature is responsible for the achievable hydrogen utilizations at each reduction step, shown in the Baur-Glässner diagram (Figure 13). At the given hydrogen flow rate and sample amount, the maximum possible oxygen removal rate can be calculated and transformed into a curve of degree of reduction against reduction time. Because of higher possible gas utilization at higher reduction temperatures, the thermodynamic limited curve of degree of reduction moves to lower required reduction times. The results show a decreasing impact of kinetics on the reduction rate with increasing temperatures. At 800 °C, the reduction proceeds close to the thermodynamic limitation until high degrees of conversion. Afterwards, the experimental reduction rate decreases. At 600°C reduction temperature, the difference between experimental results and thermodynamic equilibrium is even more pronounced. The kinetical investigation in later sections should explain this different behavior.
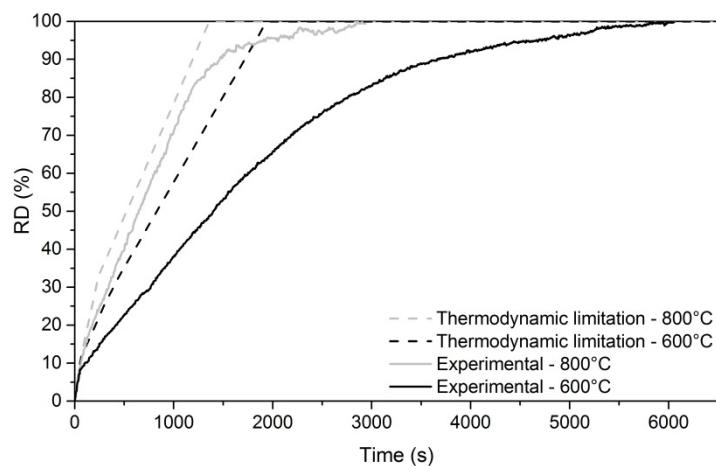
Figure 47: Comparison of experimental results with limitation given by thermodynamic boundary conditions at selected temperatures.[164]

4.3 Model-free determination of the apparent activation energy

The role of the apparent activation energy and its importance is already explained in Section 2.4.1. In the following section, the apparent activation energy against the degree of reduction is determined by using the calculation procedure shown in Section 2.4.1.1. Figure 48 shows the reduction rates (first deviation of degree of reduction over time) at different reduction temperatures against the degree of reduction between 5 and 95 % degree of reduction, where dx/dt represents dRD/dt in the present case. At high temperatures the reduction rate increases marginally between 30 and 50 % degree of reduction. This indicates

a limitation by nucleation in the area of first metallic iron formation. For the determination of the trends apparent activation energy against degree of reduction, the mathematical function f(x) is set to be 1, which ends in a model-free determination. The resulting Arrhenius plot is shown in Figure 49. The reduction rates at selected conversions for different temperatures are used. The slopes of the regression lines can be further used to determine the apparent activation energy at the selected conversion degrees. As shown, the slopes of the regression lines are not similar at different degrees of reduction, which ends in a changing apparent activation energy against the degree of reduction. The resulting curve is shown in Figure 50.
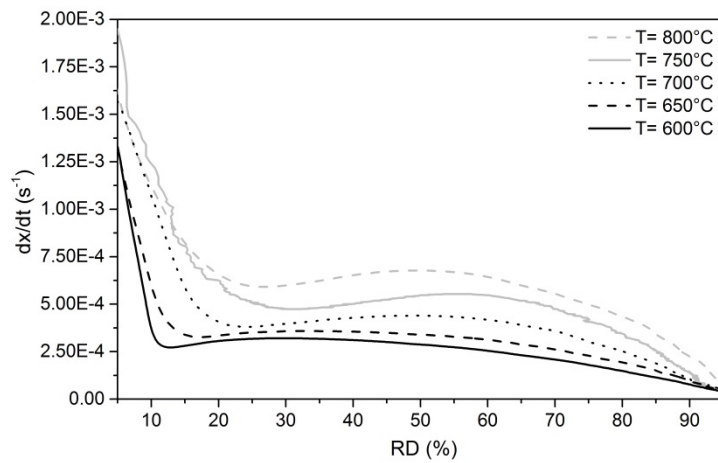
Figure 48: Reduction rate against degree of reduction for different reduction temperatures.[164]
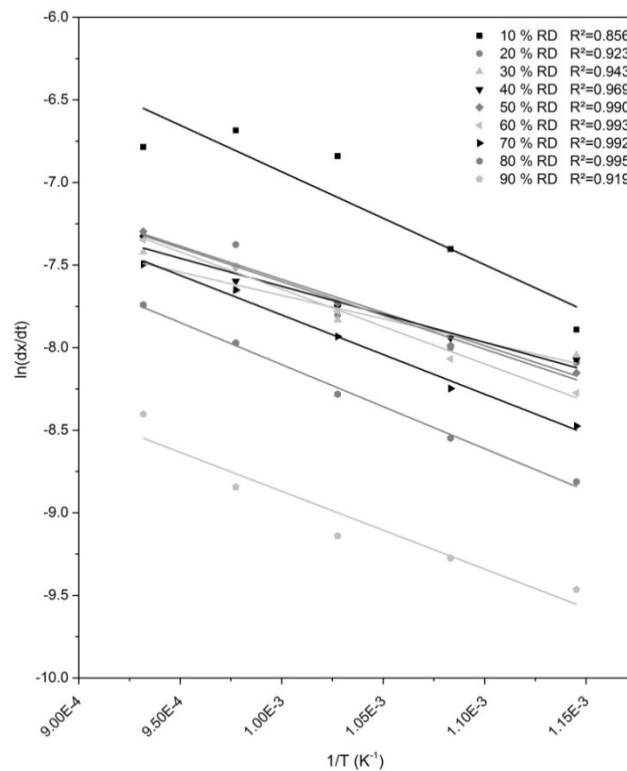
Figure 49: Arrhenius plot for selected conversions of experimental results.[164]
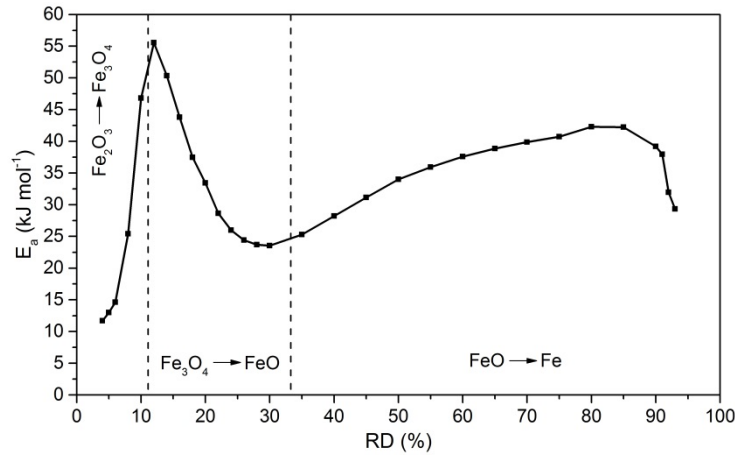
Figure 50: Curve of apparent activation energy against degree of reduction.[164]

The different slopes of the regression lines result in a two-peak-shaped curve of apparent activation energy. The vertical lines at 11.1 and 33.3 % degree of reduction correspond to the theoretical complete reduction from Fe_2O_3 to Fe_3O_4 and Fe_3O_4 to FeO, respectively. At the initial stage of reduction, the apparent activation energy increases to 55 kJ/mol until a degree of reduction of approximately 12 % is attained, closely representing a complete conversion from Fe_2O_3 to Fe_3O_4. During further reduction, it decreases to 23 kJ/mol until a degree of reduction of 30 %, which indicates closely a complete conversion from Fe_3O_4 to FeO. During reduction from FeO to metallic iron, a second peak can be observed which is not as pronounced as the first one. A level of 42 kJ/mol is reached at a degree of reduction of 85 % before it starts to decrease again. The trend of apparent activation energy against the degree of reduction shows, that the apparent activation energy does not remain constant during the reduction procedure. Chen et al.[145] defined similar shaped curves of apparent activation energy for the reduction of Fe_2O_3 by CO in a micro-fluidized bed reactor. A non-constant trend of apparent activation energy can be observed when the reduction rate at different temperatures changes in a different way. This can only occur if the rate-limiting steps change in a different way depending on reduction temperature and conversion degree. The apparent activation energy increases during ongoing reduction from FeO to Fe, indicating that the limiting mechanism changes, e.g. from nucleation to a chemical reaction. Based on Figure 50, it can be assumed, that the reduction from Fe_2O_3 to Fe_3O_4 has the highest apparent activation energy, followed by the reduction from FeO to Fe and Fe_3O_4 to FeO. Similar observations were reported by Munteanu et al.[88] and Shimokawabe et al.[112]

4.4 Results of different approaches for kinetic investigations

To gain knowledge regarding the rate-limiting mechanism occurring during hydrogen-induced fluidized bed reduction, different approaches for kinetical investigations are carried out. Three different approaches are used. Approach 1 and Approach 2 are conventional kinetic analyses based on selected models, shown in Table 3. To achieve more accurate

results, the conventional kinetical analysis is done using experimental data only from 33 to 100 % degree of reduction, representing only the conversion from FeO to Fe. For the analysis of the total reduction processes from Fe_2O_3 to Fe, multistep kinetic analysis is performed based on the model developed by Johnson, Mehl and Avrami (JMA).

4.4.1 Conventional model-fitting method- Approach 1

As mentioned previously, the experimental data of 33-100 % degree of reduction is used in this case, representing the reduction of FeO to Fe, which assumes a complete conversion to FeO at 33 % degree of reduction. The conventional models to describe gas-solid reactions, listed in Table 3, are used for the analysis. They can be classified into different groups, representing phase-boundary-controlled models, diffusion models, reaction order models, nucleation models and power law models. In the next section, the power law models are not taken into account. Plotting the integral expression g(x) against reduction time using the experimental data should end in a straight line if the model is able to describe the progress of reduction.
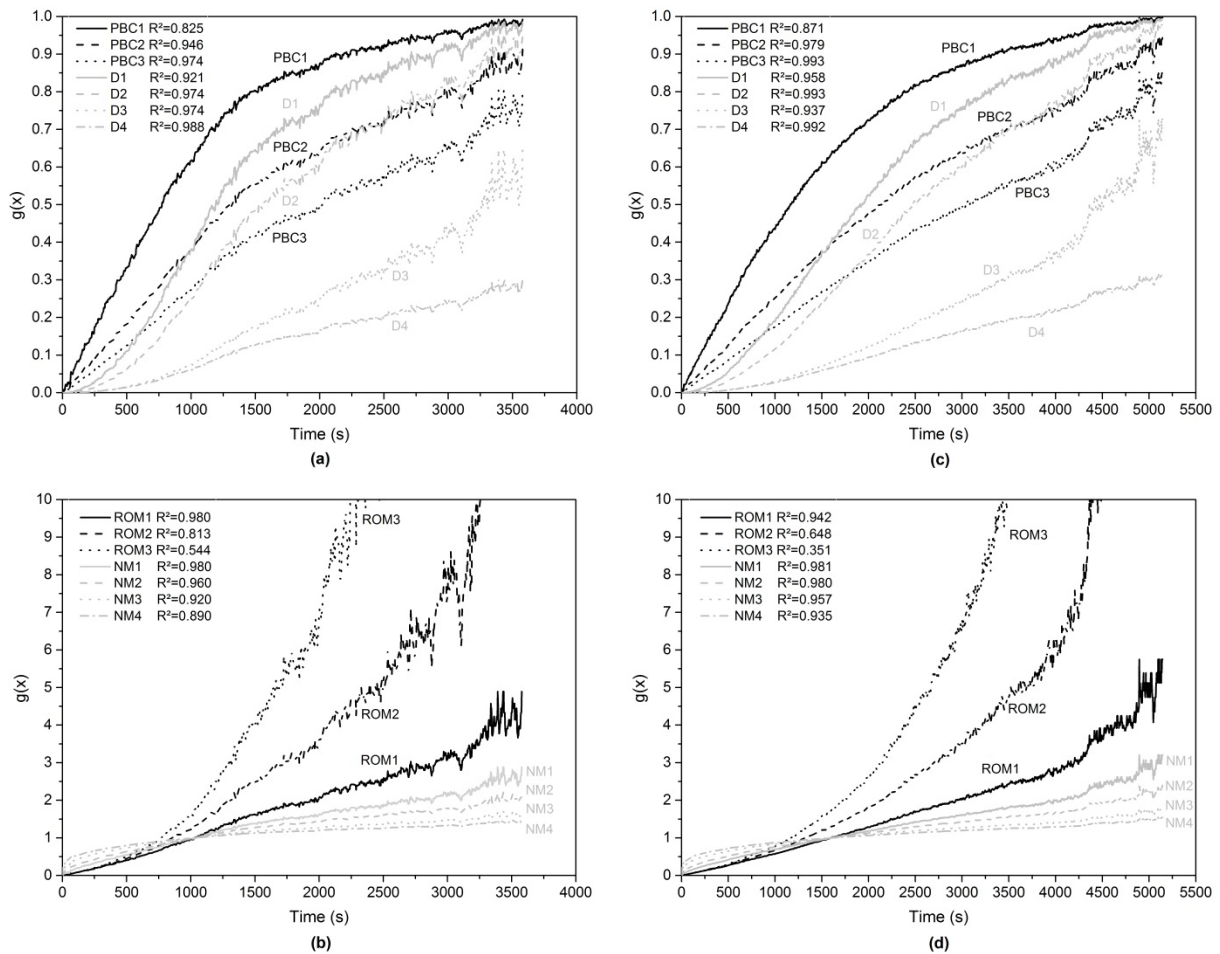
Figure 51: Model-fitting analysis of experimental results for the reduction from FeO to Fe at different temperatures using selected gas-solid models from Table 3: (a,b) 700 °C [164]; (c,d) 600 °C.

Figure 51 shows the results of the fitting procedure including the coefficients of determination (R^2) for two different reduction temperatures, 700 and 600 °C. Table 13 summarizes the coefficients of determination for all tested models at different temperatures. If the model fits to the experimental results, the coefficient of determination should be close to 1. The three best-fitting models for each temperature are marked in bold.

Table 13: Model-fitting results of experimental data for the reduction from FeO to Fe represented by the coefficient of determination for different reduction temperatures- Approach 1.[164]

	Reduction temperature (°C)				
Model	600	650	700	750	800
PBC1	0.871	0.856	0.825	0.776	0.777
PBC2	0.979	0.968	0.846	0.919	0.905
PBC3	**0.993**	**0.988**	0.974	0.957	0.941
D1	0.958	0.943	0.921	0.881	0.868
D2	**0.993**	0.984	0.974	0.952	0.932
D3	0.937	0.963	0.974	**0.980**	**0.967**
D4	**0.992**	**0.991**	**0.988**	**0.977**	**0.957**
ROM1	0.942	0.972	**0.980**	**0.979**	**0.964**
ROM2	0.648	0.758	0.813	0.798	0.780
ROM3	0.351	0.447	0.544	0.420	0.461
NM1	0.981	**0.989**	**0.980**	0.970	0.955
NM2	0.980	0.978	0.960	0.945	0.932
NM3	0.957	0.949	0.920	0.899	0.89
NM4	0.935	0.925	0.890	0.863	0.861

As it can be seen in the table, no general tendency regarding the rate limiting mechanism can be observed. The diffusion model D4 shows high coefficients of determination at all reduction temperatures. With decreasing reduction temperatures, the phase-boundary-controlled model PBC3 becomes important. The model ROM1 belongs to the three best-fitting models only at temperatures higher than 700°C. The nucleation model NM1 fits best for temperatures between 650 and 700 °C. From the given investigation method it is difficult to assess the results because the only result is the coefficient of determination. As it can be observed in this case, there are a lot of models which show a high coefficient of determination close to 1. As a result, an accurate statement regarding the occurring rate-limiting step is not possible. This type of kinetical analysis can only provide an idea regarding the occurring rate-limiting mechanism; an accurate statement is definitely not possible.

4.4.2 Conventional model-fitting method- Approach 2

As a second method for the definition of the occurring rate-limiting step, selected models from Table 3 are fitted to the experimental data by a variation of the rate constant. The root mean square deviation (RMSD) is used, defined as follows:[101]

$$RMSD = \sqrt{\frac{\sum(x_{calc}-x_{exp})^2}{n-1}}$$
(46)

where x_{calc} represents the calculated conversion from the fitting procedure, x_{exp} the experimental data and n the number of data sets.

This kind of model-fitting procedure allows an assessment as to which model fits at certain stages of reduction. According to the results obtained from the conventional kinetic analysis Approach 1, the models PBC3, D3, ROM1 and NM1 are selected for further investigation using Approach 2. Figure 52 shows the fitting results of different models for two different reduction temperatures, 700 and 600 °C. Therein, x represents the experimental data for the conversion from FeO to Fe.
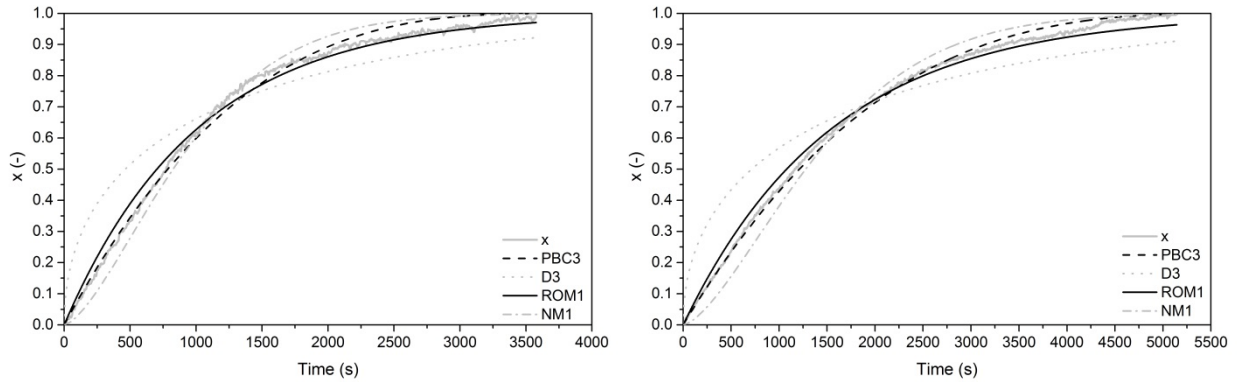
Figure 52: Model-fitting of experimental data for the reduction of FeO to Fe via fitting the rate constant of selected models from Table 3 to experimental results at different temperatures: left-700 °C[164]; right-600 °C.

Although the results indicate that different models fit well to the experimental data at different stages of conversion, there is in fact no model available which describes the whole reduction procedure accurately. At 700 °C reduction temperature, the model PBC3 fits quite well at the beginning while at the final stage, the model ROM1 fits best. For 600°C reduction temperature, the situation is quite similar but it can be observed that in the final stage of reduction, the model ROM1 does not fit as accurately as for 700 °C reduction temperature. Table 14 summarizes the resulting values from the fitting procedure, representing the fitted rate constants and the corresponding values of RMSD for all reduction temperatures. The two best-fitting models, represented by the lowest values of RMSD, are marked in bold. The models PBC3 and ROM1 show the lowest values of RMSD for reduction temperatures between 600 and 750°C. At 800 °C, however, the nucleation model NM1 fits best, which provides an indication that the mechanism of nucleation becomes important with increasing temperatures.

Table 14: Values of reaction rate and root mean square deviation (RMSD) at different reduction temperatures determined from model-fitting procedure- Approach 2.[164]

| Model | 600 °C | | 650 °C | | 700 °C | | 750 °C | | 800 °C | |
	k (s^{-1})	RMSD	k (s^{-1})	RMSD	k (s^{-1})	RMSD	k (s^{-1})	RMSD	k (s^{-1})	RMSD
PBC3	1.70 E-4	**0.016**	2.10 E-4	**0.015**	2.62 E-4	**0.025**	3.29 E-4	**0.032**	4.10 E-4	**0.029**
D3	5.95 E-5	0.098	7.37 E-5	0.099	9.18 E-5	0.099	1.16 E-4	0.097	3.66 E-1	0.108
ROM1	6.43 E-4	**0.022**	7.89 E-4	**0.025**	9.86 E-4	**0.026**	1.23 E-3	**0.034**	1.53 E-3	0.039
NM1	6.13 E-4	0.044	7.53 E-4	0.040	9.49 E-4	0.040	1.19 E-3	0.040	1.47 E-3	**0.022**

4.4.3 Comparison of Arrhenius activation energy values- Approaches 1 and 2

Values of apparent activation energy are defined for the different approaches in order to compare them with the trend of apparent activation energy shown in Figure 50. The best-fitting models from Approach 1 and all tested models within Approach 2 are selected. Regarding Approach 1, values of the rate constant are defined from the slope of the defined regression lines shown in Figure 51. For Approach 2, the values of the rate constants provided by the fitting procedure can be directly used for further determination of the apparent activation energy. The resulting Arrhenius plots are shown in Figure 53. As demonstrated, all regression lines show a coefficient of determination close to one.
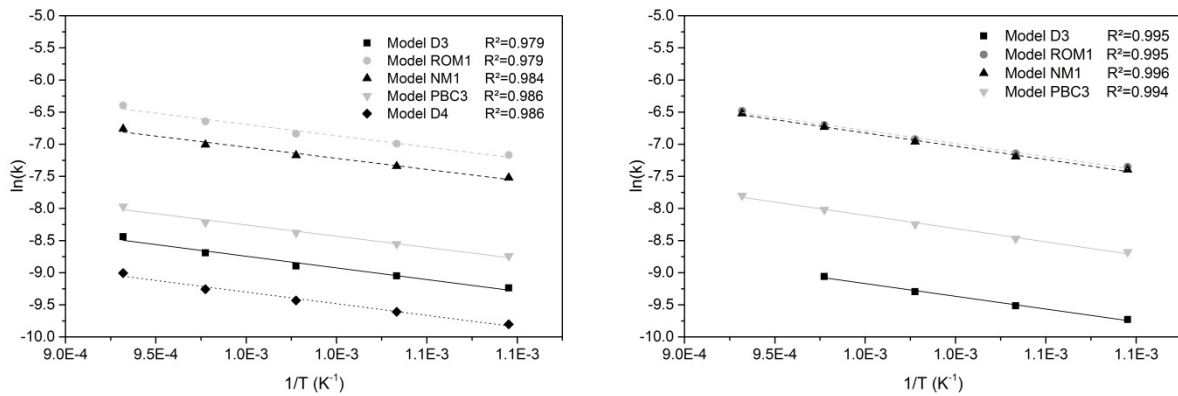
Figure 53: Arrhenius plots for the determination of the apparent activation energies from different model analysis approaches: left- Approach 1; right- Approach 2.[164]

Table 15 shows the resulting values of apparent activation energy, determined by the defined rate constants for all selected models. The resulting values of apparent activation energies for the conversion from wüstite to metallic iron are between 29 and 35 kJ/mol for all models. The trend of apparent activation energy against degree of reduction, given in Figure 50, shows a variation of the apparent activation energy between 24 and 43 kJ/mol in the area of FeO to Fe reduction. This means that the different methods are in good agreement. Values of the apparent activation energy for the conversion from FeO to Fe by hydrogen reported in literature are already given in Table 2. The values range from 11 to 104 kJ/mol. Notably, the apparent activation energy hinges on different parameters, such as input material, gas composition, type of experiment, etc. Moreover, the rate-limiting step occurring has a big impact on the values of apparent activation energy. Kuila et al.[93] defined diffusion as a rate-limiting step, resulting in values of apparent activation energy of only 11 kJ/mol.

Table 15: Determined values of apparent activation energy from different model fitting approaches.[164]

Model No.	Approach 1 E_a (kJ/mol)	Approach 2 E_a (kJ/mol)
PBC3	29.13	34.33
D3	30.19	32.98
D4	30.14	-
ROM1	29.23	33.91
NM1	28.76	34.37
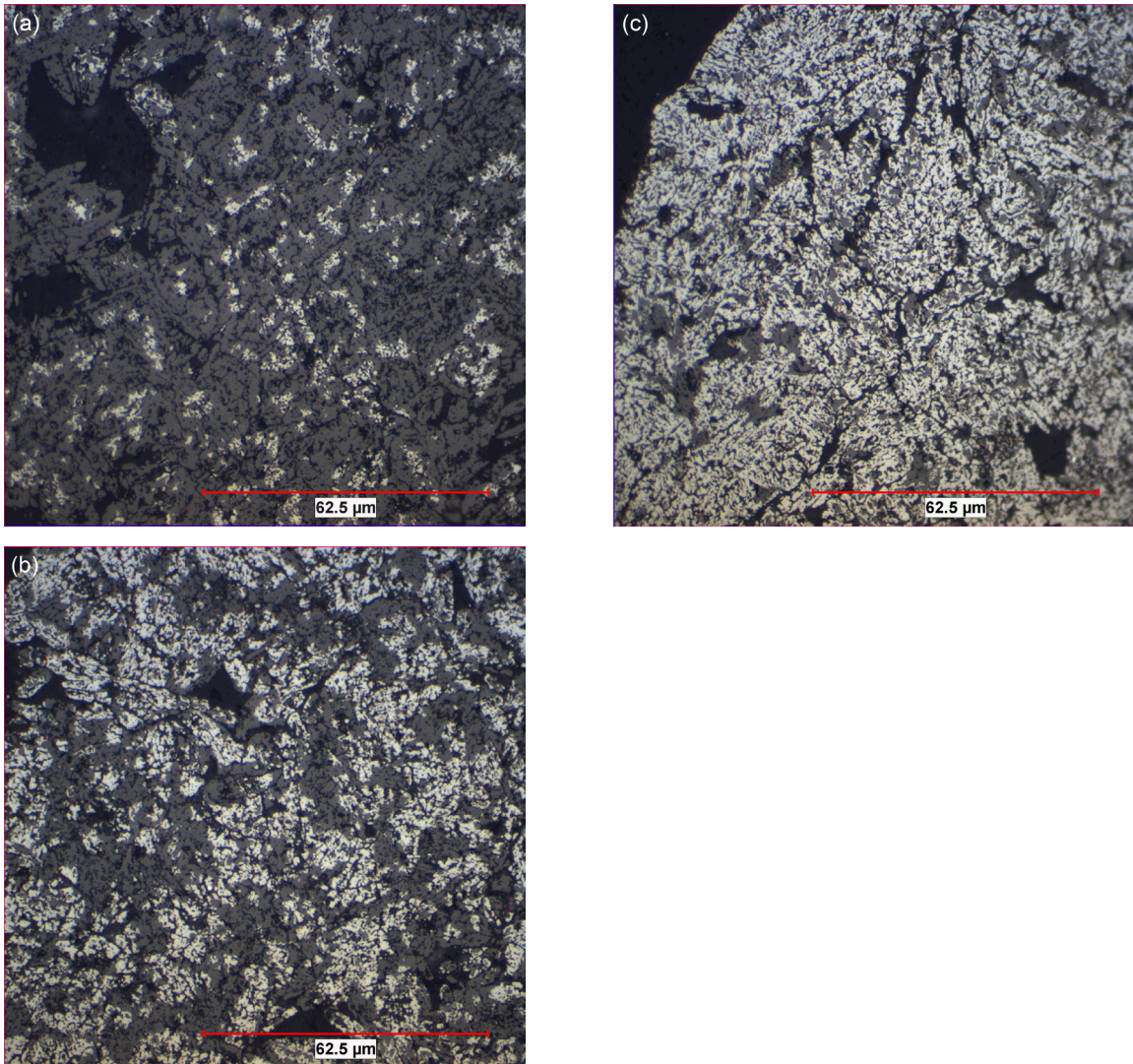
Figure 54: Polished micro-sections of partly reduced samples at 700 °C reduction temperature: (a) 40 % degree of reduction; (b) 60 % degree of reduction; (c) 80 % degree of reduction; FeO gray areas; Fe, white areas.[164]

The first two approaches carried out for the determination of the rate-limiting mechanism provide no general trend regarding the rate-limiting mechanisms for the reduction from FeO to Fe. The application of the integral g(x) expressions for the analysis show that diffusion also might be a limitation for the reduction procedure, represented by the coefficients of

determination for model D4, which are close to 1, which is somehow unexpected for the reduction of hematite by hydrogen in fluidized state because of the good diffusion behavior of hydrogen compared to carbon monoxide.[55] Diffusion might only be of relevance in case of the formation of dense iron layers around the particles, which avoids the direct contact of the reducing gas with the reaction interface. To check the behavior of the material during reduction, polished micro-sections of partly reduced samples are prepared for a reduction temperature of 700 °C, shown in Figure 54. The samples shown have a degree of reduction of approximately 40, 60 and 80 %. As it can be seen in Figure 54 (a), representing a degree of reduction of 40%, the formation of metallic iron starts uniformly, distributed over the whole area of the particles. The formation of dense iron layers cannot be observed. In Figure 54 (b) (60 % degree of reduction) it can be seen that the iron formations grow and also new iron nuclei are formed. In Figure 54 (c), the finally formed porous iron can be observed. These results confirm that diffusion might not be the limiting process during the reduction procedure. It seems that only the chemical reaction itself and the process of nucleation and growth of the nuclei limit the progress of reduction in this case. The real behavior should be clarified by further multistep kinetic analysis because of inaccuracies of the first two approaches tested.

4.4.4 Multistep kinetic analysis of total reduction procedure from Fe_2O_3 to Fe

Further multistep kinetic analysis is carried out using a parallel reaction model based on that developed by Johnson, Mehl and Avrami (JMA). Using the model in a parallel way allows the consideration that more than one rate-limiting mechanism can act together in a parallel way. Accordingly, it is also possible to evaluate the total reduction from Fe_2O_3 to Fe, so it is not necessary to focus on one selected reduction sequence. The results should allow a more accurate description of the total reduction process, compared to the different approaches explained in previous sections.

4.4.4.1 Model developed by Johnson, Mehl and Avrami (JMA)

Next, the JMA is applied for kinetical analysis which can be used for both the description of solid state transformation and gas-solid reactions. The JMA model is defined as follows:[171–174]

$$x = 1 - e^{-a * t^n} \tag{47}$$

where x represents the conversion, a gives the nucleation rate constant, t the time and n is defined as a kinetic exponent. The value of the kinetic exponent is of great importance as it can be linked to the occurring rate-limiting mechanism.[175] If n shows values below 1, the progress is considered to be diffusion-controlled; if n = 1, the progress is controlled by the chemical reaction. A value of n > 1.5 corresponds to a limitation by the nucleation process, where n = 1.5 gives a zero nucleation rate, n = 1.5 to 2.5 represents a decreasing nucleation rate and n > 2.5 an increasing nucleation rate. The rate constant k depends on the nucleation rate constant and the kinetic exponent as follows:

$$k = a^{\frac{1}{n}} \tag{48}$$

Taking into account that more than one rate-limiting mechanism can act together in a parallel way, a system of three mechanisms is selected to reproduce the experimental data as accurately as possible, shown in Equation (49):

$$x_t = x_0 + w_1 x_1 + w_2 x_2 + w_3 x_3 \tag{49}$$

x_0 gives the conversion at the beginning of the analysis, which can be set to 0 here. $w_{1,2,3}$ gives the weight factors for the different terms. A combination of Equation (47) and Equation (49) ends in Equation (50):

$$x_t = w_1 * \left(1 - e^{-a_1 * t^{n_1}}\right) + w_2 * \left(1 - e^{-a_2 * t^{n_2}}\right) + w_3 * \left(1 - e^{-a_3 * t^{n_3}}\right) \tag{50}$$

Equation (50) can be fitted to the experimental results by a variation of $w_{1,2,3}$, $a_{1,2,3}$ and $n_{1,2,3}$ in order to minimize the RMSD. The fitting is done using Microsoft Excel´s solver function.

4.4.4.2 *Multistep kinetic analysis for Ore A using parallel reaction model based on the JMA model*

The results of the fitting procedure for Ore A, using Equation (50), are demonstrated in Figure 55 for all different reduction temperatures tested. Instead of x, the degree of reduction RD is used to describe the conversion. The kinetic exponents of the appropriate terms are also shown in the diagrams. As it can be seen, in a temperature range between 600 and 700 °C, the initial stage of reduction might be controlled by reaction kinetics, designated by a kinetic exponent close to 1. The corresponding weight factors in this temperature area are in the range representing a complete conversion from hematite to magnetite. At higher temperatures, the kinetic exponents drop below one, while at the same time, the weight factors increase. Consequently, the initial stage of reduction might be controlled by diffusion at higher temperatures, while it cannot be clearly distinguished between the reduction from hematite to magnetite and from magnetite to wüstite. As a result, there is a possibility that both reduction sequences occur in parallel and not clearly separated.

The fitting results of the further reduction stages show that the process is limited by a combination of reaction kinetics and nucleation. At lower reduction temperatures, the limitation by reaction kinetics is more pronounced, shown by a big weight factor. The importance decreases with a nearly constant kinetic exponent when the temperature increases, while the weight factor of the nucleation term increases simultaneously. So, the influence of nucleation becomes more evident. At 800 °C reduction temperature, the limitation by the chemical reaction is not important anymore because the results show a limitation by nucleation only.

The influence of nucleation can also be observed based on the shapes of the reduction rates, shown in Figure 48. At the beginning of the formation of metallic iron, the reduction rate is lower compared to later stages, e.g. at 40 % degree of reduction. This behavior can be associated with an incubation period for the nucleation of metallic iron. At the final stages of reduction, nucleation is not important anymore and the progress is controlled by the chemical reaction only, except for the highest tested reduction temperature. Because of the good diffusion behavior of hydrogen compared to carbon monoxide, diffusion is not of

importance in the final reduction stages. This can be confirmed by the results of the kinetic analysis.

Table 16 summarizes the values obtained from the fitting procedure, representing the different weight factors, nucleation rate constants, kinetic exponents, rate constants and values of RMSD at different temperatures. The rate constants are calculated according to Equation (48). As it can be seen, the rate constants for the second and third terms increase with increasing temperatures. Because of the changing mechanism and the changing weight factors in case of the first term, no general trend concerning the rate constant can be observed.
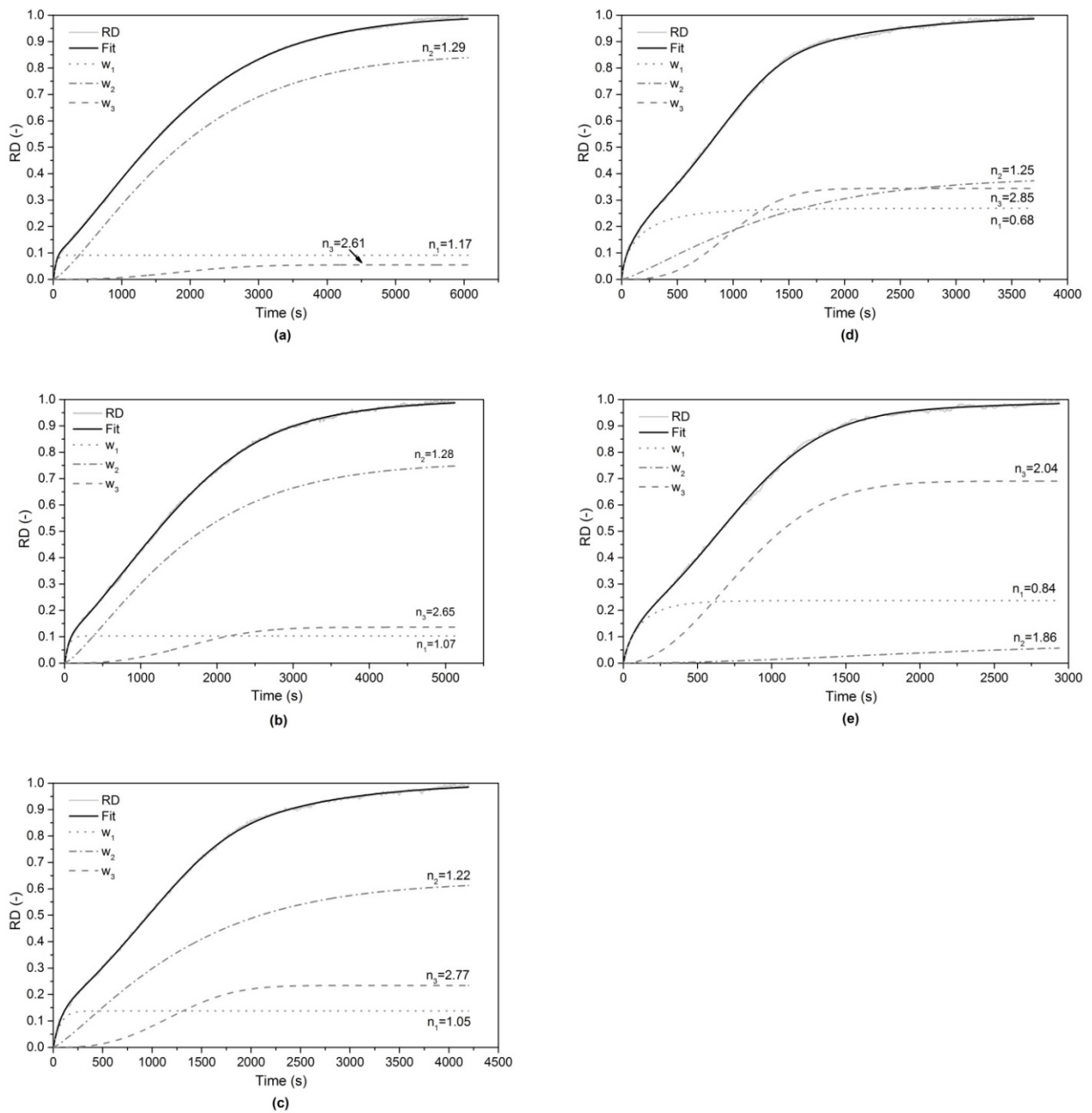
Figure 55: Kinetical investigation based on the JMA model (parallel) at different reduction temperatures for Ore A: (a) 600 °C, (b) 650 °C, (c) 700 °C, (d) 750 °C, (e) 800 °C.[164]

Table 16: Weight factors, nucleation rate constants, kinetic exponents, rate constants and RMSD for multistep kinetic analysis (parallel) at different temperatures for Ore A.[164]

Reduction temperature (°C)		600	650	700	750	800
	w_1	0.0915	0.1032	0.1379	0.2691	0.2371
Weight factors (-)	w_2	0.8535	0.7607	0.6277	0.3865	0.0722
	w_3	0.0549	0.1362	0.2344	0.3443	0.6907
	a_1	0.0117	0.0140	0.0109	0.0286	0.0176
Nucleation rate constants (s^{-1})	a_2	$5.313 \cdot 10^{-5}$	$7.287 \cdot 10^{-5}$	$1.394 \cdot 10^{-4}$	$1.201 \cdot 10^{-4}$	$5.382 \cdot 10^{-7}$
	a_3	$2.064 \cdot 10^{-9}$	$2.065 \cdot 10^{-9}$	$2.065 \cdot 10^{-9}$	$2.065 \cdot 10^{-9}$	$8.614 \cdot 10^{-7}$
	n_1	1.17	1.07	1.05	0.69	0.84
Kinetic exponents (-)	n_2	1.29	1.28	1.22	1.24	1.86
	n_3	2.61	2.65	2.76	2.86	2.04
	k_1	0.0231	0.0186	0.0138	0.0060	0.0080
Rate constants (s^{-1})	k_2	$4.94 \cdot 10^{-4}$	$5.88 \cdot 10^{-4}$	$6.99 \cdot 10^{-4}$	$7.16 \cdot 10^{-4}$	$4.33 \cdot 10^{-4}$
	k_3	$4.71 \cdot 10^{-4}$	$5.28 \cdot 10^{-4}$	$7.31 \cdot 10^{-4}$	$9.07 \cdot 10^{-4}$	$1.06 \cdot 10^{-3}$
Root mean square deviation	RMSD	0.0045	0.0048	0.0049	0.0061	0.0070

To estimate which mechanism is acting at which stages of reduction, the different terms of the fitting procedure are plotted against the experimental degree of reduction, as demonstrated in Figure 56. It can be observed that during the initial stage of reduction, the controlling mechanism changes with increasing temperature from reaction-controlled to diffusion-controlled with an increasing weight factor. This ends in higher reduction rates at higher temperatures for higher degrees of reduction (20-30%). This behavior can be linked to the first peak of apparent activation energy at a degree of reduction of approximately 12 %. Furthermore, with increasing reduction temperatures, the weight factor of nucleation mechanism also increases, while at the same time the weight factor of reaction kinetics decreases. Different changes occur in the reduction rate at different conversion degrees, which matches with the second peak of apparent activation energy at a degree of reduction of 85%. After that, only the limitation by the chemical reaction is relevant since the apparent activation energy becomes smaller. These conclusions are in agreement with those obtained by the polished micro-sections of the partly reduced samples, shown in Figure 54.

For the limiting mechanisms two and three, resulting from the multistep analysis, the apparent activation energies are again determined using the defined values of the rate constants at different reduction temperatures. The corresponding Arrhenius plot is shown in Figure 57. For the second mechanism, representing the limitation by reaction kinetics, a value of 19.30 kJ/mol can be calculated while the second term for the highest reduction temperature is not included because of the changing rate limiting mechanism. For the third term, representing limitation by nucleation, the apparent activation energy is 33.88 kJ/mol. These values are again in good agreement with those obtained by the trend of apparent activation energy against the degree of reduction, where the apparent activation energy varies between 23 and 42 kJ/mol during reduction from FeO to Fe. In that case, both mechanisms act in a parallel way. During the final reduction (RD > 90 %), nucleation is not important to any further extent (except for the highest tested reduction temperature), so the apparent activation energy decreases to a value representing only limitation related to the chemical reaction.
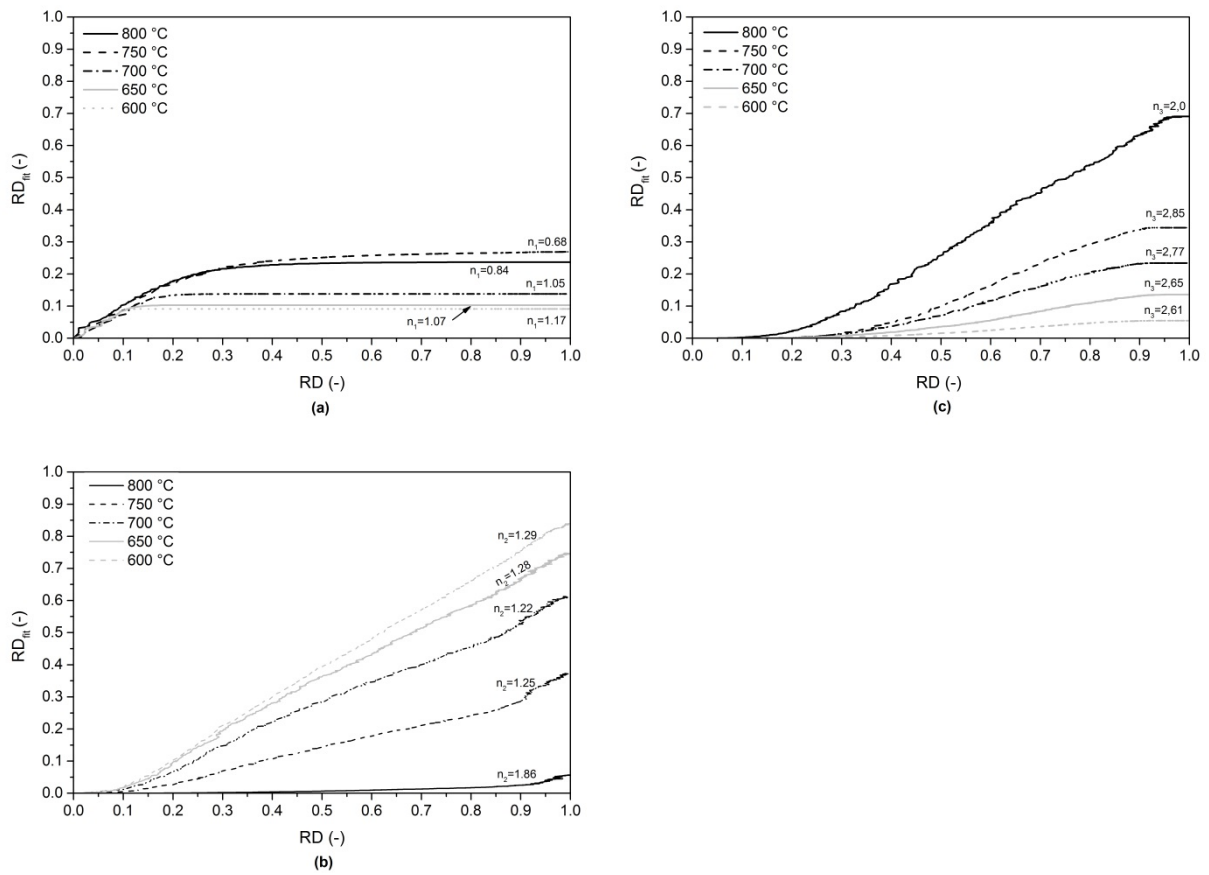
Figure 56: Plot of different weight factors (w) against experimental degree of reduction for different temperatures: (a) w_1, (b) w_2, (c) w_3.[164]
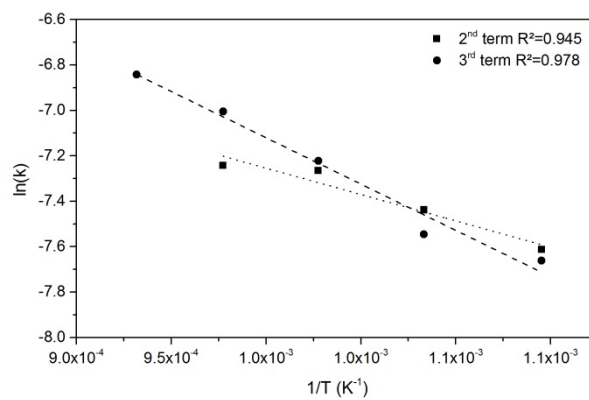
Figure 57: Arrhenius plot with resulting k-values from the JMA-model fitting procedure for the second and third term.

4.5 Comparison of different iron ores regarding kinetics and fluidization behavior

To evaluate the possibility of the investigation of the reducibility of different iron ore grades by the method developed in Section 4.4.4, various iron ore grades are tested under the same conditions explained in the previous sections. The behavior of Ore A has already been explained. Additionally, three more iron ores are investigated. Table 17 shows the summary of the iron ore properties presenting all four iron ores in terms of chemical analysis, grain size and specific surface area. The behavior of Ore A is also summarized again for comparison with the other iron ores.

Table 17: Properties of the investigated iron ore grades.[165]

	Ore A	Ore B	Ore C	Ore D
Fe_{tot} (%-wt.)	63.6	62.2	61.9	57.3
Fe^{2+} (%-wt.)	0.45	1.09	0.42	19.66
SiO_2 (%-wt.)	3.48	6.00	2.99	7.05
Al_2O_3 (%-wt.)	2.07	1.1	2.14	n.a.
Grain size (mm)	0.25–0.50	0.25–0.50	0.25–0.50	0.25–0.50
Specific surface area B.E.T. (m²/g)	11.83	2.59	20.75	n.a.

Two of the investigated ores are based on hematite (Ore A and Ore B), one consists of limonite (Ore C) and the fourth one represents a natural magnetite (Ore D), as it can be seen by the high content of divalent iron. The grain size is defined to be in between 250 and 500 μm. However, it doesn't mean that all iron ores have exactly the same mean particle diameter. The particles with a size between 250 and 500 μm are extracted by a sieve analysis from a certain grain size distribution (0.063 to 2.8 mm). The total grain size distribution is comparable for all four iron ore grades. As a result, the difference in mean particle diameter of the fraction 250 to 500 μm is insignificant. Concerning the specific surface area, Ore C shows the highest value, followed by Ore A and Ore B. That of Ore D was not analyzed. In general, a high initial porosity should end in a good reducibility because of a better permeability of the reducing gas to the reaction interfaces. Ore C should therefore show an enhanced reducibility compared to the other ores.

Figure 58 shows the progresses of reduction obtained during the experiments for Ore B and Ore C at different reduction temperatures. In the case of Ore B, an experiment without fluidization troubles at a reduction temperature of 800 °C was not possible as a result of sticking problems. As it can already be seen, big differences in reducibility exist at similar reduction temperatures, also taking into account the behavior of Ore A, shown in Figure 45. During all experiments, the initial stage of reduction, representing the conversion from Fe_2O_3 to Fe_3O_4 occurs very fast. The fast, initial reduction is followed by a nearly constant reduction rate until certain degrees of reduction, depending on temperature, in terms of Ores A and B. Thereafter, the reduction rate slows down until a complete reduction is achieved. The deceleration of the reduction rate occurs at nearly the same reduction extent at different temperatures for Ore B, which is in the range of 90 % degree of reduction. In the cases of

Ores A and Ore C, the deceleration point depends significantly on the reduction temperature. For Ore A it takes place between a degree of reduction of 75 to 90 %, while higher values correspond to higher reduction temperatures. For Ore C, this effect is even more obvious because the deceleration takes place between 65 and 90 % degree of reduction. The behavior of Ore C is also different in the second stage of reduction, where a constant reduction rate cannot be detected, especially at lower values of reduction temperature. The reduction rate shows a tendency to increase between 20 and 35 % degree of reduction.
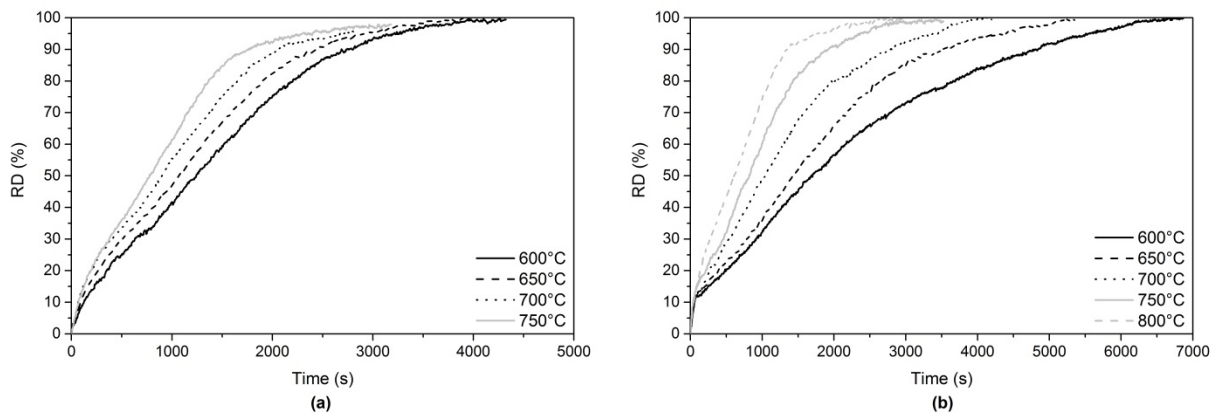
Figure 58: Progress of reduction at different reduction temperatures: (a) Ore B; (b) Ore C.[165]

Figure 59 shows the comparison of the different ores at the same reduction temperatures. As shown, at the lowest reduction temperature representing 600°C, the reducibility of the different ores is completely diverse. Ore B shows the best reducibility, followed by Ore A and Ore C. This behavior is somehow unexpected. Taking the specific surface areas of the iron ores into account, where Ore C has the highest value followed by Ore A and B, Ore C should show the best reducibility. Further kinetical analysis should explain this extraordinary behavior. With increasing reduction temperatures, the reducibility becomes more similar. At 750 °C, all three ores shows nearly the same reduction rate at the given temperature. A reduction time of approximately 3500 s (~58 min) is required for a complete conversion. Furthermore it has to be mentioned, that for all experiments with Ores A, B, and C, except those for Ore B at 800 °C, a stable fluidization was achieved during the whole reduction procedure.

The fluidization behavior of the magnetite-based ore, Ore D, is completely different compared to the other ores. A stable fluidization during the complete reduction procedure is not possible at all tested temperatures. Instantaneously in the area after first metallic iron formation, a de-fluidization of the material takes place because of particle sticking. The behavior of the pressure drop and the degree of reduction against time for a reduction temperature of 800 °C are shown in Figure 60. As it can be observed, the de-fluidization starts at a degree of reduction of approximately 20 %, indicating that the conversion from Fe_3O_4 to FeO is not completed when the first metallic iron formation appears. At a lower reduction temperature (650°C), de-fluidization also starts after the first formation of metallic iron but the pressure drop loss rate is reduced. As a result, the de-fluidization takes more time. The fluidization behavior and the reducibility of magnetite-based ores during hydrogen-induced fluidized bed reduction are discussed in more detail in Section 5.
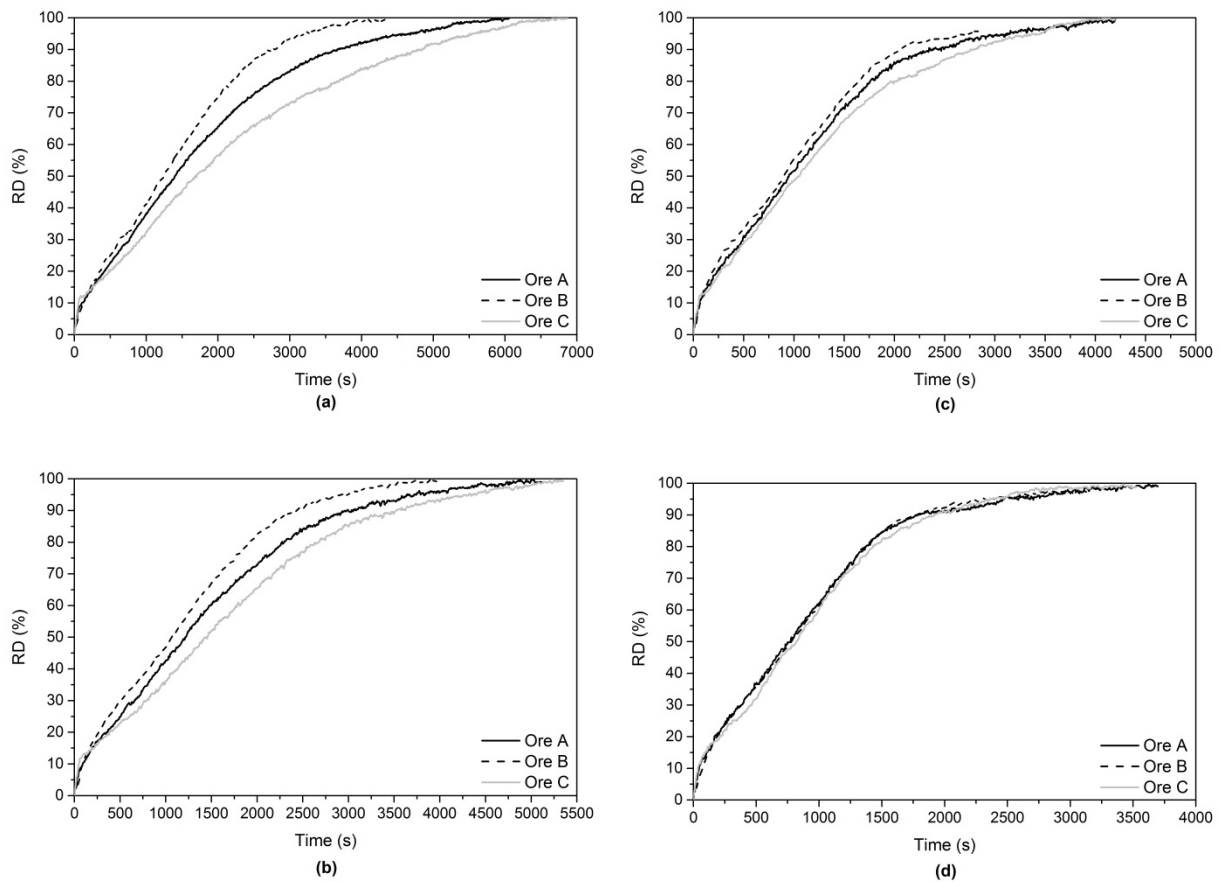
Figure 59: Comparison of the reduction progress of different ores at different reduction temperatures: (a) 600 °C [165]; (b) 650 °C; (c) 700 °C; (d) 750 °C[165].
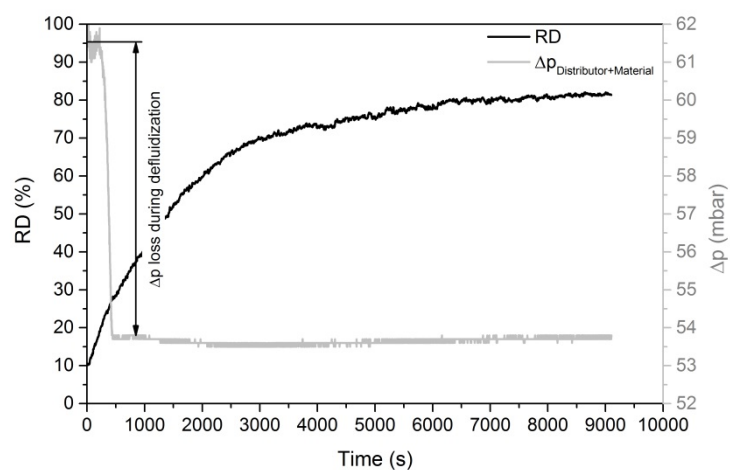
Figure 60: Pressure drop across distributor and material and degree of reduction for the reduction of Ore D at 800 °C.[165]

After de-fluidization, the samples of Ore D are further reduced at reduction temperatures of 650 and 800 °C to a degree of reduction of approximately 80 % for 71 and 150 min overall reduction time, respectively. The polished micro-sections of these samples are shown in Figure 61. Dense wüstite cores can be observed in both samples. In both cases, the wüstite cores are covered by iron layers, but the structure of the iron layers differs, depending on the reduction temperature. At lower temperatures, the iron layer formed shows a high porosity. In contrast to that, at higher reduction temperatures, the iron layer formed shows a more dense structure. This behavior explains the different reduction times required to reach a degree of reduction of 80 %, which is drastically lessened for lower reduction temperatures. As a result, the dense iron layers formed at higher reduction temperatures hinder the direct contact of the reducing gas mixture and the reaction interface indicating that diffusion and/or nucleation becomes the limiting step of the reduction progress. As a result of the fluidization troubles of Ore D, further kinetical analysis is done only using the experimental results from Ores A, B and C.
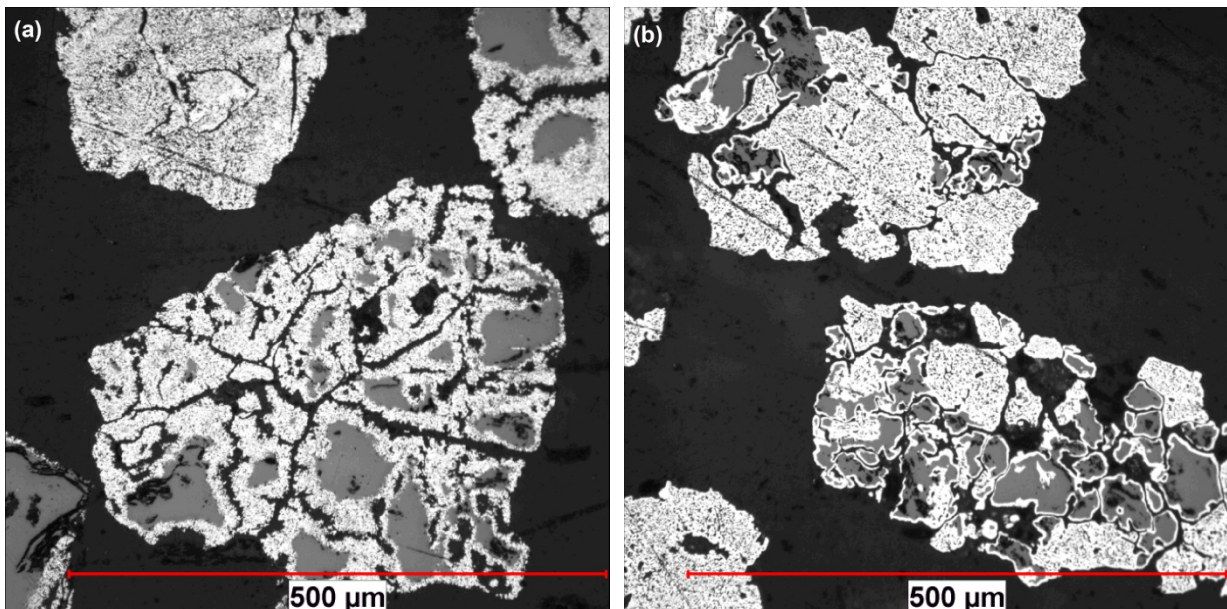
Figure 61: Polished micro-sections of partly reduced samples of Ore D at different reduction temperatures: (a) 650 °C; (b) 800 °C. Gray areas: wüstite, white areas: metallic iron.[165]

Another interesting fact observed during the reduction experiments is regarding the behavior of re-oxidation. After the reduction, the sample portions are cooled down inside the reactor to ambient temperature under inert atmosphere. During the sample discharging, the first contact of the sponge iron produced with oxygen from the air takes place. Samples reduced at reduction temperatures higher than 700 °C remain stable under ambient conditions, while for samples reduced at reduction temperatures lower than 700 °C, an instant re-oxidation after the first contact with the oxygen takes place. This behavior can also be explained by the use of polished micro-sections. Figure 62 shows those for partly reduced samples of Ore A at reduction temperatures of 600 and 800 °C, representing a degree of reduction of approximately 75 %. In case of lower reduction temperatures, the iron formations are uniformly, distributed across the whole particle area and the final iron product

seems to have high porosity. A homogenous distribution of very small iron nuclei can be observed across nearly the whole particle areas. At higher reduction temperatures, the iron formed shows a lesser degree of porosity and therefore a lower specific surface area according to the polished micro-sections. This difference in the morphology might hinder the instant re-oxidation for samples reduced at higher reduction temperatures.
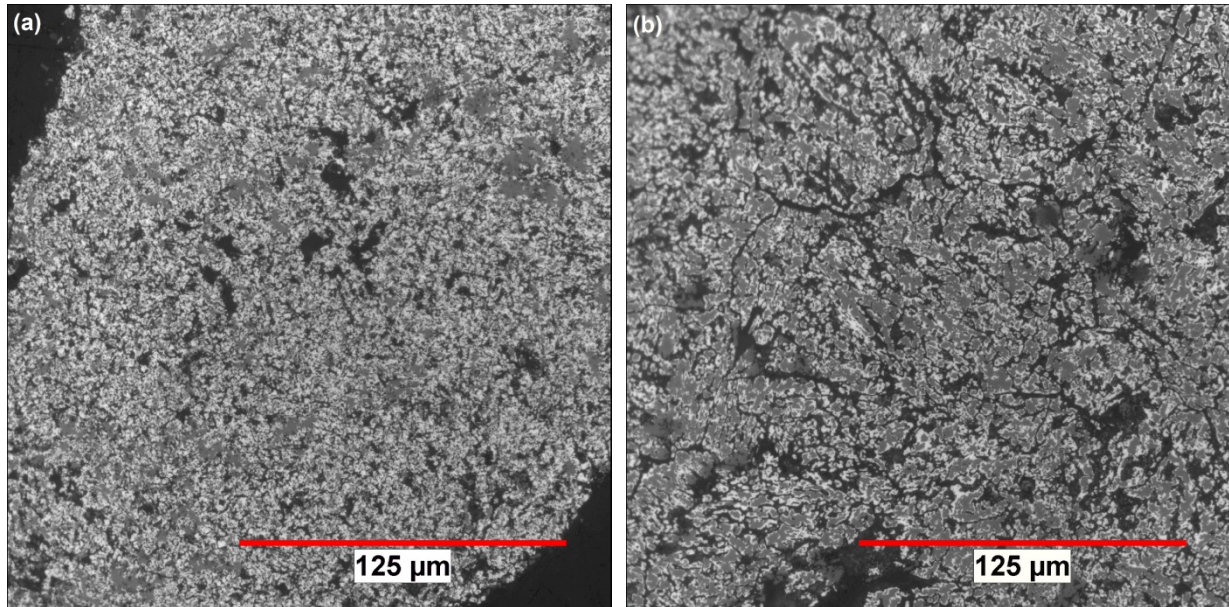
Figure 62: Polished micro-sections of partly reduced samples of Ore A at different reduction temperatures: (a) 600 °C; (b) 800 °C. Gray areas: wüstite, white areas: metallic iron.[165]

For a better understanding of the reducibility of the different ores, the trends of the apparent activation energies of Ores B and C are also determined and compared with that of Ore A using the same procedure as explained in previous sections. Figure 63 shows the comparison of the trends for the different ores against the degree of reduction. As shown, the apparent activation energy increases at the initial stage of reduction for all iron ores until a first peak can be observed, which is in the range of a degree of reduction between 10-14 % representing a complete reduction of Fe_2O_3 to Fe_3O_4. After that, the trends decrease until a degree of reduction of approximately 30 % is achieved. This behavior is also similar for all three iron ore grades. During further reduction, the behavior among the iron ores differs. As already explained, the apparent activation energy increases again in case of Ore A until a second peak can be observed at approximately 85 % degree of reduction. A similar trend can be observed for Ore C, where it also increases again in the area of FeO to Fe reduction, resulting in a peak at approximately 75 % degree of reduction. The behavior of Ore B during reduction from FeO to Fe shows differences compared to the other ores on account of the nearly constant level of the apparent activation energy. As a result, no second peak can be observed in case of Ore B. The trends of the apparent activation energies can be clearly linked to the reduction behavior. As explained above, the reduction rate of Ore B slowed down at nearly the same reduction extent at different temperatures, resulting in no second peak of apparent activation energy. Concerning Ores A and C, the deceleration point depends clearly on the reduction temperature. This effect is even more pronounced for

Ore C compared to Ore A, so an extensive second peak can be observed in the case of Ore C.
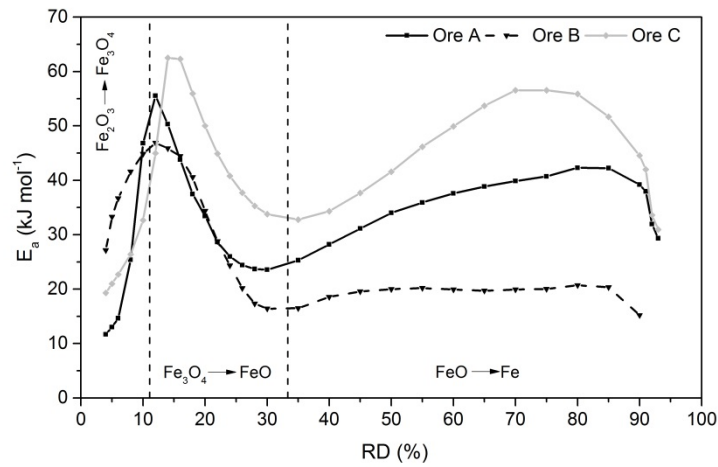
Figure 63: Comparison of trends of apparent activation energies E_a against degree of reduction for different iron ores.[165]
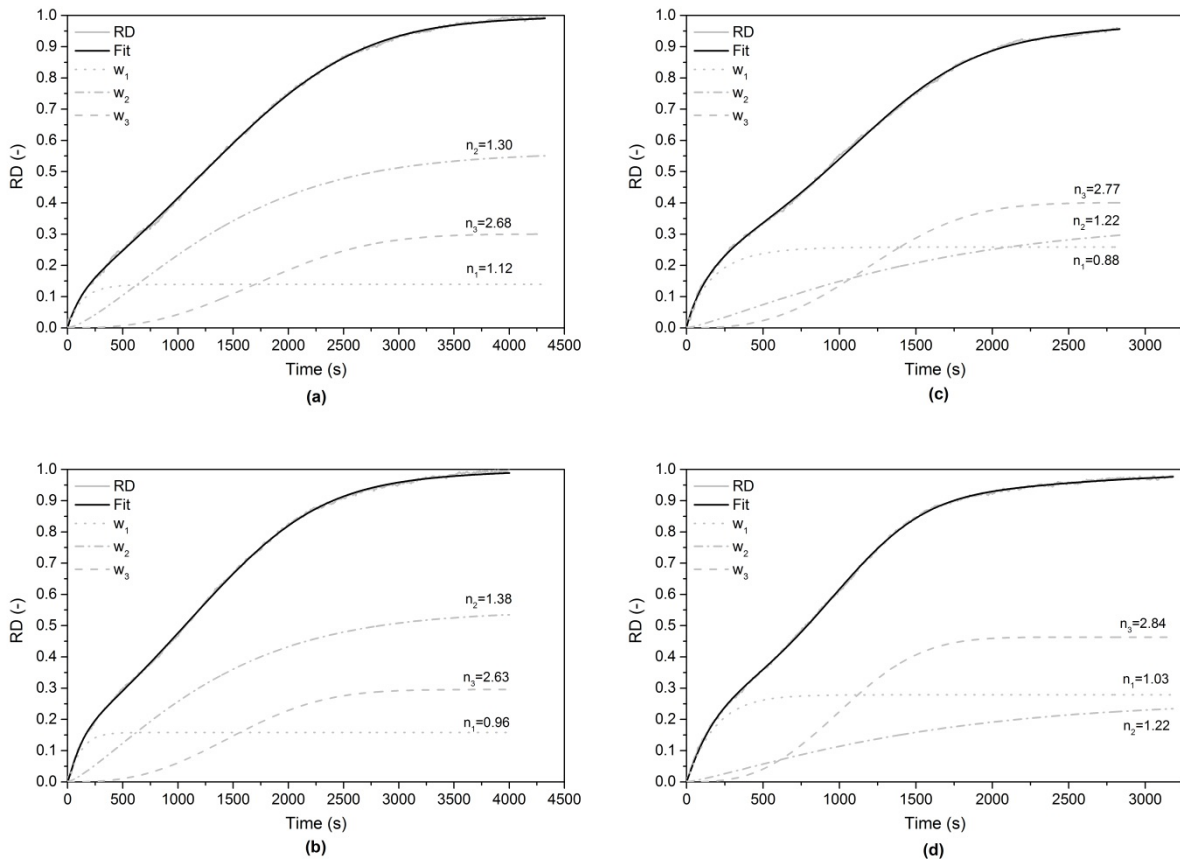
Figure 64: Kinetical investigation based on JMA model (parallel) at different reduction temperatures for Ore B: (a) 600 °C, (b) 650 °C [165], (c) 700 °C, (d) 750 °C.

Overall, the apparent activation energies vary between 10 and 65 kJ/mol for all three iron ore grades tested. The ore showing the best reducibility, Ore B, exhibits the lowest values of apparent activation energy with no secondary peak in the area of reduction from FeO to Fe. The worst reducible ore, Ore C, shows the highest level of the apparent activation energy curves and an extensive peak in the area of reduction from FeO to Fe. Further kinetical analysis using the JMA model should explain the differences in reducibility and the trends of apparent activation energy.
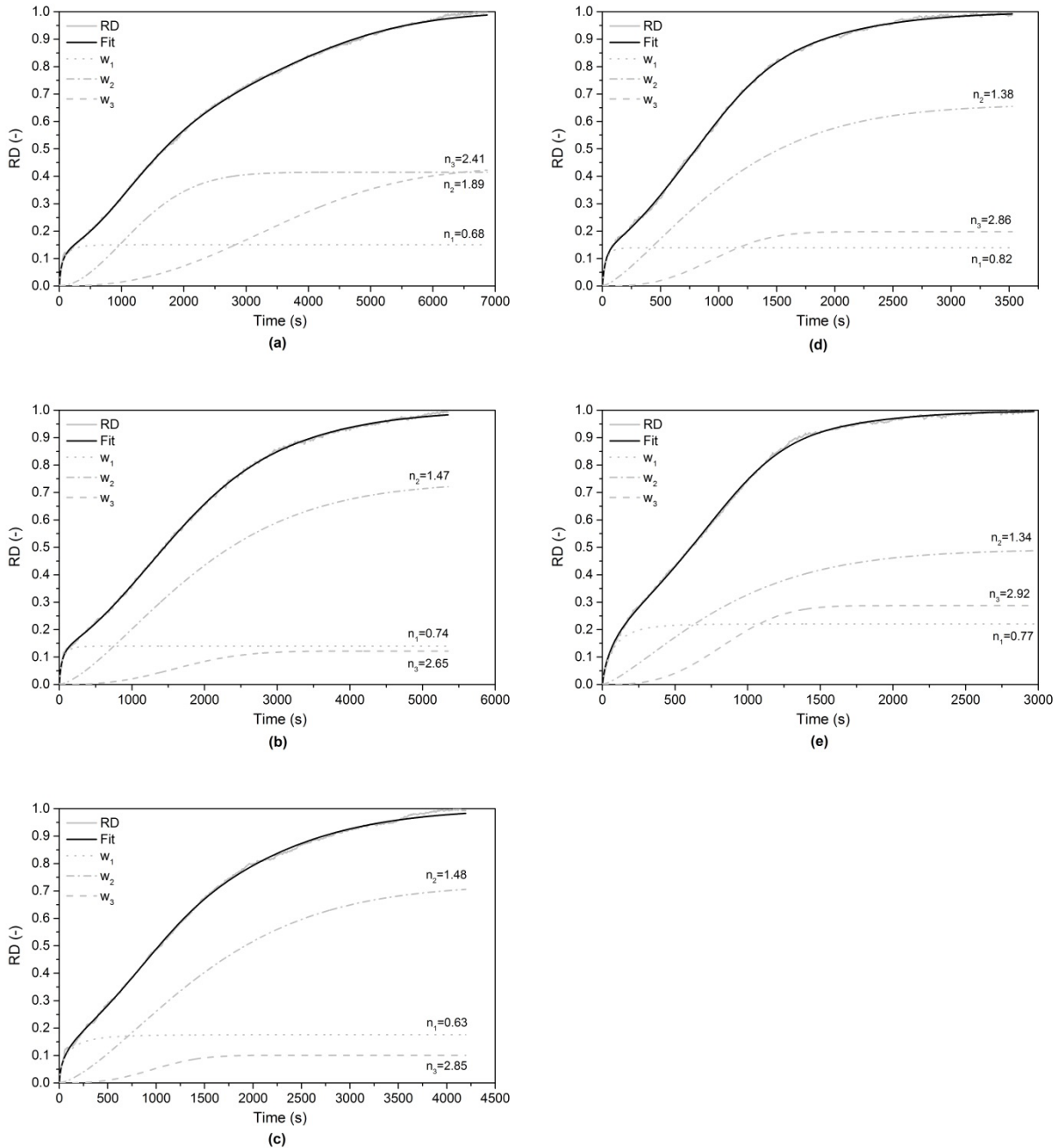
Figure 65: Kinetical investigation based on JMA model (parallel) at different reduction temperatures for Ore C: (a) 600 °C, (b) 650 °C [165], (c) 700 °C, (d) 750 °C. (e) 800 °C.

Figure 64 and Figure 65 show the results using the fitting procedure based on the JMA model at all tested temperatures for Ore B and Ore C, respectively. As it can be seen, all results fit well to the experimental data, represented by low values of RMSD. The given n-values in the figures represent again the appropriate kinetic exponent of each term. Table 18 summarizes the values obtained from the fitting procedure for Ores B and C.

Table 18: Weight factors, nucleation rate constants, kinetic exponents, rate constants and RMSD for multistep kinetic analysis (parallel) at different temperatures for Ore B and Ore C.[165]

		Ore B				
Reduction temperature (°C)		600	650	700	750	800
Weight factors	w_1	0.1394	0.1581	0.2588	0.2787	
	w_2	0.5602	0.5463	0.3402	0.2579	
	w_3	0.3000	0.2956	0.4010	0.4634	
Nucleation rate constants (s^{-1})	a_1	0.0094	0.0044	0.0104	0.0044	No results because of fluidization problems (sticking)
	a_2	$3.83 \cdot 10^{-5}$	$7.84 \cdot 10^{-5}$	$1.25 \cdot 10^{-4}$	$1.29 \cdot 10^{-4}$	
	a_3	$2.07 \cdot 10^{-9}$	$2.07 \cdot 10^{-9}$	$2.07 \cdot 10^{-9}$	$2.07 \cdot 10^{-9}$	
Kinetic exponents	n_1	0.96	1.13	0.88	1.03	
	n_2	1.38	1.30	1.22	1.22	
	n_3	2.63	2.68	2.77	2.84	
Rate constants (s^{-1})	k_1	0.008	0.008	0.006	0.005	
	k_2	$6.41 \cdot 10^{-4}$	$7.07 \cdot 10^{-4}$	$6.37 \cdot 10^{-4}$	$6.42 \cdot 10^{-4}$	
	k_3	$4.92 \cdot 10^{-4}$	$5.80 \cdot 10^{-4}$	$7.26 \cdot 10^{-4}$	$8.66 \cdot 10^{-4}$	
Root mean square deviation	RMSD	0.0046	0.0047	0.0051	0.0040	

		Ore C				
Reduction temperature (°C)		600	650	700	750	800
Weight factors	w_1	0.1506	0.1387	0.1759	0.1394	0.2205
	w_2	0.4153	0.7420	0.7229	0.6625	0.4919
	w_3	0.4340	0.1193	0.1011	0.1981	0.2876
Nucleation rate constants (s^{-1})	a_1	0.0588	0.0601	0.0577	0.0617	0.0327
	a_2	$1.00 \cdot 10^{-6}$	$1.26 \cdot 10^{-5}$	$1.60 \cdot 10^{-5}$	$5.67 \cdot 10^{-5}$	$1.03 \cdot 10^{-4}$
	a_3	$2.06 \cdot 10^{-9}$	$2.07 \cdot 10^{-9}$	$2.07 \cdot 10^{-9}$	$2.07 \cdot 10^{-9}$	$2.07 \cdot 10^{-9}$
Kinetic exponents	n_1	0.68	0.74	0.63	0.82	0.77
	n_2	1.89	1.47	1.48	1.38	1.34
	n_3	2.41	2.65	2.85	2.86	2.92
Rate constants (s^{-1})	k_1	0.015	0.023	0.011	0.034	0.012
	k_2	$6.77 \cdot 10^{-4}$	$4.62 \cdot 10^{-4}$	$5.82 \cdot 10^{-4}$	$8.38 \cdot 10^{-4}$	$1.07 \cdot 10^{-3}$
	k_3	$2.48 \cdot 10^{-4}$	$5.29 \cdot 10^{-4}$	$9.03 \cdot 10^{-4}$	$9.17 \cdot 10^{-4}$	$1.06 \cdot 10^{-3}$
Root mean square deviation	RMSD	0.0055	0.0049	0.0080	0.0055	0.0061

The behavior of Ore A was already explained in detail in Section 4.4.4.2. It is observed that n_1 changes from values representing a limitation by the chemical reaction to the diffusion-controlled mechanism with rising reduction temperatures. Simultaneously, the consistent weight factor increases. The value of the rate constant, k_1, shows an unexpected trend as it decreases with increasing temperatures. This may result from the fact that the weight factor reaches values higher than 0.11, indicating that the reduction from Fe_3O_4 to FeO is still in progress. The reduction temperature does not seem to play an important role during reduction from Fe_2O_3 to Fe_3O_4 because it occurs very fast. Ongoing reduction is limited by a combination of reaction kinetics and the mechanism of nucleation represented by kinetic exponents n_2 and n_3 close to 1 and bigger than 1.5, respectively, as given in Table 16. At lower reduction temperatures, limitation by reaction kinetics is dominant, while its effect decreases with increasing temperatures (decreasing weight factor). At the same time, the

importance of the nucleation process increases. At the highest reduction temperature, the process is controlled only by the nucleation. The values of the rate constants k_2 and k_3 increases with increasing temperature. These findings can be confirmed also by the polished micro sections of the partly reduced samples of Ore A, shown in Figure 62. At the lowest reduction temperature (600 °C), iron nuclei can be observed everywhere across the entire particle. This indicates that the progress of reduction is only limited by reaction kinetics. At the highest reduction temperature (800 °C), iron nuclei cannot be observed across the whole particle area; hence, nucleation limits the reduction progress. As a result, the different behaviors regarding re-oxidation can be explained by such an analysis.

Compared to Ore A, Ore B shows a different behavior. The initial stage of the reduction process is also controlled by reaction kinetics with values of n_1 close to 1. Later stages of reduction are again controlled by a mixture of reaction kinetics and nucleation. However, the rate constant obtained for the second term, k_2, representing the limitation by chemical reaction, remains nearly constant at different reduction temperatures. Concerning nucleation, k_3 is increased with rising temperatures, which is the reason why only nucleation is responsible for the observed differences in the reduction rates. The weight factor for the nucleation term, w_3, also increases as a function of temperature, but to a lesser degree in comparison with Ore A.

For Ore C, which shows the lowest reducibility, the following conclusions can be made from the kinetic analysis: The kinetic exponent n_1, corresponding to the initial stage of reduction, is below 1 for all temperatures, indicating a limitation by diffusion. For the corresponding weight factor, w_1, no general trend can be observed. n_2 shows significantly higher values compared to the other ores. In a temperature range between 600-700 °C, n_2 represents a limitation by nucleation while it decreases with increasing temperatures. The kinetic exponent of the third term, n_3, represents again a limitation by the nucleation process. General trends regarding w_2 and w_3 cannot be observed. It seems that the reduction of Ore C is only controlled by nucleation at low reduction temperatures, whereas at higher ones, the chemical reaction is also of importance. So it acts in an opposite way compared to Ore A. The differences in reducibility, especially at low reduction temperatures, can therefore be explained. During the initial stage of reduction of Ore C, a limitation due to diffusion is observed, which may indicate the formation of dense magnetite during this stage of reduction. As a result, ongoing reduction of the dense magnetite formed becomes more difficult and is then limited by the nucleation process, which slows down the reduction rate, especially at low reduction temperatures. Thurnhofer et al. [143] investigated different pre-reduction conditions and their effect on the final degree of reduction. They found that there is still an effect of the pre-reduction conditions on the final reduction behavior because of the formation of different structures and morphologies during the reduction procedure. Such effects may also influence the reduction procedure of Ore C with actual conditions. At higher reduction temperatures (750-800 °C), the reduction becomes limited by a mixture of reaction kinetics and nucleation, with a growing importance of nucleation with increasing temperatures. As a conclusion, the poor reducibility of Ore C, especially at low reduction temperatures, can be explained by the differences observed compared to Ores A and B.

The results from the fitting procedure can now be used again for further explanations of the trends of apparent activation energies, shown in Figure 63. The presence of the first peak for all ores occurred because of the different changes in the reduction rate at different conversions, while the effect depends on the reduction temperature. This can also be seen

by the general trend of the increasing weight factors w_1 with increasing temperatures. Additionally, the different equilibrium gas compositions at different reduction temperatures have to be kept in mind. At low reduction temperatures, the equilibrium between magnetite and wüstite is close to that of wüstite and iron. With rising temperatures, the difference is significantly higher. This can be observed within the Baur-Glässner diagram, shown in Figure 13. The variation of the reduction temperature alone can have an influence on the first peak of apparent activation energy, only considering the thermodynamic point of view because of the differences regarding the thermodynamic equilibrium between the oxides. Another interesting observation is the presence of the second peak of apparent activation energy in the cases of Ores A and C, compared to Ore B, where this peak cannot be observed. Table 19 shows the values of apparent activation energies, resulting from the k-values of the JMA fitting procedure for the second and third terms of rate-limiting mechanisms. The k-values of the four best fitting temperatures were used for the determination of the apparent activation energy using the same principle as shown in Figure 57.

Table 19: Determined values of apparent activation energy from JMA model analysis for the different ores.[165]

kJ/mol	Ore A	Ore B	Ore C
E_{a2}	19.30	~ 0	47.42
E_{a3}	33.88	28.45	35.07

As shown, the apparent activation energy of the second term of Ore B, representing the controlling mechanism of reaction kinetics, is zero because of the nearly constant rate constants. As a result, only the limitation by nucleation is responsible for the value of the apparent activation energy regarding reduction from FeO to Fe. That is why the trend of apparent activation energy shows a constant level in that case. For the other two ores, both terms show values of apparent activation energy greater than 0. By means of the changing weight factor across the degree of reduction, the apparent activation energy also changes as a function of the degree of reduction. Generally, if more than one rate-limiting step acts at the same time, the apparent activation energy changes as a function of the conversion degree.

4.6 Variation of experimental parameters

In the following section, the effect of a variation of the process parameters on the progress of reduction is investigated, including changing the specific gas rate, the grain size of the iron ore particles and the addition of water vapor to the reducing gas mixture. The process parameters vary from the SRC, presented in Table 11. The variations of the SRC are given in the appropriate sections.

4.6.1 Specific gas rate

The specific gas rate is an important value for the reduction of iron oxides as it defines the required amount of reducing gas and therefore the efficiency of the process. In the following section, the effect of a higher specific gas rate, compared to the SRC, on the reducibility of Ore A is investigated. In this case, the specific gas rate (SGR) is defined as follows:

$$SGR\left(\frac{Nm^3\,H_2}{(t\cdot h)}\right) = \frac{\dot{V}_{H_2}\,(Nm^3/h)}{m_{Ore}\,(t)} \tag{51}$$

To achieve a higher SGR, the iron ore amount is partly substituted by SiO_2. Instead of 400 g of iron ore, only 230 g are charged into the reactor. SiO_2 is added to the system (130 g) to achieve a nearly constant sample volume in order to get similar fluidization conditions. The grain size of the silica is selected in such a way to have nearly the same minimum fluidization behavior as the iron ore itself. All other process parameters, such as hydrogen flow rate, remain similar to those for the SRC. This ends in a value of SGR of 4383 Nm³ H_2/t·h, which is higher by a factor of 1.74 compared to SRC, where the SGR is 2520 Nm³ H_2/t·h.

Figure 66 shows the progress of reduction obtained by using a higher SGR for Ore A at different reduction temperatures. The reduction sequence can again be divided into three stages; a fast initial reduction stage within a range of 10 and 20 % degree of reduction, followed by a nearly constant reduction rate until high conversion degrees and a low final reduction rate until achieving a complete reduction. The deceleration of the reduction rate again depends on reduction temperature while it takes place between 75 to 85 % degree of reduction. Higher values refer to higher reduction temperatures. Compared to higher SGR, the deceleration area is even smaller.
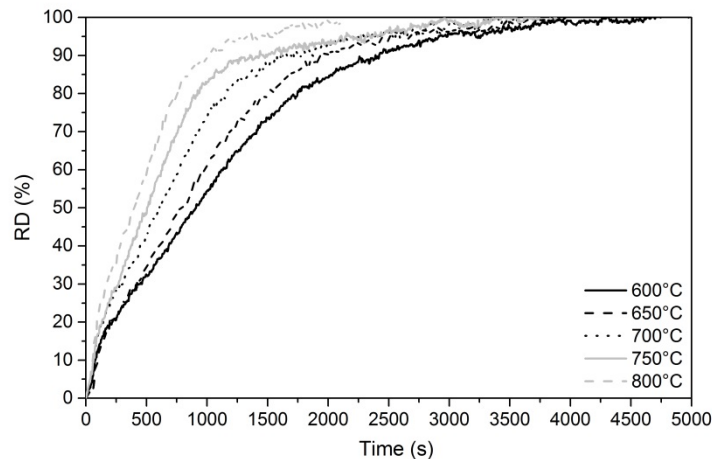
Figure 66: Progress of reduction with increased specific gas rate for Ore A at different reduction temperatures.[165]

Based on the experimental results, the trend of apparent activation energy against the degree of reduction is again determined for a higher SGR and compared with those with a lower SGR. The results are shown in Figure 67. A two-peak shaped curve of apparent activation energy can be observed. The differences compared to lower specific gas rate are

the positions and the heights of the first and second peaks. The height of the first peak decreases and the position moves to a higher value of degree of reduction. The height of the second peak also decreases but it moves to a lower degree of reduction value. An explanation will be given again after the kinetical analysis using the JMA model-fitting procedure.
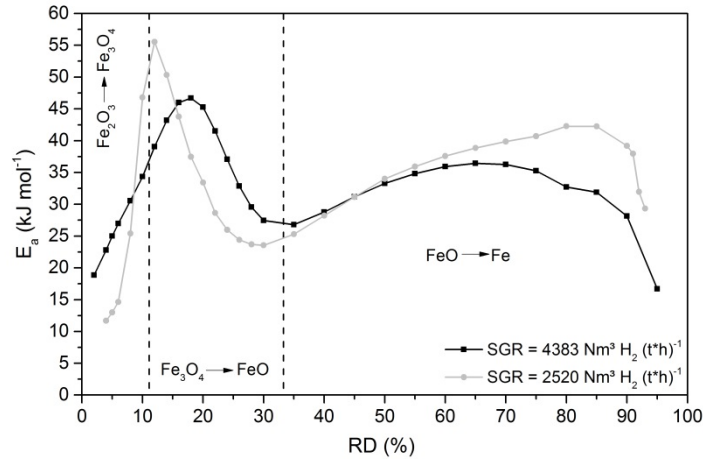
Figure 67: Trends of apparent activation energy as a function of the degree of reduction of Ore A for different specific gas rates.[165]

Figure 68 and Table 20 give the results of the fitting procedure using the JMA model for an increased specific gas rate of Ore A at different reduction temperatures. The initial stage of reduction is again controlled by the chemical reaction, represented by values of n_1 close to 1. A decrease in the n_1 value below 1 at higher reduction temperatures, as observed for a lower SGR, cannot be determined for a higher SGR.

The main difference between the progresses with higher SGR compared to lower SGR is the ratio between the limitation by the chemical reaction and that of nucleation. At a lower SGR, the reduction progress at lower temperatures is mainly controlled by a chemical reaction, while at the highest temperature, it is mainly controlled by the process of nucleation in the area of the reduction of FeO to Fe. At a higher SGR, the observed ratio changes occur in a similar way but they are not as drastic compared to a lower SGR. However, at low reduction temperatures, the limitation by the nucleation process is also present, while at the highest tested reduction temperature, the limitation by chemical reaction is present too. In case of a higher SGR, the sample input was only 230 g, compared to 400 g for a lower SGR. As a result, a lower particle surface area was available during the reduction experiments for a higher SGR. It seems that a lower value of available particle surface during reduction increases the influence of nucleation at low reduction temperatures. This can also be observed for Ore B compared to Ore A, where Ore B has a lower initial specific surface area. At higher temperatures, the system acts in the opposite direction because the chemical reaction proceeds fast and enough nuclei are formed. So it is again controlled by a combination of the chemical reaction and the nucleation process.

For the first peak of apparent activation energy, the influence of equilibrium gas composition is not as high as for a lower specific gas rate due to the smaller sample amount.

The peak height decreases and moves to a higher reduction extent. The final stage of reduction, with a very slow reduction rate, is only controlled by reaction kinetics, which can also be seen in Figure 68. The apparent activation energies determined by the fitting procedure for the second and third terms, representing limitation by chemical reaction and nucleation, are 8.18 and 36.76 kJ/mol, respectively, making the value of the chemical reaction lower than that with a higher specific gas rate (19.30 kJ/mol). This corresponds to the lower level of the second peak.
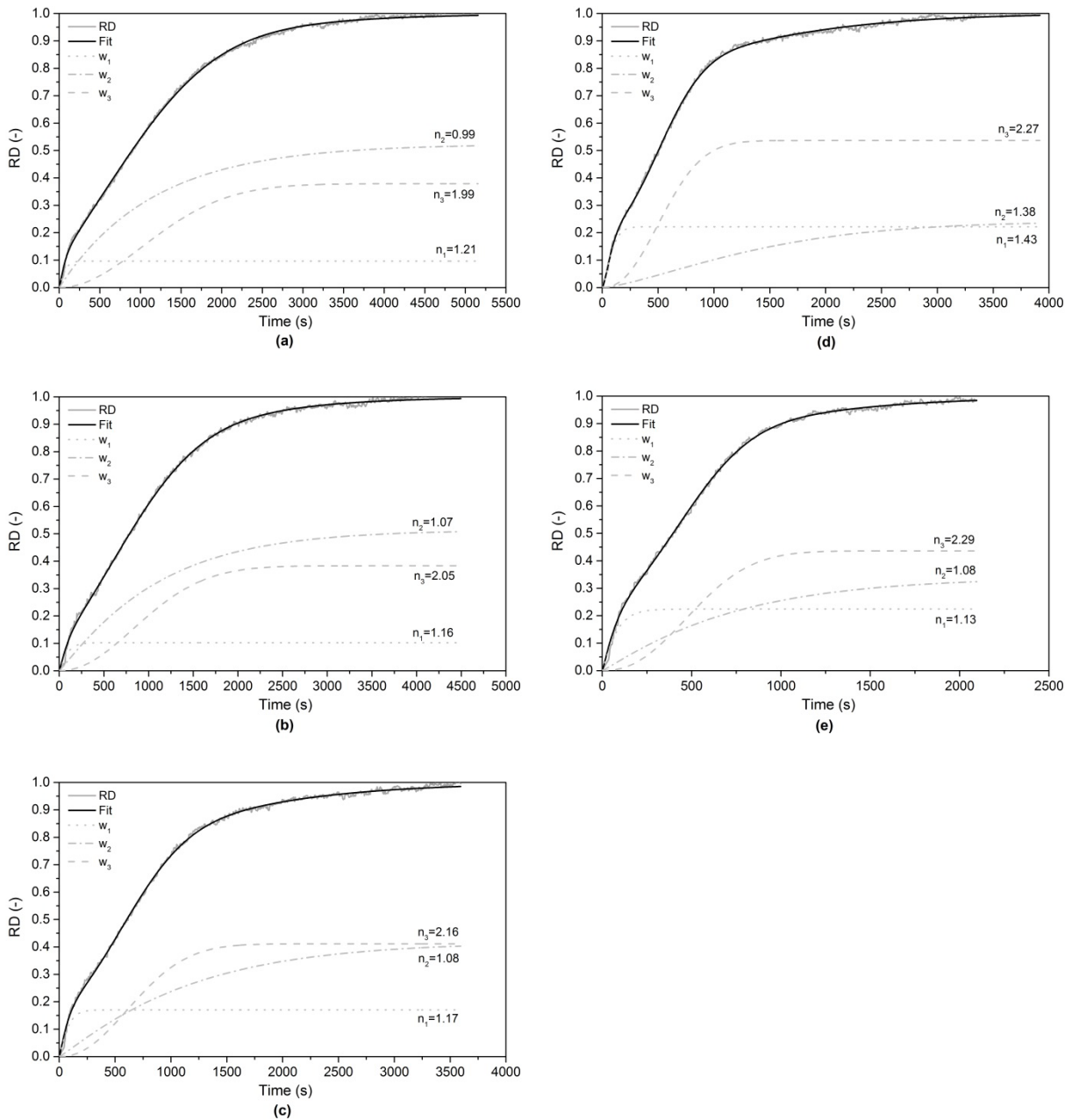
Figure 68: Kinetical investigation based on the JMA model (parallel) at different temperatures for an increased specific gas rate of Ore A: (a) 600 °C, (b) 650 °C [165], (c) 700 °C, (d) 750 °C. (e) 800 °C.

Table 20: Weight factors, nucleation rate constants, kinetic exponents, rate constants and RMSD for multistep kinetic analysis (parallel) at different temperatures for an increased specific gas rate of Ore A.[165]

Reduction temperature (°C)		600	650	700	750	800
Weight factors (-)	w_1	0.0967	0.1016	0.1706	0.2218	0.2245
	w_2	0.5242	0.5140	0.4179	0.2416	0.3393
	w_3	0.3791	0.3834	0.4115	0.5366	0.4362
Nucleation rate constants (s^{-1})	a_1	0.0059	0.0053	0.0063	0.0016	0.0072
	a_2	$9.22 \cdot 10^{-4}$	$5.54 \cdot 10^{-4}$	$4.69 \cdot 10^{-4}$	$3.95 \cdot 10^{-5}$	$8.25 \cdot 10^{-4}$
	a_3	$5.26 \cdot 10^{-7}$	$5.26 \cdot 10^{-7}$	$5.26 \cdot 10^{-7}$	$4.26 \cdot 10^{-7}$	$4.26 \cdot 10^{-7}$
Kinetic exponents (-)	n_1	1.21	1.16	1.17	1.43	1.13
	n_2	0.99	1.07	1.08	1.38	1.08
	n_3	1.99	2.05	2.16	2.27	2.29
Rate constants (s^{-1})	k_1	0.0145	0.0109	0.0128	0.0108	0.0126
	k_2	$8.63 \cdot 10^{-4}$	$9.03 \cdot 10^{-4}$	$8.53 \cdot 10^{-4}$	$6.47 \cdot 10^{-4}$	$1.36 \cdot 10^{-3}$
	k_3	$6.92 \cdot 10^{-4}$	$8.70 \cdot 10^{-4}$	$1.23 \cdot 10^{-3}$	$1.55 \cdot 10^{-3}$	$1.67 \cdot 10^{-3}$
Root mean square deviation	RMSD	0.0088	0.0105	0.0084	0.0083	0.0086

4.6.2 Variation in grain size

The grain size of the particles used during hydrogen-induced fluidized bed reduction is of great importance. On the one hand, the particle grain size has a big influence on the fluidization parameters; on the other hand it can play an important role for the kinetics during the reduction. The effect of the grain size is shown below with only one example. Therefore, Ore B particles with a grain size of 125 to 250 μm are reduced with similar conditions (SRC) as explained above at a reduction temperature of 750 °C. Figure 69 (left) shows the resulting degree of reduction compared with those of bigger particle size (250-500 μm). As shown, the progress of reduction is similar until high conversion degrees. The only difference is the final reduction stage. In the case of lower grain size, a complete reduction can be achieved earlier because the deceleration of the reduction rate appears at a higher degree of reduction while the difference is not pronounced. The reason for the nearly same reduction behavior is of course that the limiting steps during the reduction do not occur on a particle scale. They occur in a smaller scale inside the particle, which is more or less independent of the particle size, especially at the given tested grain sizes for porous ores. Figure 69 (right) shows the results of the model-fitting procedure using the JMA model.
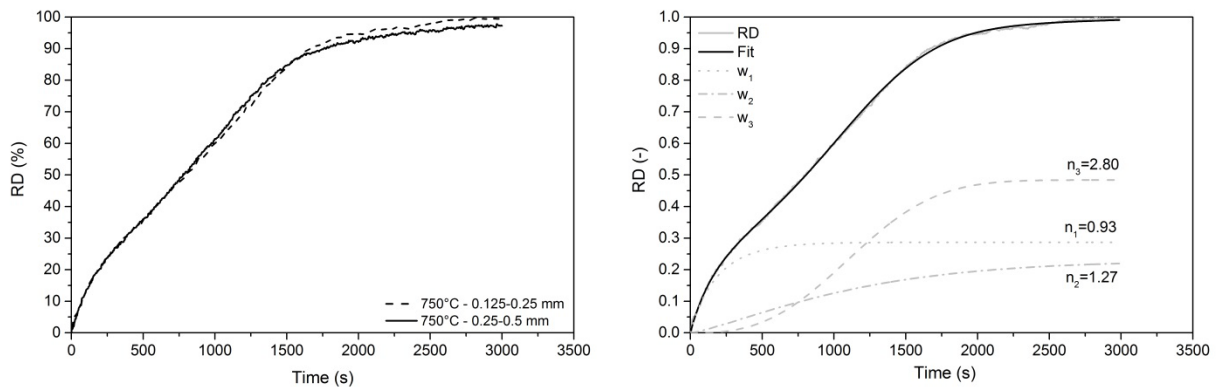
Figure 69: Effect of grain size variation on the reduction progress of Ore B at a reduction temperature of 750°C: left- progress of reduction; right- results of the JMA fitting procedure.

Table 21 shows the values obtained from the fitting procedure; those for the larger grain size are also shown for comparison reasons. In principle, the results are quite similar. Concerning the resulting rate constants, the main difference can be seen for the values of the second term. In case of a lower grain size, the rate constant is much bigger. This is a hint for a faster chemical reaction because of the smaller particle size, especially at the end of the reduction procedure.

Table 21: Weight factors, nucleation rate constants, kinetic exponents, rate constants and RMSD for multistep kinetic analysis (parallel) for different grain sizes of Ore B at 750 °C reduction temperature.

Grain size (mm)		0.25-0.5	0.125-0.25
Weight factors (-)	w_1	0.2787	0.2869
	w_2	0.2579	0.2290
	w_3	0.4634	0.4841
Nucleation rate constants (s^{-1})	a_1	0.0044	0.0075
	a_2	$1.29 \cdot 10^{-4}$	$1.22 \cdot 10^{-4}$
	a_3	$2.07 \cdot 10^{-9}$	$2.07 \cdot 10^{-9}$
Kinetic exponents (-)	n_1	1.03	0.93
	n_2	1.22	1.27
	n_3	2.84	2.79
Rate constants (s^{-1})	k_1	0.005	0.005
	k_2	$6.42 \cdot 10^{-4}$	$8.37 \cdot 10^{-4}$
	k_3	$8.66 \cdot 10^{-4}$	$7.81 \cdot 10^{-4}$
Root mean square deviation	RMSD	0.0040	0.0055

It is clear that the results obtained in this section are not enough to give general statements regarding the effect of the grain size on the reduction behavior of iron ores during hydrogen-induced fluidized bed reduction, but it seems that the effect is not really significant, especially at the initial and intermediate stages of reduction. Further investigations are required concerning different reduction temperatures, different iron ores and a further variation in the grain size.

4.6.3 Addition of water vapor to the reducing gas mixture

Water vapor in the reducing gas mixture can lead to a deceleration of the reduction rate. On the one hand it reduces the reduction potential of the gas mixture; on the other hand there is a possibility that the water vapor blocks free reaction places, as it is explained in Section 2.3.2.3. In the following section, different tests for Ore A with the addition of water vapor are done and compared with the results without any water vapor addition. The addition of water vapor is done in two different ways. First, the hydrogen flow rate is kept constant by a partial substitution of nitrogen by water vapor (Case 1); second, water vapor is added by a simultaneous increase in the hydrogen flow rate in order to achieve the same possible hydrogen utilization of the gas mixture, ending in a higher superficial gas velocity compared to those without water vapor addition (Case 2). Table 22 summarizes the process conditions of the experiments for Cases 1 and 2.

Table 22: Summary of the process conditions for the addition of water vapor for the reduction of Ore A at 700 °C reduction temperature.

	Case 1	Case 2
H_2 (%-vol.)	65	60.5
H_2O (%-vol.)	2	4.5
N_2 (%-vol.)	33	35
Flow rate (l/min-SATP)	25.9	34.1
GOD (-)	0.03	0.07
u_0 (m/s)	0.39	0.51

Figure 70 shows the results of the reduction experiments compared with those from the experiment without water vapor addition. As shown, only the addition of water vapor (Case 1-solid gray line) does not lead to a big difference in terms of overall reduction rate. Between 30 and 80 % degree of reduction, the reduction rate is slightly lower compared to the experiment without water vapor addition. This can be linked to the lower reduction potential of the reducing gas mixture. During the final stage of reduction, the reduction rate is quite similar, which ends in nearly the same required reduction time for a complete reduction. As a result, a small amount of water vapor addition to the reducing gas mixture does not have a big influence on the overall reduction rate. For the other test, representing a reducing gas mixture with the same reduction potential compared to the gas mixture without water vapor addition (Case 2), the reduction until 30 % degree of reduction occurs faster (dashed gray line). The reason is the higher reduction potential during the reduction to FeO because it is fixed that the gas mixture has the same reduction potential during reduction from FeO to Fe. The reduction rate between 30 and 80 % degree of reduction is slightly lower although the reduction potential is the same. During the final stage of reduction, it takes more time to achieve a complete reduction. In that case, it seems that the addition of water vapor still has an influence on the reduction rate. It has to be kept in mind, however, that the general process parameters such as superficial gas velocity are different to achieve the same reduction potential, which may influence the fluidization behavior. The contact time between gas and solids is also reduced.
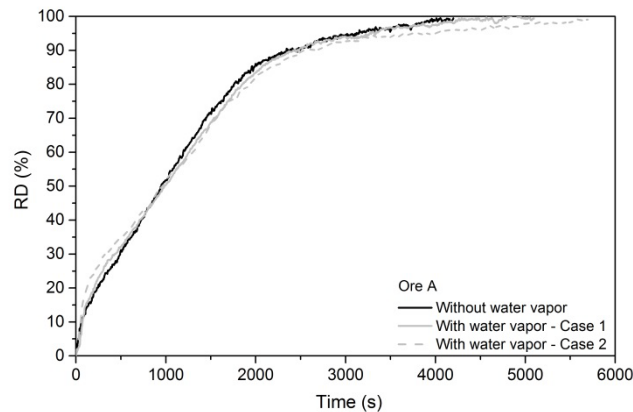
Figure 70: Effect of water vapor addition on the reduction rate of Ore A at a reduction temperature of 700 °C.

To explain the differences in more detail, the JMA fitting procedure for the experiments with water vapor addition is performed. The results are given in Figure 71 and Table 23. As shown, the reduction from FeO to Fe is again controlled by a mixture of chemical reaction and nucleation. The main differences can be defined as lower rate constants for the second and third terms, representing a chemical reaction and nucleation, respectively. The values for the rate constant of the chemical reaction decrease in terms of water vapor addition, while they are even lower in case of the same reduction potential, which explains the difference in the longer reduction time required for a complete reduction. The rate constants for the nucleation process are similar for both cases of water vapor addition, but the values are lower compared to that without water vapor addition, which is mainly responsible for the lower reduction rate between 30 and 80 % degree of reduction. The initial stage of reduction is always controlled by the chemical reaction, represented by kinetic exponents close to 1.
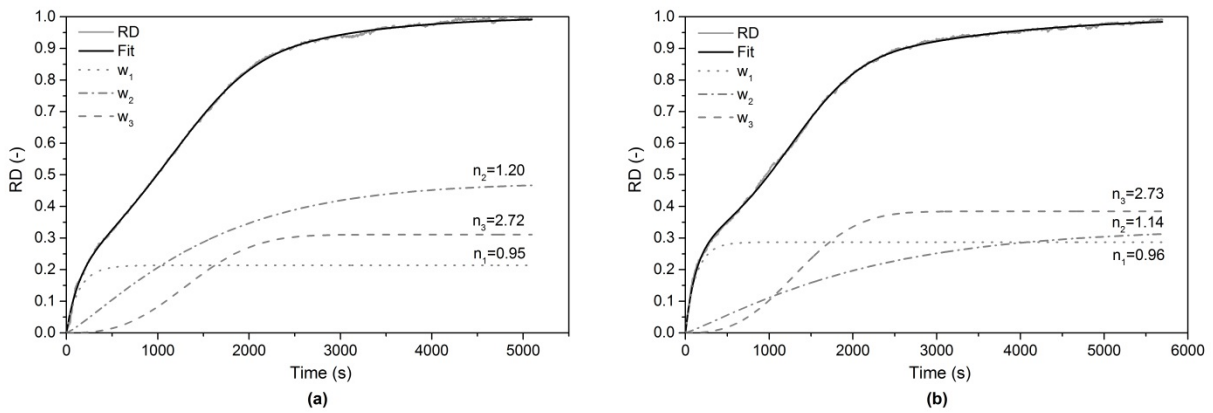
Figure 71: Results obtained by the JMA fitting procedure for the investigation of the effect of water vapor addition on the reduction progress of Ore A at a reduction temperature of 700 °C.

Table 23: Weight factors, nucleation rate constants, kinetic exponents, rate constants and RMSD for multistep kinetic analysis (parallel) for the addition of water vapor to the reducing gas mixture during the reduction of Ore A at 700 °C.

		SRC	Case 1	Case 2
Weight factors (-)	w_1	0.1379	0.2137	0.2870
	w_2	0.6277	0.4755	0.3286
	w_3	0.2344	0.3108	0.3844
Nucleation rate constants (s^{-1})	a_1	0.0109	0.0089	0.0093
	a_2	$1.40 \cdot 10^{-4}$	$1.46 \cdot 10^{-4}$	$1.55 \cdot 10^{-4}$
	a_3	$2.07 \cdot 10^{-9}$	$2.07 \cdot 10^{-9}$	$2.07 \cdot 10^{-9}$
Kinetic exponents (-)	n_1	1.05	0.95	0.96
	n_2	1.22	1.20	1.14
	n_3	2.76	2.72	2.73
Rate constants (s^{-1})	k_1	0.01383	0.00726	0.00781
	k_2	$6.99 \cdot 10^{-4}$	$6.26 \cdot 10^{-4}$	$4.62 \cdot 10^{-4}$
	k_3	$7.31 \cdot 10^{-4}$	$6.50 \cdot 10^{-4}$	$6.52 \cdot 10^{-4}$
Root mean square deviation	RMSD	0.0049	0.0054	0.0051

As a conclusion, the addition of little amounts of water vapor does not lead to a drastic deceleration in the reduction rate in case of hydrogen-induced fluidized bed reduction with the given process conditions while an effect on the rate constant of the chemical reaction can

be observed. In fact, further investigations are required to clarify the behavior in more detail. One interesting parameter is, for example, the reduction temperature, which is fixed to 700 °C in the present case. Changing the reduction temperature might also influence the effect of the addition of water vapor on the reduction rate. Other parameters which should be investigated are the effects on the reducibility of different iron ores, different amounts of water vapor addition and different fluidization conditions such as different superficial gas velocities.

4.7 Kinetic investigation of pre-reduction steps

The last investigations carried out in this section are concerning the different pre-reduction steps during iron oxide reduction, which is of importance for a stepwise reduction of iron oxides in industrial applications in separate aggregates. For example, a stepwise reduction is typically carried out in a multi-stage fluidized bed reactor cascade such as that used within the Finmet® process. Pre-reduction steps represent the reduction from hematite to magnetite and to wüstite. To achieve a reduction to the defined oxide, the temperature and GOD must be in the stability area of the corresponding oxide. Figure 72 shows the process conditions of the experiments within the Baur-Glässner diagram which are summarized also in Table 24. The flow rate of water vapor is fixed to 5.2 l/min (SATP) for all experiments. This value was used because it represents the maximum possible water vapor flow rate, limited by the reduction apparatus. All experiments in this section are done using Ore A with a grain size between 250 and 500 μm. For the reduction series from hematite to magnetite, the GOD was defined to be 0.25 for a temperature range from 450 to 550 °C. For the reduction from hematite to wüstite a GOD of 0.4 was used in a temperature range between 750 and 850 °C.
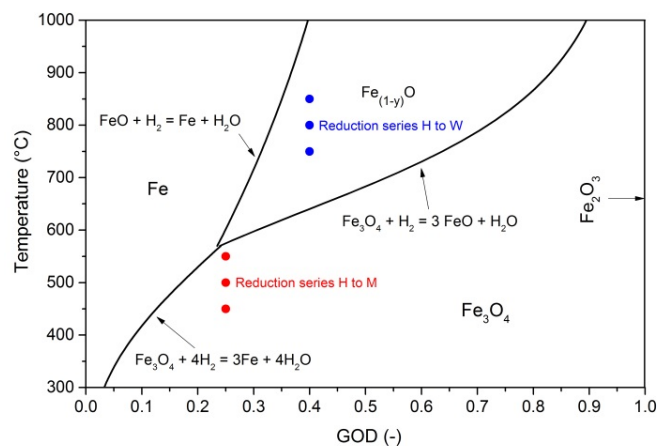
Figure 72: Baur-Glässner diagram for the Fe-O-H$_2$ system showing the process conditions for the investigation of different reduction steps.

Below, the JMA model fitting is carried out to define the rate-limiting steps depending on the reduction temperature for the different pre-reduction steps.

Table 24: Process conditions for the investigations of the pre-reduction steps.

Reduction sequence	H to M	H to W
H_2 (%-vol.)	57.6	33.9
H_2O (%-vol.)	19.2	22.6
N_2 (%-vol.)	23.2	43.5
Flow rate (l/min-SATP)	27.5	23.0
T (°C)	450-550	750-850
GOD (-)	0.25	0.40
u_0 (m/s)	0.31-0.35	0.36-0.40

4.7.1 Reduction from hematite to magnetite

As stated previously, the reduction form hematite to magnetite was carried out with a GOD of 0.25 in a temperature range between 450 and 550 °C. Figure 73 shows the progresses of reduction at different temperatures including the results from the JMA fitting procedure. Instead of the degree of reduction, the conversion is used on the ordinate. A conversion of 1 represents a complete conversion from hematite to magnetite in this case. Table 25 shows the values obtained by the fitting procedure. Two rate-limiting mechanisms are enough to describe the reduction process accurately. As shown, at the lowest reduction temperature (450 °C), the progress of reduction is controlled by the chemical reaction until a conversion degree of approximately 0.6. After that, nucleation becomes rate-limiting until a complete conversion is achieved. A similar behavior can be observed for the next temperature tested (500 °C). Two main differences can be observed compared to 450 °C reduction temperature. First, the conversion degree where the nucleation becomes rate-limiting is shifted to higher values (approximately 0.65); second, the kinetic exponent of the second term decreases from 2.56 to 1.81 with increasing temperatures, representing a change from increasing nucleation rate to a decreasing nucleation rate. For the highest tested reduction temperature (550 °C), the progress of reduction can be explained by a limitation by the chemical reaction only. As a result, an increasing temperature decreases the effect of nucleation during the reduction from hematite to magnetite.
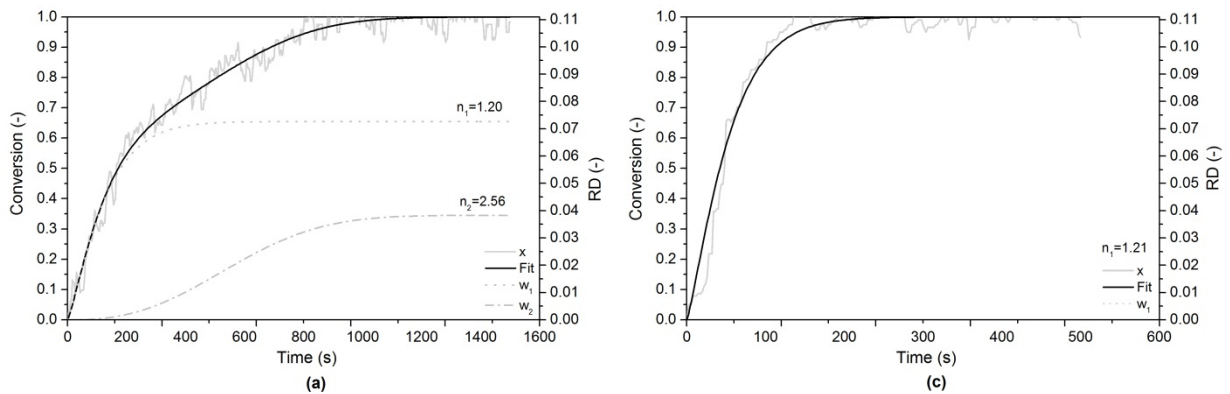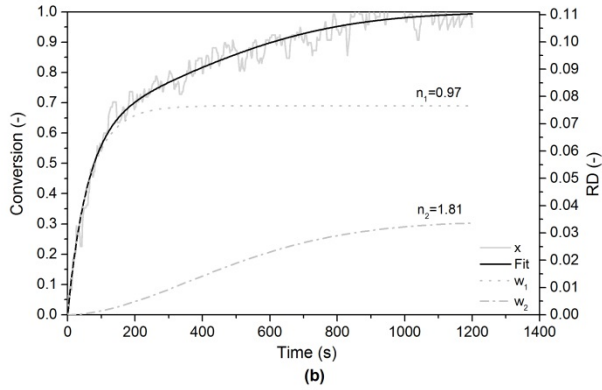
Figure 73: JMA fitting procedure for the investigation of the reduction from hematite to magnetite of Ore A at different temperatures: (a) 450 °C; (b) 500 °C; (c) 550 °C.

The resulting rate constants for the first and second terms increase with rising temperatures, ending in values of apparent activation energies, determined from the results of the fitting procedure, of 42.4 and 10.2 kJ/mol, respectively. Compared to the trend of apparent activation energy against the degree of reduction for Ore A, shown in Figure 50, the values are in good agreement (between 0-11% degree of reduction) with that defined in the current case.

Table 25: Weight factors, nucleation rate constants, kinetic exponents, rate constants and RMSD for multistep kinetic analysis (parallel) for the investigation of hematite to magnetite reduction of Ore A at different temperatures.

Reduction temperature (°C)		450	500	550
Weight factors (-)	w_1	0.6547	0.6905	1.0000
	w_2	0.3453	0.3095	0.0000
Nucleation rate constants (s^{-1})	a_1	0.0029	0.0181	0.0075
	a_2	$6.86 \cdot 10^{-8}$	$1.07 \cdot 10^{-5}$	-
Kinetic exponents (-)	n_1	1.20	0.97	1.21
	n_2	2.56	1.81	-
Rate constants (s^{-1})	k_1	0.0076	0.0159	0.0177
	k_2	0.0016	0.0018	-
Root mean square deviation	RMSD	0.0361	0.0341	0.0435

4.7.2 Reduction from hematite to wüstite

The reduction form hematite to wüstite is carried out with a GOD of 0.40 in a temperature range between 750 and 850 °C. Figure 74 shows the progress of the reduction and the results of the JMA fitting procedure. Again, the conversion is used on the ordinate, while a conversion of 1 represents a complete reduction from hematite to wüstite and a conversion of 0.3 represents a complete reduction from hematite to magnetite. In this case, three terms of rate-limiting mechanisms are used because of the fact that two reduction reactions occur, from hematite to magnetite and from magnetite to wüstite. The results from the fitting procedure show that the initial stage of reduction, representing the reaction from hematite to

magnetite, is controlled by the chemical reaction only, at all temperatures tested. The further progress of reduction is controlled by a mixture of chemical reaction and nucleation for the reduction temperatures of 750 and 800 °C. At the highest temperature tested, the later stage of reduction is only controlled by the nucleation process.

As a result, different pre-reduction temperatures lead to different rate-limiting mechanisms. This can be observed for the reduction from hematite to wüstite and for the reduction from hematite to magnetite. Different rate-limiting steps occurring during the pre-reduction will lead to different textures and morphologies of the pre-reduction product, which might influence the reducibility during further reduction to metallic iron. The effect of different pre-reduction conditions on the reducibility was investigated by Thurnhofer et al. [143], as already mentioned in previous sections. They found that the pre-reduction has a significant influence on the texture and morphology of the product, which influences the reducibility during further reduction to metallic iron. This is why the conditions during pre-reduction have to be kept in mind to guarantee the best conditions for the final reduction and ensure the highest possible process efficiency.
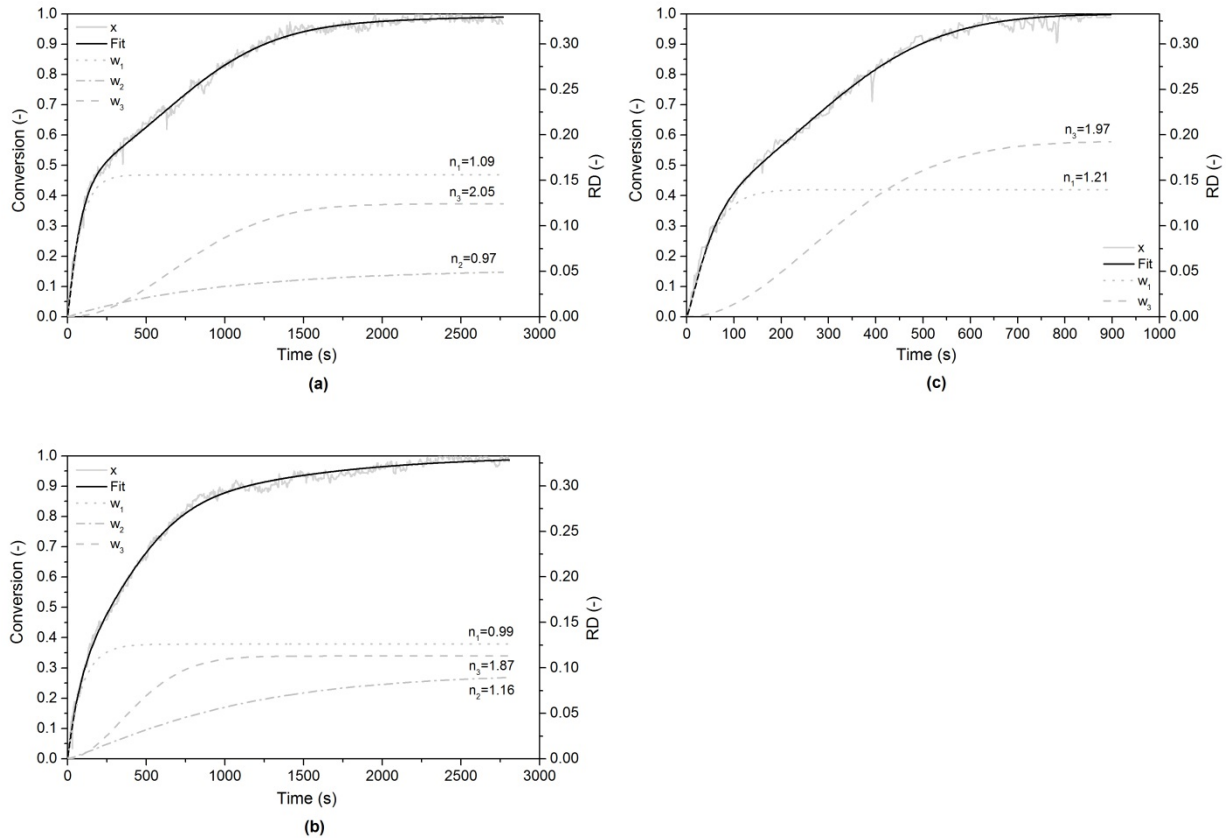
Figure 74: JMA fitting procedure for the investigation of the reduction from hematite to wüstite of Ore A at different temperatures: (a) 750 °C; (b) 800 °C; (c) 850 °C.

Table 26: Weight factors, nucleation rate constants, kinetic exponents, rate constants and RMSD for multistep kinetic analysis (parallel) for the investigation of hematite to wüstite reduction of Ore A at different temperatures.

Reduction temperature (°C)		750	800	850
Weight factors (-)	w_1	0.4688	0.3790	0.4199
	w_2	0.1579	0.2816	0.0000
	w_3	0.3732	0.3393	0.5801
Nucleation rate constants (s^{-1})	a_1	0.0082	0.0110	0.0082
	a_2	0.0013	$3.20 \cdot 10^{-4}$	-
	a_3	$8.60 \cdot 10^{-7}$	$8.49 \cdot 10^{-6}$	$8.32 \cdot 10^{-6}$
Kinetic exponents (-)	n_1	1.09	0.99	1.21
	n_2	0.97	1.15	-
	n_3	2.05	1.87	1.97
Rate constants (s^{-1})	k_1	0.0120	0.0107	0.0185
	k_2	0.0010	$9.39 \cdot 10^{-4}$	-
	k_3	0.0011	0.0020	0.0027
Root mean square deviation	RMSD	0.0138	0.0144	0.0180

5 Use of magnetite-based iron ore for hydrogen-induced fluidized bed reduction

Aside from hematite-based iron ores, the occurrence of magnetite-based ores is also very common in nature. The use of magnetite-based ores during hydrogen-induced fluidized bed reduction is therefore of great interest. There are two major problems regarding the direct use of magnetite-based iron ores for fluidized bed reduction: the first one is the poor reducibility compared to other ore types because of the dense structure of such ores; the second one is the poor fluidization behavior due to the high sticking tendency, as shown in Section 4.5. In the following section, different influencing parameters on the fluidization and reduction behavior of magnetite-based ores are investigated. The first point is the effect of a prior oxidation. The oxidation of magnetite based ores to Fe_2O_3 is a major issue for possible industrial hydrogen-induced fluidized bed reduction processes. The reason for this is the endothermic behavior of the reduction reactions using hydrogen as a reducing agent. Consequently, it is necessary to ensure a sufficient energy supply to the reduction system, for example by pre-heating the iron ore before the reduction sequence. Generally, it does not make sense to operate the pre-heating procedure under inert atmosphere. The magnetite-based iron ore will start to oxidize at a certain temperature, given by the following reaction:

$$2Fe_3O_4 + \frac{1}{2}O_2 \rightarrow 3Fe_2O_3 \quad \Delta H_{25°C} = -242.5 \; kJ \tag{52}$$
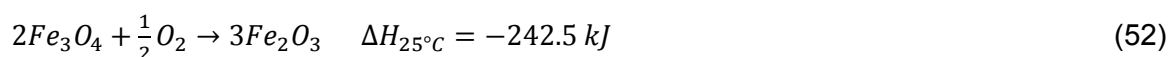
As shown, the oxidation reaction is exothermic, which ends in the production of heat. This is quite beneficial for the pre-heating procedure because the primary energy input can be reduced. That is the reason why the investigations of the effect of a prior oxidation on the reduction and fluidization behavior are carried out.

The second point investigated is the effect of MgO on the fluidization and reduction behavior. The addition of MgO to the iron ore can have an influence on the occurrence of the sticking phenomena and on the reducibility. Therefore, experiments with different amounts of MgO addition are done. In the end, a concept for a successful hydrogen-induced fluidized bed reduction of magnetite-based iron ores is presented.

5.1 Experimental conditions and materials

For the experimental work, the fluidized bed reactor with an inner diameter of 68 mm is used, as explained in Section 3.1.1. The process conditions are a little bit different from those used for the experiments described in Section 4, which are defined as standard reduction conditions (SRC). The main differences are the grain size distribution, which is in the range of 125 to 500 μm in the present case, and the fact that the superficial gas velocity was kept constant at 0.4 m/s for all different temperatures. This is achieved by a constant hydrogen flow rate, balanced by different nitrogen flow rates. The reason for keeping the gas velocity constant is that the main focus is now on the fluidization behavior, in contrast to previous experiments, where the focus was on the reducibility. Table 27 summarizes the process parameters of the reduction experiments.

Table 27: Summary of the process parameters for the reduction experiments with magnetite-based ores.

Sample mass iron ore (g)	400
Grain size iron ore (mm)	0.125–0.5
Temperature (°C)	600–800
Gas components	H_2, N_2
Flow rate H_2 (l/min-STAP)	15.9
Gas velocity (m/s)	0.4

The grain size distribution of the iron ore consists of 50 %-wt. 125–250 μm and 50 %-wt. 250–500 μm. The chemical analyses of the magnetite-based iron ore used in its natural and oxidized state are shown in Table 28. The iron content after oxidation is lower because of the higher oxygen content in the sample. The oxidation procedure takes place in a heat treatment furnace at a temperature of 1000 °C. To ensure a complete oxidation of the particles, the residence time of the particles at high temperatures is chosen to be in between 5-6h, and every 30 min, the door of the furnace is opened to exchange the atmosphere and provide a sufficient amount of oxygen. The principal oxidation of magnetite to Fe_2O_3 has been investigated by many different authors.[176–180] They all found that the kinetics of the oxidation procedure strongly depends on the temperature, while a higher temperature is preferable to achieve high conversion degrees in an acceptable time. That is the reason for choosing such a high oxidation temperature and long residence time.

To investigate the effect of MgO on the reduction and fluidization behavior, MgO powder with high purity is added to the iron ore (>99.5 %-wt. MgO). The size of the MgO particles is mesh -325, representing 100 %-wt. below 44 μm. The MgO is mixed with the iron ore before charging the material into the reactor. Mixing takes place in such a way that the iron ore particles are totally covered by the MgO fines.

Table 28: Chemical composition of the input materials used.

Species	Composition %-wt.			
	Fe_{tot}	Fe^{2+}	SiO_2	MgO
Iron ore– natural	59.5	19.66	7.05	
Iron ore– oxidized	57.8	0.39	6.84	
MgO additive				>99.5

Figure 75 and Figure 76 show SEM- surface images of the iron ore in its natural state and in oxidized state. The surface images of the natural magnetite demonstrate that the particle surface is not smooth; sharp edges can be observed. The reason for this might be that the fine particles are produced by a crushing procedure of lump ore. It seems that the particles break along these edges, a hint about the brittle character of the magnetite. After oxidation, the particle surface appears smoother. The structure observed in natural state cannot be found anymore after oxidation, but as shown, small cactus-like needles can be observed on the surface of the oxidized particles. Song et al.[181] detected a formation of hematite whiskers during the oxidation of magnetite fines. This might also be the reason for the formation of this cactus-like structure which may consist of hematite needles.
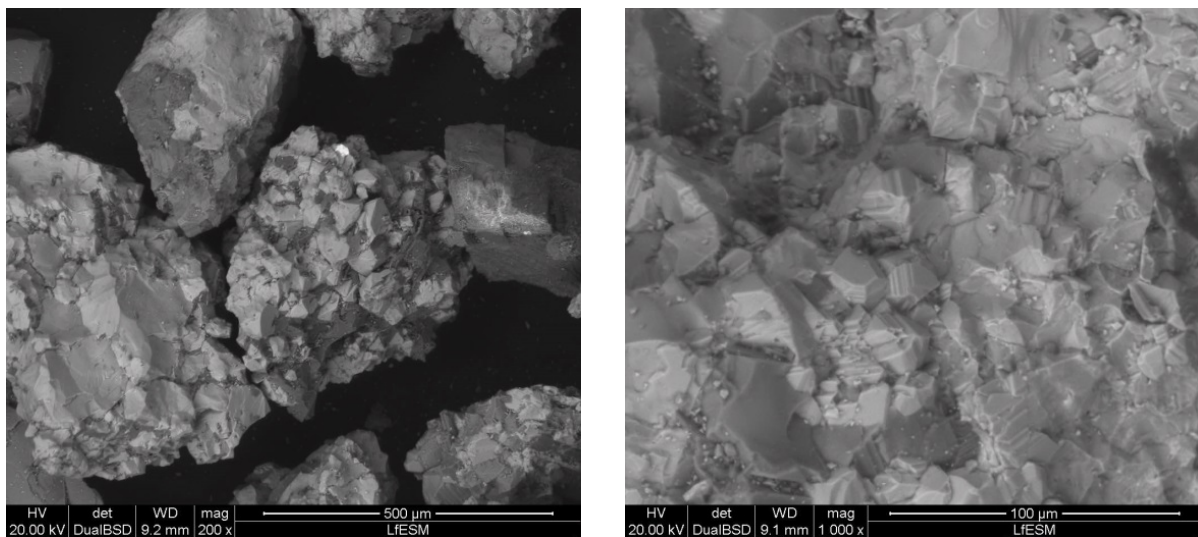
Figure 75: SEM surface images of the magnetite-based iron ore used in natural state with different magnifications.
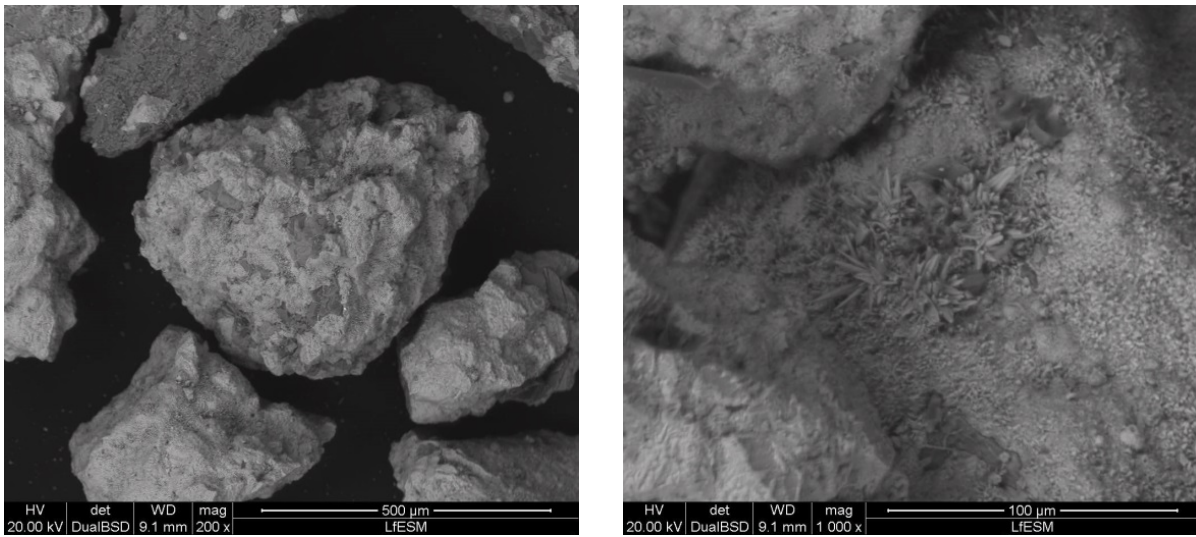
Figure 76: SEM surface images of the magnetite-based iron ore used in oxidized state with different magnifications.

For the reduction experiments, two abort criteria are defined. The first one is a complete reduction in the case of no fluidization troubles; the second one is a complete de-fluidization of the material. The state of de-fluidization is defined by the pressure drop measured across the material. If the value fits the theoretical pressure drop of the material in completely fluidized state, it is defined as fully fluidized. If there are deviations between these two values, the status is defined as partly or completely de-fluidized. For that reason, a de-fluidization index (DFI) is implemented, defined as follows:

$$DFI \ (\%) = \frac{(\Delta p_{Bed-theoretical} - \Delta p_{Bed-measured})}{(\Delta p_{Bed-theoretical} - \Delta p_{Fixed\ bed})} \cdot 100 \qquad (53)$$

A value for DFI of 0 therefore represents a complete fluidization; a value of 100 represents a complete de-fluidization, while all other values in between give the percentage of de-fluidized material. The value of $\Delta p_{Fixed-bed}$ is defined as pressure drop, occurring after complete de-fluidization under given process conditions. It is defined that values of $\Delta p_{Bed} \leq 2$ mbar refer to a fixed bed, which means that if the measured pressure drop across the bed is lower than 2 mbar, the material is not in fluidized state anymore and the DFI becomes 100 %. A value of 2 is chosen because of the observations of the fluidized bed reactor. If the material is in fluidized state, the reactor shows a short movement. In case of a fixed bed, this movement cannot be observed anymore. As a critical value, 2 mbar of pressure drop across the bed material is observed.

5.2 Results obtained from reduction experiments

In what follows, the results obtained from the reduction experiments are shown and discussed in case of using the natural magnetite-based ore, the oxidized ore and the effect of the addition of different additives to the ore. The trends of degree of reduction and pressure drop against reduction time are shown and compared.

5.2.1 Fluidization behavior of untreated magnetite during reduction by hydrogen

First, the fluidization and reduction behavior of the natural magnetite is tested which should serve as a reference for all further investigations. In this case, five different temperatures are used: 600, 625, 650, 700 and 800 °C. Figure 77 shows the results of the reduction experiments including the degree of reduction and metallization, DFI and the behavior of the pressure drop across the material against reduction time.

In the present, the curve of the degree of reduction always starts at 11 % because magnetite is defined to already have a reduction degree of 11 %. For the lowest temperature tested, representing 600 °C, it can be seen, that a complete reduction is achieved after approximately 110 min, although a partial de-fluidization of the material starts at a degree of reduction of 35 %, indicated by the behavior of the pressure drop and the DFI. As a result, the reduction proceeds even after some of the material is not in fluidized state. At the end of the reduction experiment, approximately half of the material is fluidized and half of the material is de-fluidized. The measurement can be confirmed during the discharging procedure. Half of the material leaves the reactor only by tilting it; the other half sticks inside the reactor, which clearly indicates the partial de-fluidization. At the next temperature tested, 625 °C, a slow de-fluidization takes place, ending in a complete de-fluidization of the whole material. The DFI indicates that the de-fluidization already starts at a degree of reduction of approximately 20 %. Taking the necessity of the presence of metallic iron for the sticking phenomenon into account, it can be assumed that the formation of metallic iron already starts before the reduction to wüstite is completed. This can be related to the dense structure of the original magnetite ore. At complete de-fluidization, a degree of reduction of approximately 95 % is achieved. Compared to 600 °C reduction temperature, the de-fluidization takes place more rapidly. A further increase in the reduction temperature leads to faster de-fluidization of the material. At 650 °C, a complete de-fluidization is observed at a degree of reduction of approximately 60 %. At 700 °C, it is only 30 % and at 800 °C, the degree of reduction is even below 30 %. However, the effect of reduction temperature on the de-fluidization behavior can be clearly confirmed.

(a)

(b)

(c)

(d)

(e)
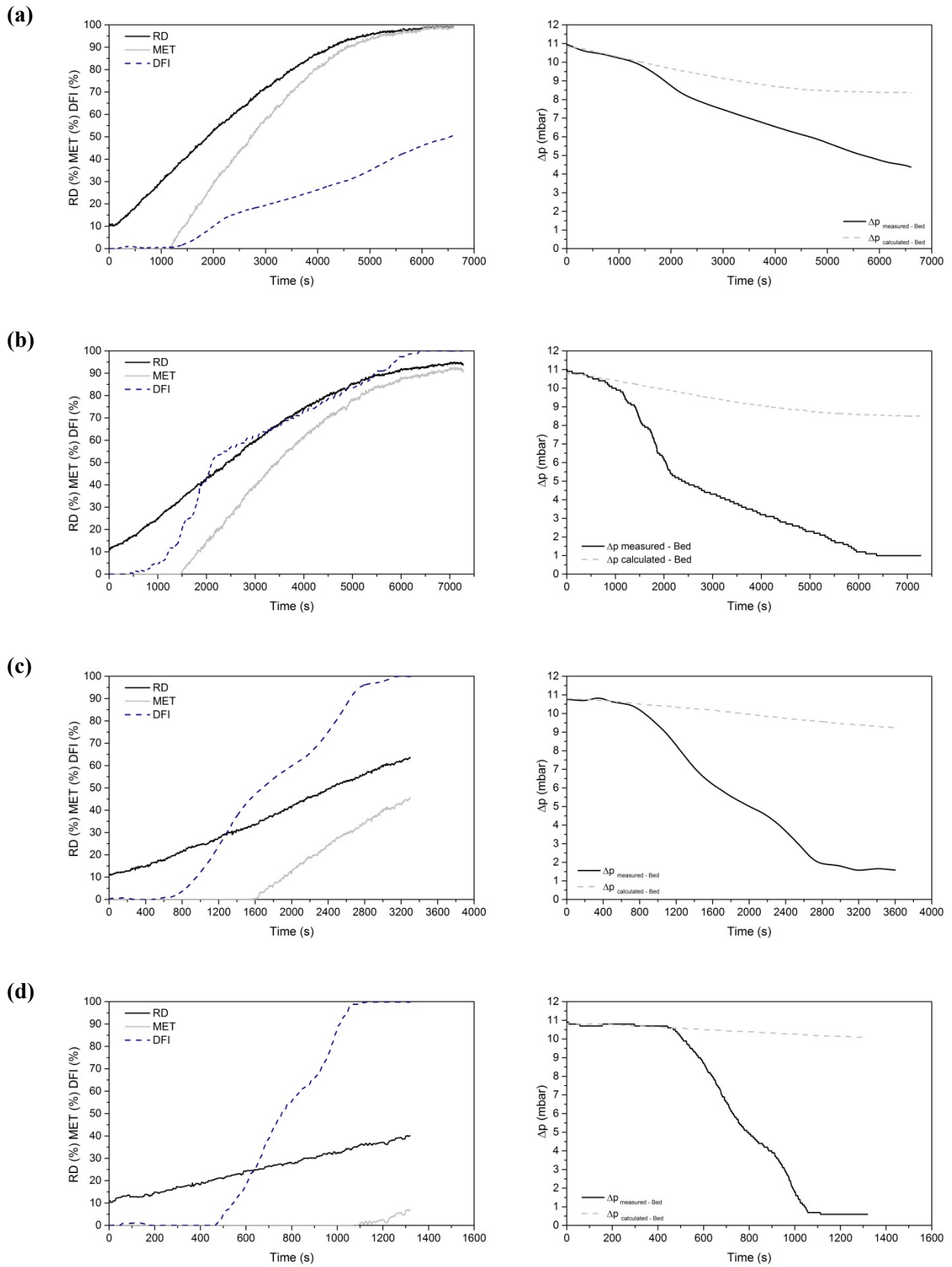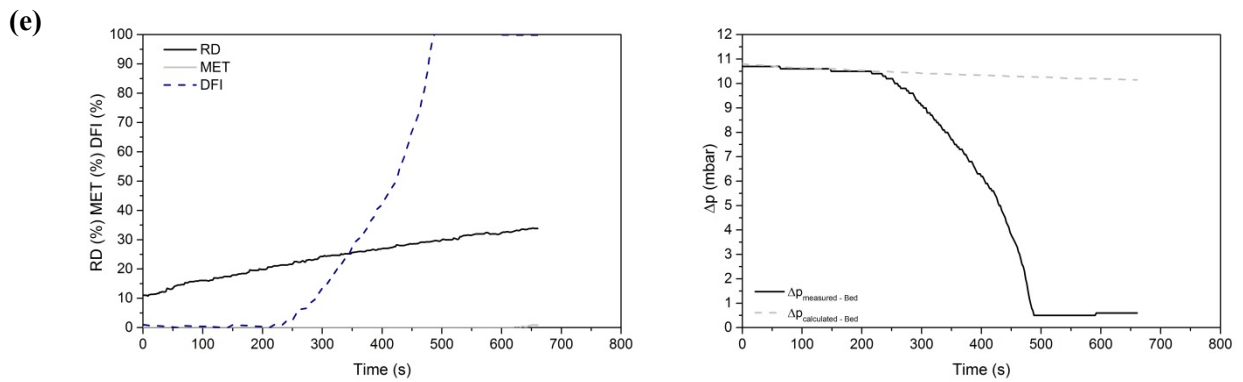
Figure 77: Behavior of magnetite during hydrogen-induced reduction concerning reducibility and fluidization behavior at different temperatures: (a) 600 °C; (b) 625 °C; (c) 650 °C; (d) 700 °C; (e) 800 °C.

Figure 78 (left) shows the plot of DFI against the degree of reduction for different reduction temperatures. Only for a reduction temperature of 600 °C can a complete reduction be achieved before the complete de-fluidization of the material takes place. For all other temperatures, the complete de-fluidization occurs before the complete reduction could be attained, while the degree of reduction reached decreases with increasing reduction temperatures. Based on this information, a fluidization regime diagram is defined, shown in Figure 78 (right). Three different areas are defined; a complete fluidization area, a de-fluidization area and an area where the material is completely de-fluidized. As shown, the de-fluidization starts at nearly the same reduction extent for temperatures > 625 °C. Only for the 600 °C reduction temperature, the degree of reduction where the de-fluidization starts is clearly higher. The area for complete de-fluidization expands with increasing reduction temperatures. As a result, natural magnetite-based ore cannot be successful reduced without fluidization troubles in a temperature range between 600 and 800 °C under these conditions.
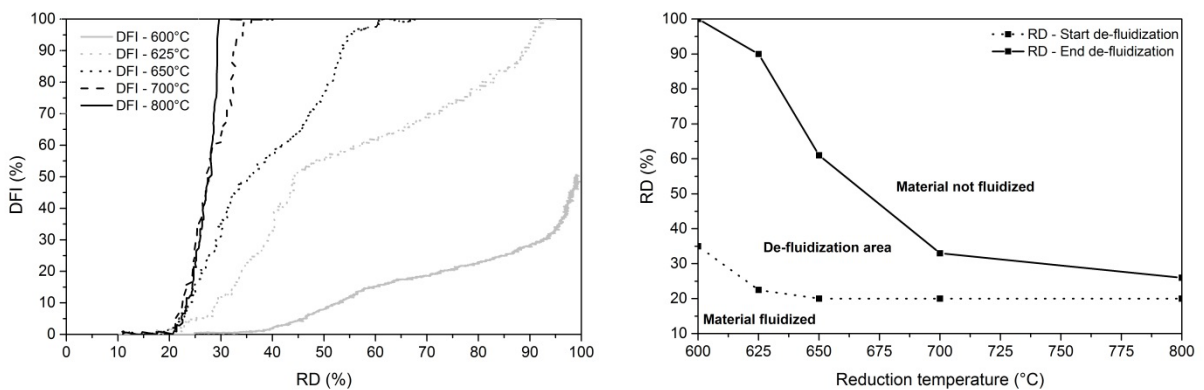
Figure 78: Behavior of natural magnetite during hydrogen-induced fluidized bed reduction; Left: De-fluidization index against degree of reduction; Right: Fluidization regime diagram showing the start and the end of de-fluidization.

5.2.2 Fluidization behavior of oxidized magnetite during reduction by hydrogen

As a next step, the behavior of the oxidized material during hydrogen-induced fluidized bed reduction is shown and discussed. Figure 79 shows the results from the reduction experiments at different temperatures, 600, 625, 650, 700 and 800 °C. From the pressure drop measurements for the lowest reduction temperature, 600 °C, it can be observed that no de-fluidization take place during the experiment because the measured pressure drop follows the theoretical, calculated one. On the other hand, as shown within the curve of degree of reduction, a complete reduction cannot be achieved in an acceptable time range because of a very low reduction rate at degrees of reduction higher than 80 %. That is the reason why the experiment was stopped after 110 min. Further morphological investigations should clarify the reason for this behavior. At 625 °C reduction temperature, the results show that a partial de-fluidization (approximately 7 %) of the material takes place in the range of a degree of reduction of 30 %. After that, the pressure drop remains constant, representing no further material de-fluidization. The final degree of reduction achieved is slightly higher at the same reduction time compared to 600 °C reduction temperature, but the reduction rate is also very low at the final stage of reduction. For 650 °C reduction temperature, a similar behavior to 625 °C can be observed. The main difference is the extent of de-fluidization. In this case, approximately 60% of the material is de-fluidized between 25 to 50 % degree of reduction. After that the behavior of the pressure drop shows no more material de-fluidization. An overall degree of reduction of 85 % is achieved but it is not clear how many particles were in contact with the reducing gas mixture because of the fluidization troubles. At 700 °C reduction temperature, a complete de-fluidization of the material takes place which starts in the area of 25 % degree of reduction. The de-fluidization occurs very fast. The low degree of reduction in the area of starting de-fluidization is again a hint that the reduction to FeO is not completed before the formation of metallic iron starts, similar to 650 °C reduction temperature. At 800 °C again a fast de-fluidization occurs, starting at a degree of reduction of 30 %. This is quite different compared to lower reduction temperatures because this value is even higher and represents a nearly complete reduction to FeO. It seems that the higher reduction temperature increases the conversion rate until FeO, which is nearly finished before the formation of metallic iron starts, responsible for the de-fluidization.

Figure 80 shows again the DFI against the degree of reduction and the defined fluidization regime diagram for the hydrogen-induced fluidized bed reduction of the oxidized magnetite. The trends of the DFIs show that a complete de-fluidization takes place only at temperatures higher than 700°C. A complete fluidization can only be achieved at the lowest temperature tested and it is observed that the reduction rate slows down drastically at high conversion degrees. The fluidization regime diagram shows a very small de-fluidization area at high reduction temperatures while it expands with decreasing temperatures. Compared to the natural magnetite, starting points of de-fluidization can be shifted to higher degrees of reduction. The size of the area representing a complete de-fluidization can be reduced by the oxidation treatment, especially at low reduction temperatures. The biggest difference occurs at the lowest reduction temperature, where in the case of the oxidized material, no de-fluidization is observed and for the natural magnetite around 50 % of the material becomes

de-fluidized. Up to 650 °C, a complete de-fluidization can be avoided by the prior oxidation of the material.

(a)

(b)

(c)

(d)

(e)
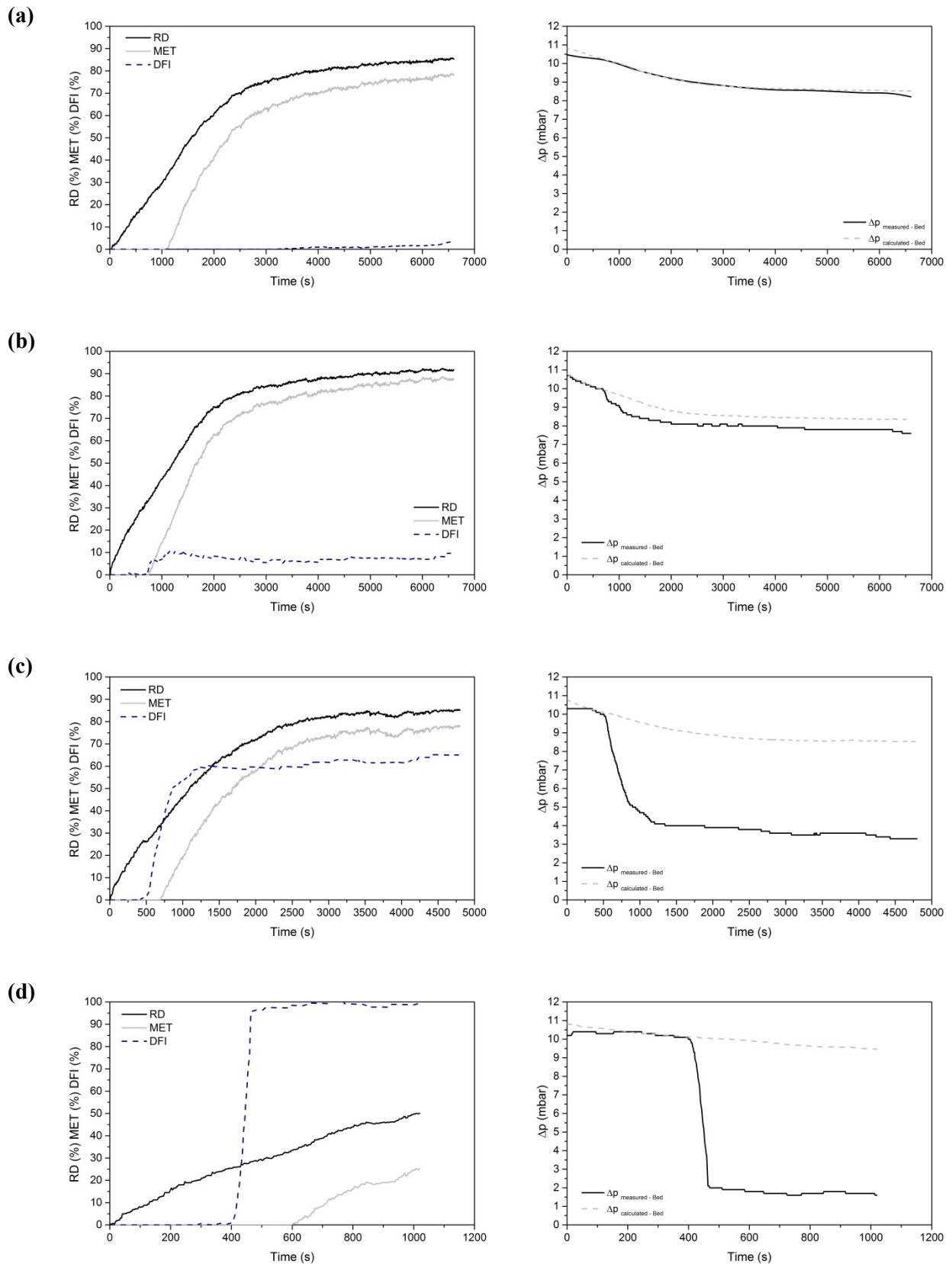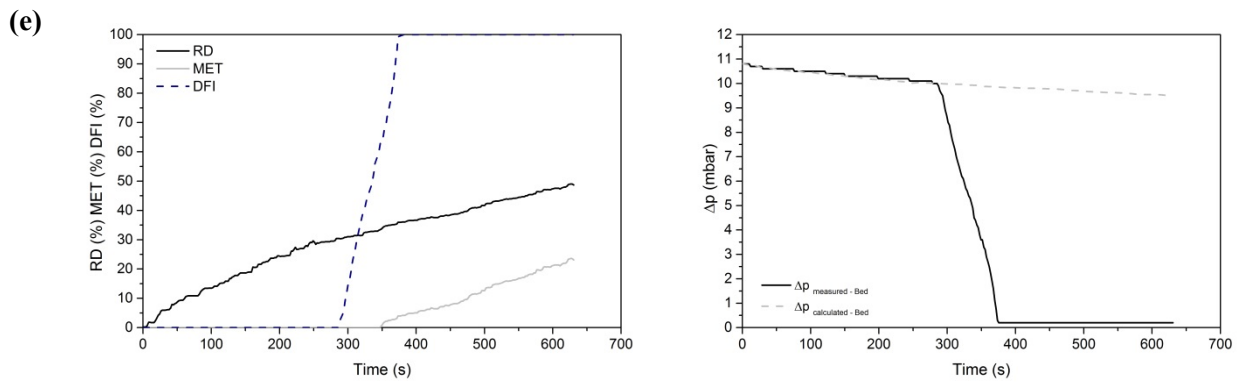
Figure 79: Behavior of oxidized magnetite during hydrogen-induced reduction concerning reducibility and fluidization behavior at different temperatures: (a) 600 °C; (b) 625 °C; (c) 650 °C; (d) 700 °C; (e) 800 °C.

In general, the effect of the prior oxidation is beneficial for the fluidization behavior but it is still not sufficient to ensure a complete, stable fluidization, also at high reduction temperatures. In the current case it seems that the final reduction is very slow. Further investigations concerning the polished micro-sections of the reduced samples should clarify the reasons for this behavior. But first, the focus is on the fluidization behavior. As a next step, the effect of MgO on the fluidization behavior should be investigated.
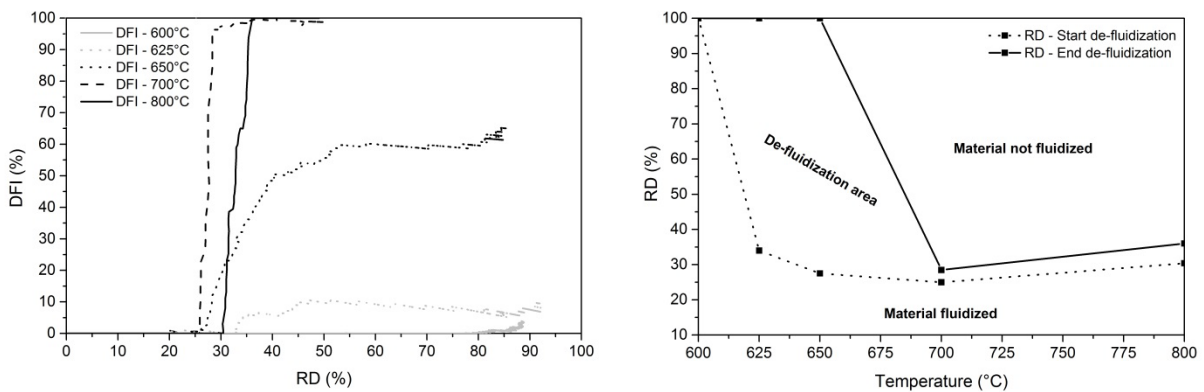
Figure 80: Behavior of oxidized magnetite during hydrogen-induced fluidized bed reduction; Left: De-fluidization index against degree of reduction; Right: Fluidization regime diagram showing the start and the end of de-fluidization.

5.2.3 Effect of MgO addition on the fluidization behavior and reducibility

MgO is known as an anti-sticking agent for different reasons. On the one hand, it can avoid the formation of iron whiskers because of the solubility in the wüstite lattice, which makes the diffusion of iron more difficult; on the other hand, it can form a coating layer around the

particles which avoids the direct contact of newly generated iron, as already explained in Section 2.5.3.

For the experiments, MgO is added by the mixing it together with the iron ore. The amount of MgO refers to the iron ore amount; 1 %-wt. MgO represents 4 g in case of a 400 g iron ore sample. Because of the better fluidization results of the iron ore in oxidized state, the focus for the investigations of the effect of the MgO addition is on the oxidized sample supplemented by selected tests with the natural magnetite. Reduction temperatures of 700 and 800 °C are selected for the experiments on the assumption that a defined amount of MgO for a successful experiment at 700 °C will also lead to a successful operation at lower reduction temperatures. As shown above, at 600 °C reduction temperature a successful fluidization is possible even without MgO addition. Figure 81 demonstrates the results of the reduction experiments at 700 °C reduction temperature for different amounts of MgO addition, which vary in the range between 0.25 and 1 %-wt. MgO in terms of degree of reduction, metallization, de-fluidization index and pressure drop against reduction time.

(a)

(b)

(c)
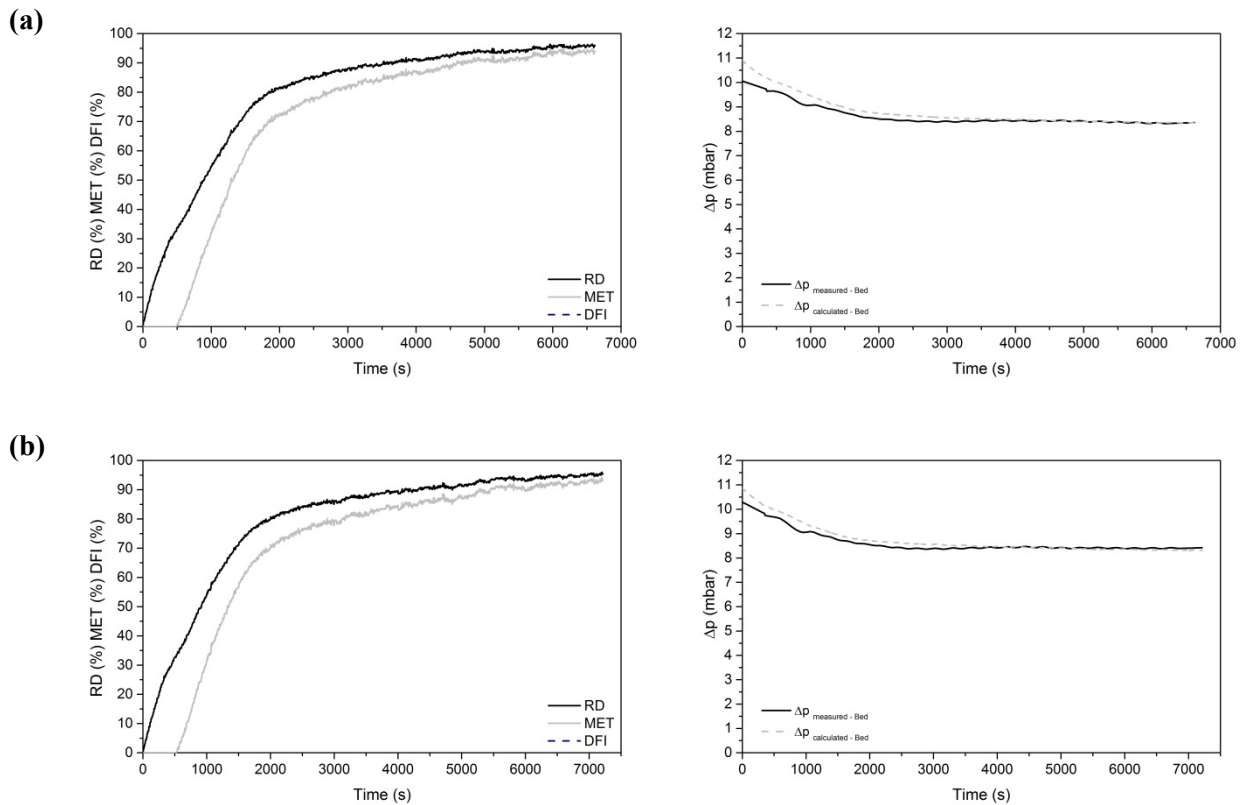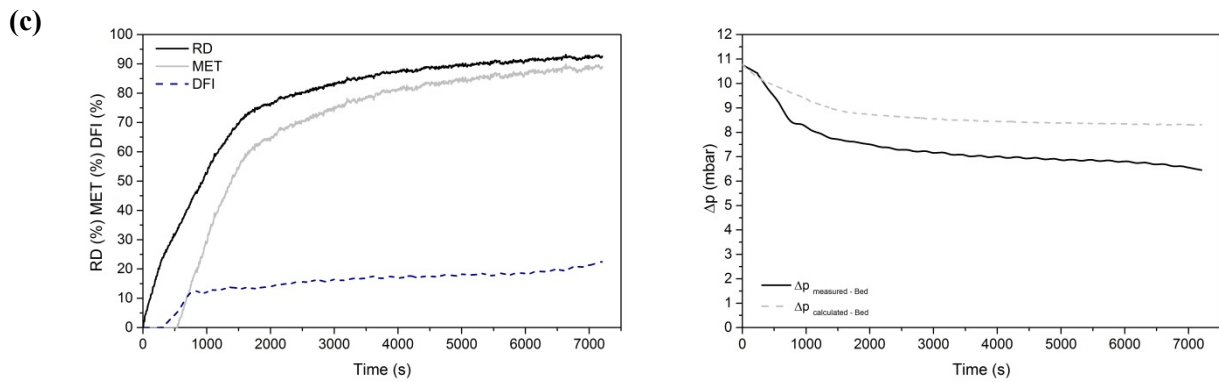
Figure 81: Effect of different amounts of MgO addition on the fluidization behavior of oxidized magnetite at 700°C reduction temperature: (a) 1.0 %-wt. MgO; (b) 0.5 %-wt. MgO; (c) 0.25 %-wt. MgO.

As shown by the trends of the pressure drop, a successful complete fluidization can be achieved in the cases of the addition of 1 and 0.5 %-wt. MgO. At 0.25 %-wt. MgO, a partial de-fluidization occurs between 25 and 40 % degree of reduction. As a result, 0.5 %-wt. MgO is sufficient to achieve a constant stable fluidization of the material during the whole reduction procedure at a reduction temperature of 700 °C. Without MgO addition, the material de-fluidizes very fast and completely at a degree of reduction of 25 %. The curves of reduction degree again show a fast reduction rate until approximately 80 % degree of reduction, followed by a very slow reduction rate until high conversion degrees. After 110 and 120 min of reduction for 1, 0.5 and 0.25 %-wt. MgO, the experiments are terminated because of the very slow progress. Figure 82 shows the comparison of the progress of reduction for different amounts of MgO addition. For the trends of 1.5, 1.0 and 0.5 %-wt. MgO addition, a slightly faster reduction can be observed with an increasing amount of MgO addition while the difference is unincisive. So, different amounts of MgO additions do not have a big influence on the reducibility. The experiment with 0.25 %-wt. MgO cannot be taken into account because of the partial de-fluidization of the material.
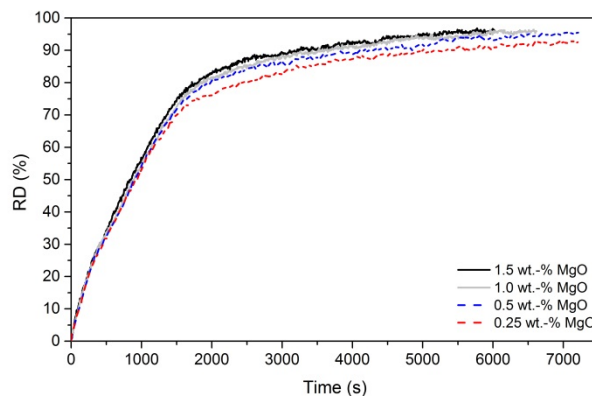
Figure 82: Effect of different MgO additions on the progress of hydrogen-induced reduction of oxidized magnetite at 700 °C.
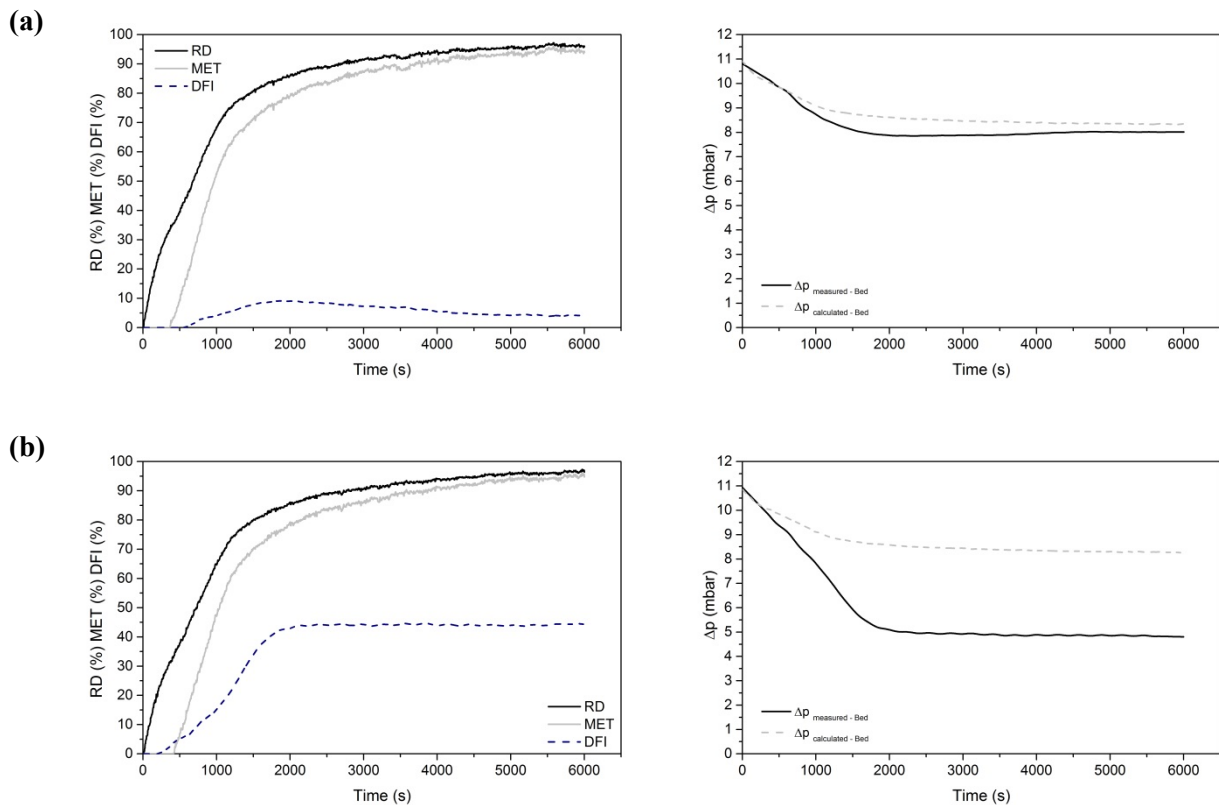
Figure 83: Effect of different amounts of MgO addition on the fluidization behavior of oxidized magnetite at 800°C reduction temperature: (a) 1.0 %-wt. MgO; (b) 0.5 %-wt. MgO.

Figure 83 shows the results obtained for the reduction experiments at 800 °C reduction temperature with an MgO addition of 1.0 and 0.5 %-wt. For the addition of 1.0 %-wt. MgO, the curves of pressure drop show a partial de-fluidization of approximately 10 % of the material, starting at 45 % degree of reduction. At the end of reduction, the difference in pressure drop becomes smaller, signifying that some of the de-fluidized material becomes fluidized again (decreasing DFI). In case of lower MgO addition amounts (0.5 %-wt.), around half of the material becomes de-fluidized between 25 and 85 % degree of reduction. After that, no further de-fluidization occurs. The progress of reduction shows a similar behavior compared to 700 °C reduction temperature: a fast reduction until approximately 80 % degree of reduction is followed by a slow reduction rate in the final stage of reduction. Without MgO addition at 800 °C reduction temperature, de-fluidization occurs completely and happens quite fast, starting at a degree of reduction of 30 %.

In general, the investigation with the addition of MgO shows that only small amounts of MgO have a substantial impact on the fluidization behavior. It is observed that in the case of 700 °C reduction temperature, 0.5 %-wt. MgO is sufficient to achieve a stable fluidization during the whole reduction procedure. With increasing reduction temperatures, the amount of MgO addition for a successful fluidization also increases. At 800 °C, 1.0 %-wt. MgO is not enough to completely avoid fluidization troubles, either. Figure 84 summarizes the effect of a prior oxidation and the addition of different amounts of MgO on the DFI at different reduction temperatures. A prior oxidation affects the starting point of de-fluidization, but it cannot prevent de-fluidization at 700 and 800 °C reduction temperatures. The combination of prior

oxidation and the addition of MgO can also lead to successful experiments at high reduction temperatures.
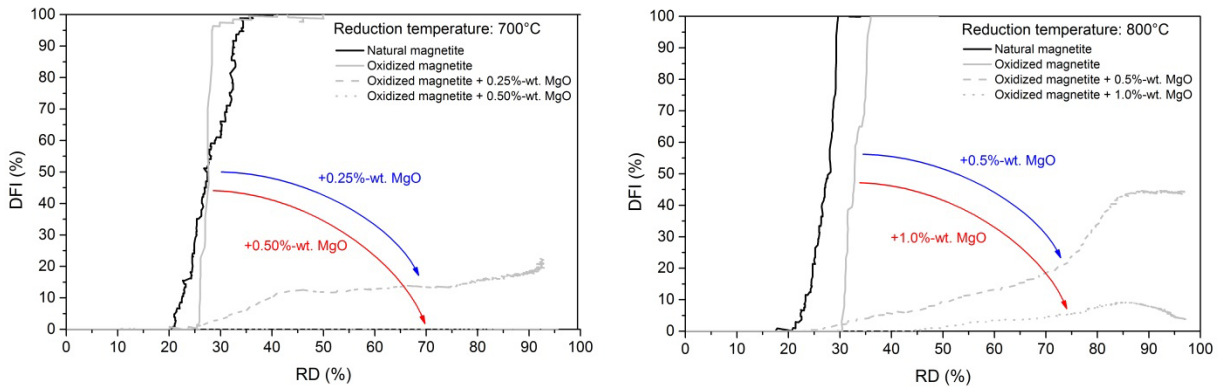
Figure 84: Effect of oxidation and MgO addition on the DFI at different reduction temperatures: left-700°C; right-800°C.

It is not possible to define the reasons for the de-fluidization based on the reduction experiments alone. The results of the experiments can only be used for comparison and show the effect of changing different parameters. To get a deeper understanding of the mechanisms responsible for the de-fluidization, observations of the morphology of the reduced samples are required using optical microscopy and particle surface investigations by an SEM. The results are shown in the following section.

5.3 Morphological investigations of the reduced samples

Below, polished micro-sections and SEM particle surface images of the natural magnetite and the oxidized magnetite, reduced at the same temperature, are shown and compared. Figure 85 exhibits the samples obtained after reduction at 600 °C. The results from the reduction experiments show that the natural magnetite sample is reduced completely, although approximately half of the material is de-fluidized. The oxidized magnetite shows no fluidization troubles at this reduction temperature, but the reduction rate, especially at high conversion degrees, is very low. Figure 85 (a) and (c) shows the polished micro-sections of those samples. The complete reduction of the natural magnetite samples can be confirmed because only metallic iron is observed across the entire particle sections (white areas), which show high porosity. For the oxidized sample, remaining FeO islands (gray areas) can be observed inside the particles which are covered by formations of metallic iron. This behavior can be defined as the reason for the low reduction rate at the final stage because the reducing gas mixture is not able to reach the reaction interface anymore. From the SEM surface images shown in Figure 85 (b) and (d), a clear reason for the aggregating de-fluidization of the natural magnetite during the reduction cannot be defined; no clear agglomerates can be found. The cause for that might be the handling procedure of the samples. During discharging from the fluidized bed reactor and transporting the material to the SEM, there is a risk of the destruction of possible formed agglomerates if the stability is low. The main difference between the two samples is the smoother surface of the oxidized

sample, compared to the natural one. This is definitely preferable for the fluidization behavior.
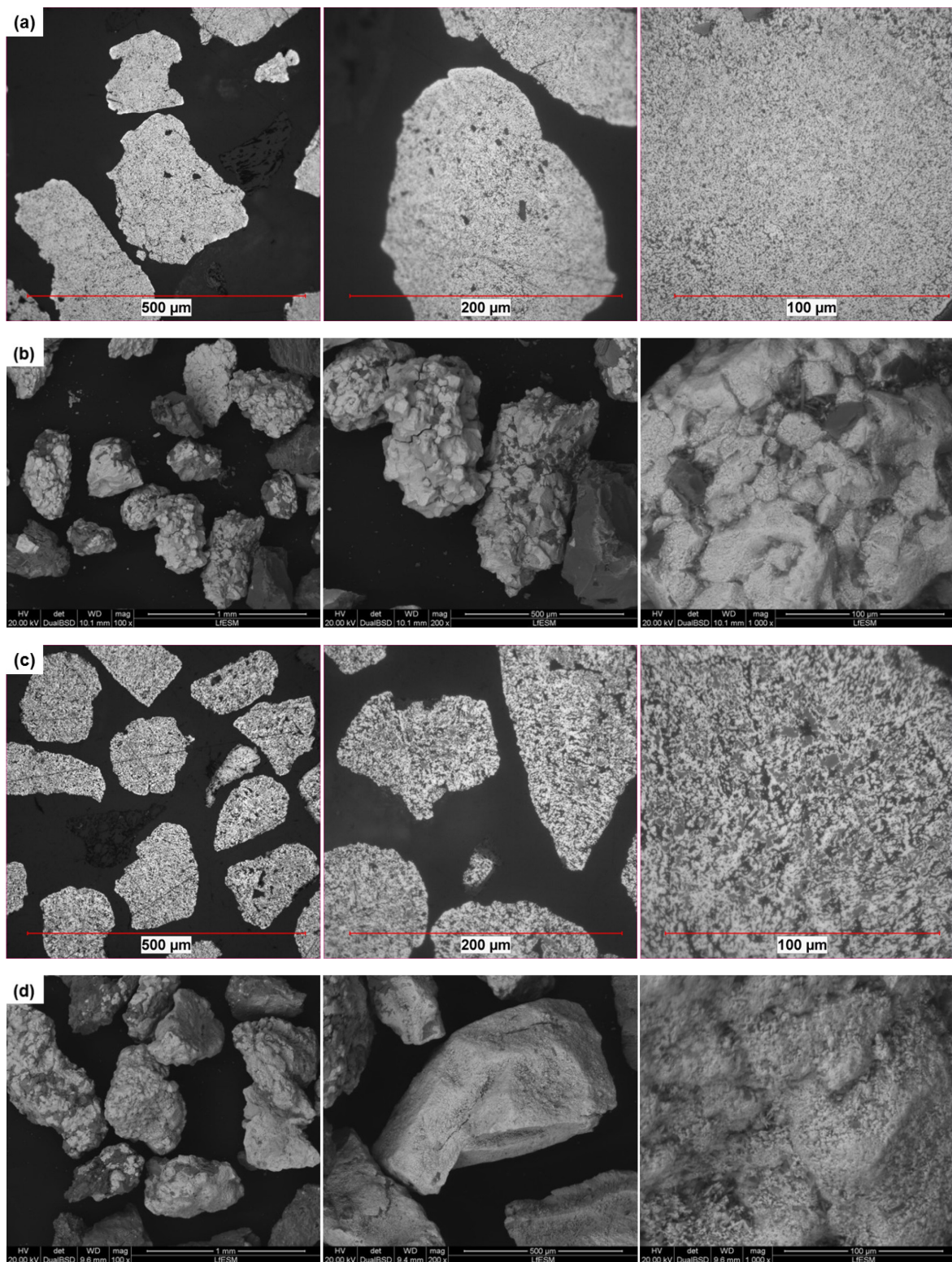
Figure 85: Morphological investigation of (partly) reduced samples reduced at 600 °C: (a) Polished micro-sections natural magnetite; (b) SEM surface images natural magnetite; (c) Polished micro-sections oxidized magnetite; (d) SEM surface images oxidized magnetite.
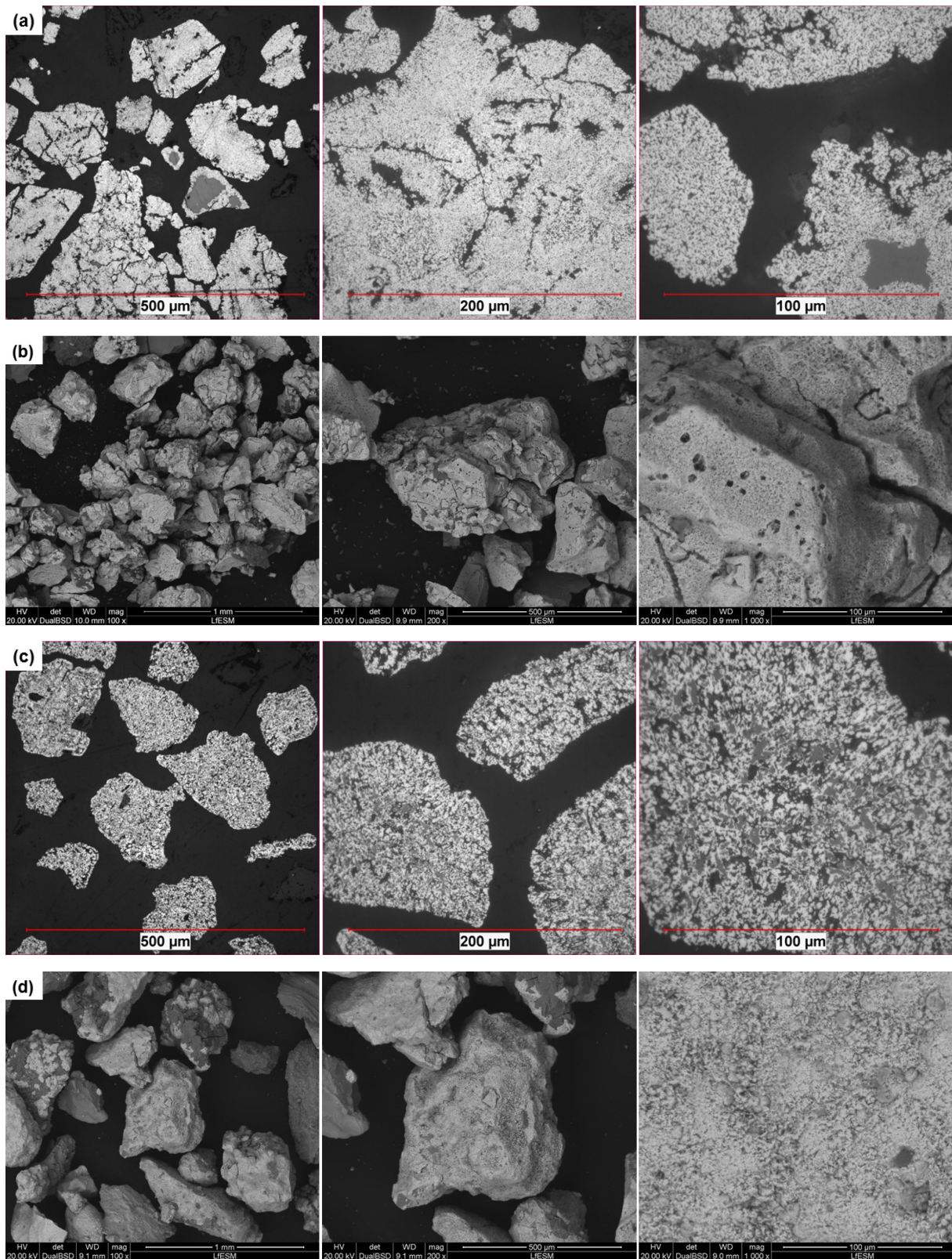
Figure 86: Morphological investigation of (partly) reduced samples reduced at 625 °C: (a) Polished micro-sections natural magnetite; (b) SEM surface images natural magnetite; (c) Polished micro-sections oxidized magnetite; (d) SEM surface images oxidized magnetite.

Figure 86 presents the morphological investigations for the next higher reduction temperature, 625 °C. The natural magnetite shows a complete de-fluidization at 95 % degree of reduction, while the oxidized sample only shows a partial de-fluidization of approximately 10 % of the material. Based on the polished micro-sections shown in Figure 86 (a) and (c), the effect of the oxidation on the reduction behavior can be seen clearly. In case of the natural magnetite, a porous iron shell grows from the particle surface to the center, while in the core, a dense remaining wüstite core can be observed. The oxidized sample shows different behavior. The iron is formed uniformly, distributed over the whole particle area and the remaining wüstite can be found everywhere in the particle. It is evident that the prior oxidation leads to more porous structure during the reduction procedure but again, the small wüstite areas are covered by metallic iron formations, slowing down the reduction rate at the final stages. The reason for aggregating de-fluidization can again not be clearly identified. Within the SEM surface images, Figure 86 (b) and (d), no formation of iron whiskers can be observed. The mechanism of de-fluidization can only be related to the activity of the freshly generated iron, as explained in Section 2.5.3. The porous character of the generated iron shell of the natural magnetite can be clearly observed in the surface images, while for the oxidized sample, the surface structure appears denser.
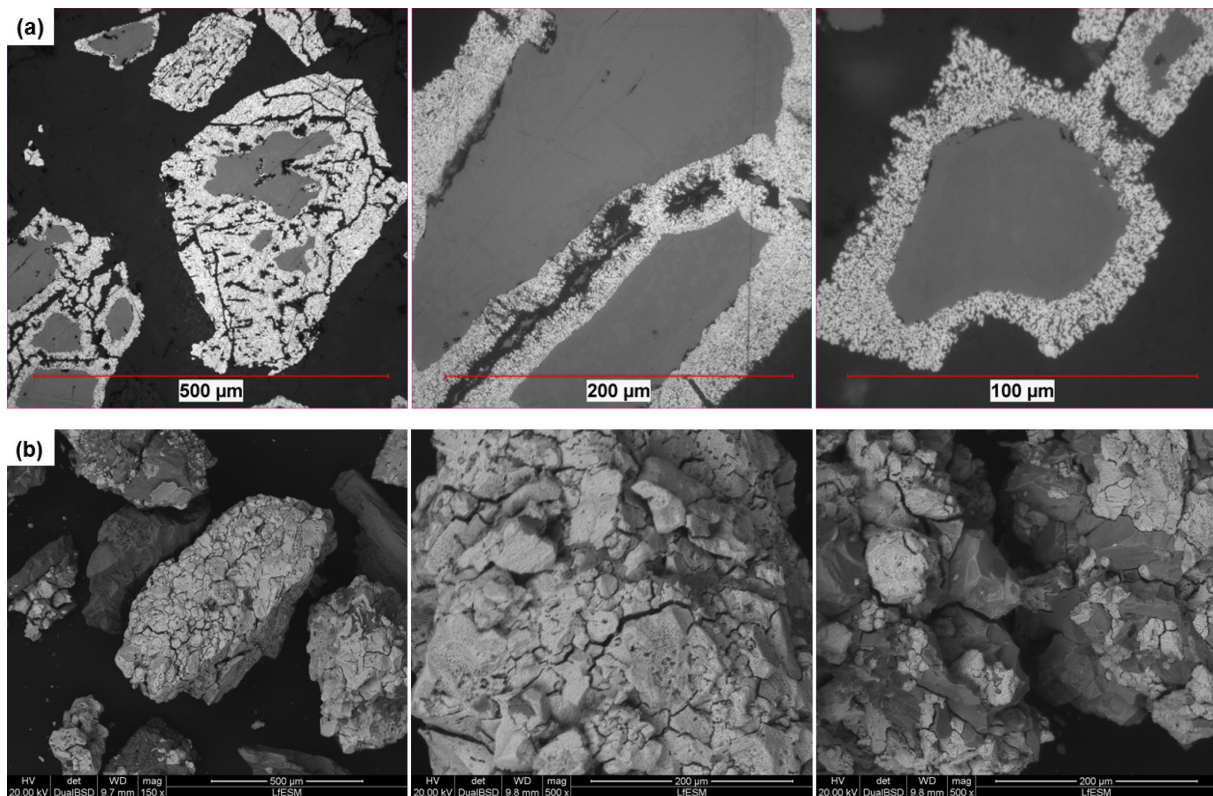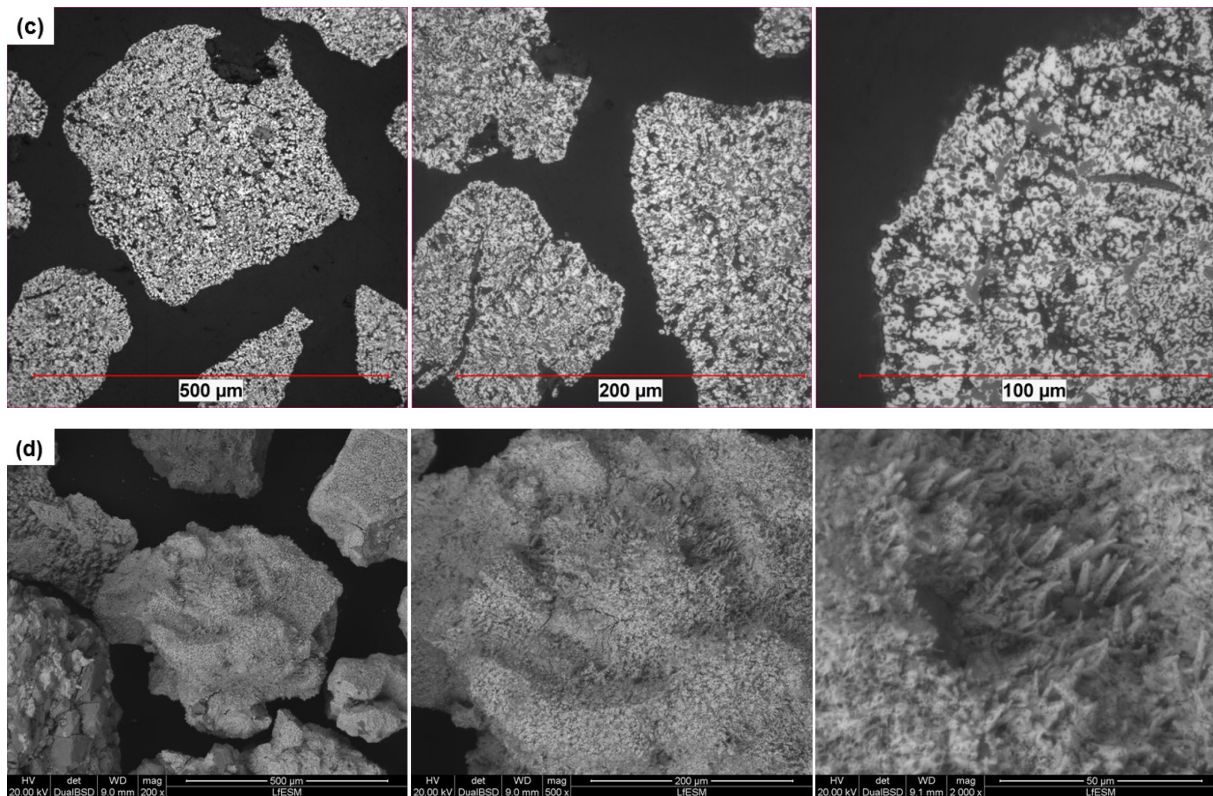
Figure 87: Morphological investigation of (partly) reduced samples reduced at 650 °C: (a) Polished micro-sections natural magnetite; (b) SEM surface images natural magnetite; (c) Polished micro-sections oxidized magnetite; (d) SEM surface images oxidized magnetite.

The results of the morphological investigations for a reduction temperature of 650 °C are displayed in Figure 87. The natural magnetite shows a complete de-fluidization at a degree of reduction of 55 %, while in the oxidized sample, a partial de-fluidization of approximately 60 % of the material takes place. Taken from the polished micro-section of the natural magnetite samples shown in Figure 87 (a), two main outcomes can be observed: First, single particles are connected by the formation of porous metallic iron bridges, which ends in an agglomeration and a corresponding aggregating partial de-fluidization. Second, the remaining oxide cores inside the particles show two different shades of gray, demonstrating that aside from FeO, Fe_3O_4 is also available in the remaining oxide core. Accordingly, no complete reduction to FeO takes place before the formation of metallic iron starts. This explains why the de-fluidization started already at overall reduction degrees below 33 %. The formation of agglomerates cannot be clearly observed in the SEM surface images presented in Figure 87 (b), maybe again because of the handling procedure of the material. The polished micro-sections and SEM surface images of the oxidized sample shown in Figure 87 (c) and (d) show the formation of iron needles (whiskers) on the surface of the particles. In the presence of iron whiskers, the tendency of particles to form agglomerates is higher because the whiskers can act as hooks between the particles, but the formation of agglomerates cannot be clearly observed. In fact, surfaces with iron whiskers increase the friction between the particles during the fluidization, which requires a higher force of the fluidization gas exerted to the particles. If the friction between the particles becomes

considerable, fluidization might be not possible anymore. This is the reason for the partial de-fluidization here.
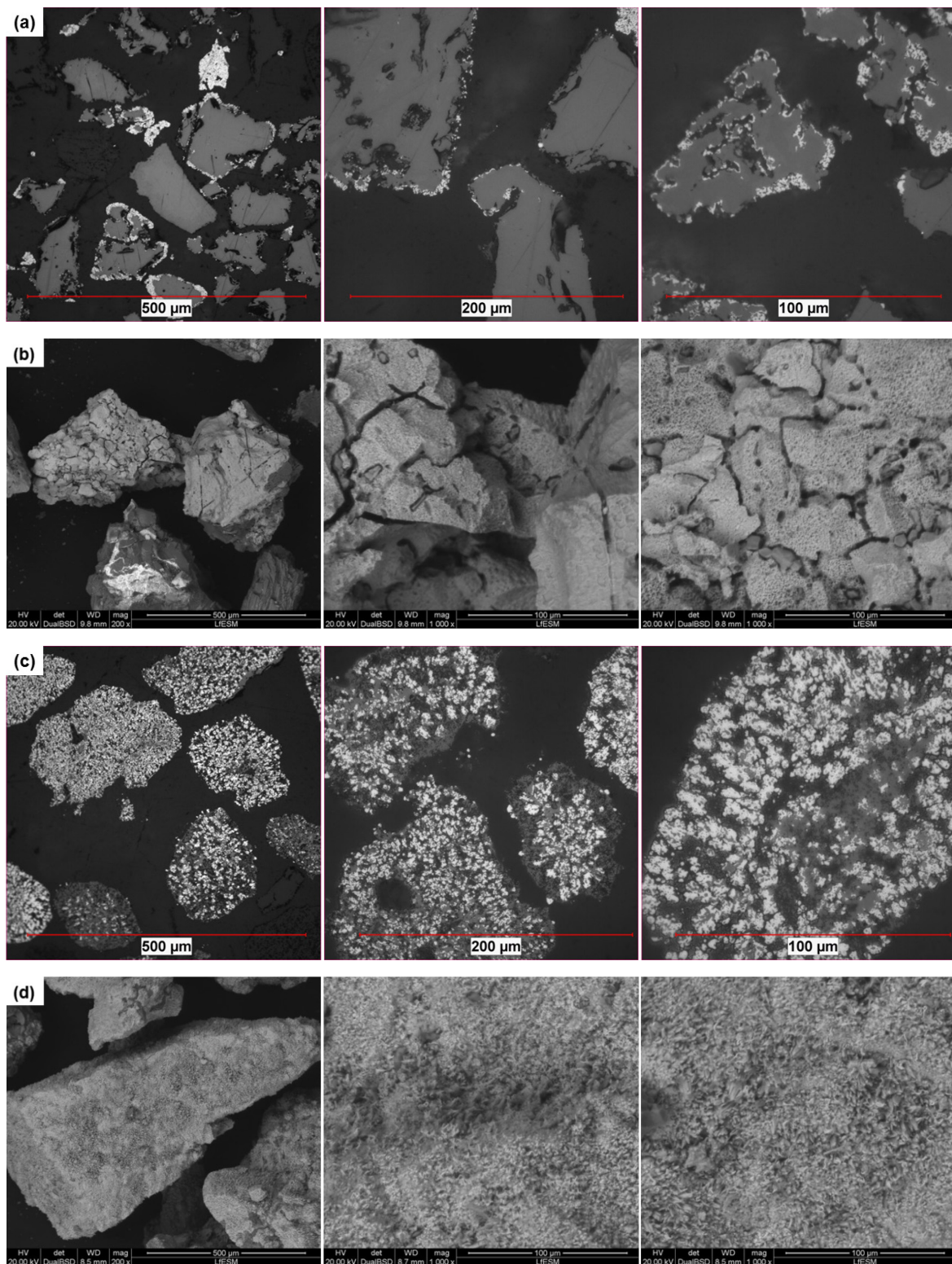
Figure 88: Morphological investigation of (partly) reduced samples reduced at 700 °C: (a) Polished micro-sections natural magnetite; (b) SEM surface images natural magnetite; (c) Polished micro-sections oxidized magnetite; (d) SEM surface images oxidized magnetite.

Figure 88 demonstrates the results of the morphological investigations for the samples at 700°C reduction temperature. For both cases, the natural and oxidized magnetite, a fast, complete de-fluidization take place, starting at 20 and 25 % degree of reduction, respectively. The polished micro-sections and the SEM surface images of the natural magnetite (Figure 88 (a) and (b)) show a non-uniform iron formation around the particles. Some of the particles even show no metallic iron. A coalescence of particles can be observed if metallic iron is available, which is an explanation for the de-fluidization. Again, Fe_3O_4 can also be observed inside the particles (different shades of gray), which explains the low degree of reduction at the start of de-fluidization. For the oxidized sample (Figure 88 (c) and (d)), a similar behavior as for 650 °C reduction temperature can be observed. In the polished micro-sections, some particles show an oxide shell on the surface, which is an indication of a partial re-oxidation of the material. This can occur while the material from is discharged from the reactor or during sample preparation of the polished micro-sections.

Figure 89 gives the results of the morphological investigations of the reduced samples at a reduction temperature of 800 °C. Again for both cases, the natural and oxidized magnetite, a fast, complete de-fluidization takes place, starting at 20 and 30 % degree of reduction, respectively. The images of the natural magnetite sample (Figure 89 (a) and (b)) show that only a small amount of metallic iron was formed on the particles' surface, which is enough to initiate the complete de-fluidization of the material. In the SEM surface image another interesting point can be observed, representing a lamellar-like structure on the surface of some particles.
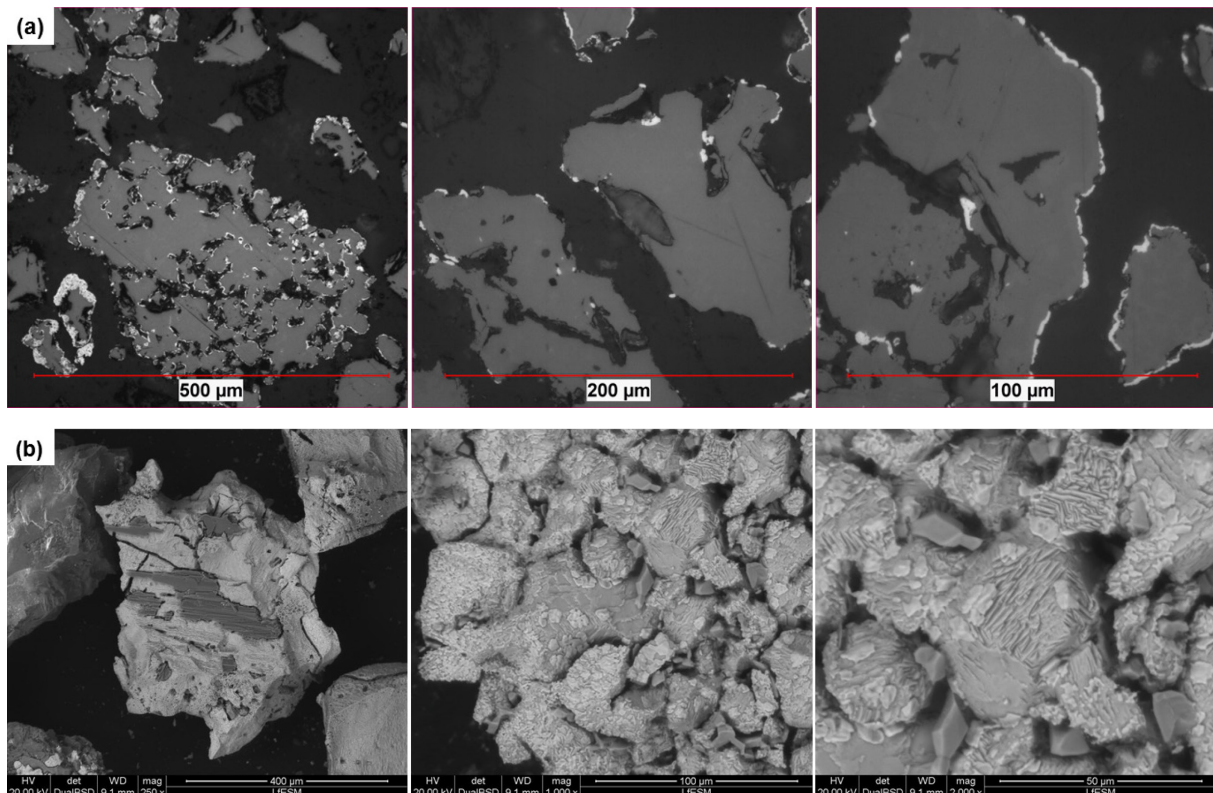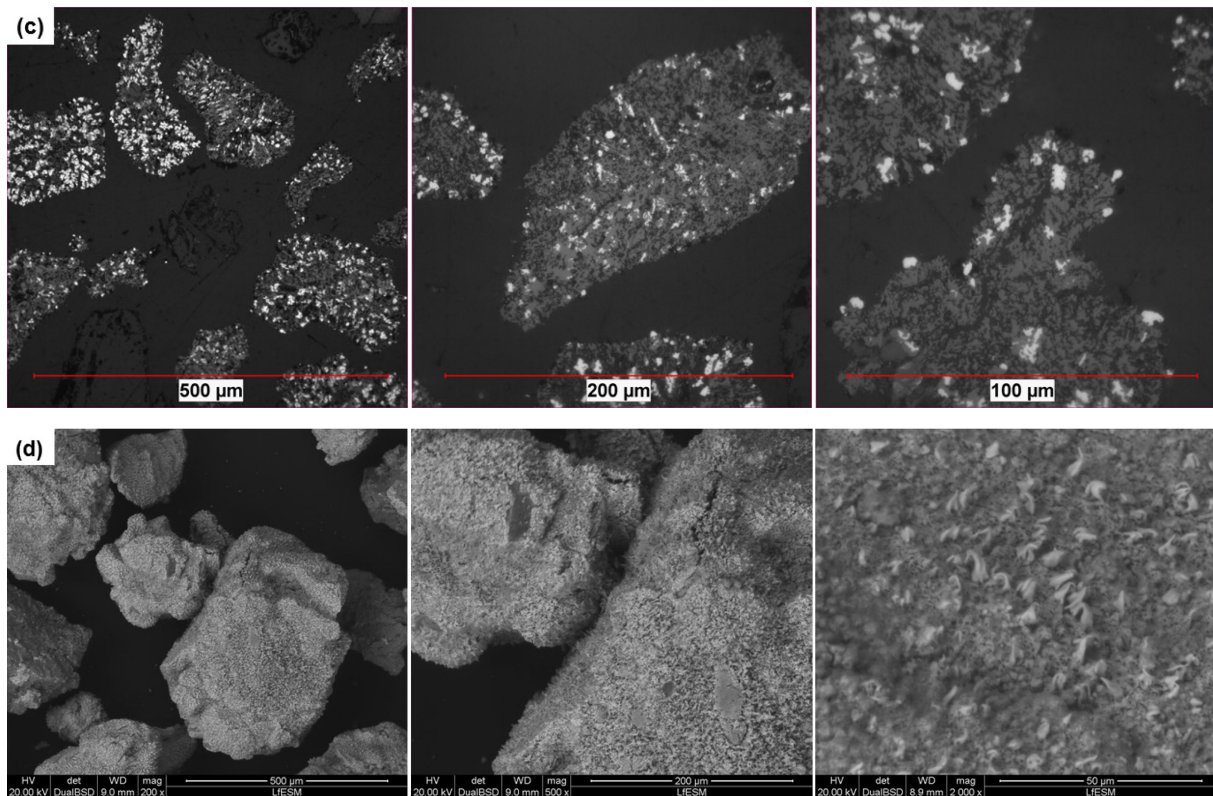
Figure 89: Morphological investigation of (partly) reduced samples reduced at 800 °C: (a) Polished micro-sections natural magnetite; (b) SEM surface images natural magnetite; (c) Polished micro-sections oxidized magnetite; (d) SEM surface images oxidized magnetite.

It cannot be clearly determined if this lamellar structure belongs to the reduction from Fe_3O_4 to FeO or FeO to Fe, but it is assumed that this structure occurs during the reduction from Fe_3O_4 to FeO because only a very small amount of metallic iron is formed which can be clearly defined in the SEM surface images. For the oxidized sample, shown in Figure 89 (c) and (d), again the formation of iron whiskers can be observed in the SEM surface image and also in the polished micro-sections. The very low amount of metallic iron formed is sufficient to initiate a complete, fast de-fluidization.

As a next step, the effect of the MgO on the morphology of the reduced samples should be clarified. For that reason, again polished micro-sections and SEM surface images of the samples with different amounts of MgO addition are prepared, displayed in Figure 90 for a reduction temperature of 700 °C.
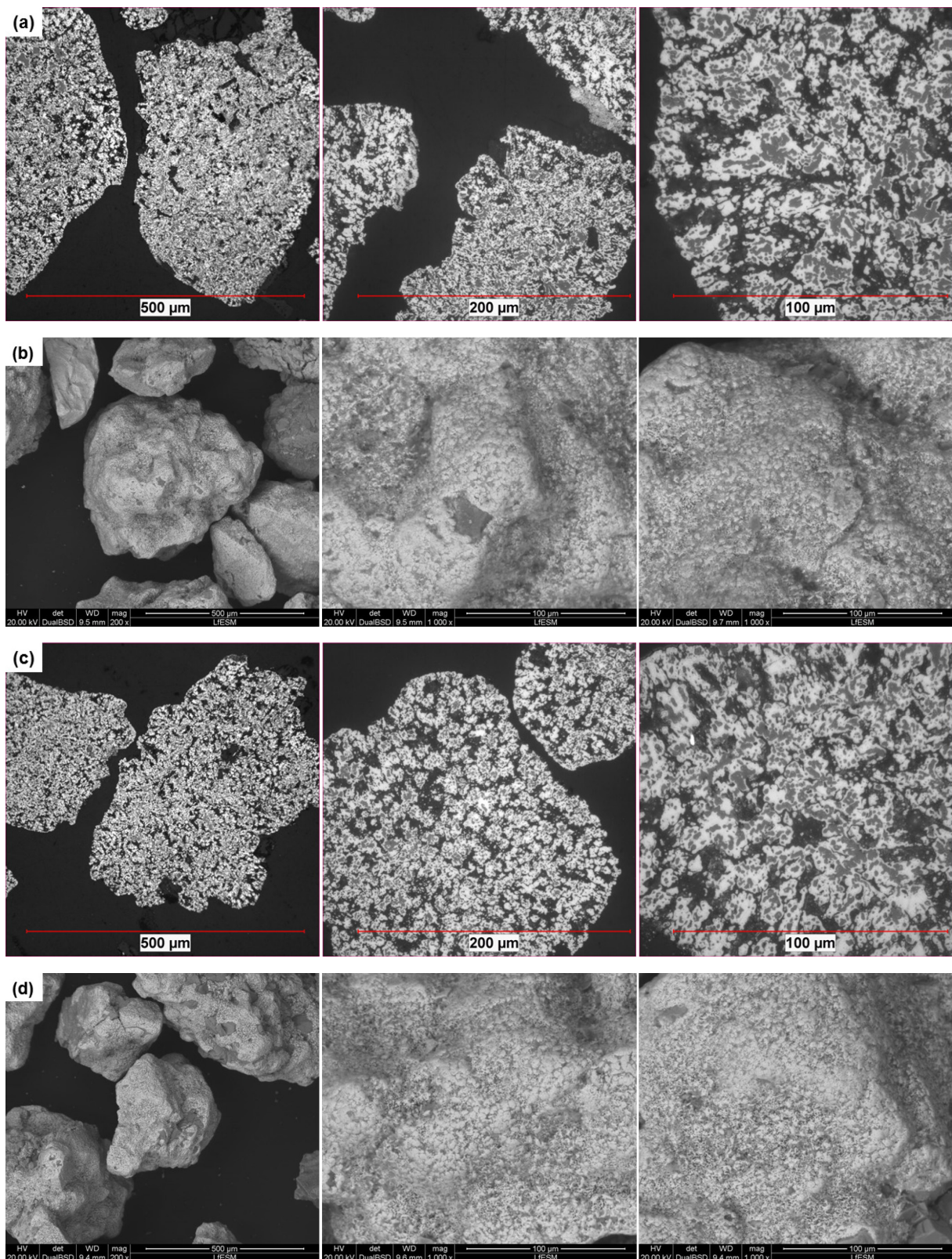
Figure 90: Morphological investigation of (partly) reduced samples of oxidized magnetite reduced at 700 °C with different amounts of MgO addition: (a) Polished micro-sections 1 %-wt. MgO; (b) SEM surface images 1 %-wt. MgO; (c) Polished micro-sections 0.5 %-wt. MgO; (d) SEM surface images 0.5 %-wt. MgO; (e) Polished micro-sections 0.25 %-wt. MgO; (f) SEM surface images 0.25 %-wt. MgO.

At 700 °C reduction temperature, an addition of >0.5 %-wt. MgO is required to avoid any fluidization issues. The samples for 1.0 and 0.5 %-wt. MgO addition are shown in Figure 90 (a), (b), (c) and (d). As shown, the surface of the particles appears much smoother compared to the sample without MgO addition. The formation of iron whiskers can be avoided, ending in a stable fluidization during the whole reduction procedure. Concerning the reduction behavior, the polished micro-sections again show remaining small wüstite cores covered by dense metallic iron layers. That is again the reason for the low reduction rate at the final stages of reduction. In order to achieve high degrees of reduction (>95 %), long reduction times might be required, which can lead to problems with industrial applications in terms of process efficiency. The images of the sample doped with 0.25 %-wt. MgO addition which showed a partial de-fluidization of the material during the experiment yield similar results (Figure 90 (e) and (f)). No difference can be observed compared to the samples with higher MgO amounts. One possible explanation for the partial de-fluidization might be that the MgO amount is still not enough to cover all the particles, which ends in the de-fluidization of the partially uncovered material.

Figure 91 shows the polished micro-sections and the SEM surface images of the oxidized samples with different amounts of MgO addition (1.0 and 0.5 %-wt. MgO) reduced at a temperature of 800 °C. Both samples showed a partial de-fluidization during the reduction experiments while the amount of de-fluidized material in the case of 1.0 %-wt. MgO addition

is low. As shown, the remaining wüstite cores are much bigger compared to lower reduction temperatures and they are again covered by a dense iron layer that hinders fast progress in the final stage of reduction. As shown by the SEM surface images, with lower content of MgO addition, needle-like iron formations can be observed on the surface of the particles. This might be the reason for the de-fluidization of around 50 % of the bed material. Such iron formations on the particle surface cannot be observed when there is an MgO addition of 1 %-wt. This explains the better fluidization behavior with higher amounts of MgO addition.
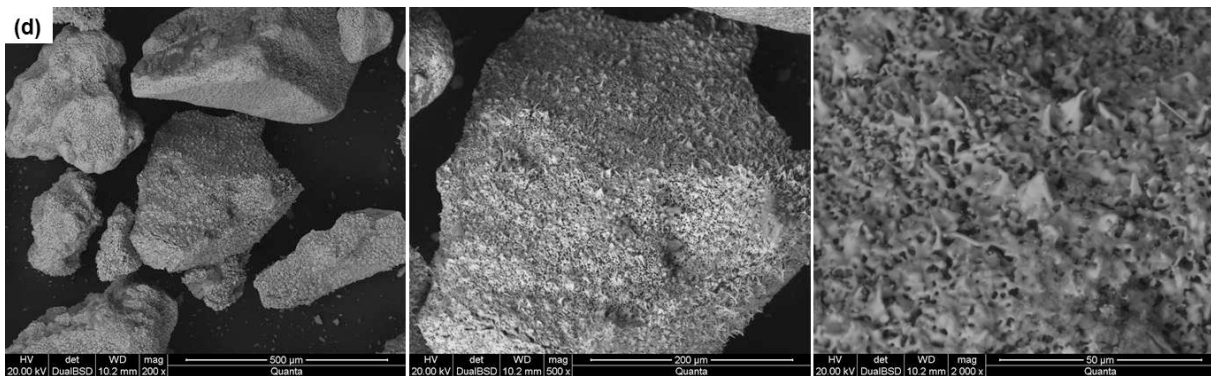
Figure 91: Morphological investigations of (partly) reduced samples of oxidized magnetite reduced at 800 °C with different amounts of MgO addition: (a) Polished micro-sections 1 %-wt. MgO; (b) SEM surface images 1 %-wt. MgO; (c) Polished micro-sections 0.5 %-wt.; (d) SEM surface images 0.5 %-wt. MgO.

The effect of a partial prior oxidation is discussed in the next section. The idea behind it is improved fluidization behavior due to an oxidized surface of the particles, which should lead to the formation of a smooth surface, as shown for the complete oxidized samples. The occurrence of wüstite cores covered by a dense iron layer should be avoided by remaining Fe_3O_4 in the particles after oxidation to achieve a similar behavior as it was observed during the reduction of the natural magnetite at 600°C reduction temperature.

5.4 Improvement of the reducibility and fluidization behavior by prior partial oxidation

The partial oxidation of the magnetite sample should combine the better fluidization behavior obtained for the experiments with complete oxidation as well as a better reducibility, especially in the final stage of reduction, observed during the reduction of the natural magnetite. Figure 92 compares the results of the reduction experiments for the natural magnetite (NM) and the completely oxidized magnetite (OM) for a reduction temperature of 600 °C without MgO addition (left) and 700°C reduction temperature with an addition of 0.5 %-wt. MgO (right). At 600°C reduction temperature, the reduction rate of the oxidized magnetite until 70% degree of reduction is much faster compared to the natural magnetite. Afterwards, the reduction rate slows down drastically while the reduction rate of the natural magnetite keeps constant until high conversion degrees. Although a certain de-fluidization took place during the reduction of the natural magnetite, represented by the DFI, a complete reduction could be achieved much faster. The reasons for that behavior are explained by the polished micro-sections in previous sections. At 700 °C reduction temperature with an MgO addition of 0.5 %-wt., the differences in the reducibility are similar. The DFI for the natural magnetite is much higher compared to 600 °C, but again the reduction occurs faster, especially at the final stage of reduction, compared to the completely oxidized material. Based on these results, a partial oxidation of the material should combine the advantages in terms of better reducibility and fluidization behavior.
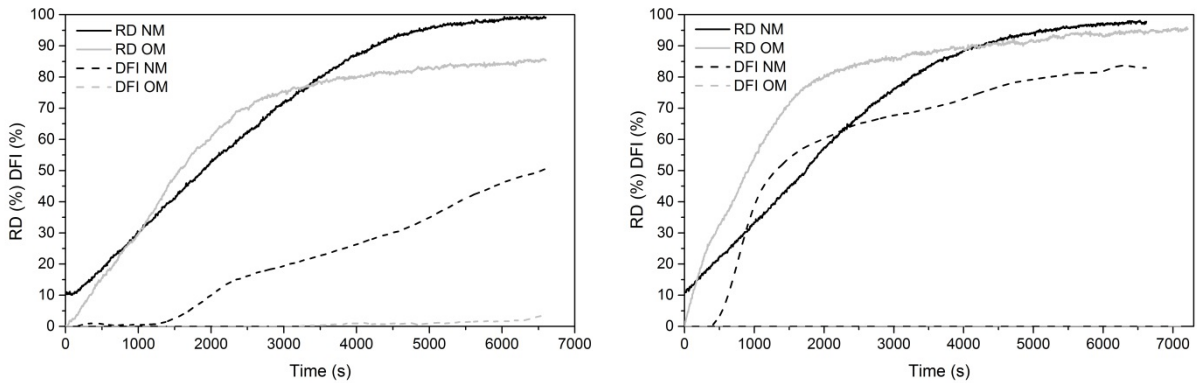
Figure 92: Comparison of RD and DFI for natural magnetite (NM) and oxidized magnetite (OM): left-600 °C reduction temperature without MgO addition; right- 700 °C reduction temperature and 0.5 %-wt. MgO addition.

The preparation of the partially oxidized sample again takes place in a heat treatment furnace. Compared to the complete oxidation, the temperature was lowered from 1000 °C to 800 °C because of easier sample handling and lower oxidation kinetics, making it much easier to achieve the required degree of oxidation. The oxidation degree of the sample is 50 %, determined by the sample mass before and after oxidation and the chemical analysis of the iron ore.

Figure 93 shows the results of the reduction experiment at 700 °C reduction temperature with an MgO addition of 0.5 %-wt. for the partly oxidized sample. As demonstrated, the amount of de-fluidized material is lowered to approximately 10 % compared to the natural magnetite, where 80 % of the material was de-fluidized under the same process conditions. The curve of degree of reduction shows that a nearly complete reduction can be achieved in an acceptable time.
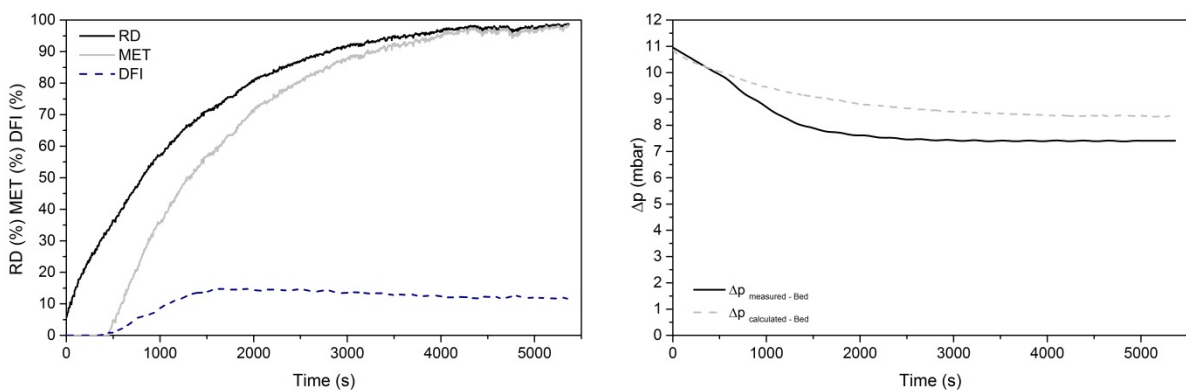
Figure 93: Behavior of partly oxidized magnetite during hydrogen-induced reduction concerning reducibility and fluidization behavior at 700 °C reduction temperature and 0.5 %-wt. MgO addition.

Figure 94 compares the progresses of reduction under the same process conditions for the natural magnetite (80 % de-fluidization), the completely oxidized material (no de-fluidization)

and the partly oxidized sample (10 % de-fluidization), POM. The reduction rate of the partly oxidized sample is similar to that of the completely oxidized sample until approximately 80 % degree of reduction. In the final stage of reduction, it is even higher. As a result, a nearly complete reduction can be achieved much faster compared to the other investigated samples.
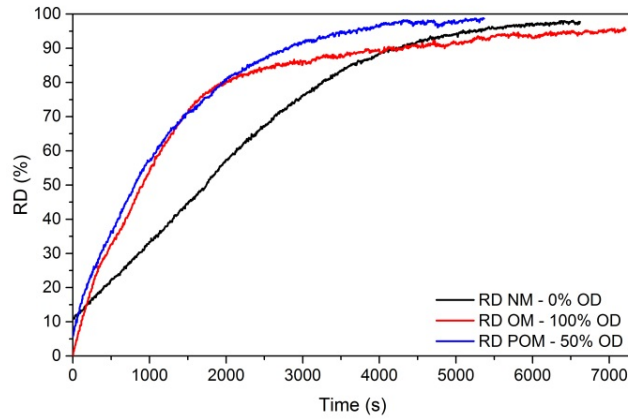
Figure 94: Effect of different oxidation degrees (OD) on the reducibility at 700°C reduction temperature and 0.5 %-wt. MgO addition
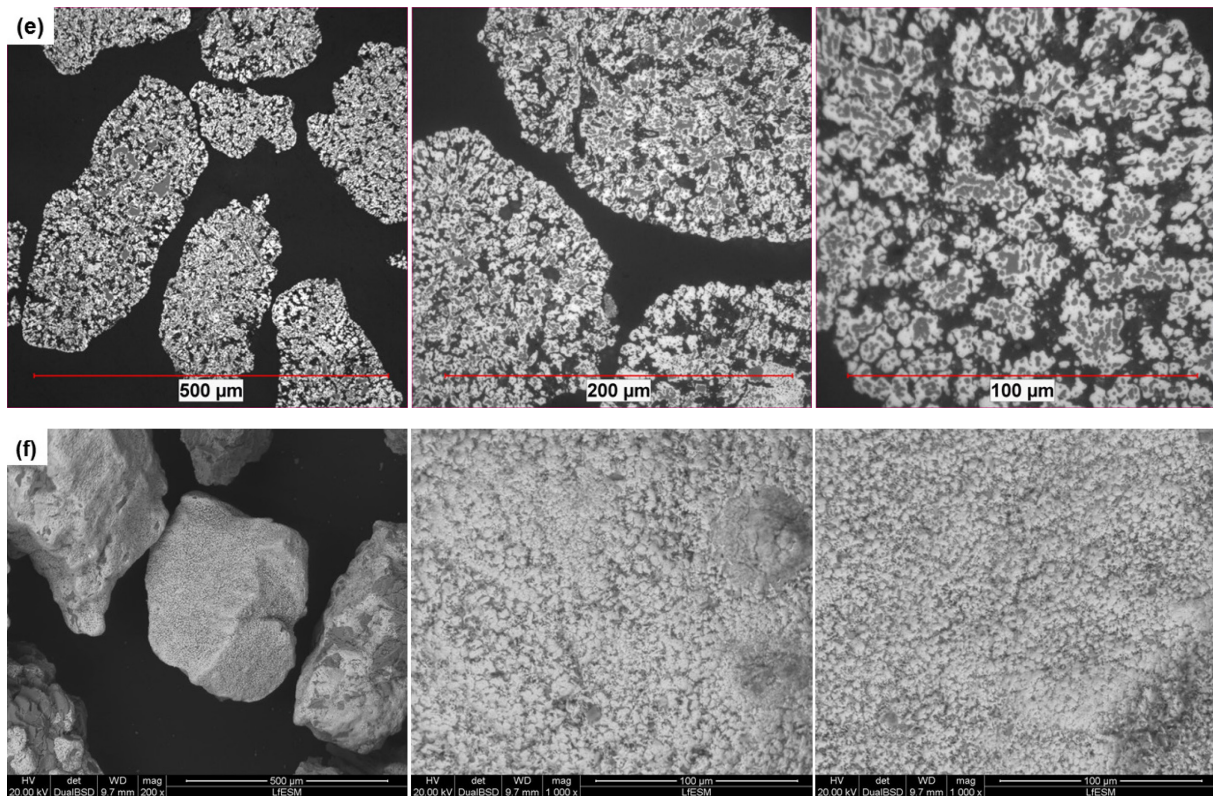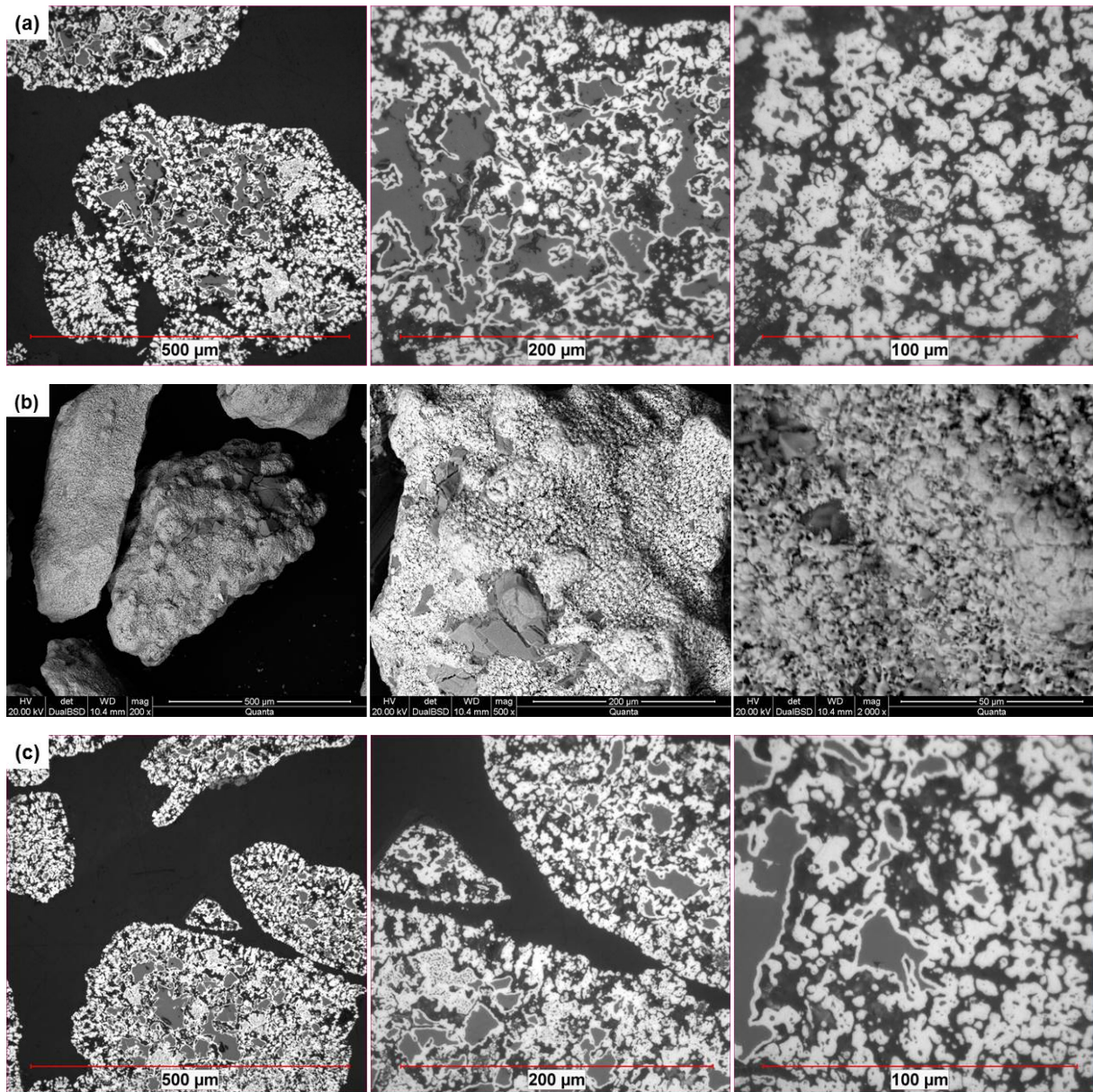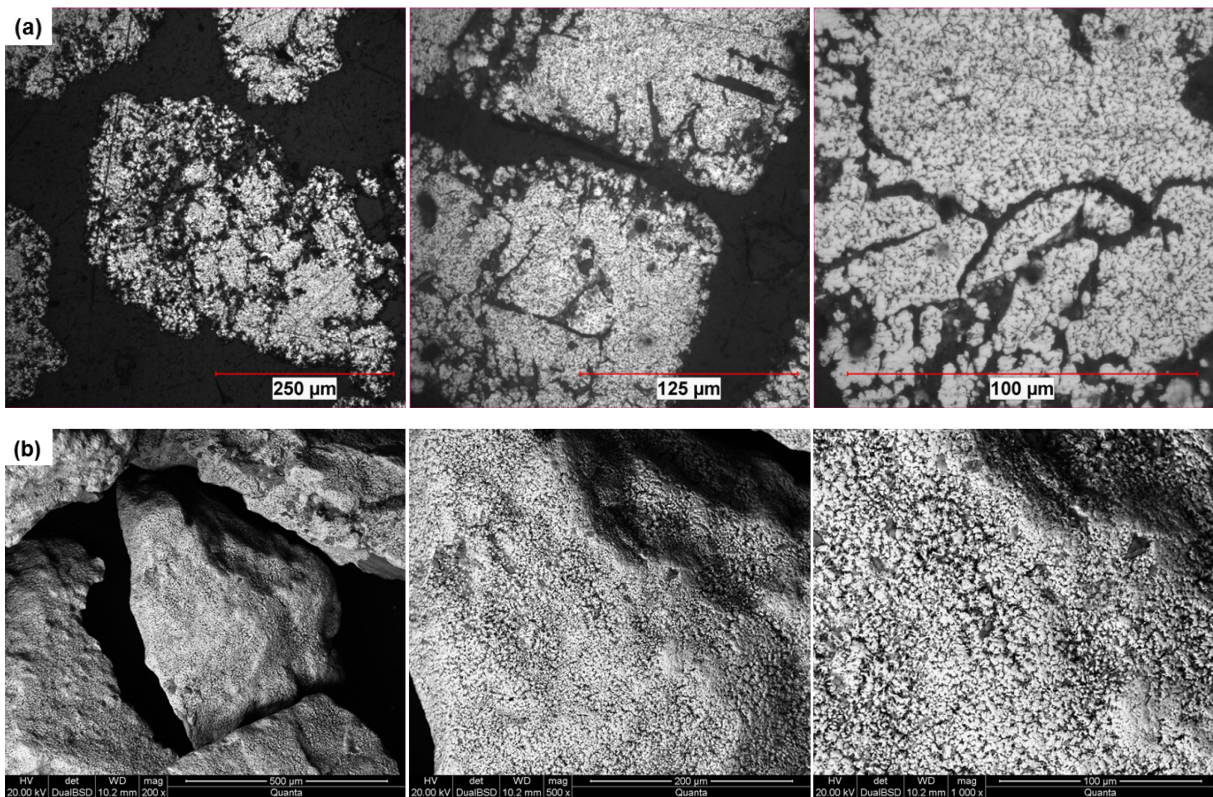

Figure 95: Morphological investigation of reduced samples of partially oxidized magnetite reduced at 700 °C with 0.5 %-wt. of MgO addition: (a) Polished micro-sections; (b) SEM surface images.

Figure 95 shows the morphological investigation of the reduced sample using the partly oxidized magnetite sample and an MgO-addition of 0.5 %-wt. As shown within the polished micro sections, small wüstite cores, which are covered by a dense iron layer, cannot be observed in comparison to completely oxidized samples shown before. The surface of the particles, shown within the SEM-images, represents a smooth behavior without any iron whiskers. That outcome confirms the trends of the degree of reduction against time, where the partly oxidized sample shows the best reducibility. As a result, a prior partial oxidation is the best pre-treatment in order to achieve the best combination between fluidization behavior and reducibility.

5.4.1 Determination of rate-limiting steps occurring during reduction of a magnetite-based ore with different oxidation degrees

For a better understanding of the differences in reducibility of the samples with different oxidation degrees, again the JMA model-fitting procedure is carried out. It has to be mentioned that in case of the natural magnetite, a de-fluidization of nearly 85 % of the material took place during the reduction experiment, as shown in Figure 92. As a consequence, the questions of validity for the results obtained by the fitting procedure must be asked. Figure 96 shows the results of the fitting procedure for the experiments at 700 °C reduction temperature and an MgO addition of 0.5 %-wt. for the input materials with different oxidation degrees, given in Figure 94.

(a)

(c)

(b)
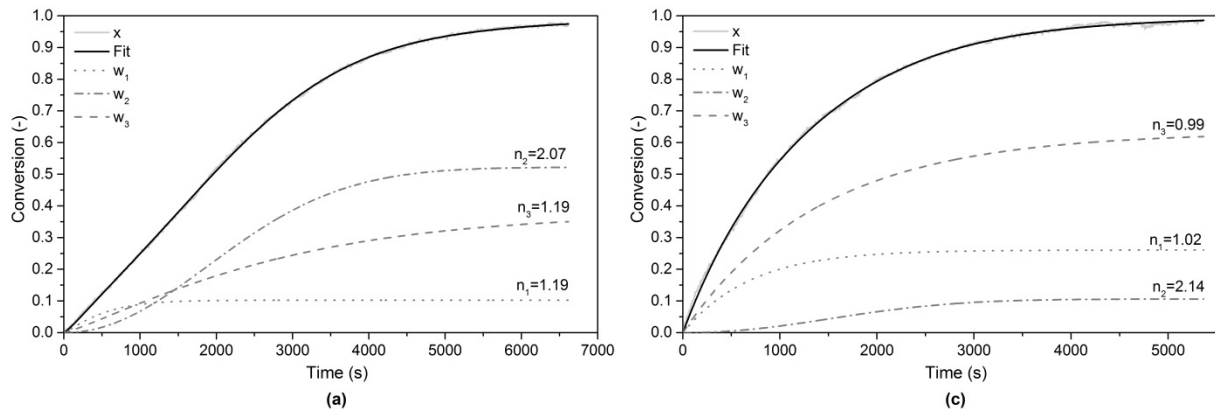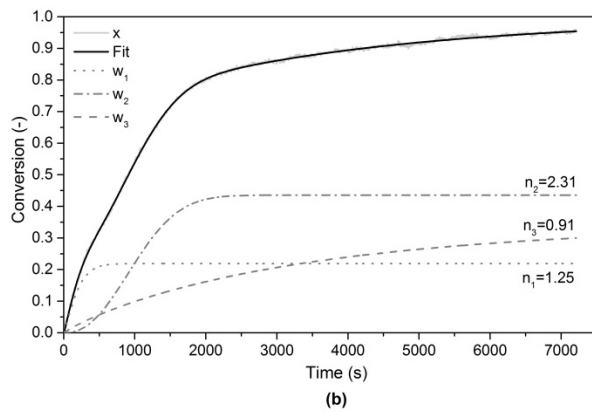
Figure 96: JMA fitting procedure for the investigation of the reduction from magnetite based samples with different oxidation degrees at 700 °C reduction temperature and 0.5 %-wt. MgO addition: (a) NM; (b) OM; (c) POM.

As shown in Figure 96 (a), the reduction of natural magnetite without prior oxidation (NM) seems to be controlled by a mixture of the nucleation processes and the chemical reaction. These results are in good agreement with the observations from the polished micro-section, where a porous shell can be observed which is growing from the particle surface to the center. At the iron/oxide interface, the processes of nucleation and chemical reaction challenge each other and therefore both are responsible for the limitation of the reduction rate. The results for the completely oxidized magnetite (OM), given in Figure 96 (b), indicate a limitation by the nucleation process and diffusion ($n_3 < 1$), while the diffusion mechanism is responsible for the low reduction rate at the final stage of reduction. This is again in good agreement with the observations from the polished micro-sections, where small remaining wüstite cores are covered by dense iron shells. As a result, the reducing gas is not able to reach the reaction interface anymore and the mechanism of diffusion becomes rate-limiting. For the partly oxidized magnetite (POM), the situation changes completely, as given in Figure 96 (c). Diffusion is not important anymore and the reduction is mainly controlled by the chemical reaction, also at the final stage. That is the reason why a nearly complete reduction could be achieved faster compared to the completely oxidized sample. This is also in good agreement with the results obtained from the polished micro-sections where the dense iron layers around small wüstite cores cannot be observed. Table 29 summarizes the results obtained from the fitting procedure.

Table 29: Weight factors, nucleation rate constants, kinetic exponents, rate constants and RMSD for multistep kinetic analysis (parallel) for the investigation of the reduction with different oxidation degrees at 700°C reduction temperature and 0.5 %-wt. MgO addition.

Sample		NM	OM	POM
Weight factors (-)	w_1	0.1023	0.2190	0.2608
	w_2	0.5223	0.4356	0.1060
	w_3	0.3753	0.3454	0.6332
Nucleation rate constants (s^{-1})	a_1	$5.69 \cdot 10^{-4}$	0.0013	0.0013
	a_2	$8.41 \cdot 10^{-8}$	$8.40 \cdot 10^{-8}$	$8.41 \cdot 10^{-8}$
	a_3	$7.49 \cdot 10^{-5}$	$6.37 \cdot 10^{-4}$	$7.38 \cdot 10^{-4}$
Kinetic exponents (-)	n_1	1.19	1.25	1.02
	n_2	2.07	2.31	2.14
	n_3	1.19	0.91	0.99
Rate constants (s^{-1})	k_1	0.0018	0.0050	0.0015
	k_2	$3.85 \cdot 10^{-4}$	$8.61 \cdot 10^{-4}$	$4.95 \cdot 10^{-4}$
	k_3	$3.49 \cdot 10^{-4}$	$3.01 \cdot 10^{-4}$	$7.11 \cdot 10^{-4}$
Root mean square deviation	RMSD	0.0039	0.0045	0.0058

Generally, further investigations are required concerning the ideal degree of oxidation and the corresponding optimal amount of MgO addition in order to achieve the fastest possible reduction and a complete fluidization. Based on the present investigations, complete prior oxidation is not beneficial for a fast complete reduction with the grain size distribution and process parameters given. An addition of MgO is definitely helpful to ensure a stable fluidization during the reduction procedure.

6 Use of iron ore ultra-fines for hydrogen-induced fluidized bed reduction

The direct use of iron ore ultra-fines for ironmaking is an interesting topic. Iron ore ultra-fines are characterized by their low grain size distribution. Typically, all particles have a size below 125μm. This type of iron ore is generally used as an input material for pelletizing plants that produce iron ore pellets for use in the conventional blast furnace or in different direct reduction aggregates. A direct use of these concentrates without prior agglomeration is only possible by using the fluidized bed technology. Using these ultra-fines in a shaft furnace-based direct reduction process will lead to problems regarding gas permeability and high dust generation and is therefore not possible. A direct use is of great industrial interest because the energy-intensive agglomeration step can be avoided. Pelletizing plants have an energy consumption up to 1.3 GJ/t iron ore pellets, depending on the process concept and the type of iron ore used.[182–184] Generally, the availability of iron ore concentrate has increased continuously in recent years, as already mentioned in Section 1.2 because of lower available iron ore qualities. This is yet another fact as to why a direct use of the iron ore ultra-fines will be of such interest in the future.

The low grain size distribution can lead to some troubles during hydrogen-induced fluidized bed reduction. The first ones are the cohesive forces that can act between the fine particles. If those forces become bigger than that which the fluid can exert to the particles, a fluidization would not be possible anymore. The second problem which might occur is the amount of elutriation. Because of the low grain size of the particles, the superficial gas velocity inside the reactor has to be kept low in order to keep the amount of elutriation in an acceptable range. The consequence of that is longer reduction times in order to provide a sufficient amount of reducing agent.

Figure 97 shows the powder classification diagram with respect to their fluidization properties. As demonstrated, typical iron ore ultra-fines are in between the Geldart particle groups C and A. Particles which belong to group C are known as hardly fluidizable because of the cohesive forces which are acting between the particles. One possibility to improve the fluidization behavior is the use of mechanical vibrators, which is often discussed in

literature.[123–125] An industrial application might be difficult and will decrease the efficiency of the overall process because of additionally required equipment.
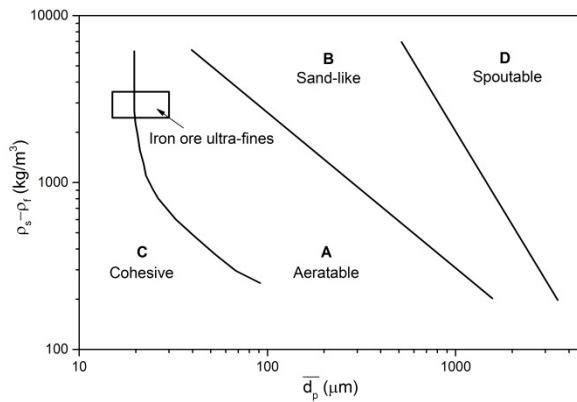
Figure 97: Powder classification regarding their fluidization properties including the area of typical iron ore ultra-fines.

Next, the general suitability of the iron ore ultra-fines for a hydrogen-induced fluidized bed reduction is investigated, with the focus on the fluidization behavior and the amount of elutriation occurring. First, hematite-based concentrates are investigated because hematite is known to have better fluidization properties and second, the special behavior of magnetite-based ultra-fines during hydrogen-induced fluidized bed reduction is discussed.

6.1 Direct reduction of hematite-based iron ore ultra-fines

In the following section, the principal aptitude of hematite based iron ore ultra-fines is discussed in terms of fluidization behavior and elutriation. To assess the behavior of the elutriation, fluid dynamic calculations are carried out and compared with the results obtained during the reduction experiments. For a more accurate description, different approaches for the elutriation rate constants are used. To evaluate the reducibility of the ore and define the efficiency of the process, values for the required specific gas rate at different superficial gas velocities are defined.

6.1.1 Experimental conditions and materials

For the experiments with the iron ore ultra-fines, the FBR 160 mm is used, as explained in detail in Section 3.1.2. The experiments are carried out at a reduction temperature of 700 °C and an absolute pressure of 1.1bar. The superficial gas velocities are varied between 0.1 and 0.3 m/s. Only hydrogen is used as the reducing and fluidization gas. The flow rates vary between 35.8 and 107.5 l/min (SATP), representing superficial gas velocities of 0.1 and 0.3 m/s, respectively. The values of superficial gas velocity are referred to the core reactor with a diameter of 160 mm. Because of the cross-section expansion to the freeboard, the superficial gas velocity is reduced by a factor of 0.36, which is essential for the further calculations.

Table 30 summarizes the process conditions. For the experiments with hematite-based iron ore ultra-fines, a perforated plate with 489 orifices (0.15 mm in diameter) is used to achieve the required pressure drop across the distributor.

Table 30: Process conditions for the reduction experiments.

Temperature (°C)	700
Pressure abs. (bar)	1.1
Gas composition (%-vol.)	100 H_2
Flow rate (l/min-SATP)	35.8–107.5
Superficial gas velocity (m/s)	0.1-0.3
Input mass iron ore (g)	5000

The hematite ultra-fines used for the investigations are characterized by a grain size distribution below 125 μm. The specified grain size distribution is achieved by mixing three different fractions together; <20 μm, 20-60 μm and 60-125 μm using a weight ratio of 40, 50 and 10 %-wt. Figure 98 (left) shows the grain size distribution of each fraction used. The specified mixture has a d_{50} value of 26μm (50 %-wt. of the particles are smaller than 26 μm). The iron ore ultra-fines employed are characterized by a high initial porosity, shown within the polished micro-section of the ore in Figure 98 (right). The combination of the fluidized bed technology, the porous iron ore structure and low grain size along with the exclusive use of hydrogen as a reducing agent should lead to very good kinetical behavior during the reduction procedure.
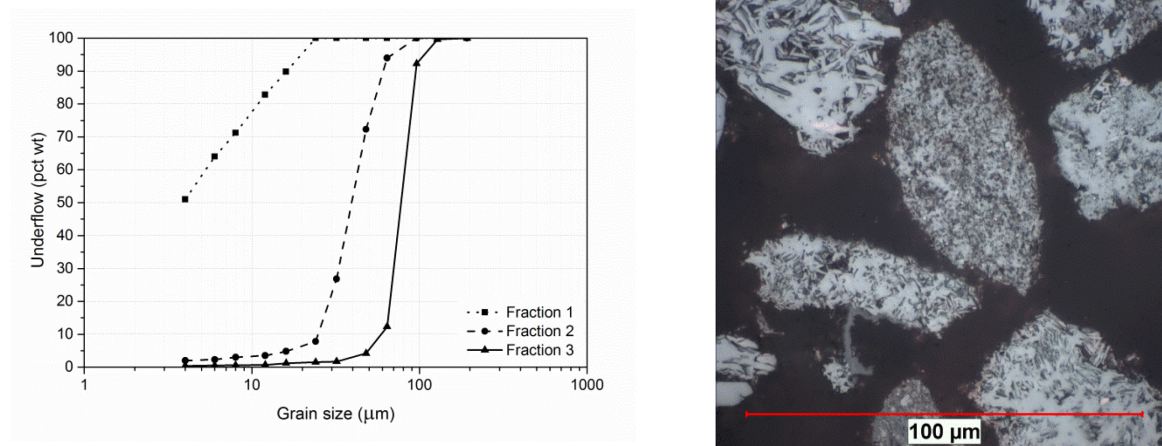
Figure 98: Grain size distribution (left) and polished micro section (right) of the iron ore input material (hematite-based ultra-fines).

Table 31 shows the chemical analysis and the corresponding ratios of each iron ore fraction used and that for the iron ore mixture. For each experiment, 5000 g of iron ore are charged into the reactor, ending in approximately 1350 g of oxygen in the sample, which is bonded on iron.

For the experiments, the reactor is pre-heated to the defined reduction temperature before the material is charged. The pre-heating of the material takes place under constant nitrogen

flow with a flow rate of 30 l/min (SATP), which means a superficial gas velocity of 0.084 m/s at 700 °C temperature. After reaching the required temperature, the nitrogen is replaced by the reducing gas and the reduction takes place until achieving a constant weight signal, signifying a complete reduction.

Table 31: Chemical composition of different iron ore fractions.

	Fraction 1	Fraction 2	Fraction 3	Feed material
Fe_{tot} (%-wt.)	62.46	63.24	62.87	62.89
Fe^{2+} (%-wt.)	0.10	0.10	0.10	0.10
CaO (%-wt.)	0.35	0.27	0.55	0.33
MgO (%-wt.)	0.07	0.05	0.23	0.08
SiO_2 (%-wt.)	5.90	5.95	6.18	5.95
Al_2O_3 (%-wt.)	2.21	1.61	0.19	1.71
Grain size (µm)	<20	20-60	60-125	0-125
Mixture (%-wt.)	40	50	10	100
Mixture (g)	2000	2500	500	5000

6.1.2 Fluid dynamics of the reduction experiments and expected amount of elutriation

To check the fluid dynamics of the reduction experiments and the amount of theoretical elutriation which can be expected during the experiments, a calculation of the Grace diagram is done again which also includes the operation area of the reduction experiments. The calculation procedure is already explained in Section 2.5.1. Table 32 shows the parameters used for the calculation procedure. The calculation of the operation areas is done for two different cases, representing two different solid densities. For Case 1, the solid particle density was assumed to be 4000 kg/m³, representing the density of the initial iron ore. During reduction, oxygen is removed from the iron ore sample. As a result, the gross density decreases because of the nearly constant volume of the particles and increasing porosity. The second calculation case is therefore carried out with a solid gross density of 2800 kg/m³, which represents the reduced sponge iron. As mentioned earlier, hydrogen is the only gas component in the reducing gas mixture. Thus, density and kinematic viscosity of hydrogen were calculated at reduction temperature (700 °C). During the reduction procedure, a change in the gas composition occurs. At the initial stage of reduction, a substantial amount of hydrogen is oxidized by the oxygen which is removed from the iron ore. This ends in a high amount of water vapor in the gas mixture. If the reduction is already finished, no further oxidation of the hydrogen takes place, ending in a lower gas density compared to the beginning of the experiment. To consider this, calculations for two different gas compositions for both cases were carried out. The first one represents only hydrogen; the second one represents a mixture of hydrogen and water vapor. The mixture of H_2/H_2O was assumed to be on the equilibrium between FeO and Fe_3O_4 at a reduction temperature of 700 °C, representing a gas mixture of 46.3 %-vol. H_2 and 53.7 %-vol. H_2O. For the assumption of the expected elutriation amount, only the case with pure hydrogen is considered. The sphericity of the particles was supposed to be 0.86, to be more consistent with the real behavior of the iron ore particles. A value of 1 would represent an ideal spherical shape of the particles, which is definitely not realistic, as already explained in previous sections.

Table 32: Calculation parameters Grace diagram.

		Case 1		Case 2		
		H_2	H_2/H_2O	H_2	H_2/H_2O	
Density fluid at 700 °C	ρ_F	0.027	0.072	0.027	0.072	kg/m³
Gross density solids	ρ_S	4,000	4,000	2,800	2,800	kg/m³
Viscosity fluid at 700 °C	η	$2.03 \cdot 10^{-5}$	$3.54 \cdot 10^{-5}$	$2.03 \cdot 10^{-5}$	$3.54 \cdot 10^{-5}$	Pa s
Minimum fluidization porosity	ε_{mf}	0.39	0.39	0.39	0.39	-
Sphericity solids	ϕ_s	0.86	0.86	0.86	0.86	-

Figure 99 shows the resulting Grace diagrams for the two different solid densities. The solid black operation area represents the calculation considering only hydrogen, while the dashed blue operation area represents the gas mixture containing hydrogen and water vapor. The values of the superficial gas velocities in the diagram refer to the gas velocities occurring in the core reactor (160 mm diameter). All calculations are done with the gas velocities occurring in the freeboard (265 mm diameter) which are lower by a factor of 0.36 following to the different cross-section areas. The operation areas cover the range from 0.1 to 0.3 m/s superficial gas velocity and particle sizes between 4 and 100 μm. Particles bigger than 100 μm were not considered in the calculations because of the small weight ratio in the sample portion. Additionally, the terminal velocities of the particles with a size of 4, 20 and 100 μm are shown within the diagram.
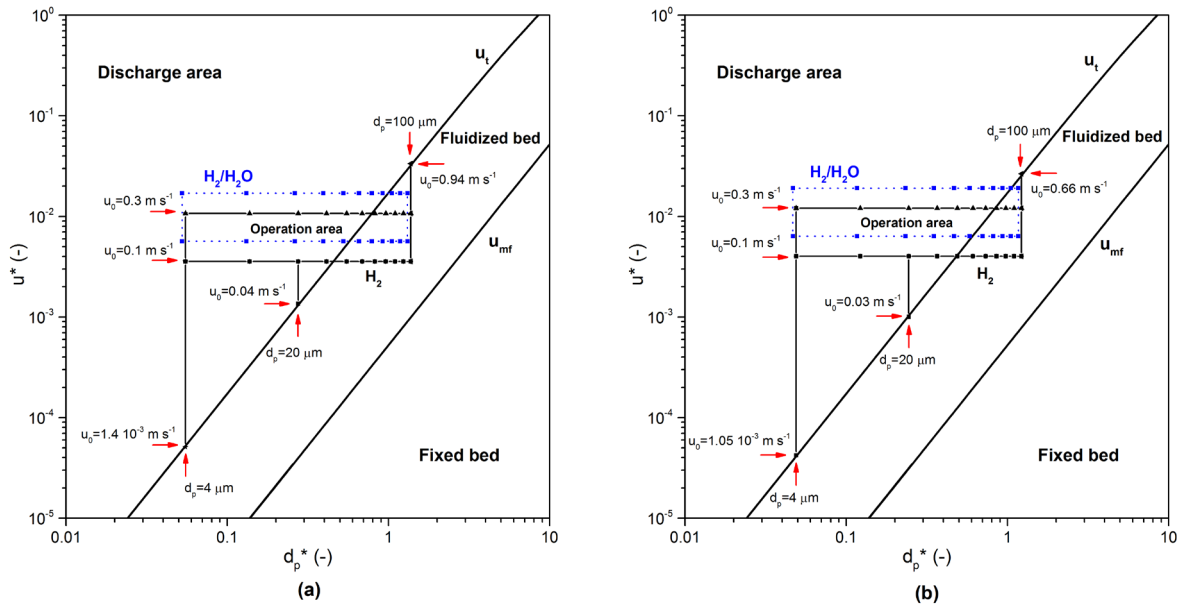
Figure 99: Grace diagram including operation areas for the experimental trials: (a) Case 1- solid density 4000 kg/m³ representing iron ore concentrate; operation area solid black represents pure H_2; operation area dashed blue represents H_2/H_2O mixture, (b) Case 2–solid density 2800 kg/m³ for reduced sponge iron, operation area solid black represents pure H_2; operation area dashed blue represents H_2/H_2O mixture.

For the different superficial gas velocities, the theoretical amount of elutriation can be estimated using the calculated Grace diagram by the determination of the critical particle diameter where the elutriation starts. It is given by the intersection between the operation area with the curve, representing the terminal velocity at the given superficial gas velocity.

Based on this information and the given grain size distribution, shown in Figure 98 (left), the amount of expected elutriation can be estimated. The results for the case of pure hydrogen and different solid densities are presented in Table 33.

Table 33: Resulting values of expected amount of elutriation according to the Grace diagram for pure hydrogen and different solid densities.

u_0 fluidized bed (m/s)	u_0 freeboard (m/s)	Particle diameter elutriation (µm)	Expected elutriation (%-wt.)	Expected elutriation (g)
Case 1 H$_2$ – Solid density 4000 kg/m³				
0.040	0.015	20	~40	~2000
0.100	0.037	31	~54	~2700
0.300	0.109	58	~84	~4200
0.940	0.343	100	~100	~5000
Case 2 H$_2$ – Solid density 2800 kg/m³				
0.030	0.011	20	~40	~2000
0.100	0.037	39	~65	~3250
0.300	0.109	68	~87.5	~4375
0.660	0.241	100	~100	~5000

As shown, a superficial gas velocity during the reduction experiments of 0.1 m/s would end in a theoretical amount of elutriation in the range of 54 to 65 %-wt. of the input material for solid densities of 4000 and 2800 kg/m³, respectively. An increase in the superficial gas velocity to 0.3 m/s also increases the amount of theoretical elutriation to 84 and 87.5 %-wt. of the input material for solid densities of 4000 and 2800 kg/m³, respectively.

If these high values of elutriation were to really occur during the reduction experiments, a useful design of the process conditions would not be possible anymore. Lowering the superficial gas velocity below values of 0.1 m/s could decrease the amount of elutriation but it would take too much time to provide the sufficient amount of reducing agent to the material, leading to unacceptably long reduction times.

After the experiments, the amount of elutriation was measured by collecting all the material that left the reactor during the experiments. This includes the material which was collected in the external cyclone, the dust filter units and also in the connection pipe between the reactor and the off-gas duct. The internal cyclone was removed from the system before the experiments because the design of the cyclone does not fit to the given process conditions. As a result, there was no possibility to return the elutriated material into the fluidized bed.

6.1.3 Experimental results and discussion

In the following section, the results of the reduction experiments are shown and discussed. First of all, it is required that the fluidization behavior during the reduction procedure be clarified. If a stable fluidization during the whole reduction is not possible a further evaluation of the experiments will be not useful. Figure 100 shows the detailed test evaluation of the experiment which was carried out with a superficial gas velocity of 0.14 m/s. Figure 100 (c) shows the values of pressure drop across the distributor and the material during the experiment and the calculated, theoretical pressure drop across the material only. For the calculation, the curve of weight loss is used. To compare the measured results with the

calculated ones, the pressure drop across the distributor only was measured under reduction conditions before the experiment without any material inside the reactor. Subtraction of the pressure drop across the distributor from the measured values during the experiments yields the gray line, representing the pressure drop across the material only. As can be seen, the measured pressure drop follows the calculated, theoretical one. As a result, a complete and stable fluidization of the iron ore ultra-fines was achieved during the experiments without any troubles, also at high degrees of reduction. Although the very low grain size distribution was used, no sticking occurred during the experiments. Spontaneous de-fluidization of the material can be observed by a sharp decrease in the pressure drop in a very short time, which is not the case here.
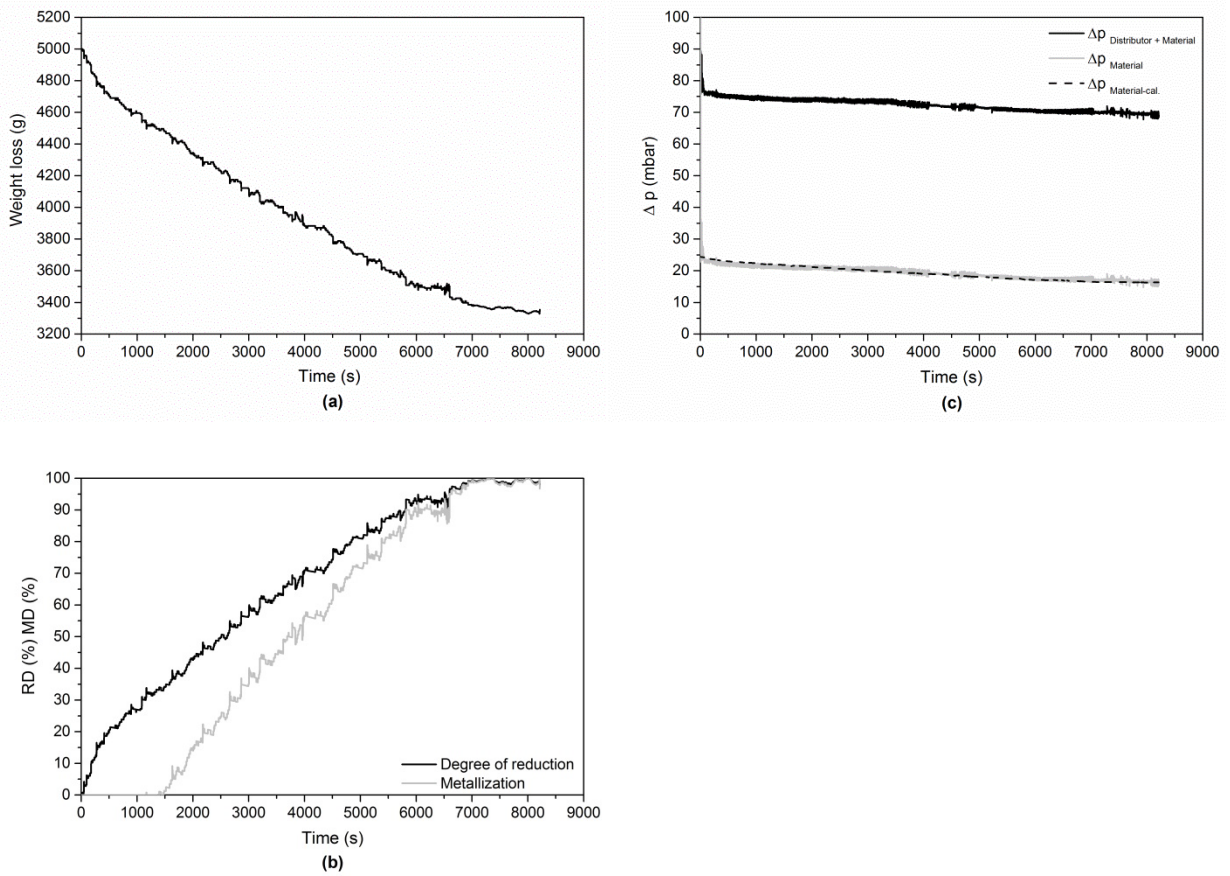
Figure 100: Detailed test evaluation for a superficial gas velocity of 0.14 m/s: (a) weight loss against reduction time; (b) degree of reduction and metallization against reduction time; (c) pressure drop across distributor and material against reduction time.

Figure 100 (a) and (b) shows the measured weight change of the sample portion observed during the reduction experiment as well as the calculated curves of the degree of reduction and metallization. As shown, a reduction time of approximately 7000s is required to obtain a complete reduction with the present conditions. The progress of reduction can be divided into two stages: a fast initial reduction stage to a degree of reduction of approximately 20 %, corresponding to the reduction from Fe_2O_3 to Fe_3O_4 and partly to FeO, followed by a nearly constant reduction rate until a high conversion degree is achieved. Nearly no deceleration of

the reduction rate at high degrees of reduction takes place, signifying the very good kinetics of the material.

The amount of elutriation for the experiment at 0.14 m/s superficial gas velocity was 642 g, representing the remaining material after the experiment in the external cyclone, the dust filter units and the connection pipe between the reactor and the off-gas duct. This represents an amount of 12.8 %-wt. of the iron ore input. For the test evaluation, it is assumed that the elutriation occurs in a linear way during the whole reduction time. The reason for this assumption is the change in the density of the solids during the reduction, starting from 4000 kg/m³ at the beginning and ending at 2800 kg/m³ at the end of reduction. For a better description, a measurement of the elutriated material during certain times of reduction would be required, which is not possible in this case because the system cannot be opened during the reduction sequence when the reducing gas is inside the system. In fact, the assumption that the elutriation occurs in a linear way is not really accurate. A method for a better description of the elutriation behavior will be given in Section 6.1.4.

The amount of elutriation is considered (in a linear way) during the calculation of the curve of degree of reduction, which only represents the progress of the reduction of the bed material. Considering an overall degree of reduction of 50 % for the elutriated particles, the weight of elutriation can be recalculated to 0 % degree of reduction, ending in 738 g of elutriated material. This amount signifies 14.8 %-wt. of the iron ore input. The expected amount of elutriation at a superficial gas velocity of 0.14 m/s using only hydrogen as fluidization according to the calculations within the Grace diagram should be 67.5 and 79.6 %-wt. for solid densities of 4000 and 2800 kg/m³, respectively. This is 4.6-5.4 times higher than the real elutriation amount during the experiment.

Figure 101 shows the progress of reduction at 700 °C reduction temperature for different superficial gas velocities, ranging from 0.1 to 0.3 m/s. The curves are smoothed to achieve better readability. The time to reach a degree of reduction of 95 % decreases with increasing superficial gas velocity from 143 to 50 min for 0.1 and 0.3 m/s, respectively. For the calculation, the elutriation is considered to occur in a linear way for all experiments.
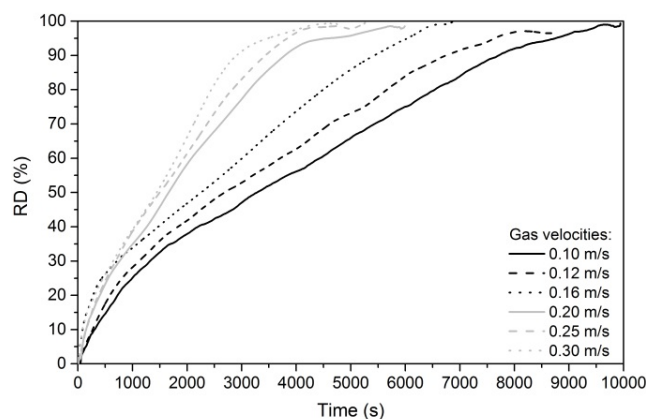
Figure 101: Progress of reduction (smoothed) at different superficial gas velocities representing different hydrogen flow rates.

For all experiments, shown in Figure 101, a complete and stable fluidization was achieved during the whole reduction procedure.

Figure 102 displays the dependence of elutriation (%/min) for the recalculated amount of elutriation (0 % RD) and the required reduction time to reach a degree of reduction of 95 % against superficial gas velocity. As it can be seen, in both cases a nearly linear relationship depending on the superficial gas velocity exists. With increasing superficial gas velocity, the elutriation increases, while at the same time, the required reduction time decreases.
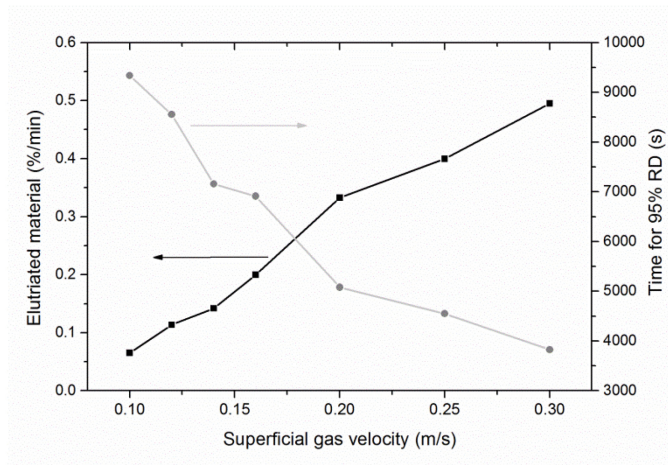
Figure 102: Elutriated material and required reduction time for 95% degree of reduction.

Table 34 summarizes the main results from the reduction experiments at different superficial gas velocities including the time to reach a degree of reduction of 95 %, the amount of elutriation and the theoretically calculated values for the expected elutriation from the Grace diagram.

Table 34: Main results of reduction experiments carried out with different superficial gas velocities at 700°C reduction temperature.

Test No.	Superficial velocity (m/s)	Flow rate (l/min – SATP)	Time for 95 % reduction (min)	Elutriation (% of input)	Elutriation recalc. from 50 to 0 % RD (% of input)	Expected Elutriation – Grace (% of input)
1	0.10	35.8	143	8.1	9.3	54.0–65.0
2	0.12	43.0	125	12.3	14.1	57.5–70.0
3	0.14	50.2	104	12.8	14.8	63.8–73.8
4	0.16	57.3	96	16.6	19.1	68.8–76.3
5	0.20	71.6	68	19.7	22.7	75.0–82.0
6	0.25	89.5	60	20.9	24.0	77.5–85.0
7	0.30	107.5	50	21.5	24.7	84.0–87.5

As shown, the ratio between expected and real elutriation decreases from 5.8-7 for the lowest gas velocity to 3.4-3.5 for the highest gas velocity, representing 0.1 and 0.3 m/s, respectively. One reason for the big difference between the real and expected amount of elutriation is the formation of agglomerates during the reduction procedure. Figure 103 shows SEM surface images of the raw material (a,b) and the sample portion after reduction (c,d). The reduction in that case took place at 700°C reduction temperature and a superficial

gas velocity of 0.1 m/s. In contrast to the raw material, spherical agglomerates with a diameter up to 100 µm can be observed the images of the reduced sample. It can be seen that small particles stick on the surface of bigger ones, leading to the formation of agglomerates. This phenomenon might decrease the amount of elutriation but the size of the agglomerates during the reduction became too small to influence the fluidization behavior. The amount of elutriation of this experiment was in the range of 9 %-wt. of the iron ore input. In the raw material mixture 40 %-wt. of the particles are smaller than 20 µm. The SEM surface images of the reduced sample show a lower number of particles smaller than 20 µm, compared to the raw material. This fact confirms the assumption that small particles are involved in the formation of agglomerates.
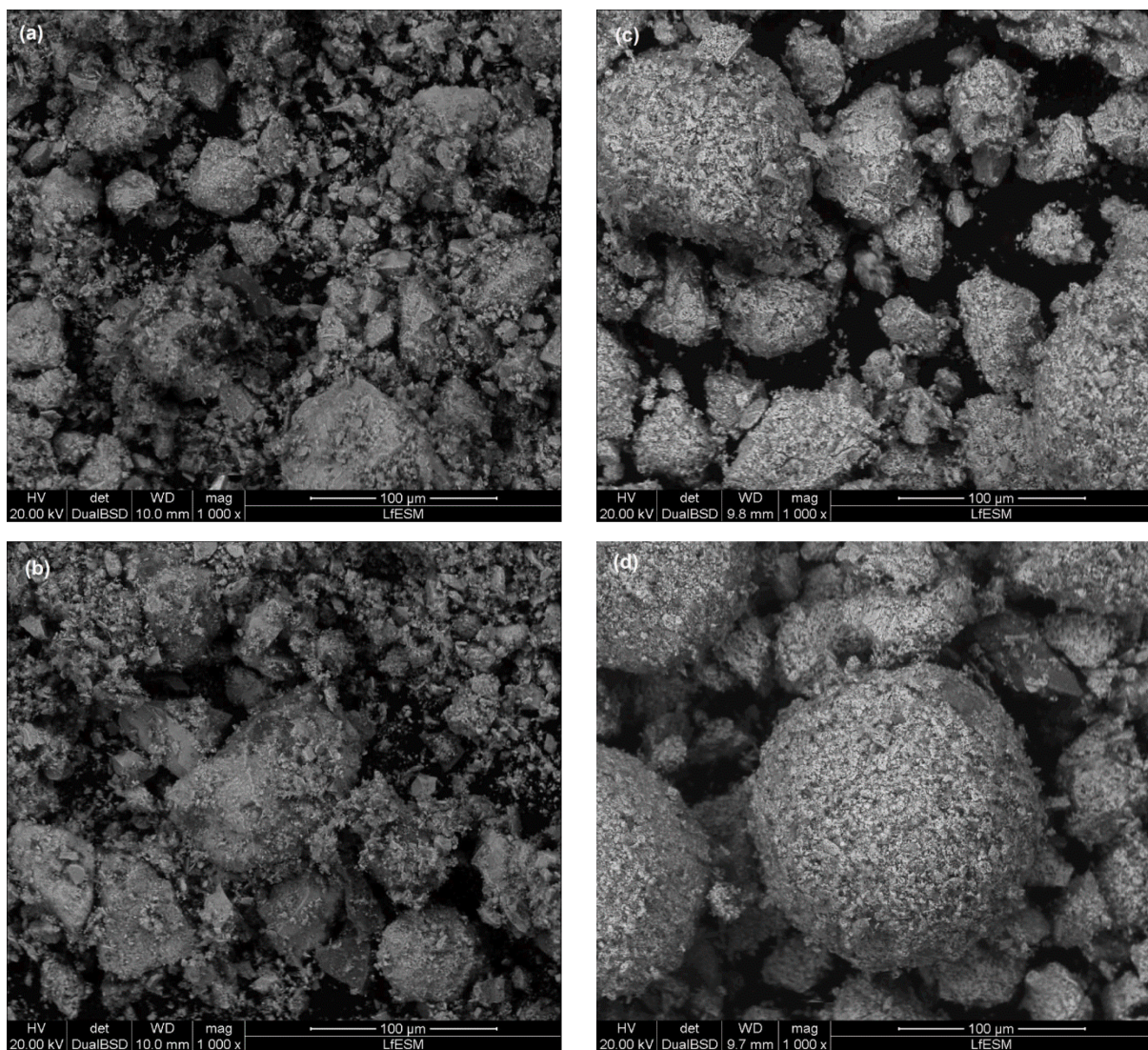
Figure 103: SEM surface images of particles with a magnification of 1000: (a) and (b) iron ore concentrate; (c) and (d) sponge iron reduced at 700°C and a superficial gas velocity of 0.1 m/s showing agglomerates.

The formation of particle agglomerates during the fluidization processes has been investigated by many authors.[140,185–188] Lei et al.[185] defined a fluidization regime diagram for

iron powder using nitrogen as a fluidization agent. Four different regions were determined: stable fluidization, agglomerating fluidization, gradual de-fluidization and fast de-fluidization, depending on temperature, superficial gas velocity and gas density. Higher temperature and lower gas velocity as well as lower gas density will support gradual and fast de-fluidization. During the present investigations, only hydrogen acts as a fluidization and reducing agent. Because of this difference and the fact that the fluidization is stable during the whole reduction procedure, as demonstrated by the trends of measured pressure drop against reduction time, it can be assumed that the conditions of the present investigations are in the area of agglomerating fluidization. A similar behavior was found by He et al.[140]

6.1.4 Elutriation correlations for a better description of the elutriation behavior

For better understanding and a more accurate prediction of the amount of elutriation occurring in the reduction experiments, different elutriation correlations for gas-solid fluidization are tested and the results are compared with the amount of elutriation which occurred during the reduction experiments. Chew at el.[135] reviewed a wide range of different correlations which are reported in literature. Based on this investigation, three different elutriation correlations are chosen which fits best to the present process conditions. The correlations used were published by Lin et al.[189] in 1980, Geldart and Wong[190] in 1987 and Tasirin and Geldart[191] in 1999. They are shown in Equation (54), Equation (55) and Equation (56), respectively.

$$K_{ih}^* = 9.43 \cdot 10^{-4} \cdot \rho_g \cdot u_g \left(\frac{u_g^2}{g \cdot d_{pi}} \right)^{1.65} \tag{54}$$

$$K_{ih}^* = 13.52 \cdot \rho_g \cdot u_g \cdot exp \left(-30.3 \frac{u_{ti}}{u_g} \right) \tag{55}$$

$$K_{ih}^* = 2.66 \cdot 10^{-5} \cdot \rho_p \cdot \left(\frac{u_g}{0.2} \right)^3 \cdot \left(1 - \frac{u_{ti}}{u_g} \right)^{0.3} \tag{56}$$

K_{ih}^* represents the elutriation rate constant, ρ_g the density of the gas, u_g the superficial gas velocity, g the gravitational constant, d_{pi} the mean particle size of size i particles, u_{ti} the terminal velocity of size d_{pi} particles and ρ_p the density of the particles.

The calculated elutriation rate constant can be used for the prediction of the amount of elutriation against the reduction time using the following equation, which is already explained in Section 2.5.1.2:

$$m_{i,t} = x_{Bi0} \cdot M_B \left[1 - exp \left(-K_{ih}^* \frac{A \cdot t}{M_B} \right) \right] \tag{57}$$

For the prediction of the amount of elutriation, different calculations with different assumptions are carried out. The calculation parameters used are summarized in Table 35.

For the calculations, the geometry of the reactor itself has to be kept in mind. Above the grid, a cylindrical shaped part follows with a height of 200 mm. After that, the reactor cross-section area expands from 160 mm to 265 mm with an opening angle of 8°. In the case of charging 5 kg of the given iron ore concentrate and a superficial gas velocity of 0.1 m/s, the bed surface in fluidized state appears at the level of the starting cross-section expansion, illustrating Case 1. Increasing the gas velocity also increases the bed expansion. Therefore, at 0.2 and 0.3 m/s superficial gas velocity in the cylindrical core reactor, the bed surface in fluidized state appears in the area where the cross-section area expansion takes place. Resulting from cold-fluidization tests, the level of the bed surface is observed to be approximately 50 and 100 mm above the cylindrical shaped core reactor for superficial gas velocities of 0.2 and 0.3 m/s, respectively. So, for the calculations of the amount of elutriation for Cases 2 and 3, representing 0.2 and 0.3 m/s superficial gas velocity in the core reactor, the reactor area and the corresponding superficial gas velocity on the bed surface in the area of the cross section expansion are used.

For Cases 1-3, values for the gas density and viscosity representing pure hydrogen at 700 °C are used. The particle density was assumed to be 3400 kg/m³, indicating an average value of the iron ore and the reduced sponge iron.

Table 35: Calculation parameters for the prediction of elutriation using different correlations.

	Case 1	Case 2	Case 3	Case 4	Case 5	
	Gas velocity 0.1 m/s	Gas velocity 0.2 m/s	Gas velocity 0.3 m/s	Gas velocity 0.1 m/s - variable process parameters	Gas velocity 0.036 m/s in the freeboard – variable process parameters	
Gas density ρ_g	0.027	0.027	0.027	0.245-0.046	0.245-0.046	kg/m³
Gas viscosity μ_g	$20.3 \cdot 10^{-6}$	$20.3 \cdot 10^{-6}$	$20.3 \cdot 10^{-6}$	$(37.3\text{-}32.4) \cdot 10^{-6}$	$(37.3\text{-}32.4) \cdot 10^{-6}$	Pa·s
Particle density ρ_p	3400	3400	3400	4000-3200	4000-3200	kg/m³
Gas velocity core reactor	0.1	0.2	0.3	0.1	0.1	m/s
Gas velocity bed surface u_g	0.1	0.17	0.22	0.1	0.036	m/s
Reactor area bed surface A	0.0196	0.0232	0.0272	0.0196	0.0551	m²
Mean particle size of size i particles d_{pi}	$10 \cdot 10^{-6}$	$10 \cdot 10^{-6}$	$10 \cdot 10^{-6}$	$10 \cdot 10^{-6}$	$10 \cdot 10^{-6}$	m
Terminal velocity of size i particles u_{ti}	0.019	0.019	0.019	0.014-0.019	0.014-0.019	m/s
Mass fraction of size i particles w_i	40	40	40	40	40	%-wt.
Sample mass M_B	5	5	5	5	5	kg

Only the iron ore fraction below 20 μm is used in the calculation as possible elutriation material. A mean particle size of 10 μm was assumed with a mass fraction of 40 %-wt. of the total iron ore input material. This ends in a value of 0.019 m/s for the terminal velocity of these particles under the given process conditions. For a superficial gas velocity of 0.1 m/s in the core reactor, two additional calculations with varying values of gas density and gas viscosity as well as density of the particles are done, representing Cases 4 and 5. For that reason, three different elutriation rate constants were calculated; one for the initial stage of reduction, representing the reduction from Fe_2O_3 to Fe_3O_4 on the assumption that the entire hydrogen is converted to water vapor; a second one for the reduction from Fe_3O_4 to FeO where it is assumed that the gas composition is on the equilibrium between Fe_3O_4 to FeO; and a third one for the reduction from FeO to Fe where it is assumed that the gas composition is on the equilibrium between FeO and Fe. The density of the solids is assumed to be decreased from 4000 to 3600 and to 3200 kg/m³ in the second and third stages. These assumptions should reproduce the real behavior during the reduction sequence more accurately. For Case 5, the superficial gas velocity and reactor diameter in the freeboard of the reactor are chosen.

The results for the three different elutriation correlations used at different superficial gas velocities (Cases1 to 3) and the calculation parameters given in Table 35 are shown in Figure 104. The orange dot in the diagrams depicts the real amount of elutriation which occurred during the reduction experiments.
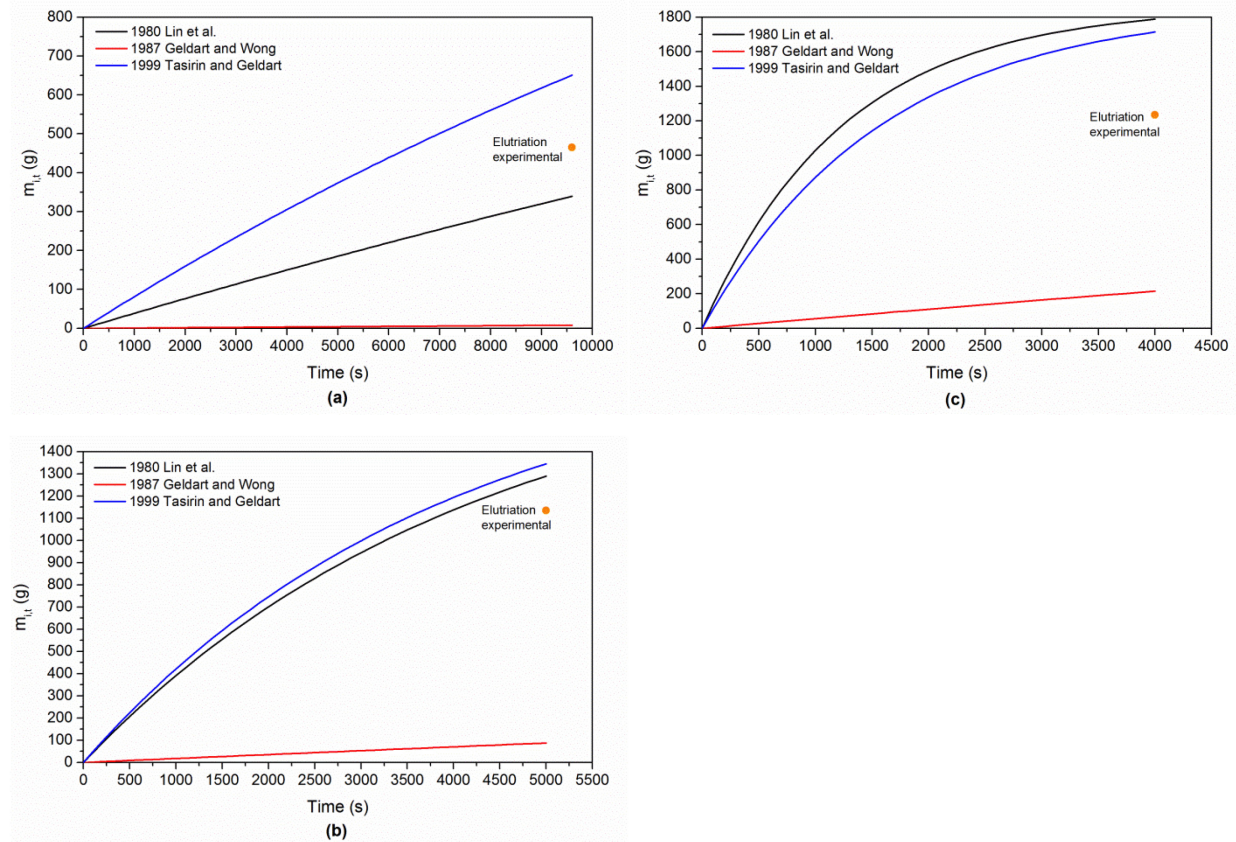
Figure 104: Prediction of the amount of elutriation occurring at different superficial gas velocities: (a) Case 1–0.1 m/s; (b) Case 2–0.2 m/s; (c) Case 3–0.3 m/s.

As shown, the elutriation correlation by Geldart and Wong delivers values for the elutriation which are highly underestimated in all three cases. For Case 1, the correlation by Lin et al. shows an amount of elutriation that is too low compared to the real value, while the correlation by Tasirin and Geldart shows values which are slightly overestimated. For the second case, both correlations provide values of elutriation which are slightly too high, while those of Lin et al. are even closer to the real amount of elutriation. At the highest superficial gas velocity, illustrated in Case 3, the situation changes. Therefore, the correlation by Tasirin and Geldart is closest to the real value, while the difference is bigger compared to the case of lower superficial gas velocities.

Figure 105 shows the results of the elutriation prediction for Cases 4 and 5. For Case 4, the superficial gas velocity and the cross-section area in the core reactor are used for the calculation. For Case 5, the superficial gas velocity and the cross-section area in the freeboard are used for the calculation. As shown, for Case 4, an overestimation of the amount of elutriation can be observed in case of the use of the elutriation correlations of Lin et al. and Tasirin and Geldart. For Case 5 all correlations show too low values of elutriation.
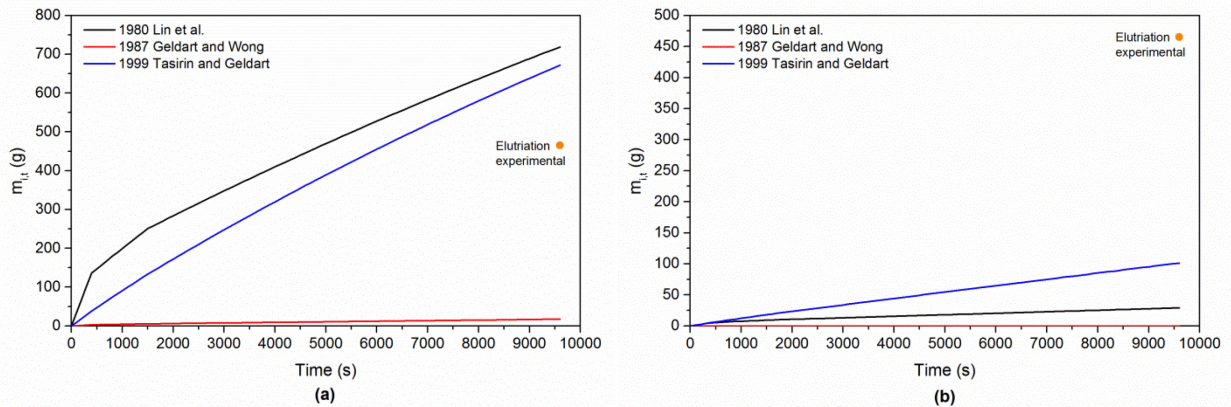
Figure 105: Prediction of amount of elutriation: (a) Case 4–with regard to 0.1 m/s occurring in the core reactor (160 mm); (b) Case 5– with regard to lower superficial gas velocity in the freeboard.

In fact, based on the actual calculations, no general elutriation correlation can be defined which describes the real elutriation behavior accurately for all cases. Generally, these correlations are based on empirical assumptions defined for a special case. Therefore, using these correlations for the current investigations will lead to some inaccuracies. Compared to the results, using only the terminal velocity of the particles for the calculation of the expected amount of elutriation, the predictions are much closer to the real amount of elutriation, as summarized in Table 36. For superficial gas velocities up to 0.2 m/s, the correlation by Lin et al. is the most suitable one for describing the amount of elutriation. At the highest gas velocity, the correlation published by Tasirin and Geldart fits best.

It has to be noted, that different assumptions were made for the calculations, as explained above. As a result, it is not really possible to draw accurate conclusions, but it is the only possibility for the rough estimation of the amount of elutriation occurring in the fluidized bed reactor system used in the present investigations.

Table 36: Comparison of the amount of elutriation of experimental data and different calculation procedures.

| Elutriation | Superficial gas velocity core reactor | | | | | |
| | 0.1 m/s | | 0.2 m/s | | 0.3 m/s | |
	(g)	Difference (%)	(g)	Difference (%)	(g)	Difference (%)
Experimental	465	-	1135	-	1235	-
Terminal velocity	2975	+540	3630	+220	4288	+247
Elutriation correlations						
Lin et al.	340	-27	1290	+14	1788	+45
Geldart and Wong	8	-98	87	-92	215	-83
Tasirin and Geldart	623	+34	1325	+17	1705	+38
Case 4						
Lin et al.	719	+55				
Geldart and Wong	18	-96				
Tasirin and Geldart	670	+44				

6.1.5 Required specific gas rate

The specific gas rate (SGR) is an important value that defines the gas consumption and therefore the efficiency of the reduction process. The SGR is defined as the required hydrogen demand to reach a degree of reduction of 95 %, as shown in the following equation:

$$SGR_{95} = \frac{V_{H_2 95\% RD}(m^3 - SATP)}{m_{Ore}(t)}$$
(58)

Table 37 summarizes the values of the SGR_{95} obtained in the reduction experiments with different superficial gas velocities to reach a degree of reduction of 95 %. The amount of elutriation was also considered in the calculation to be reduced to 95 % degree of reduction. A general trend of rising values for SGR_{95} with increasing superficial gas velocity can be observed.

Table 37: SGR$_{95}$ at different superficial gas velocities considering the amount of elutriated material.

Superficial velocity (m/s)	SGR$_{95}$ (m³/t$_{Ore}$ –SATP)$^)$
0.10	1115.4
0.12	1226.3
0.14	1197.2
0.16	1348.0
0.20	1213.5
0.25	1374.7
0.30	1397.9

Figure 106 shows the comparison between the experimental degree of reduction and the thermodynamic limitation at a reduction temperature of 700 °C for different superficial gas velocities. The thermodynamic limitations were calculated using the equilibrium gas compositions between Fe and FeO as well as FeO and Fe$_3$O$_4$ at the given reduction temperature according to the Baur-Glässner diagram. Because of the fact that the amount of elutriation cannot be clearly linked to a certain time of the reduction experiment, the calculations of the thermodynamic equilibriums were done on the assumption that the entire amount of elutriation had already been elutriated at the start of the reduction period. As a result, the experimental results would be even closer to the thermodynamic limitation because in that case, the amount of elutriation was considered to occur in a linear way during the whole reduction procedure. Nevertheless, at a low superficial gas velocity, representing 0.1 m/s, the amount of elutriation is in an acceptable range and the reduction proceeds near the thermodynamic limitation, which ends in a nearly maximum possible gas utilization of hydrogen. At higher superficial gas velocities, representing 0.3 m/s, the deviation is also not so big, but it is still larger compared to the lower superficial gas velocity also due to the higher amount of elutriated material. In fact, no general kinetic limitation occurs because the supply of the reducing agent limits the progress of reduction, especially at low gas velocities.
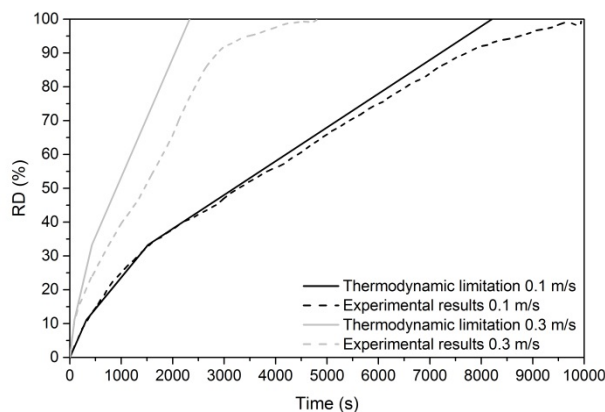
Figure 106: Comparison of experimental data with thermodynamic limitation at a reduction temperature of 700 °C at different superficial gas velocities.

Figure 107 compares the theoretical minimum reduction time for 95 % degree of reduction with those received during the experiments at different superficial gas velocities. Again, the reduction time was recalculated in such a way that the elutriated material would also have a

degree of reduction of 95 %. The gray line depicts the theoretical minimum reduction time. As it is shown, the achieved reduction time is always quite close to the theoretical minimum value which can be achieved. It is clear that the specific gas rate increases slightly with increasing superficial gas velocities.
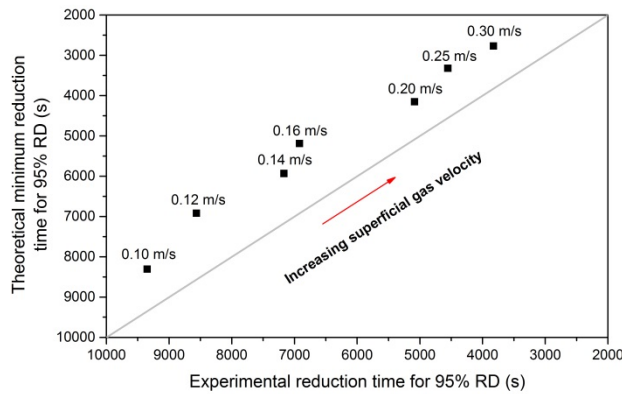
Figure 107: Comparison between experimental and theoretical minimum reduction time to reach 95 % degree of reduction for different superficial gas velocities.

6.2 Direct reduction of magnetite-based iron ore ultra-fines

As shown in the previous sections, hematite-based ultra-fines can be reduced by hydrogen to high degrees of reduction without any fluidization troubles at reduction temperatures up to 700 °C. With respect to magnetite-based ultra-fines, the situation is completely different. In natural state, the fluidization behavior is quite critical. Not even in cold state is a fluidization of the material possible without issues at low superficial gas velocities, compared to hematite-based concentrates. There are strong inter-particle forces acting that influence the fluidization behavior. This leads to the formation of channels where the gas passes through the material without fluidization of the material occurring. For that reason, the magnetite-based iron ore ultra-fines are investigated in terms of reducibility and fluidization behavior only in oxidized state. General information regarding the fluidization behavior and the kinetics of the oxidation of the magnetite-based iron ore ultra-fines is given in [192]. In the following section, only two different experiments with magnetite-based iron ore ultra-fines are shown and discussed.

6.2.1 Experimental conditions and materials

For the experiments with the magnetite-based iron ore ultra-fines, again the FBR 160 mm, explained in detail in Section 3.1.2, was used. Table 38 summarizes the process conditions of the two experiments discussed in this section. Experiment 1 is carried out at a reduction temperature of 700 °C with a superficial gas velocity of 0.2 m/s and an MgO addition of 150 g to the 5000 g of iron ore input. Experiment 2 is done at 600 °C reduction temperature with a

superficial gas velocity of 0.2 m/s and an MgO addition of 100 g to the 5000 g of iron ore input. Both experiments are carried out with pure hydrogen as the fluidization and reducing agent at an absolute pressure of 1.1 bar.

Table 38: Process conditions for the reduction of magnetite-based ultra-fines.

	Experiment 1	Experiment 2
Temperature (°C)	700	600
Pressure abs. (bar)	1.1	1.1
Gas composition (%-vol.)	100 H_2	100 H_2
Flow rate (l/min–SATP)	71.6	79.9
Superficial gas velocity (m/s)	0.2	0.2
MgO-addition (g)	150	100
Input mass iron ore (g)	5000	5000

Figure 108 shows the grain size distribution (left) and the polished micro-section of the natural magnetite (right). The grain size distribution is similar to that of the hematite-based iron ore ultra-fines used for previous investigations. The polished micro-section of the natural magnetite shows a very dense structure of the single particles. No pores can be observed inside the particles, in contrast to the hematite-based iron ore ultra-fines.
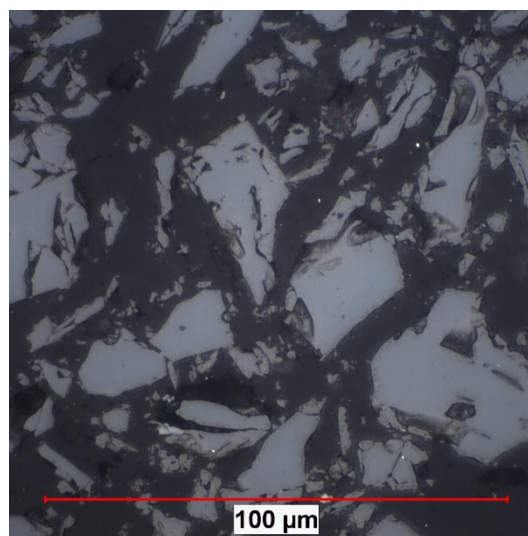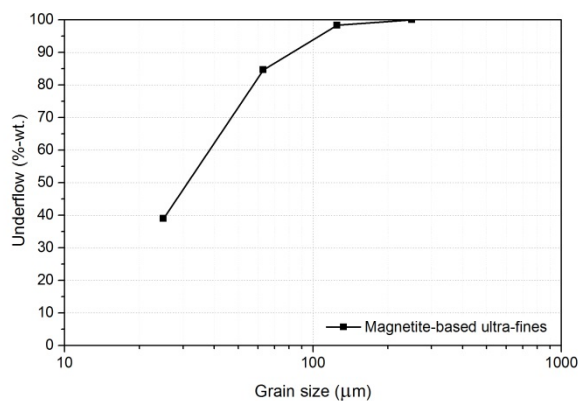
Figure 108: Grain size distribution (left) and polished micro section (right) of the iron ore input material (magnetite-based ultra-fines)[192].

Table 39 gives the chemical analysis of the magnetite-based ultra-fines used in natural and oxidized state. The oxidation is carried out in a heat treatment furnace at a temperature of 700 °C. To achieve a complete oxidation of the particles, the residence time of the particles at the given temperature is selected to be 6-8 h. According to the mass balance before and after the oxidation, a complete oxidation can be confirmed. To avoid a drastic change in the grain size distribution as a consequence of the oxidation procedure, the particles are sieved again after the oxidation treatment to destroy possible agglomerates formed.

Table 39: Chemical analysis of the magnetite-based iron ore ultra-fines in natural and fully oxidized state.

	Natural magnetite ultra-fines	Oxidized magnetite ultra-fines
Fe_{tot} (%-wt.)	65.65	63.86
Fe^{2+} (%-wt.)	21.50	0.90
CaO (%-wt.)	1.62	1.58
MgO (%-wt.)	1.04	1.01
SiO_2 (%-wt.)	3.33	3.24
Al_2O_3 (%-wt.)	1.16	1.13
Grain size (µm)	<125	<125
Mixture (%-wt.)	100	100
Mixture (g)	5000	5000

6.2.2 Results and discussion

The results of the reduction experiments are shown and discussed below. Figure 109 demonstrates the outcomes in terms of weight loss against reduction time (a, d), degree of reduction and metallization (smoothed) against reduction time (b, e) and the trends of measured and calculated pressure drop against reduction time (c, f) for both experiments. The most important information can be observed from the trends of the pressure drop against reduction time. In the case of 700 °C reduction temperature (Figure 109 (c)), a stable fluidization was achieved until approximately 2250 s reduction time. After that, the pressure drop across the material dropped down and the material became de-fluidized. One indicator for the de-fluidization is of course the measured pressure drop; the second one is the movement of the reactor during the experiments. If the material remains in fluidized state, the reactor system shakes. If the material becomes de-fluidized, the reactor movement can no longer be observed. This is one possibility to confirm the measured results of the pressure drop. As for the 700 °C reduction temperature, no reactor movement was observed after 2500 s reduction time. This is in good agreement with the measured values of the pressure drop across the material. As shown by the measured trend of the weight loss (Figure 109 (a)) and the calculated curves of degree of reduction and metallization (Figure 109 (b)), the de-fluidization occurred at a degree of reduction of approximately 80%. Although 150 g of MgO were added to the iron ore, it was not possible to achieve a complete, stable fluidization during the whole reduction procedure at 700 °C reduction temperature under the present process conditions, in contrast to the results obtained in Section 5. The main difference in this case is the lower grain size distribution, which ends in a higher specific surface of the particles. As a result, it seems that the amount of MgO addition is not enough to cover the surface of all particles. This decreases the positive effect of the MgO addition on the avoidance of the de-fluidization. There are two possibilities two improve the behavior. The first one is an increase in the MgO addition amount. This would not be beneficial from an industrial point of view, since higher amounts would lead to high MgO contents in the DRI product, which leads to a high MgO content in steelmaking slags. The second possibility is a decrease in the grain size distribution of the MgO powder. For that purpose, further

investigations are required. In this case, the fluidization behavior would be increased by a decrease in the reduction temperature with a simultaneous decrease in the MgO addition amount to 100g (2 %-wt. of the iron ore input). The results for 600 °C reduction temperature are provided in Figure 109 (d-f).
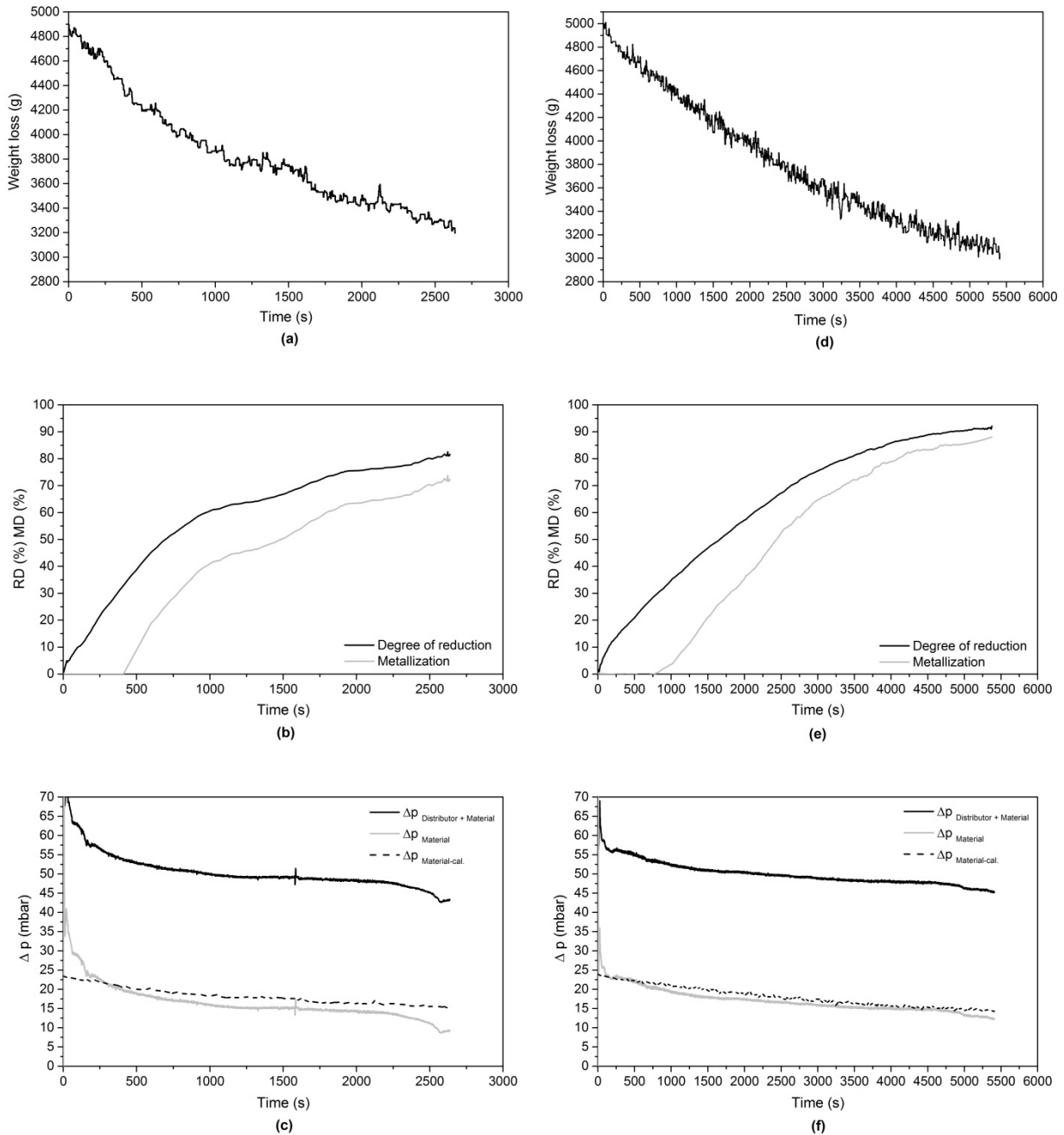
Figure 109: Experimental results of the two different experiments at different reduction temperatures: (a) weight loss against time 700 °C; (b) degree of reduction and metallization 700 °C; (c) measured pressure drop 700 °C; (d) weight loss against time 600°C; (e) degree of reduction and metallization 600 °C; (f) measured pressure drop 600 °C.

As shown by the trends of the pressure drop, at 600 °C a stable, complete fluidization was achieved until approximately 5000 s reduction time, which is in the range of 90 % degree of

reduction. After that, a short decrease in the pressure drop took place, signaling a partial de-fluidization of the material. During the experiment, a movement of the reactor was observed during the whole reduction procedure, still indicating a fluidization of the material. In fact, it was possible to reach a degree of reduction higher than 90 % without complete de-fluidization of the material. Further morphological investigations should confirm the results of the reduction experiments which are shown in Figure 110 for a reduction temperature of 600 °C. A degree of reduction higher than 90 % can be confirmed based on the polished micro sections. The SEM surface images clearly indicate a formation of agglomerates during the reduction procedure. Some of the agglomerates become larger than 200 μm. It is assumed that at the final stage of reduction, the size of some agglomerates became too big to be fluidized anymore. This might be the reason for the decreasing pressure drop at the end of the reduction procedure. An increase in the superficial gas velocity at the end of the reduction procedure might be the only solution to avoid the de-fluidization of the big agglomerates formed. This is also a topic for further research work.
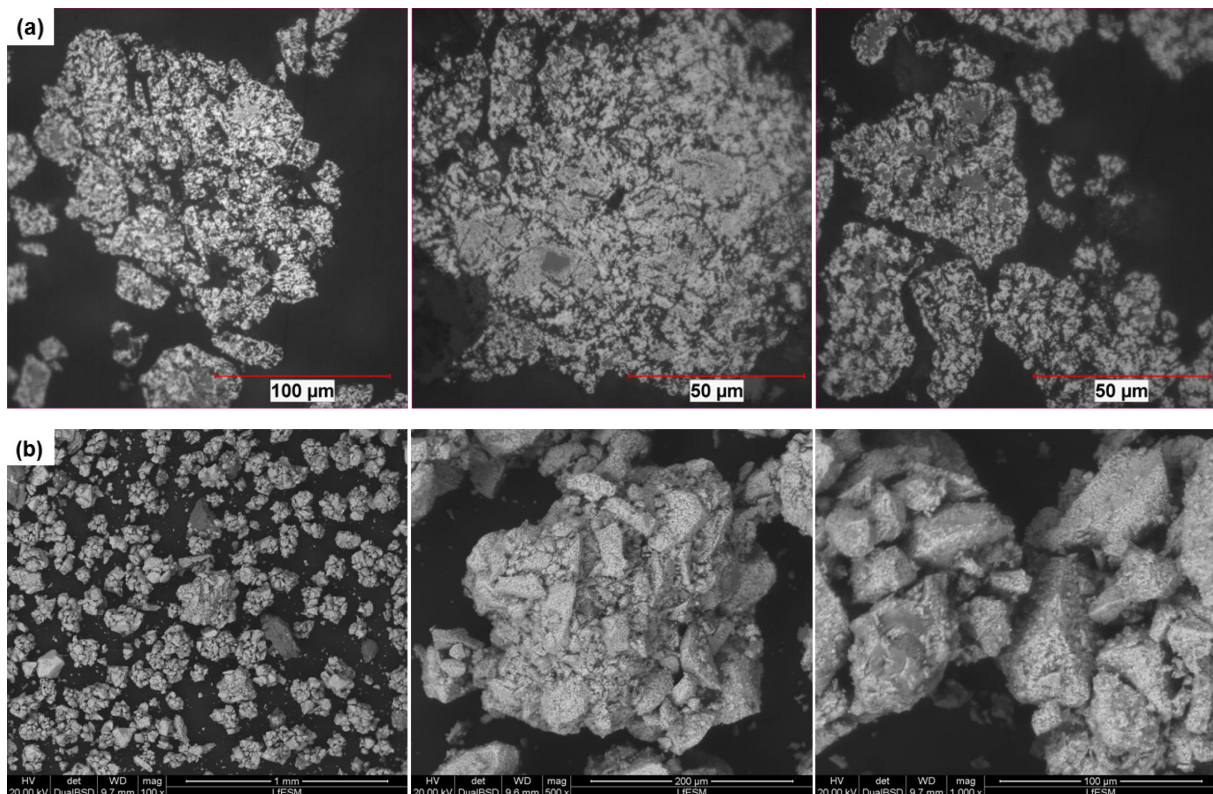
Figure 110: Morphological investigations of (partly) reduced samples of oxidized magnetite ultra-fines at 600 °C reduction temperature with 2 %-wt. amount of MgO addition: (a) Polished micro-section; (b) SEM surface images.

As a matter of fact, a lower reduction temperature is still beneficial for better fluidization behavior of the magnetite-based iron ore ultra-fines but it is also more challenging to treat this kind of iron ore compared to the hematite based iron ore ultra-fines. A lower reduction temperature and prior oxidation are still required; otherwise, a successful hydrogen-induced fluidized bed reduction of magnetite-based iron ore ultra-fines would not be possible.

7 Conclusion

Three main topics are investigated in this thesis; first, the kinetical behavior of different iron ore grades during hydrogen-induced fluidized bed reduction; second, the use of magnetite-based iron ores for during hydrogen-induced fluidized bed reduction and third, a direct use of iron ore ultra-fines for hydrogen-induced fluidized bed reduction. Based on the investigations, the following main conclusions can be drawn:

Kinetic investigation of hydrogen-induced fluidized bed reduction of iron ore fines– Section 4

Kinetic investigation of Ore A:

- The influence of kinetic limitation on the reduction rate decreases drastically with increasing reduction temperatures. At 800 °C reduction temperature it proceeds near the thermodynamic limitation while at 600 °C the deviation between thermodynamic limitation and experimental results is much bigger.
- The reduction kinetics of hematite during hydrogen-induced fluidized bed reduction cannot be described using only one simple gas-solid reaction model. The limiting factors vary with reduction temperature and degree of conversion. As a result, the apparent activation energy is not constant during the whole reduction procedure.
- A two-peak-shaped curve of apparent activation energy can be defined over the degree of reduction. The values of apparent activation energy vary from 11 to 55, 55 to 23 and 23 to 42 kJ/mol for the reduction from Fe_2O_3 to Fe_3O_4, Fe_3O_4 to FeO and FeO to Fe, respectively.
- The polished micro-sections show that at the beginning of the formation of metallic iron, the iron is formed uniformly and distributed over the whole particle area, indicating that diffusion of the reducing gas to the reaction interface does not limit the progress of reduction in this case.
- The multistep kinetic analysis using the JMA model shows that the initial stage of reduction might be controlled by reaction kinetics and diffusion, depending on the temperature. The reduction from FeO to Fe is limited by the chemical reaction and the process of nucleation, while the importance of the nucleation process increases

with increasing reduction temperatures. Moreover, diffusion is not important in the case of fluidized bed reduction from FeO to Fe using hydrogen as a reducing agent.

Other conclusions of further investigations (different iron ore grades and variation of process and material parameters):

- A stable fluidization of hematite and limonite-based iron ores is possible across the tested temperature range (600-800 °C) during the entire reduction process. Magnetite-based iron ores cannot be fluidized because sticking occurs immediately after the formation of first metallic iron.
- The dependence of instant re-oxidation of the reduced material on the reduction temperature after the first contact with oxygen from the air can be explained by the results of the kinetical analysis. If highly porous iron is formed at low reduction temperatures (limitation by chemical reaction, not nucleation), the product is vulnerable to re-oxidation.
- A high specific surface area of the initial iron ore is not necessarily a sign of good reducibility. The limonitic iron ore (Ore C) tested with the highest initial specific surface area showed the lowest reducibility potential compared to the hematite-based iron ores tested.
- The trends of apparent activation energies show the highest levels for the iron ores with the worst reducibility. As a result, lower E_a values represent an enhanced reducibility.
- An increased specific gas rate does not influence the general trend regarding the behavior of E_a or the kinetic analysis, however, in comparison with lower specific gas rate; the limitation by nucleation is also an important factor at low reduction temperatures.
- The change in grain size does not lead to a drastic change in reduction rate. Only at the final stage of reduction can a complete reduction be achieved earlier in case of lower particle size. Futhermore, the addition of different amounts of water vapor does not have a major effect on the reduction rate during hydrogen-induced fluidized bed reduction under the given process conditions.
- Kinetical investigations of the pre-reduction from hematite to magnetite and from hematite to wüstite were also carried out. The results show that in the case of reduction from hematite to magnetite, the progress of reduction is controlled by a mixture of chemical reaction and nucleation at lower tested temperatures, whereas at higher tested temperatures, the progress is limited by the chemical reaction only, under the given process conditions. For the reduction from hematite to wüstite, the first part of reduction, representing the conversion from hematite to magnetite, is controlled by the chemical reaction only. Afterwards, at lower tested temperatures, the progress of reduction is controlled by a mixture of chemical reaction and nucleation while at the highest temperature, only nucleation might control the progress.

The new method of applying the JMA model for analysis of the kinetics of the reduction using the fluidized bed technology developed within this section allows a simple analysis of the kinetics of the total reduction sequence, taking into account that more than one rate-limiting steps can act together in a parallel way. This is beneficial and quite unique compared to most other techniques for kinetical analysis reported in literature.

<u>Use of magnetite-based iron ore for hydrogen-induced fluidized bed reduction– Section 5</u>

From the investigations carried out in Section 5, the following main conclusions can be drawn:

- The fluidization of magnetite-based iron ores without any pre-treatment is not possible because at high reduction temperatures, immediately after the occurrence of first metallic iron, the particles tend to stick and a fast complete de-fluidization takes place. At lower reduction temperatures, the material also starts to de-fluidize but not completely and not as spontaneously as at higher reduction temperatures.

- A prior oxidation of the magnetite to Fe_2O_3 leads to an improvement of the fluidization behavior. At the lowest reduction temperature tested (600 °C), a complete and stable fluidization could be achieved. At higher reduction temperatures, the material also de-fluidized very fast and completely, immediately after the first metallic iron formation took place.

- The addition of MgO to the completely oxidized material improves the fluidization drastically. An MgO amount of 0.5 %-wt. was defined to be sufficient to ensure a stable fluidization behavior during the whole reduction procedure at a reduction temperature of 700 °C. With increasing reduction temperatures, the required MgO-amount also increases. The addition of MgO leads to a smoother surface structure of the particles, which is beneficial for the fluidization behavior.

- Because of the formation of small wüstite islands in the particles covered by a dense iron layer, the final reduction rate of the previously oxidized, MgO-doped samples is very low. A prior partial oxidation instead of a complete oxidation can prevent this drastic decrease in the reduction rate at the final stage. As a result, the best combination for treating magnetite-based iron ores during hydrogen-induced fluidized bed reductions is a prior partial oxidation in combination with an addition of MgO. This statement is only valid for the process conditions and iron ore employed.

In literature, the information available concerning a successful treatment of magnetite-based ores during fluidized bed reduction is limited. As a result, the information gained during the present investigations is a good basis which can be very helpful for the development of future ironmaking processes based on the fluidized bed technology.

<u>Use of iron ore ultra-fines for hydrogen-induced fluidized bed reduction– Section 6</u>

Based on the investigations carried out in Section 6, the following main conclusions can be drawn:

- In contrast to data reported in literature, a stable fluidization of hematite-based iron ore ultra-fines was achieved during the whole reduction procedure. Generally, such

materials are classified as poorly fluidizable. The typical sticking phenomenon was not observed during the reduction procedure under the tested process conditions.

- The calculated values of expected elutriation, shown by the calculations using the terminal velocity of the particles under the given process conditions, were much higher than the real values of elutriation occurring during the experiments. The use of elutriation rate constants for the prediction of the amount of elutriation provided more accurate results, but the results are still not extremely precise.

- The progress of reduction shows a high reduction rate until high degrees of conversion. The typical deceleration of the reduction rate at degrees of reduction around 70-80% cannot be observed. Especially at low superficial gas velocities, the reduction rate only slows down at very high degrees of reduction, larger than 95 %.

- The reduction proceeds near the thermodynamic limitation, especially at low superficial gas velocities. Consequently, gas utilizations can be achieved which are close to the theoretical maximum value.

- The required specific gas rate for reaching 95 % degree of reduction increases with increasing temperatures from approximately 1115 to 1400 m³ (SATP) hydrogen per ton of iron ore for 0.1 and 0.3 m/s, respectively.

- The treatment of magnetite-based iron ore ultra-fines is more critical than that of hematite-based ultra-fines. Although MgO was added to the iron ore mixture, a successful fluidization during the whole reduction procedure is difficult. At lower reduction temperature, representing 600 °C and the addition of MgO, high degrees of reduction can be achieved without de-fluidization.

The results obtained in this section, especially concerning the hematite-based ultra-fines are somehow unexpected. A stable fluidization during the whole reduction procedure at a reduction temperature of 700 °C can be achieved, which is in contradiction with all data reported in literature. These results can serve as a basis for the development of hydrogen based direct reduction process based on the use of iron ore ultra-fines, signifying a break-through ironmaking technology.

8 Outlook

The results obtained in this work deliver information regarding the kinetics during hydrogen-induced fluidized bed reduction and some general possibilities for a successful treatment of magnetite-based iron ore fines. The suitability of a direct use of iron ore ultra-fines for direct ironmaking was tested and as a result, it is still possible to treat these kinds of iron ore fines directly in a fluidized bed reactor.

Based on the results of the investigations, additional research should be carried out to gain further knowledge regarding hydrogen-based fluidized bed reduction:

- <u>Kinetic investigations:</u> Further variation of process parameters such as superficial gas velocity, composition of the reducing gas mixture and grain size of the iron ore particles in combination with a kinetical analysis by using different kinetical approaches should be carried out to verify the investigations conducted in this thesis.

- <u>Use of magnetite-based iron ore fines:</u> Further investigation of different oxidation procedures and their effect on the reducibility and fluidization behavior should be carried out. The parameters like oxidation temperature and degree of oxidation should be varied. In general, a more physical-based understanding of the oxidation mechanism should be gained. The effect of different superficial gas velocities and different particle sizes on the sticking behavior should also be investigated. The influence of different additives should also be investigated in more detail, e.g. a substitution of MgO by other additives like CaO or dolomite.

- <u>Use of iron ore ultra-fines:</u> In that case, the focus of further investigations should be on the treatment of magnetite-based iron ore ultra-fines. An optimum processing concept still has not been defined up to now. Therefore, further investigations regarding the effect of additives and on a stepwise increase in the superficial gas velocity on the fluidization behavior and the amount of elutriation should be pursued. A model for a better prediction of the elutriation should also be investigated. One further point that has to be studied in more detail is the formation of agglomerates. Therefore, it should be investigated which mechanisms are

responsible for the formation of the agglomerates and what the effect is on the further fluidization properties and the material elutriation.

The hydrogen-induced fluidized bed reduction of iron ore fines is an opportunity for sustainable ironmaking in the future which can fulfill the environmental requirements. There are still a lot of challenges that have to be solved for an industrial application, such as the supply of the enormous amounts of hydrogen or the further processing of hydrogen-based DR products. The importance of this technology will definitely increase in the near future.

9 List of references

[1] World Steel Association, *World Steel in Figures 2019*, https://www.worldsteel.org/steel-by-topic/statistics/steel-statistical-yearbook/World-Steel-in-Figures.html., accessed 03/2020.

[2] World Steel Association, *Steel statistical yearbook 2001*, https://www.worldsteel.org/steel-by-topic/statistics/steel-statistical-yearbook.html., accessed 01/2020.

[3] World Steel Association, *Steel statistical yearbook 2019*, https://www.worldsteel.org/steel-by-topic/statistics/steel-statistical-yearbook.html., accessed 01/2020.

[4] J.L. Schenk, H.B. Lüngen, *Stahl Eisen* **2016**, *136*, 41–47.

[5] European Environment Agency, *Greenhouse gas emission trend projections and target*, https://www.eea.europa.eu/data-and-maps/figures/greenhouse-gas-emission-trend-projections, accessed 02/2020.

[6] Hatch Beddows, *Ultrafine supply*, http://www.steelconsult.com/images/SteelConsult-International-01102018.pdf, accessed 02/2020.

[7] VDEh, *Hot metal and crude steel production*, https://www.vdeh.de/en/technology/steelmaking.html., accessed 01/2020.

[8] V. P. Lyalyuk, A. K. Tarakanov, D. A. Kassim, P. I. Otorvin, D. V. Pinchuk, *Steel Transl.* **2017**, *47*, 469–472.

[9] S. Nomura, T. G. Callcott, *ISIJ Int.* **2011**, *51*, 1033–1043.

[10] J. Schenk, *Particuology* **2011**, *9*, 14–23.

[11] Lockwood Greene, *Ironmaking Process Alternatives Screening Study, Volume I: Summary Report,* **2000**.

[12] S.-H. Yi, M.-E. Choi, D.-H. Kim, C.-K. Ko, W.-I. Park, S.-Y. Kim, *Ironmaking Steelmaking* **2019**, *46*, 625–631.

[13] C. Thaler, T. Tappeiner, Schenk J., W. L. Kepplinger, J. F. Plaul, S. Schuster, *steel research int.* **2012**, *83*, 181–188.

[14] Y. Qu, Z. Zou, Y. Xiao, *ISIJ Int.* **2012**, *52*, 2186–2193.

[15] A. Chatterjee, *Sponge Iron Production by Direct Reduction of Iron Oxide*, PHI Learning Private Limited, New Delhi **2012**.

[16] A. Shams, F. Moazeni, *JOM* **2015**, *67*, 2681–2689.

[17] A. Zugliano, A. Primavera, D. Pignattone, A. Martinis, presented at IAFC Symposium on Automation in Mining, Material and Metal Processing, San Diego, California **2013**.

[18] Midrex Technologies Inc., *World Direct Reduction Statistics,* **2018**.

[19] T. Buergler, I. Kofler, *Berg Huettenmaenn Monatsh* **2017**, *162*, 14–19.

[20] J. Kopfle, R. Hunter, *Ironmaking Steelmaking* **2013**, *35*, 254–259.

[21] M. Kirschen, K. Badr, H. Pfeifer, *Energy* **2011**, *36*, 6146–6155.

[22] S. A. Elmquist, P. Weber, H. Eichberger, *Stahl und Eisen* **2002**, *122*, 56–64.

[23] J.-P. Nepper, S. Sneyd, T. Stefan, J. Weckes, presented at 6 th ECIC, Düsseldorf **2011**.

[24] outokumpu, presented at IFSA, South Africa, **2002**.

[25] D. Nuber, H. Eichberger, B. Rollinger, *Stahl Eisen* **2006**, *126*, 47–51.

[26] W. Hillisch, J. Zirngast, *Steel Times Int.* **2001**, 20–22.

[27] R. Lucena, R. Whipp, W. Albarran, *Stahl Eisen* **2007**, *127*, 567–580.

[28] Downstreamconsulting, *Finmet*, http://www.downstreamconsulting.com.au/node/22, accessed 03/2020.

[29] D. Spreitzer, J. Schenk, *steel research int.* **2019**, *90*, 1–17.

[30] B. Weiss, J. Sturn, F. Winter, J. L. Schenk, *Ironmaking Steelmaking* **2013**, *36*, 212–216.

[31] A. Rist, N. Meysson, *J. Met.* **1967**, 50–59.

[32] A. Habermann, F. Winter, H. Hofbauer, J. Zirngast and J.L. Schenk, *ISIJ Int.* **2000**, *40*, 935–942.

[33] C. Feilmayr, A. Thurnhofer, F. Winter, H. Mali and J.L. Schenk, *ISIJ Int.* **2004**, *44*, 1125–1133.

[34] O. Levenspiel, *Chemical reaction engineering*, Wiley, New York, USA **1999**.

[35] H. E. L.v. Bogdandy, *Die Reduktion der Eisenerze*: *Wissenschaftliche Grundlagen und technische Durchführung*, Stahleisen, Düsseldorf, Germany **1967**.

[36] H. W. Gudenau, *Rheinisch-Westfälische Technische Hochschule Aachen, Institut für Eisenhüttenkunde* **1997**.

[37] M. Bahgat, M.H. Khedr, *Mat. Sci. Eng., B* **2007**, *138*, 251–258.

[38] H. Chen, Z. Zheng, Z. Chen, W. Yu, J. Yue, *Metall and Materi Trans B* **2017**, *48*, 841–852.

[39] A.A. El-Geassy, M.I. Nasr, *Trans. Iron Steel Inst. Jpn.* **1988**, *28*, 650–658.

[40] S.K. El-Rahaiby, Y.K. Rao, *Metall. Trans. B* **1979**, *10*, 257–269.

[41] A. Bondale, A. Henriquez, M. Manrique, *ISIJ Int.* **2005**, *45*, 1255–1260.

[42] A.A. El-Geassy, V. Rajakumar, *Trans. Iron Steel Inst. Jpn.* **1985**, *25*, 449–458.

[43] O. A. Teplov, *Russ. Metall. (Engl. Transl.)* **2012**, *1*, 8–21.

[44] R. Corbari, R.J. Fruehan, *Metall. Mater. Trans. B* **2010**, *41 B*, 318–329.

[45] K. Higuchi, R.H. Heerema, *ISIJ Int.* **2005**, *45*, 574–581.

[46] J. O. Edström, *J. Iron Steel Inst.* **1953**, 289–304.

[47] E.T. Turkdogan, J.V. Vinters, *Metall. Trans.* **1971**, *2*, 3175–3188.

[48] E.T. Turkdogan, J.V. Vinters, *Metall. Trans.* **1972**, *3*, 1561–1574.

[49] E.T. Turkdogan, R.G. Olson, J.V. Vinters, *Metall. Trans.* **1971**, *2*, 3189–3196.

[50] D. Liu, X. Wang, J. Zhang, Z. Liu, K. Jiao, X., R. Wang, *Metall. Res. Technol.* **2017**, *114*, 1–9.

[51] N. Thüns, B. M. Krooss, Q. Zhang, H. Stanjek, *Int. J. Hydrogen Energy* **2019**, *44*, 27615–27625.

[52] K. Sato, Y. Ueda, Y. Nishikawa, T. Goto, *ISIJ Int.* **1986**, 697–703.

[53] E. Kawasaki, J. Sanscrainte, T. J. Walsh, *AIChE J.* **1962**, *8*, 48–52.

[54] E.T. Turkdogan, J. V. Vinters, *Can. Metall. Q.* **1973**, *12*, 9–21.

[55] H. Zuo, C. Wang, J. Dong, K. Jiao, R. Xu, *Int. J. Miner., Metall. Mater.* **2015**, *22*, 688–696.

[56] E. Mazanek, S. Jasienska, A. Brachuey, C. Bryk, *Metal. Odlew.* **1982**, *8*, 53–70.

[57] R. Steffen, K.-H. Tacke, W. Pluschkell, *Grundlagenuntersuchungen zur umweltfreundlichen Reduktion von Eisenerz mit Wasserstoff oder wasserstoffreichen Gemischen*, Europäische Kommission, Luxemburg **1998**.

[58] W. H. Kim, S. Lee, S.M. Kim, D.J. Min, *Int. J. Hydrogen Energy* **2013**, *38*, 4194–4200.

[59] E. Lorente, J. Herguido, J.A. Pena, *Int. J. Hydrogen Energy* **2011**, *36*, 13425–13434.

[60] F. Chen, Y. Mohassab, T. Jiang, H.Y. Sohn, *Metall. Mater. Trans. B* **2015**, *46B*, 1133–1145.

[61] M. Skorianz, *PhD thesis,* Montanuniversitaet Leoben **2012**.

[62] B. Weiss, *PhD thesis,* Technische Universität Wien **2008**.

[63] H. Mali, B. Spuida, *Berg- Huettenmaenn. Monatsh.* **2013**, *158*, 47–52.

[64] H. T. Wang, H. Y. Sohn, *Ironmaking Steelmaking* **2013**, *38*, 447–452.

[65] B. B. L. Seth, H. U. Ross, *Can. Metall. Q.* **1963**, *1*, 15–30.

[66] P. K. Strangway, H. U. Ross, *Can. Metall. Q.* **1965**, *4*, 97–111.

[67] L.H. Hsieh, J.A. Whiteman, *ISIJ Int.* **1989**, *29*, 24–32.

[68] E. Mazanek, M. Wyderko, *Archiv Eisenhüttenwesen* **1976**, *47*, 457–463.

[69] A. Cores, A. Babich, M. Muniz, S. Ferreira, J. Mochon, *ISIJ Int.* **2010**, *50*, 1089–1098.

[70] U.S. Yadav, B.D. Pandey, B.K. Das, D.N. Jena, *Ironmaking Steelmaking* **2013**, *29*, 91–95.

[71] Y. Kapelyushin, Y. Sasaki, J. Zhang, S. Jeong, O. Ostrovski, *Metall. Mater. Trans. B* **2017**, *48*, 889–899.

[72] Y. Kapelyushin, X. Xing, J. Zhang, S. Jeong, Y. Sasaki, O. Ostrovski, *Metall. Mater. Trans. B* **2015**, *46*, 1175–1185.

[73] T. Paananen, K. Heinänen, J. Härkki, *ISIJ Int.* **2003**, *43*, 597–605.

[74] H.W. Gudenau, J. Fang, T. Hirate, U. Gebel, *Steel Res.* **1989**, *60*, 138–144.

[75] S. EL Moujahid, A. Rist, *Metall. Trans. B* **1988**, *19*, 787–802.

[76] S. P. Matthew, T. R. Cho, P. C. Hayes, *Metall. Mater. Trans. B* **1990**, *21 B*, 733–741.

[77] B. Zhang, X. Gong, Z. Wang, Z. Guo, *ISIJ Int.* **2011**, *51*, 1403–1409.

[78] H.W. Gudenau, J. Hochhaus, R. Degel, presented at 9. Aachener Stahlkolloquium, Aachen **1994**.

[79] A. Habermann, *PhD thesis,* Technische Universität Wien **2001**.

[80] L. Guo, S. Zhong, Q. Bao, J. Gao, Z. Guo, *Metals* **2019**, *9*, 750.

[81] F. Lu, L. Wen, J. Li, J. Wei, J. Xu, S. Zhang, *Comput. Mater. Sci* **2016**, *125*, 263–270.

[82] K. S. Abdel Halim, M. Bahgat, H. A. El-Kelesh, M. I. Nasr, *Ironmaking Steelmaking* **2013**, *36*, 631–640.

[83] X. Gong, Z. Zhao, Z. Wang, B. Zhang, L. Guo, Z. Guo, *Metall and Materi Trans B* **2016**, *47*, 1137–1146.

[84] R. J. Fruehan, Y. Li, L. Brabie, E. J. Kim, *Scand. J. Metall.* **2005**, *34*, 205–212.

[85] A. Pineau, N. Kanari, I. Gaballah, *Thermochim. Acta* **2006**, *447*, 89–100.

[86] M. Sastri, R.P. Viswanath, B. Viswanathan, *Int. J. Hydrogen Energy* **1982**, *7*, 951–955.

[87] G. Munteanu, L. Ilieva, D. Andreeva, *Thermochim. Acta* **1999**, *329*, 157–162.

[88] G. Munteanu, L. Ilieva, D. Andreeva, *Thermochim. Acta* **1997**, *291*, 171–177.

[89] M.H. Abd Elhamid, M.M. Khader, A.E. Mahgoub, B.E. El Anadouli, B.G. Ateya, *J. Solid State Chem.* **1996**, *123*, 249–254.

[90] H.Y. Lin, Y.W. Chen, C. Li, *Thermochim. Acta* **2003**, *400*, 61–67.

[91] A.A. Barde, J.F. Klausner, R. Mei, *Int. J. Hydrogen Energy* **2016**, *41*, 10103–10119.

[92] G.Y. Lee, J.P. Choi, J.I. Song, S.S. Jung, J.S. Lee, *Mater. Trans.* **2014**, *55*, 1611–1617.

[93] S. K. Kuila, R. Chatterjee, D. Ghosh, *Int. J. Hydrogen Energy* **2016**, *41*, 9256–9266.

[94] S.K. Kuila, S. Chaudhuri, R. Chatterjee, D. Ghosh, presented at ICChE, Dhaka, Bangladesh **2014**.

[95] W. K. Jozwiak, E. Kaczmarek, T. P. Maniecki, W. Ignaczak, W. Maniukiewicz, *Appl. Catal., A* **2007**, *326*, 17–27.

[96] B. Hou, H. Zhang, H. Li, Q. Zhu, *Chin. J. Chem. Eng.* **2012**, *20*, 10–17.

[97] M. Pijolat, L. Favergeon, M. Soustelle, *Thermochim. Acta* **2011**, *525*, 93–102.

[98] P. Simon, *J. Therm. Anal. Calorim.* **2004**, *76*, 123–132.

[99] A. Ortega, *Int. J. Chem. Kinet.* **2001**, *6*, 343–353.

[100] A. Pineau, N. Kanari, I. Gaballah, *Thermochim. Acta* **2007**, *456*, 75–88.

[101] K. Piotrowski, K. Mondal, H. Lorethova, L. Stonawski, T. Szymanski, T. Wiltowski, *Int. J. Hydrogen Energy* **2005**, *30*, 1543–1554.

[102] Z. Wang, Z. Liu, J. Tang, M. Chu, X. Xue, *J. Iron Steel Res. Int.* **2014**, *21*, 16–23.

[103] A. Khawam, D. R. Flanagan, *J. Phys. Chem. B* **2006**, *110*, 17315–17328.

[104] A. Khawam, D.R. Flanagan, *Thermochim. Acta* **2005**, *429*, 93–102.

[105] A. Ortega, *Thermochim. Acta* **1996**, *284*, 379–387.

[106] B. Janković, B. Adnađević, J. Jovanović, *Thermochim. Acta* **2007**, *452*, 106–115.

[107] G. Munteanu, P. Budrugeac, L. Ilieva, T. Tabakova, D. Andreeva, E. Segal, *J. Mater. Sci.* **2003**, *38*, 1995–2000.

[108] K. Piotrowski, K. Mondal, T. Wiltowski, P. Dydo, G. Rizeg, *Chem. Eng. J.* **2007**, *131*, 73–82.

[109] E. Nyankson, L. Kolbeinsen, *IJERT* **2015**, *4*, 934–940.

[110] M.J. Tiernan, P.A. Barnes, G.M.B. Parkes, *J. Phys. Chem. B* **2001**, *105*, 220–228.

[111] W. Du, S. Yang, F. Pan, J. Shangguan, J. Lu, S. Liu, H. Fan, *J. Chem.* **2017**, 1–11.

[112] M. Shimokawabe, R. Furuichi, T. Ishii, *Thermochim. Acta* **1979**, *28*, 287–305.

[113] Y. D. Wang, X. N. Hua, C. C. Zhao, T. T. Fu, W. Li, W. Wang, *Int. J. Hydrogen Energy* **2017**, *42*, 5667–5675.

[114] X. Hua, W. Wang, F. Wang, *Front. Environ. Sci. Eng.* **2015**, *9*, 1130–1138.

[115] I.J. Moon, C.H. Rhee, D.J. Min, *Steel Res.* **1998**, *69*, 302–306.

[116] D. Kunii, O. Levenspiel, *Fluidization Engineering*, Butterworth-Heinemann, Stoneham **1991**.

[117] J. Schenk, *Vorlesungsskriptum "Spezielle metallurgische Prozesstechnik", Montanuniversitaet Leoben,* **2016**.

[118] H. A. Khawaja, *Int. J. Multiphys.* **2015**, *9*, 397-408.

[119] L. Reh, *Chem.-Ing.-Tech.* **1977**, *49*, 786–795.

[120] J. R. Grace, *Can. J. Chem. Eng.* **1986**, *64*, 353–363.

[121]   D. Geldart, *Gas Fluidization Technology*, John Wiley and Sons, Chichester, New York, Toronto, Singapore **1986**.

[122]   D. Geldart, *Powder Technol.* **1973**, *5*, 285–292.

[123]   S. Kaliyaperumal, S. Barghi, L. Briens, S. Rohani, J. Zhu, *Particuology* **2011**, *9*, 279–287.

[124]   Y. Mawatari, Y. Tatemoto, K. Noda, *Powder Technol.* **2003**, *131*, 66–70.

[125]   C. Xu, J. Zhu, *Chem. Eng. Sci.* **2005**, *60*, 6529–6541.

[126]   S. Shaul, E. Rabinovich, H. Kalman, *Powder Technol.* **2012**, *228*, 264–271.

[127]   S. Shaul, E. Rabinovich, H. Kalman, *Part. Sci. Technol.* **2014**, *32*, 197–205.

[128]   J. Szekely, J. W. Evans, H. Y. Sohn, *Gas-Solid Reactions*, Academic Press, INC. LTD., London **1976**.

[129]   C. Y. Wen, Y. H. Yu, *AIChE J.* **1966**, *12*, 610-612.

[130]   A. Anantharaman, R. A. Cocco, J. W. Chew, *Powder Technol.* **2018**, *323*, 454–485.

[131]   A. Haider and O. Levenspiel, *Powder Technol.* **1989**, *58*, 63–70.

[132]   C. Y. Wen, R. F. Hashinger, *AIChE J.* **1960**.

[133]   J. Li, T. Nakazato, K. Kato, *Chem. Eng. Sci.* **2004**, *59*, 2777–2782.

[134]   J. H. Choi, Suh, J.M., Chang, I.Y., D. W. Shun, C. K. Yi, J. E. Son, S. D. Kim, *Powder Technol.* **2001**, *121*, 190–194.

[135]   J. W. Chew, A. Cahyadi, C. M. Hrenya, R. Karri, R. A. Cocco, *Chem. Eng. J.* **2015**, *260*, 152–171.

[136]   D. Geldart, J. Baeyens, *Powder Technol.* **1985**, *42*, 67–78.

[137]   A.E. Qureshi, D. E. Creasy, *Powder Technol.* **1979**, *22*, 113–119.

[138]   N. Dİlmaç, S. Yörük, Ş. M. Gülaboğlu, *Metall and Materi Trans B* **2015**, *46*, 2278–2287.

[139]   L. Guo, H. Gao, J.-t. Yu, Z.-l. Zhang, Z.-c. Guo, *Int J Miner Metall Mater* **2015**, *22*, 12–20.

[140]   S. He, H. Sun, C. Hu, J. Li, Q. Zhu, H. Li, *Powder Technol.* **2017**, *313*, 161–168.

[141]   J.-m. Pang, P.-m. Guo, P. Zhao, *J. Iron Steel Res. Int.* **2015**, *22*, 391–395.

[142]   S. Schuster, C. Pawlik, F. Winter, H. Mali, Fischer H., J. L. Schenk, *AISTech Proceedings* **2006**, 297–307.

[143]   A. Thurnhofer, M. Schachinger, F. Winter, H. Mali, J. Schenk, *ISIJ Int.* **2005**, *45*, 151–158.

[144]   B. Weiss, J. Sturn, S. Voglsam, S. Strobl, H. Mali, F. Winter, J. Schenk, *steel research int.* **2010**, *81*, 93–99.

[145]   H. Chen, Z. Zheng, Z. Chen, X. T. Bi, *Powder Technol.* **2017**, *316*, 410–420.

[146]   L. Guo, Q. Bao, J. Gao, Q. Zhu, Z. Guo, *ISIJ Int.* **2020**, 1–17.

[147]   B. Zhang, Z. Wang, X. Gong, Z. Guo, *Powder Technol.* **2012**, *225*, 1–6.

[148]   Y. Zhong, J. Gao, Z. Guo, Z. Wang, in *Iron Ores and Iron Oxide Materials* (Ed: V. Shatokha), InTech **2018**.

[149]   Z. Du, Q. Zhu, C. Fan, F. Pan, H. Li, Z. Xie, *steel research int.* **2016**, *87*, 789–797.

[150]   Y. Zhong, Z. Wang, Z. Guo, Q. Tang, *Powder Technol.* **2012**, *230*, 225–231.

[151]   S. Hayashi, Y. Iguchi, *ISIJ Int.* **1992**, *32*, 962–971.

[152]   J. Shao, Z. Guo, H. Tang, *steel research int.* **2013**, *84*, 111–118.

[153]   L. Guo, J. Tang, H. Tang, Z. Guo, presented at Joint 3rd UK-China Steel Research Forum & 15th CMA-UK Conference on Materials Science and Engineering **2015**.

[154]   Y. Zhong, Z. Wang, Z. Guo, Q. Tang, *Powder Technol.* **2013**, *241*, 142–148.

[155]   L. Guo, Y. Zhong, J. Gao, Z. Yang, Z. Guo, *Powder Technol.* **2015**, *284*, 210–217.

[156]   L. Guo, Z. Yang, J. Gao, Y. Zhong, Z. Guo, *ISIJ Int.* **2016**, *56*, 736–743.

[157]   Z. Zhao, H. Tang, B. Zhang, Z. Guo, *Sci. China Technol. Sci.* **2012**, *55*, 3029–3035.

[158]   J. Fang, *Stickingprobleme im Fluidatbett zur Schmelzreduktion,* RWTH Aachen, Aachen **1988**.

[159]   X. Gong, B. Zhang, Z. Wang, Z. Guo, *Metall and Materi Trans B* **2014**, *45*, 2050–2056.

[160]   S. Hayashi, S. Sawai, Y. Iguchi, *ISIJ Int.* **1993**, *33*, 1078–1087.

[161]   Q. Xu, H. Wang, Y. Fu, J. Wang, *ISIJ Int.* **2016**, *56*, 1929–1937.

[162]   Y. Zhong, Z. Wang, Z. Guo, Q. Tang, *Powder Technol.* **2014**, *256*, 13–19.

[163]   Y.-W. Zhong, Z. Wang, X. Gong, Z. Guo, *Ironmaking Steelmaking* **2012**, *39*, 38–44.

[164]   D. Spreitzer, J. Schenk, *Metall and Materi Trans B* **2019**, *12*, 2471–2484.

[165]   D. Spreitzer, J. Schenk, *Particuology* **2020**, 52, 36-46.

[166]   D. Spreitzer, *Optimierung der Prozessparameter für die Reduktion von Feineisenerzen mittels Wirbelschichtverfahren,* Montanuniversitaet Leoben, Leoben **2016**.

[167]   F. Hauzenberger, J. Reidetschläger, J. Schenk, H. Mali, *Berg- Huettenmaenn. Monatsh.* **2004**, *149*, 385-392.

[168]   M. Skorianz, H. Mali, A. Pichler, F. Plaul, J. Schenk, B. Weiss, *steel research int.* **2016**, *87*, 633–641.

[169]   A. Pichler, H. Mali, F. Plaul, J. Schenk, M. Skorianz, B. Weiss, *steel research int.* **2016**, *87*, 642–652.

[170]   VDI-Gesellschaft Verfahrenstechnik und Chemieingenieurwesen, *VDI Heat Atlas*, Springer-Verlag, Berlin Heidelberg **2010**.

[171]   M. Avrami, *J. Chem. Phys.* **1939**, *7*, 1103–1112.

[172]   M. Avrami, *J. Chem. Phys.* **1940**, *8*, 212–224.

[173]   M. Avrami, *J. Chem. Phys.* **1941**, *9*, 177–184.

[174]   W. A. Johnson, R. F. Mehl, *Trans. AIME* **1939**, *135*, 416–458.

[175]   J. Malek, *Thermochim. Acta* **1995**, *267*, 61–73.

[176]   H. J. Cho, M. Tang, P. C. Pistorius, *Metall and Materi Trans B* **2014**, *45*, 1213–1220.

[177]   E. R. Monazam, R. W. Breault, R. Siriwardane, *Ind. Eng. Chem. Res.* **2014**, *53*, 13320–13328.

[178]   T. K. Sandeep Kumar, N. N. Viswanathan, H. Ahmed, A. Dahlin, C. Andersson, B. Bjorkman, *Metall and Materi Trans B* **2019**, *50*, 150–161.

[179]   M. Tang, H. J. Cho, P. C. Pistorius, *Metall and Materi Trans B* **2014**, *45*, 1304–1314.

[180]   D. Zhu, C. Yang, J. Pan, X. Li, *Metall and Materi Trans B* **2016**, *47*, 2919–2930.

[181]   S. Song, P. C. Pistorius, *ISIJ Int.* **2019**, *59*, 1765–1769.

[182]   A. Carpenter, *CO2 abatement in the iron and steel industry*, IEA Clean Coal Centre, London **2012**.

[183]   K. Meyer, *Pelletizing of iron ores*, Stahleisen m.b.H., Düsseldorf **1980**.

[184]   W. Schlebusch, Strohmeier Gerolf, W. Gerlach, T. Schwalm, *Stahl Eisen* **1998**, *118*, 115–121.

[185]   C. Lei, Q. Zhu, H. Li, *Chem. Eng. Sci.* **2014**, *118*, 50–59.

[186]   J. Li, J. Kong, S. He, Q. Zhu, H. Li, *Chem. Eng. Sci.* **2018**, *177*, 455–463.

[187]   H. Liu, L. Zhang, T. Chen, S. Wang, Z. Han, S. Wu, *Chem. Eng. J.* **2015**, *262*, 579–587.

[188]   Y. Zhong, J. Gao, Z. Wang, Z. Guo, *ISIJ Int.* **2017**, *57*, 649–655.

[189]   L. Lin, J. T. Sears, C. Y. Wen, *Powder Technol.* **1980**, *27*, 105–115.

[190]   D. Geldart, A.C.Y. Wong, *AIChE Symp. Ser* **1987**, *255*, 1–9.

[191]   S. M. Tasirin, D. Geldart, *Chem. Eng. Commun.* **1999**, *173*, 175–195.

[192]   T. Wolfinger, *Bestimmung der Korrelation zwischen Oxidation und Reduktion von magnetitischem Eisenerzkonzentrat,* Montanuniversitaet Leoben, Leoben **2018**.

Appendix

A.1 Publications

Journal publications related to this work

D. Spreitzer and J. Schenk, Reduction of Iron Oxides with Hydrogen–A Review, *steel research international*, **2019**, 90, 1-17.

D. Spreitzer and J. Schenk, Iron Ore Reduction by Hydrogen Using a Laboratory Scale Fluidized Bed Reactor: Kinetic Investigations–Experimental Setup and Method for Determination, *Metallurgical and Materials Transactions B*, **2019**, 50, 5, 2471-2484.

D. Spreitzer and J. Schenk, Fluidization behavior and reducibility of iron ore fines during hydrogen-induced fluidized bed reduction, *Particuology*, **2020**, 52, 36-46.

Conference paper related to this work

A. Sormann, J. Schenk, M. Naseri, M.A. Zarl and D. Spreitzer, The way to a carbon free steelmaking, *Multidisciplinary international conference advances in metallurgical processes and material*s, Kiev, Ukrain, **2018**.

Other journal publications

T. Wolfinger, D. Spreitzer, M.A. Zarl, A. Pichler and J. Schenk, KIC RawMaterials: Iron Balance-Austria, *Berg- und Hüttenmännische Monatshefte*, **2019**, 164, 4, 183-187.

N. Naseri, J. Schenk, D. Spreitzer and M.A. Zarl, Slag Formation during Reduction of Iron Oxide using Hydrogen Plasma Smelting Reduction, *Materials*, **2020**, 13, 4, 1-25.